Monte-Carlo simulation of phase transition in the vortex system of high-temperature superconductors (A review)

M. E. Gracheva, M. V. Katargin, V. A. Kashurnikov, and I. A. Rudnev

*Moscow State Engineering Physics Institute (Technical University), 115409 Moscow, Russia**
(Submitted March 25, 1997; revised June 23, 1997)
Fiz. Nizk. Temp. **23**, 1151–1161 (November 1997)

Recent publications on the Monte-Carlo simulation of vortex systems in HTS are reviewed. Dependences of the main parameters of the vortex state (such as energy, heat capacity, thermal motion, and structural order parameter) on extrinsic parameters (temperature and magnetic field) are described. The vortex glass phase, the influence of defects on phase diagrams, as well as the main phase transitions in two- and three-dimensional vortex structures including melting and $2D$-$3D$ transition are considered. © *1997 American Institute of Physics.* [S1063-777X(97)00111-4]

INTRODUCTION

The discovery of superconductors with a high superconducting transition temperature stimulated interest towards the nature of the mixed state in which a superconductor exists with a nonuniform magnetic field in the bulk of the material.

The H-T phase diagram of traditional low-temperature superconductors contains a region of mixed state[1] bounded by the temperature dependences $H_{c2}(T)$ and $H_{c1}(T)$ of the upper and lower critical fields. In high-temperature superconductors (HTS materials), the combination of high temperatures, small coherence length, and strong anisotropy in the properties enhances the role of thermal fluctuations for magnetic flux lines, leading to noticeable changes in the nature and phase diagram of the mixed state. The most significant effect of inclusion of thermal fluctuations is manifested in the possibility of the vortex lattice melting and transition to a flux liquid at temperatures much lower than the superconducting transition temperature.[2,3] The phase diagram acquires a region occupied by the flux liquid.[4] The presence of defects in the material leads to vortex line pinning increasing the number of possible vortex states. For example, disordering of the vortex lattice leads to its transition to vortex glass.[5–8] It should be noted that fluctuations in traditional superconductors are also being studied intensely by using various approaches (see, for example, Refs. 9, 10), which are based on the standard analysis of the Ginzburg-Landau functional described by the order parameter Ψ. An analysis of fluctuations $\langle|\Psi|^2\rangle$ for magnetic fields close to H_{c2} and a large Ginzburg number leads to points at which the value of $\langle|\Psi|^2\rangle$ increases at $T<T_c$, which can be attributed to melting of the Abrikosov lattice.[9,10] In our opinion, the descriptions of thermal fluctuations in the mixed state on the basis of the ensemble of vortex lines and with the help of order parameter fluctuations form two different approaches to the explanation of the same physical phenomenon, viz., disappearance of the long-range order in a superconducting system in a magnetic field at a temperature lower than the superconducting transition temperature.

It was proved in Refs. 4–6 that flux liquid freezing and transition to vortex glass (i.e., to a disordered vortex lattice) in defective superconducting crystals, as well as the formation of a vortex lattice for H_{c2}, occurs through a continuous second-order phase transitions. On the other hand, if was found that melting of a vortex lattice in the absence of pinning and in the presence of thermal fluctuations is a first-order thermodynamic transition.[11]

The existence of a layered structure in HTS materials complicates the phase diagram still further. The melting of the vortex lattice in layered materials occurs through two independent stages: a transition of the vortex lattice to a flux liquid (melting curve $T_m(H)$) and the loss of coherence between layers within a vortex line, viz., the ''decoupling'' transition (the coherence loss curve $T_{dc}(H)$).[12–14] Moreover, a transition of a flux liquid to two-dimensional vortex ''pancakes'' ($3D$-$2D$ transition) can also be a second-order transition.[14] The phase ratio can be different depending on the residual or induced pinning. Residual pinning is the term applied to natural defects in a superconductor formed during its synthesis, while induced defects are those caused by external action on the superconductor (irradiation, pressure, etc.). The curves on the phase diagram bounding regions of a vortex lattice, vortex glass, and flux liquid as well as the coherence loss curve might be displaced relative to one another, coincide and even intersect.

The structure of various vortex structures and the type of phase transitions between them have become the central problem in the physics of mixed state, attracting serious attention of the scientists.[15–19]

An experimental proof of the fact that vortex melting is a first-order transition was obtained for the first time from the observation of a kink on the curve of resistive transition in a pure crystal of $YBa_2Cu_3O_7$ (YBCO) in a magnetic field.[20–25] In spite of clarity and definiteness of the experiments, their interpretation is doubtful since resistance is a dynamic characteristic of the material, and hence cannot be used for determining the type of transitions between different thermodynamic phases. A true first-order phase transition must have the following thermodynamic features: latent heat and a jump in specific volume or density, which was demonstrated by Zeldov *et al.*[26] In their experiment, a series of miniature Hall probes was used to carry out local measurements of magnetic induction in a pure $Bi_2Sr_2CaCu_2O_x$ single crystal, and it was shown that a jump in the local vortex

density (which is a thermodynamic parameter) is observed in the range of low fields $H<380$ G. This jump was interpreted by these authors as a proof of the fact that vortex lattice melting occurs as a first-order phase transition. Proceeding from this assumption, the melting curve for the pure $Bi_2Sr_2CaCu_2O_x$ single crystal was determined as well as the critical point above which no jump in the vortex density is observed (on the field scale). A similar critical point was observed in experiments with YBCO.[25] A possible reason behind the emergence of the critical point on the melting curve of a vortex medium lies in the influence of residual disorder or pinning on vortex lines. As a result, translational correlations in an Abrikosov vortex lattice are confined in actual practice to a maximum size determined by the degree of disorder.[27]

Subsequent publications[28–30] confirmed the existence of a magnetic induction jump detected not only in local, but also in macroscopic measurements of magnetization.[26,31,32]

A thermodynamic proof of the existence of a first-order phase transition was also obtained for $YBa_2Cu_3O_7$ single crystal from equilibrium magnetization measurements.[33,34] Moreover, it was proved in a recent communication[35] that the results obtained from resistive and magnetic measurements carried out simultaneously in $Bi_2Sr_2CaCu_2O_x$ single crystal are identical and indicate a first-order phase transition.

However, Nelson,[27] who did not deny the fact of magnetic induction jump, doubted the conclusion concerning the vortex lattice melting. He believed that the jump is not a convincing proof of lattice melting since the observed jump lies in the reversible region of the magnetization curve. Besides, the melting curve is separated from the irreversibility line which is determined by the Bean–Livingston barrier rather than by depinning under the given conditions. Thus, Nelson stated that the magnetic induction jump indicates not melting, but ''decoupling'', which is also a first-order transition.

A direct observation of vortex lattice melting was carried out (without determining the phase-transition type) with the help of a small-angle neutron scattering.[36] It was shown that diffraction peaks disappear at field values much lower than $H_{c2}(T)$. The results correspond to the Lindemann criterion of melting with the parameter $C_L=0.15$.

Difficulties involved in an analysis of the phase diagram of a vortex structure based on the Lindemann/melting criterion or some other physical approaches (see, for example, Refs. 4, 37, 38), the lack of a consistent theory of melting, and a large number of external factors that must be taken into account necessitate the application of numerical methods including the Monte Carlo technique.[39–47]

1. SIMULATION OF A VORTEX LATTICE

In most cases, the behavior of a lattice of Abrikosov vortices in HTS materials is analyzed by using computer simulation based on the Monte Carlo (MC) method.[41–51] The standard Metropolice algorithm is used in such cases.[52] The Ginzburg–Landau functional is normally treated as a Hamiltonian of interacting particles (such an approach is substantiated, for example, in Ref. 53).

In the case of a two-dimensional ($2D$) problem, vortices are regarded as classical particles with a long-range interaction on a planar mesh. For example, in Refs. 41–43, 45, 47–49, $2D$ vortex systems were simulated by using the following effective Hamiltonian:

$$H=\frac{1}{2}\sum_{i,j}\ (n_i-f\ )(n_j-f\ )V(\mathbf{x}_i-\mathbf{x}_j), \tag{1}$$

where the sum is taken over a discrete mesh whose **i** nodes can be either empty ($n_i=0$) or contain a vortex ($n_i=1$)[41,43,45,48] or an antivortex ($n_i=-1$) as in models of a Coulomb lattice gas.[47,49] Here f is the phonon charge density defined as

$$f=(\sqrt{3}a_0^2/2)(B/\Phi_0),$$

where B is the magnetic field, $\Phi_0=2.0679\cdot 10^{-15}T\cdot \mathrm{m}^2$ the magnetic flux quantum, a_0 the triangular lattice constant, and $V(r)$ the two-dimensional lattice potential ($2D$ potential) which is the solution of the equation

$$\Delta_{x,y}V(\mathbf{x})=-2\pi\delta_{x,0} \tag{2}$$

with $V(\infty)=0$.[48]

While modeling a layered superconductor, we consider a system of parallel plates pierced by vortex filaments. In each plane, the problem is formulated in the same way as in the $2D$ case. For superconducting layers, we assume that within a vortex line vortex points interact only with two nearest neighbors above and below the given point in the plane. In Refs. 41, 43, a model system was simulated by using the following potential:

$$V_i^{z,z+1}=\begin{cases} U_0\left[\dfrac{|r_i^{z,z+1}|}{r_g}-2\right], & |r_i^{z,z+1}|>2r_g, \\ U_0\left[\dfrac{|r_i^{z,z+1}|^2}{4r_g^2}-1\right], & |r_i^{z,z+1}|<2r_g, \end{cases} \tag{3}$$

where $r_i^{z,z+1}=r_{i,z}-r_{i,z+1}$; $r_g=\xi_{ab}/\sqrt{g}$; ξ_{ab} is the coherence length in the crystallographic plane ab, and $g=1/2500$ (for $Bi_2Sr_2CaCu_2O_x$(BSCCO)). The dimensionless energy of interaction between the layers is $U_0=(T_0a/\pi d)\times[1+\ln(\lambda_{ab}/a)]$ where $a=12.3$ Å is the separation between the levels, $d=2.7$ Å the thickness of the superconducting layer, λ_{ab} the magnetic field penetration depth in the ab plane, and T_0 the coefficient of the interaction potential.

Typical vortex systems under investigation normally consist of 100–1000 vortices. A further increase in the number of vortices increases the computer time of the problem which, however, is much shorted than in other methods, e.g., the molecular dynamics method (MDM). On the other hand, a decrease in the applied magnetic field reduced the number of Abrikosov vortices in the system, and hence their density, which complicates the application of the MC method in view of weak coupling between vortex points and dictates the employment of other methods including the MDM.

Vortex systems are simulated on the basis of the MC method by using the two main approaches. In the first approach, the Abrikosov lattice is taken as the initial state of the system. Simulation is carried out at a fixed temperature and with a definite number of MC steps.[42,43,45,51] Another

approach involves the simulation of cooling of a disordered system of vortices.[45,51] Starting from a disordered system of vortices, the temperature of the system is reduced after a certain number of steps (e.g., by 1 K after 15000 steps).[45] The results of such numerical experiments are used for determining the temperature at which the lattice is disordered. A comparison of the results of the two approached can be used for refining the melting temperature.

It was found that thermalization of the system after a random distribution of vortices occurred after 5000–10000 MC steps.[41–51]

2. PARAMETERS AND CHARACTERISTICS OF A VORTEX LATTICE. EXPERIMENT AND SIMULATION

2.1. Magnetic field distribution in a vortex, vortex structure, and range of interaction of vortices

The solution of the boundary value problem (2) has the form[43,48]

$$V_{ij}^{z}=T_0K_0\left(\frac{|r_{i,z}-r_{j,z}|}{\lambda_{ab}}\right), \tag{4}$$

where $T_0=\Phi_0 d/2\pi\lambda_{ab}^2\mu_0$; $\mu_0=4\pi\cdot 10^{-7}$ V·s/Am; $d=2.7$ Å is the superconducting layer thickness, $\Phi_0=2.0679\cdot 10^{-15}\ T\cdot m^2$ the magnetic flux quantum, $\lambda_{ab}(T)=\lambda_{ab}(0)[1-(T/T_c)^n]^{-1/2}$, where we normally choose $n=3.3$ (according to experiments), T_c is the superconducting transition temperature, and $K_0(x)$ a modified Bessel's function.

Since the vortex interaction energy decreases rapidly with increasing distance, the effective vortex interaction radius is introduced. It is usually assumed to be equal to 3–10 separations between modes in an equilibrium triangular lattice. On one hand, this allows one to obtain results in a reasonable time, and on the other hand, takes into account the interaction of vortices correctly.

2.2. Equilibrium state of a vortex lattice

Obviously, all model approaches must satisfy the main test for a vortex lattice: the vortex system must form a regular triangular Abrikosov lattice[1] with the lattice constant

$$a_0=\left(\frac{2\Phi_0}{\sqrt{3}B}\right)^{1/2},$$

in a reasonable count time, viz., thermalization time.

It was noted in Refs. 44 and 51 that the time in which the system reaches equilibrium (i.e., is transformed into a triangular lattice) depends on the number of introduced defects (pinning centers) confining the lattice and on their intensity. For example, in the case of a moderate pinning, thermal motion of vortices over distances $\sim a_0$ (triangular lattice constant) is observed; this effect does not depend on the number of pinning centers.

A vortex system can also form a rectangular lattice. In should be noted, however, that the energies of rectangular and triangular vortex lattices coincide for systems containing approximately 200 vortices.[45] It follows hence that since the rectangular and triangular vortex lattices have close energies, their melting temperatures also differ insignificantly. Besides, a mixture of such structures is always observed in vortex systems.[45]

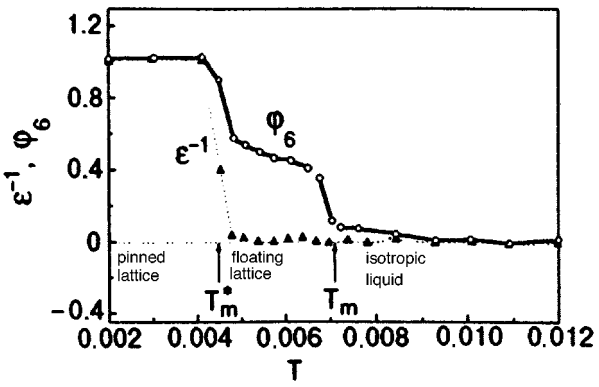

FIG. 1. Dependences of reciprocal dielectric constant and correlation parameter on normalized temperature for $f=1/49$ and $N=169$.[48]

2.3. Structural factor. Order parameter

In order to analyze the melting of a two-dimensional vortex lattice, the following quantity is usually calculated:[41]

$$\psi_6\propto\left\langle\sum_{i=1}^{N}\frac{1}{Z_i}\sum_{j=1}^{Z_j}e^{i6\theta_{ij}(r_j)}\right\rangle, \tag{5}$$

where θ_{ij} is the angle between nearest neighbors, Z_i the coordination number for the ith vortex, and N the number of vortices in the system.

A similar orientational correlation parameter (sixfold orientational order correlation) was also used by other authors.[48] A sharp change (decrease) in φ_6 indicates the violation of vortex lattice regularity and a transition to the flux liquid state.

In addition, a structural factor of the form[48]

$$S(k)\equiv\frac{1}{N}\langle n_k n_{-k}\rangle=\frac{1}{N}\sum_{ij}e^{ik(r_i-r_j)}\langle n_i n_j\rangle, \tag{6}$$

is considered, where $n_k=\Sigma_i n_i\exp(-i\mathbf{k}r_i)$.

It follows from the definition of the parameter φ_6 in (5) and the structural factor $S(k)$ in (6) that the factor $S(k)$ must decrease strongly upon the violation of the long-range order, while φ_6 is also sensitive to the violation of the short-range order. As the temperature increases, two melting phases can be distinguished;[48]

(1) at first, $S(k)\to 0$, and $\varphi_6\neq 0$,
(2) then $\varphi_6\to 0$ at $T=T_m$.

Phase (1) (floating lattice) is a homogeneous state of the lattice with a short-range order. The melting temperature T_m is lower than T_c. Thus, the phase exists in the interval $T_m<T<T_c$. This is the region in which vortices still exists in the presence of pinning, but are completely disordered. In this respect, such a phase state in unstable and is transformed to the normal state in the absence of pinning, i.e., $T_c\equiv T_m$ in a pure superconductor.

Figure 1 shows the $\varphi_6(T)$ and $\varepsilon^{-1}(T)$ dependence (ε is

the permittivity which is calculated from $S(k)$)[48] for a system with $N=63$ and $f=1/49$ at three different temperatures: $T=0.003$ (below T_m^*; pinned lattice), $T=0.0065$ (below T_m; floating lattice), and $T=0.0075$ (above T_m; liquid).

At low temperatures ($T<T_m$) and in moderate fields ($B<B_{2D}$), vortex ''pancakes'' can form a nearly perfect Abrikosov lattice (φ_6 is close to unity), while above T_m the parameter φ_6 is close to zero.[43]

2.4. Heat capacity of a vortex lattice

Heat capacity is another visual characteristic of the phase-transition point. The melting point of a vortex lattice must be characterized by singularities in the temperature dependence $C(T)$ of heat capacity. The value of heat capacity can be calculated most conveniently by using the fluctuation-dissipative theorem[45]

$$C(T)=(1/k_B^2T^2)(\langle E^2\rangle-\langle E\rangle^2), \tag{7}$$

where T is the temperature in kelvins, E the energy of the system, and k_B the Boltzman's constant.

The result of MC simulation of a $2D$ vortex system in the absence of pinning in a field of $1T$[45] show that the heat capacity of the system has a peak which is the sharper, the larger the number of vortices in the system (we modelled systems containing 108, 243, and 300 vortices).

If we define T_m as the temperature at which $C(T)$ has a peak, the value of T_m changes insignificantly with increasing number of vortices,[45] i.e., the system is large enough, and a change in the number of vortex points does not affect the quantities being measured.

2.5. Mobility of vortices

In order to determine the possibility of melting of the vortex lattice in a $2D$ system, we can use the Lindemann criterion according to which the lattice melts when the standard deviation σ_{TM} (thermal motion) becomes approximately equal to 1/10 of the distance a_0 in an equilibrium vortex lattice.[45]

The standard deviation σ_{TM} of vortices which is equal to the displacement of a vortex from its initial position, is defined as[45]

$$\sigma_{TM}=\left[\sum_{i=1}^{N}\frac{(r_{if}-r_{is})^2}{N}\right]^{1/2}, \tag{8}$$

where r_{is} is the initial position of the vortex, r_{if} its final position, and N the number of vortices in the system.

According to calculations,[45] the motion of vortices at $T<T_m(T_m=18.5\ \mathrm{K})$ is small, but at $T\sim T_m$ the deviation σ_{TM} increases rapidly, i.e., the lattice melts. Thermal motion is also intensified upon an increase in the number of vortices in the system at $T\sim T_m$ (in the field $H=1T$) and remains virtually unchanged at a lower temperature.

It would be interesting to trace the effect of pinning on the motion of vortices. For example, it was found that the behavior of a vortex lattice with a moderate and strong pinning is different.[44] In the case of a moderate pinning, Yates *et al.*[44] proved that the density of pinning centers affects the thermal motion insignificantly so that the value of σ_{TM} is of the order of a_0 irrespective of the number of defects (pins). In the case of strong pinning, σ_{TM} has a minimum for $N_{\mathrm{pin}}\approx N_{\mathrm{vor}}/4$ (N_{pin} is the number of defects and N_{vor} the number of vortices) and a maximum for N_{pin} in the region from $N_{\mathrm{vor}}/2$ to N_{vor}. The decrease in the thermal mobility for $N_{\mathrm{pin}}=N_{\mathrm{vor}}/4$ was explained by Yates *et al.* by approximate coincidence of pinned positions with the vortex lattice. As the number of pinning defects increases, the defects form clusters trapping vortices at distances smaller than in an unpinned lattice. This is accompanied by the formation of channels on the potential energy surface of the system, through which unpinned vortices can diffuse. Yates *et al.*[44] drew the following conclusions: the defect concentration $N_{\mathrm{pin}}\approx N_{\mathrm{vor}}/4$ stabilizes the lattice, for $N_{\mathrm{vor}}4<N_{\mathrm{pin}}<N_{\mathrm{vor}}$ the lattice is okey and diffusion is initiated, while for $N_{\mathrm{vor}}\ll N_{\mathrm{pin}}$ the motion of vortices and the lattice structure are suppressed.

3. PHASE DIAGRAMS (VORTEX LATTICE, ''GLASS'', FLUX LIQUID; LOSS OF COHERENCE BETWEEN LAYERS

3.1. Melting of vortex lattice in a 2D system

Two-dimensional systems are being studied intensely in view of the quasi-two-dimensional nature of layered superconductors and weak interplanar interaction in them. For example, simulation of a $2D$ vortex lattice by the MC method was carried out in Refs. 44, 45, 48–50.

A transition (lattice melting) observed by Franz and Teitel[48] in a $2D$ system was identified as a weak first-order transition. The system under investigation had two characteristic temperatures: T_m^* and T_m. The temperature T_m^* was determined from the temperature dependence of the dielectric function, which vanishes at T_m^*. The temperature T_m was determined from the vanishing of the orientational correlation function $\varphi_6(T)$. It was noted earlier in Sec. 2.3 that $T_m^*<T_m$ in the given system; for $T<T_m^*$, the lattice is pinned (pinned solid), for $T_m^*<T<T_m$ the lattice drifts (floating solid), and for $T>T_m$ the lattice melts (isotropic fluid). The change in free energy ΔF increases linearly with the linear size L of the system, which leads to the conclusion[48] that the system experiences a first-order transition.

Yates *et al.*[45] determined the melting point (17 K) of a $2D$ vortex lattice from the peak on the lattice heat capacity and from the behavior of the correlation function as well as thermal motion of vortices.

Lee and Teitel,[49] who simulated a $2D$ lattice gas, established that lattice melting is a first-order transition. Xing and Tesanovic[50] studied a transition of a flux liquid to a flux solid. A transition to the liquid state in the system at 18 K was also observed by Yates *et al.*[44]

3.2. Melting and vortex glass phase

Melting in a $3D$ system of vortices was investigated in Refs. 41–43, 54, 55. Figure 2a[41] shows the phase diagram of a system of 64 vortex lines simulated by the MC method in the range of magnetic field $12.5\ \mathrm{G}\leqslant B\leqslant 50\ \mathrm{T}$. Figure 2b illustrates the case of very low densities (16 lines). Parameters for the MC simulation were taken for $Bi_2Sr_2CaCu_2O_8$. Two phase-transition curves were obtained. Curves *1* were deter-

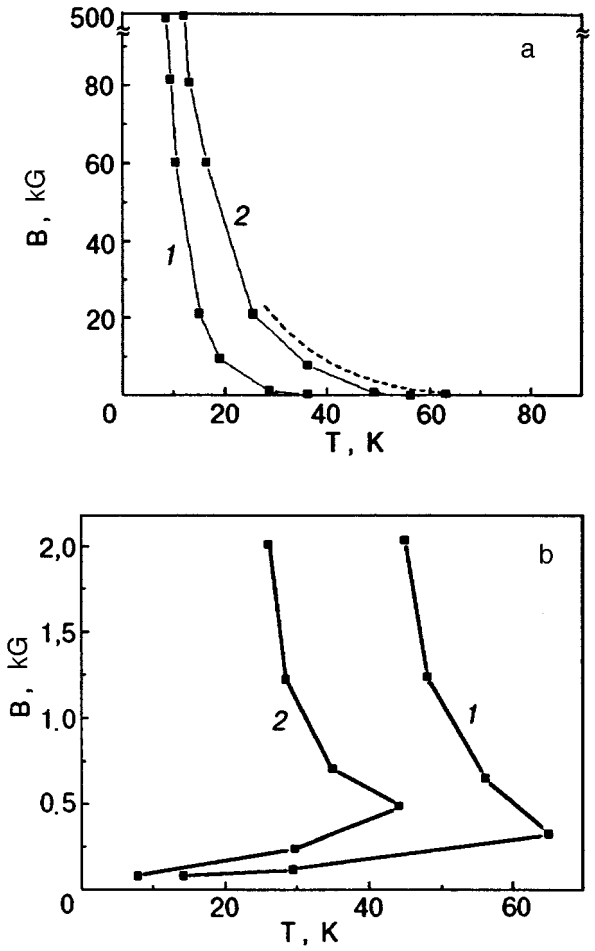

FIG. 2. $B-T$ phase diagram for $12.5\ \mathrm{G} \leqslant B \leqslant 50\ \mathrm{T}$.[61] Dashed curve corresponds to the results of calculations (a). Low-density mode (b).

mined from the disappearance of translational order in the plane $S(q=G_1)$, which is a Fourier transform of the density-density correlation function at the boundary of the Brillouin zone. This dependence has sharp peaks in the solid phase, which reflect the existence of a long-range order in the system. On the contrary, the structural factor in the liquid phase has no peaks and attains saturation (at the temperature T_m). Curves *2* were obtained from a similar analysis of the hexactic order parameter φ_6. Melting occurs in two stages in the same way as in the case of a $2D$ system. The asymptotic form of such a curve at high temperatures is the $2D$ limit. In the low-field mode, the interplanar interaction is relatively strong (stronger than correlations in the plane). As a result, the system contains straight vortex lines which form a ''fragile'' lattice. In the case of a low density of vortices, the authors of Ref. 41 observed the vortex line reconnection effect: in the model of coupled planes, vortices can switch the bonds. tending to a lower energy of the system.

Schneider *et al.*[43] calculated the hexactic order parameter Ψ_6 and the standard deviation of a vortex ''pancake'' from the average position in order to observe melting of the vortex lattice. For a system of $8\times8\times16$ vortices, the melting point of the vortex lattice in the field $B=45$ mT was defined as $T_m \simeq 60$ K (the experimental value is $T_m=57$ K). The magnetic field distribution was also calculated for three different cases: (a) $T=10$ K, $B=45$ mT, $\Psi_6 \simeq 1$ ($3D$ line vortex phase), (b) $T=80$ K, $B=45$ mT, $\Psi_6 \simeq 0$ (liquid phase), and (c) $T=5$ K, $B=90$ mT (a system without correlation between layers, but with an Abrikosov lattice in the planes corresponding to the $2D$ phase). The results are in good agreement with the experimental data for BSCCO samples.

Sasik and Strous' [54] also studied the melting transition and the $T_m(H)$ dependence. They used the MC method for $k \gg 1$ (k is the Ginzburg-Landau parameter); for $k=52$ and $T_{c0}=93$ K, the compound YBaCuO was simulated. The number of vortices was 100, the number of layers was 10, and $H=50$ kOe. A detailed comparison with experimental data revealed a satisfactory agreement with the results of simulation. The transition was determined from the parameter $S(q)$. The vortex solid state was obtained at $T=82.8$ K and the vortex liquid state at $T=83.0$ K, i.e., a transition occurring at $T_m \simeq 83$ K and $H=50$ kOe is a first-order transition.

The Abrikosov theory predicts a second-order transition for a homogeneous type II superconductor in a magnetic field. Herbut and Tesanovic[55] noted that strong fluctuations in type II superconductors can change the order of the transitions and established that the melting of a vortex lattice in a strong type II superconductor ($\kappa \gg 1$) in a magnetic field is a first-order transition. The values of the constants were taken for YBaCuO. The range or experimental fields was $0.1-10\ T$. The results obtained in Ref. 55 confirmed that the liquid-solid transition of a vortex lattice in a type II homogeneous superconductor is a first-order transition.

The transition curve for melting on the phase diagram can be displaced when point of columnar defects are introduced in the system in view of pinning of vortex ''pancakes'' or entire vortex lines on them, which results in the formation of the vortex glass phase. Tauber and Nelson[51] analyzed the effect of interaction and pinning energy in the vortex glass phase by the MC method and considered low-temperature excitations of vortices ''frozen'' at columnar defects in superconductors taking into account the long-range interaction between vortices.

3.3. 2D-3D Transition

Vortex lines in a layered material are formed by individual ''pancakes'', the interaction between ''pancakes'' along parallel layers being relatively weak.[56] Accidental displacement of these ''pancakes'' can suppress coherence between the layers. Thermal fluctuations of ''pancakes'' can also be responsible for this effect at temperatures much lower than the melting temperature of the vortex lattice. This violation of coherence can be described on the basis of an exponentially strong temperature dependence of critical current in the c direction (across the layers). At low temperatures, vortex ''pancakes'' in different layers are aligned in the absence of disorder, and the coherence between the layers is restored. Heterogeneities of the material create a random potential which controls displacements of ''pancakes'' even at $T=0$, and these displacements caused by disorder also suppress the phase coherence between the layers. Ko-

shelev *et al.*[56] analyzed the effect of relatively weak pinning on Josephson junctions between layers and on random motion of vortex lines.

The importance of pinning for interlayer coupling in layered HTS materials was also presumed in some experimental works.[57–61]

Benkraouda and Clem[62] analyzed the stability of a vortex line as a pile of vortex ''pancakes'' to transverse displacements.

In the MC simulation of a $3D$ system of vortex lines, the following states of the system can be singled out[41,43]: the $3D$ phase, the liquid phase, and the $2D$ phase. In addition. Ruy *et al.*[41] investigated the effect of reconnection of couplings between vortices in different planes, which was mentioned in Sec. 3.2. An analysis carried out in by Daemou *et al.*[57] proved that the $2D$-$3D$ transition is of the second order.

4. INFLUENCE OF DEFECTS ON VORTEX LATTICE

It was noted by Yates *et al.*[44] that the introduction of defects into a system affects the vortex mobility in the plane. It was observed that defects with a weak to moderate pinning force weakly affect the melting in the system. In the case of strong pinning, the vortex structure is stabilized even by a small number of pinning centers approximately equal to $N_{\text{pin}} < N_{\text{vor}}/4$. Yates *et al.*[44] state that an increase in the number of defects to $N_{\text{vor}}/2$ initiates diffusion of vortices in the system.

Rudnev *et al.*[63] used the MC method to analyze the behavior of a $2D$ vortex system with defects. Vortices were regarded as zero-mass classical particles with a long-range repulsion. Pinning was presented by a finite number of randomly distributed potential wells with a short-range attraction. They analyzed the behavior of systems with 100–225 vortex points distributed over a square mesh of size 450×390 or over a triangular mesh of size 320×320 cells. Periodic boundary conditions were used. Simulation parameters were typical of layered HTS materials. In order to observe vortex lattice melting, the hexactic order parameter S_6 was calculated. It was found that the value of S_6 is close to unity in the case of an almost perfect Abrikosov lattice and is equal to zero at temperatures above the melting point of the vortex lattice. It was also found that pinning shifts the melting point and modifies the phase diagram Figure 3 shows a typical structure of a vortex lattice at a low temperature after $4 \cdot 10^4$ MC steps. The series of Figs. 4a–c illustrates the vortex lattice dynamics at various temperatures. Dark spots indicate regions near pinning centers, in which vortex ''pancakes'' are unstable. Clear-cut spots correspond to ''pancakes'' located at large distances from pinning centers. It can be seen that the vortex lattice is destroyed at high temperatures, and vortices do not experience the action of pinning forces. Figure 5 shows the temperature dependences of S_6 at various numbers of pinning centers. In addition, it should be noted that the transition (melting) temperature decreases upon an increase in the concentration of pinning centers, which corresponds to a shift of the phase boundary on the $B-T$ diagram.

In a perfect layered superconductor at a low temperature, vortex ''pancakes'' in different layers are aligned. Koshelev

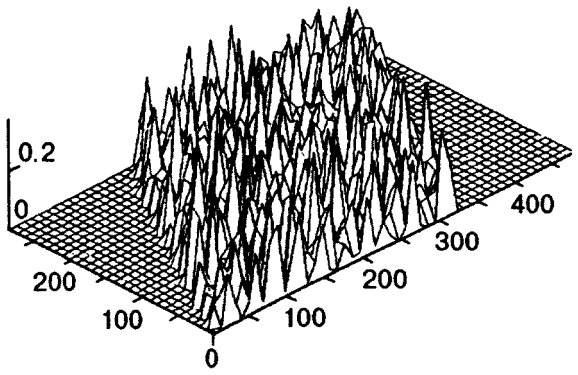

FIG. 3. Vortex line distribution in a triangular lattice for $B = 100$ mT, $T = 5$ K; the number of pinning centers $N_{\text{pin}} = 10$ for $U = -0.005$ eV.

et al.[56] analyzed the situation when point defects generate a random potential acting on each vortex, which destroys vortex lines.

Machida and Kaburaki[64] studied the pinning of vortices at columnar and point defects as well as the dynamics of stepwise vortices.

Tauber and Nelson[51] studied the behavior of a vortex system in the ''vortex glass'' phase. They analyzed the situation when each vortex line is connected to one of the defects, while some defects remain vacant. This phase is associated with the phase of Bose glass known from simulation of Bose systems with defects.[65] Tauber and Nelson[51] also studied the case when a vortex is pinned to two nearest columnar defects. The description of such a system at a low temperature[51] can be reduced to a quantum lattice Bose gas with the so-called hard-core statistics: bosons at different sites are characterized by a symmetric function, while those at the same site obey the Pauli principle, i.e., obey the fermion statistics.[66] In this case, the phase transition from the pinned lattice to a mobile lattice is equivalent to the well-known transition from a Mott insulator to superfluidity for a Bose gas.[67]

CONCLUSIONS

The variety of phase diagrams for the vortex state of HTS materials, the complexity of layered strongly correlated structures under investigation, and the lack of rigorous analytic approaches necessitate intense studies of phase transitions in a vortex lattice by using effective numerical methods. The results of numerical simulation by using the Monte Carlo method presented in this review make it possible to describe satisfactorily the available experimental facts in some cases and to obtain the phase diagrams as well as important parameters of the system (including their numerical value).

In conclusion, it would be appropriate to outline a number of problems which can be proposed as topics for further investigations in the field of modeling of the vortex lattice of HTS materials and for experimental investigation of the mixed state. For example, it would be important to carry out experiments demonstrating the changes in the melting curve and the position of the critical point induced by disorder. It is

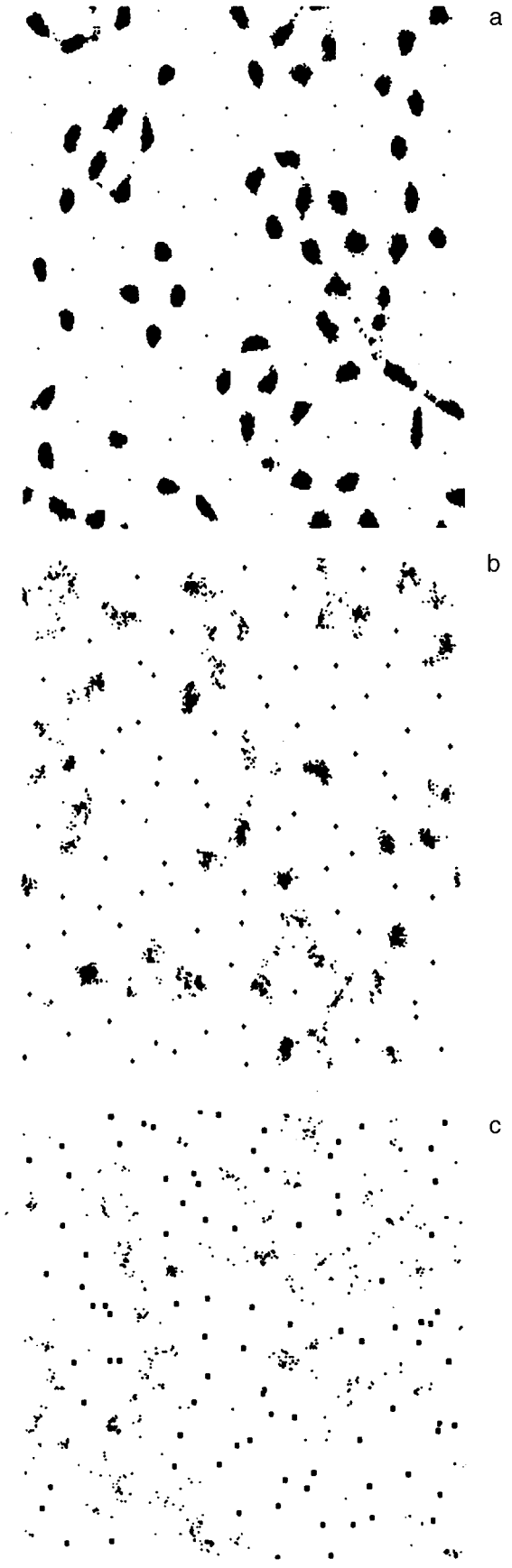

FIG. 4. Temperature evolution of a vortex lattice in a square mesh with the number of pinning centers $N_{pin}=100$ for $B=45$ mT, and various temperatures T, K: 5 (a), 30 (b), and 50 (c).

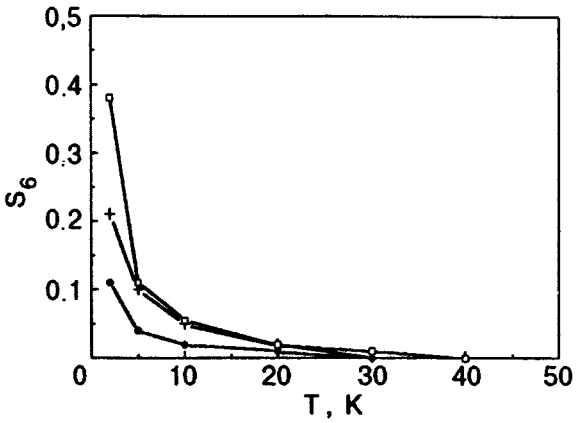

FIG. 5. Hexactic parameter S_6 as a function of temperature for a square mesh after $3\cdot10^4$ MC steps for $B=45$ mT and various number of pinning centers N_{pin} 0(●), 25(+), and 100 (□). The pinning potential $U=-0.1$ eV.

interesting to calculate phase diagrams of the vortex state for various extent of disorder, to determine the state of the system above the melting point of the vortex lattice, to investigate the region of low fields and temperatures, in which the vortex lattice can also experience melting, and finally, it would be important to carry out exact calculation of current-voltage characteristics (see recent publications devoted to an analysis of current-voltage characteristics of a vortex system with defects)[68,69] reflecting the dynamics of the vortex state in the regions of the phase diagram corresponding to the state of vortex crystal, glass, and flux liquid.

This research was carried out under financial support of the Russian science and engineering program ''Modern Problems in Physics of Condensed State: Superconductivity'', projects Nos. 95019 and 96026.

*E-mail: kash@supercon.mephi.ru

[1] A. A. Abrikosov, Zh. Éksp. Teor. Fiz. **8**, 1174 (1957).
[2] D. J. Bishop, P. L. Gammel, L. F. Schineemeyer, and J. V. Waszczak, Bull. Am. Phys. Soc. **33**, 606 (1988).
[3] D. R. Nelson, Phys. Rev. Lett. **60**, 1973 (1988).
[4] G. Blatter, M. V. Feigel'man, V. B. Geshkenbein *et al.*, Rev. Mod. Phys. **66**, 1125 (1994).
[5] M. P. A. Fisher, Phys. Rev. Lett. **62**, 1415 (1989).
[6] D. S. Fisher, M. P. A. Fisher, and D. A. Huse, Phys. Rev. B **43**, 130 (1989).
[7] A. I. Larkin, Zh. Éksp. Teor. Fiz. **31**, 784 (1970) [*sic*].
[8] V. M. Vinokur, M. V. Feigel'man, V. B. Geshkenbein, and A. I. Larkin, Phys. Rev. Lett. **65**, 259 (1990).
[9] V. A. Marchenko and A. V. Nikulov, Pis'ma Zh. Tekh. Fiz. **34**, 19 (1981) [JETP Lett. **34**, 17 (1981)].
[10] A. V. Nikulov, Phys. Rev. B **52**, 10429 (1995).
[11] E. Berzin, D. R. Nelson, and A. Thiaveill, Phys. Rev. B **31**, 7124 (1985).
[12] M. V. Feilgel'man, V. B. Geshkenbein, and A. I. Larkin, Physica **C167**, 177 (1990).
[13] L. I. Glazman and A. E. Koshelev, Phys. Rev. B **43**, 2835 (1991).
[14] L. L. Daemen, L. N. Bulaevskii, M. P. Maley, and J. Y. Couter, Phys. Rev. Lett. **70**, 1167 (1993); Phys. Rev. B **47**, 11291 (1993).
[15] D. A. Huse, M. P. A. Fisher, and D. S. Fisher, Nature (London) **358**, 553 (1992).
[16] D. J. Bishop, P. L. Gammel, D. A. Huse, and V. A. Murray, Science **225**, 165 (1992).
[17] R. Cubitt, E. M. Forgan, G. Yang *et al.*, Nature (London) **365**, 407 (1993).
[18] R. Batto, L. Ya. Vinnikov, L. A. Gurevich, and M. V. Dugaev, Pis'ma Zh.

Éksp. Teor. Fiz. **62**, 139 (1995) [JETP Lett. **62**, 153 (1995)].
[19] G. M. Genkon and A. V. Okomel'kov, Zh. Éksp. Teor. Fiz. **107**, 784 (1995) [JETP **80**, 445 (1995)].
[20] H. Safar, P. L. Gammel, D. A. Huse *et al.*, Phys. Rev. Lett. **69**, 824 (1992).
[21] W. K. Kwok, S. Fleshler, U. Welp *et al.*, Phys. Rev. Lett. **69**, 3370 (1992).
[22] W. K. Kwok, J. Frendrich, S. Fleshler *et al.*, Phys. Rev. Lett. **72**, 1092 (1994); U. Welp, J. Frendrich, W. K. Kwok *et al.*, Phys. Rev. Lett. **76**, 4809 (1996); J. Frendrich, U. Welp, W. K. Kwok *et al.*, Phys. Rev. Lett. **77**, 2073 (1996).
[23] M. Charalambous, J. Chaussy, P. Lejay, and V. Vinokur, Phys. Rev. Lett. **71**, 436 (1993).
[24] W. Jiang, N.-C. Yeh, D. S. Reed *et al.*, Phys. Rev. Lett. **74**, 1438 (1994).
[25] H. Safar, P. L. Gammel, D. A. Huse *et al.*, Phys. Rev. Lett. **70**, 3800 (1993).
[26] E. Zeldov, D. Majer, M. Konczykovski *et al.*, Nature (London) **375**, 373 (1995); U. Welp, Phys. Rev. Lett. **76**, 4809 (1996).
[27] D. R. Nelson, The Vortex State, Kluwer, Dordreccht (1994); Nature, **375**, 356 (1995).
[28] E. Zeldov, D. Majer, A. I. Larkin *et al.*, Europhys. Lett. **30**, 367 (1995).
[29] D. Majer, E. Zeldov, and M. Konczykovski, Phys. Rev. Lett. **75**, 1166 (1995).
[30] D. Majer, B. Khaykovich, T. W. Li *et al.*, Compos. Sci. Technol. **46**, 1563 (1996).
[31] T. Hanaguri *et al.*, Physica **C256**, 111 (1996).
[32] T. Hanaguri, T. Tsuboi, A. Maeda *et al.*, Czech. J. Phys. **46**, 1559 (1996).
[33] R. Liang, D. A. Bonn, and W. N. Hardy, Phys. Rev. Lett. **76**, 835 (1996).
[34] T. Nishizaki, Y. Onodera, N. Kobayashi *et al.*, Phys. Rev. B **53**, 82 (1996).
[35] D. T. Fuchs, E. Zeldov, D. Majer *et al.*, Czech. J. Phys. **46**, 1583 (1996).
[36] M. T. Wylie, E. M. Forgan, S. Lloyd *et al.*, Czech. J. Phys. **46**, 1569 (1996).
[37] H.-R. Ma and S. T. Chui, Phys. Rev. Lett. **67**, 505 (1991).
[38] S. Sengupta, C. Dasgupta, H. R. Krishnamurthy *et al.*, Phys. Rev. Lett. **67**, 3444 (1991).
[39] Y.-H. Li and S. Teitel, Phys. Rev. Lett. **66**, 3301 (1991).
[40] Y.-H. Li and S. Teitel, Phys. Rev. B **47**, 359 (1993).
[41] S. Ruy, S. Doniach, G. Deutscher, and A. Kapitulnik, Phys. Rev. Lett. **68**, 710 (1992).
[42] R. E. Hetzel, A. Sudbo, and D. A. Huse, Phys. Rev. Lett. **69**, 518 (1992).
[43] J. W. Schneider, S. Schafroth, and P. F. Meier, Phys. Rev. B **52**, 3790 (1995).
[44] K. Yates, D. J. Newman, and P. A. J. de Groot, Phys. Rev. B **52**, R13149 (1995).
[45] K. Yates, D. J. Newman, and P. A. J. de Groot, Physica **C241**, 111 (1995).
[46] H. Safar, P. L. Gammel, D. A. Huse *et al.*, Phys. Rev. B **52**, 6211 (1995).
[47] H. Weber, M. Wallin, and H. J. Jensen, Phys. Rev. B **53**, 8566 (1996).
[48] M. Franz and S. Teitel, Phys. Rev. Lett. **73**, 480 (1994).
[49] J.-R. Lee and S. Teitel, Phys. Rev. B **46**, 3247 (1992).
[50] L. Xing and Z. Tesanovic, Phys. Rev. Lett. **65**, 794 (1990).
[51] U. C. Tauber and D. R. Nelson, Phys. Rev. B **52**, 16106 (1995).
[52] D. V. Kheerman, *Methods of Computer Experiment in Theoretical Physics*, Nauka, Moscow (1990).
[53] P. Minnhagen, Phys. Rev. B **23**, 5745 (1981).
[54] R. Sasik and D. Stroud, Phys. Rev. Lett. **75**, 2582 (1995).
[55] I. F. Herbut and Z. Tesanovic, Physica **C255**, 324 (1995).
[56] A. E. Koshelev, L. I. Glazman, and A. I. Larkin, Phys. Rev. B **53**, 2786 (1996).
[57] L. L. Daemen, L. N. Bulaevskii, M. P. Maley, and J. Y. Conter, Phys. Rev. Lett. **70**, 1167 (1993); Phys. Rev. B **47**, 1129 (1993).
[58] J. H. Cho, M. P. Maley, S. Flescher *et al.*, Phys. Rev. B **50**, 6493 (1994).
[59] E. Rodriguez, M. F. Goffman, A. Arriebere *et al.*, Phys. Rev. B **194–196**, 2151 (1994).
[60] O. K. C. Tsui, N. P. Ong, Y. Matsuda *et al.*, Phys. Rev. Lett. **73**, 724 (1994).
[61] L. N. Bulaevskii, M. P. Maley, and M. Tachiki, Phys. Rev. Lett. **74**, 801 (1995).
[62] M. Benkraouda and J. R. Clem, Phys. Rev. B **53**, 438 (1996).
[63] I. A. Rudnev, V. A. Kashurnikov, and M. A. Katargin, *Proceedings of the 8th Workshop on Critical Current in Superconductors*, Japan, May 27–29 (1996).
[64] M. Machida and H. Kaburaki, Phys. Rev. Lett. **75**, 3178 (1995).
[65] M. P. A. Fisher, P. B. Weichman, G. Grinstein, and D. S. Fisher, Phys. Rev. B **40**, 546 (1989).
[66] R. T. Scalettar, G. G. Batrouni, A. P. Kampf, and G. T. Zimanyi, Phys. Rev. B **51**, 8467 (1995).
[67] A. P. Kampf and G. T. Zimanyi, Phys. Rev. B **47**, 279 (1993); V. A. Kashurnikov, A. I. Podlivaev, and B. V. Svistunov, Pis'ma Zh. Éksp. Teor. Fiz. **61**, 375 (1995) [JETP Lett. **61**, 381 (1995)].
[68] K. Moon, R. T. Scalettar, and G. T. Zimanyi, Phys. Rev. Lett. **77**, 2778 (1996).
[69] S. Ryu, M. Hellerqvist, S. Doniach, *et al.*, Phys. Rev. Lett. **77**, 5114 (1996).

Translated by R. S. Wadhwa

On critical rates of vortex formation in rotating helium

T. I. Zueva

B. Verkin Institute for Low Temperature Physics and Engineering, National Academy of Sciences of the Ukraine, 310164 Kharkov, Ukraine
(Submitted April 8, 1997; revised June 23, 1997)
Fiz. Nizk. Temp. **23**, 1162–1171 (November 1997)

The vortex flow of a superfluid liquid between concentric cylinders rotating with the same angular velocity is studied. A general expression is obtained for the free energy of a liquid with vortices of *arbitrary* intensity. The possibility of emergence of vortices whose vorticity is opposite in sign to the angular velocity (negative vortices) is studied. It is shown that the formation of negative vortices in a liquid corresponds to larger values of free energy than for positive vortices. The friction force exerted by the normal component on a vortex dislodged from equilibrium position is derived, and the energy barrier overcome by a vortex in crossing from one wall to another is calculated. It is shown that in view of the presence of the energy barrier, the probability of vortex formation is significant only for angular velocities considerably exceeding the theoretical angular velocity. Parametric equations are obtained for the envelope of a family of lines expressing the free energy as a function of the angular velocity of a rotating vessel with different numbers of vortices. An approximate relation between the angular velocity of a rotating vessel and the number of vortices formed at this angular velocity is obtained. © *1997 American Institute of Physics.* [S1063-777X(97)00211-9]

In most works devoted to investigation of vortex states in rotating superfluid helium, it is assumed (tacitly or otherwise) that vortices formed at a certain rotational velocity have vorticity of the same sign as the angular velocity of the rotating vessel. This means that the circulation around the vortex defined in an appropriate manner (see, for example, Ref. 1)

$$\oint \mathbf{v}_s \cdot \mathbf{dl} = 2\pi\gamma \tag{1}$$

is positive if the vessel rotates in counterclockwise direction.[2] If the motion is considered in a doubly connected region (ring), the vortex motion in the liquid itself is supplemented by a (quantized) circulation around the inner cylinder which neutralizes the difference between the linear velocities at the outer and inner walls for low rotational velocities.[3] This circulation has the same sign as the angular velocity, which means that we can write the following expression for a vessel rotating in the counterclockwise direction:

$$\oint_{r=R_1} \mathbf{v}_s \cdot \mathbf{dl} = 2\pi\gamma L > 0.$$

Here, $r=R_1$ is the inner radius of the ring under consideration, R_2 its outer radius ($R_1 \leqslant r \leqslant R_2$), L the number of circulation quanta measured in units of $2\pi\gamma$.

According to Kelvin's theorem on conservation of circulation (see Ref. 4), circulation around the inner cylinder cannot commence on its own. If the circulation around the inner cylinder was equal to zero at the initial instant, then according to the ideal liquid model which we are following here, it cannot change simply as a result of the formation of a *vortex* near a wall followed by its annihilation at another wall. If the vortex is formed at the *inner* wall, its detachment from the wall must lead to a circulation around the inner cylinder that is opposite to the vortex (so that the total circulation around any liquid contour is conserved). However, if the vortex is detached from the **outer** wall, absorption by its image at the inner wall leads to a circulation **of the same sign** as the vortex ''descending'' to the inner cylinder. This means that circulation may have the same direction as the angular velocity of the rotating vessel upon a detachment of a negative vortex (according to the definition (1) of the vortex sign) from the inner wall, or of a positive vortex from the outer wall.

Thus, it can be assumed that intensity vortices can have a sign opposite to that of the angular velocity. We shall proceed from this assumption to construct a refined theory of vortex motion of a superfluid liquid in rings of any size.

FREE ENERGY AND EQUILIBRIUM CONDITIONS

While solving the two-dimensional problem for the flow function of an ideal liquid in a ring,[5] we obtained expressions for the flow function $\psi(r,\theta)$ and the complex-conjugate velocity $\overline{v(z)}$ of an ideal liquid containing N vortices of *arbitrary* intensity γ_k, located at *arbitrary* points $z_k = r_k \exp(i\theta_k)$. All vortices are assumed to be infinitely long filaments stretched along the rotational axis of the ring. We shall rewrite these expressions after eliminating the components associated with the circulation around the inner cylinder (since no constraints are imposed *a priori* on the sign of the vortex, and the existence of circulation is not presumed):

$$\psi(r,\theta)=\sum_{k=1}^{N}\gamma_k \ln\frac{r}{R_1}+\sum_{k=1}^{N}\gamma_k\left[\mathrm{Re}\ln\sigma\left(i\ln\frac{z}{z_k}\right)\right.$$
$$\left.-\mathrm{Re}\ln\sigma\left(i\ln\frac{zz_k}{Z_k^2}\right)-\frac{2\eta}{\omega_1}\ln\frac{r_k}{R_1}\ln\frac{r}{R_1}\right]; \quad (2)$$

$$\overline{v(z)}=-\frac{i}{z}\sum_{k=1}^{N}\gamma_k+\frac{1}{z}\sum_{k=1}^{N}\gamma_k\left[\zeta\left(i\ln\frac{z}{z_k}\right)\right.$$
$$\left.-\zeta\left(i\ln\frac{zz_k}{Z_k^2}\right)+\frac{2i\eta}{\omega_1}\ln\frac{r_k}{R_1}\right]. \quad (3)$$

Here, $z=r\exp(i\theta)$ is a complex variable in the ring, (r,θ) are polar coordinates of a point, σ and ζ are the Weierstrass sigma- and zeta-functions with half-periods $\omega_1=\pi$, $\omega_2=i\ln(R_2/R_1)$; $\eta=\zeta(\omega_1)$; $Z_k=R_1\exp(i\theta_k)$.

In deriving the expressions for the free energy, we replaced the assumption concerning the existence of N vortices of arbitrary intensity by the assumption that all vortices have *the same* intensity γ whose sign coincides with that of the angular velocity of the rotating vessel. However, one can easily obtain a *general* expression for the free energy of a superfluid liquid in a ring containing N vortex lines of arbitrary (both in magnitude and sign) intensity γ_k (the presence of circulation is not assumed).

It was shown by us earlier[7] that

$$F_N\equiv F_{N,0}=\frac{1}{2}\rho_s 2\pi\psi_2\sum_{k=1}^{N}\gamma_k-\frac{1}{2}\rho_s 2\pi\psi_1\sum_{k=1}^{N}\gamma_k$$
$$-\frac{1}{2}\rho_s 2\pi\sum_{j=1}^{N}\psi_j\gamma_j-\rho_s\int_{V'}\mathbf{v}_s\cdot\mathbf{v}_n dV$$
$$+\frac{1}{2}\rho_s\pi\sum_{k=1}^{N}\gamma_k^2.$$

The values of flow functions ψ_1 and ψ_2 at the inner ($r=R_1$) and outer ($r=R_2$) boundaries of the ring were obtained while deriving the expression for the flow function:

$$\psi_1=0, \quad \psi_2=\sum_{j=1}^{N}\gamma_j\ln\frac{R_2}{r_j}.$$

The values of the flow functions ψ_i at the vortex surfaces (which are assumed to be cylinders of radius a) can be obtained from the general expression (2) for the flow function by putting $z=z_j=r_j\exp(i\theta_j)$ in all terms but one in which $\sigma[i\ln(z_j/z_k)]$ has a singularity for $k=j$. In this term, we assume that $z=z_j+a\exp(i\varphi)$, where φ is the angle measured from the vortex center. In this case, we obtain (to within terms of the order of a/r_j)

$$\psi_j=\left(\sum_{k=1}^{N}\gamma_k\right)\ln\frac{r_j}{R_1}+\sum_{\substack{k=1\\k\neq j}}^{N}\gamma_k\left[\mathrm{Re}\ln\sigma\left(i\ln\frac{z_j}{z_k}\right)\right.$$
$$\left.-\mathrm{Re}\ln\sigma\left(i\ln\frac{z_jz_k}{Z_k^2}\right)-\frac{2\eta}{\omega_1}\ln\frac{r_k}{R_1}\ln\frac{r_j}{R_1}\right]+\gamma_j\ln\frac{a}{r_j}$$
$$-\gamma_j\,\mathrm{Re}\ln\sigma\left(2i\ln\frac{r_j}{R_1}\right)-\frac{2\eta\gamma_j}{\omega_1}\ln^2\frac{r_j}{R_1}.$$

The expression for the free energy assumes the form

$$F_N=\pi\rho_s\sum_{j=1}^{N}\gamma_j\left\{\frac{\gamma_j}{2}-\gamma_j\ln\frac{a}{r_j}+\sum_{k=1}^{N}\gamma_k\ln\frac{R_1R_2}{r_kr_j}\right.$$
$$+\gamma_j\,\mathrm{Re}\ln\sigma\left(2i\ln\frac{r_j}{R_1}\right)+\sum_{k=1}^{N}\frac{2\eta\gamma_k}{\omega_1}\ln\frac{r_j}{R_1}\ln\frac{r_k}{R_1}$$
$$-\sum_{\substack{k=1\\k\neq j}}^{N}\gamma_k\left[\mathrm{Re}\ln\sigma\left(i\ln\frac{z_j}{z_k}\right)-\mathrm{Re}\ln\sigma\left(i\ln\frac{z_jz_k}{Z_k^2}\right)\right]$$
$$\left.-\omega(R_2^2-r_j^2)\right\}. \quad (4)$$

This is just the general expression for the free energy of a superfluid in rings rotating with an angular velocity ω and containing N vortices of arbitrary intensity γ_k.

The equilibrium condition for a vortex system can be presented in the form of $2N$ equations

$$\frac{\partial F}{\partial r_i}=0; \quad \frac{\partial F}{\partial\theta_i}=0, \quad i=1,2,...,N.$$

It is not difficult to write these equations, but we shall require in future only equations corresponding to vortices with positive and negative unit intensity γ. Hence we shall write only these equations.

Note that all terms in the expression (4) for free energy except one contain the *product* of intensities $\gamma_j\gamma_k$ (or γ_j^2). The only exception is the term $\omega(R_2^2-r_j^2)$ which contains the factor γ_j to the first power [or outside the brackets, which leaves a term of the type $(\omega/\gamma)(R_2^2-r_j^2)$, as in the case of a system of one-quantum positive vortices].[7] Thus, a reversal of the sign of intensity of one or more vortices reverses the sign of only a few cross-multiplication terms (for $k\neq j$) and of the term proportional to ω for $N>1$, or only of the last term if $N=1$ or all vortices have the same sign.

We shall consider the last case only, and endeavor to determine the sign of vortices emerging for low angular velocities of a rotating vessel as well as the reason behind it.

Let us assume that a ring is filled with superfluid helium rotating at such a low angular velocity ω that no vortices are formed in the liquid, and hence

$$\mathbf{v}_s\equiv 0.$$

A vortex appears in the liquid for a certain angular velocity $\omega=\omega_c$. We shall show that this vortex, which emerges near a wall, is *unstable* irrespective of its sign and is annihilated by its image relative to the other wall, resulting in a circulation around the inner cylinder.

FORMATION OF ARBITRARY-SIGN VORTEX

The free energy of a superfluid liquid in a ring containing a vortex of intensity $-\gamma$ at the point $z_1=r_1$ can be written in the form

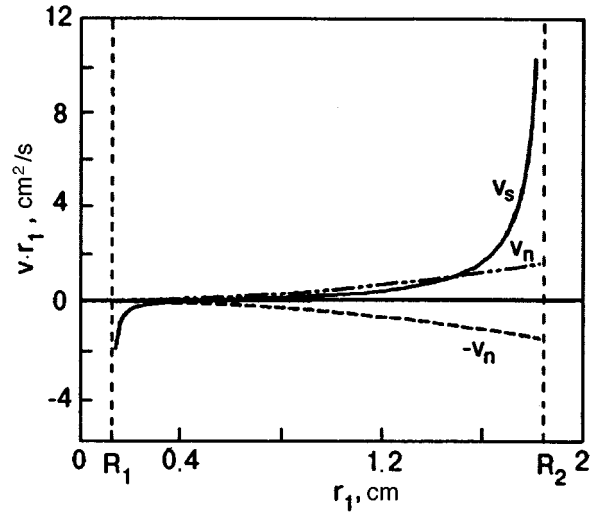

FIG. 1. Dependence of velocity of the superfluid (v_s) and normal (v_n) components on the vortex position r_1. The figures correspond to $R_1 = 0.1$ cm and $R_2 = 1.5$ cm.

$$F_{-1} = \pi\rho_s\gamma^2\left\{\frac{1}{2} - \ln\frac{a}{r_1} + \mathrm{Re}\,\ln\sigma\left(2i\,\ln\frac{r_1}{R_1}\right) + \frac{2\eta}{\omega_1}\ln^2\frac{r_1}{R_1} + \frac{\omega}{\gamma}(R_2^2 - r_1^2)\right\}. \tag{5}$$

This expression differs from the corresponding expression for a vortex with positive intensity $+\gamma$ *only* in the sign of the last term. It turns out, however, that it is this term that plays a decisive role in studying the behavior of a vortex system. In order to prove this, let us turn to the detailed analysis of the system with one *positive* vortex, which was carried out by us earlier[7] as a first step towards the study of a multivortex system, but was not presented there since we considered a more general problem about the formation of a whole ring of vortices.

The equilibrium condition for a vortex of arbitrary intensity assumes the form

$$\frac{1}{2r_1} + \frac{1}{r_1}\,\mathrm{Im}\,\zeta\left(2i\,\ln\frac{r_1}{R_1}\right) - \frac{2\eta}{\omega_1 r_1}\ln\frac{r_1}{R_1} = \pm\frac{\omega}{\gamma}r_1. \tag{6}$$

The upper sign corresponds to a positive vortex and the lower one to a negative vortex. We shall consider in detail the curves describing the functions on the left- and right-hand sides of Eq. (6) (having premultiplied the equation by $r_1 \neq 0$ for convenience) (Fig. 1).

It can easily be seen that for $\gamma > 0$, Eq. (6) has only one root for any fixed value of the angular velocity.[1)] This root is close to the value R_2 and, as was shown earlier, unstable. For $\gamma < 0$, Eq. (6) cannot have more than one root which is always close to R_1, i.e., the equilibrium position of the vortex is closer to the *inner* wall of the ring. We shall find out whether this equilibrium is stable. For this purpose, we calculate the second variation of the free energy (5):

$$\frac{d^2F}{dr_1^2} = 2\pi\rho_s\gamma^2\left\{\frac{1}{2r_1^2} + \frac{1}{r_1^2}\,\mathrm{Im}\,\zeta\left(2i\,\ln\frac{r_1}{R_1}\right) - \frac{2}{r_1^2}\,\mathrm{Re}\,\zeta'\left(2i\,\ln\frac{r_1}{R_1}\right) + \frac{2\eta}{\omega_1 r_1^2}\left(1 - \ln\frac{r_1}{R_1}\right) - \frac{\omega}{\gamma}\right\}. \tag{7}$$

The condition for the positiveness of the second variation has the form

$$\frac{1}{2} + \mathrm{Im}\,\zeta\left(2i\,\ln\frac{r_1}{R_1}\right) - 2\,\mathrm{Re}\,\zeta'\left(2i\,\ln\frac{r_1}{R_1}\right) + \frac{2\eta}{\omega_1}\times\left(1 - \ln\frac{r_1}{R_1}\right) - \frac{\omega}{\gamma}r_1^2 \geqslant 0. \tag{8}$$

Let us determine $(\omega/\gamma)r_1^2$ from the equilibrium condition (6) and substitute it into (8):

$$-\mathrm{Re}\,\zeta'\left(2i\,\ln\frac{r_1}{R_1}\right) + \frac{\eta}{\omega_1} - \frac{\omega}{\gamma}r_1^2 \geqslant 0. \tag{9}$$

We now calculate the first two terms, taking into account the expression for ζ-functions[6] and substituting the values of half-periods $\omega_1 = \pi$ and $\omega_2 = i\,\ln(R_2/R_1)$, as well as the denominator $q = R_1/R_2$:

$$\mathrm{Re}\,\zeta'\left(2i\,\ln\frac{r_1}{R_1}\right) - \frac{\eta}{\omega_1} = \frac{1}{4\sinh^2(\ln r_1/R_1)} + 2\sum_{n=1}^{\infty}\frac{q^{2n}}{1-q^{2n}}\cosh 2n\,\ln\frac{r_1}{R_1} = \left(\frac{R_1 r_1}{r_1^2 - R_1^2}\right)^2 + 2\sum_{n=1}^{\infty}\frac{q^{2n}}{1-q^{2n}}\,n \times\cosh 2n\,\ln\frac{r_1}{R_1} > 0.$$

Thus, inequality (9) is *never* satisfied: a negative-intensity vortex is *unstable* (like any number of negative vortices, since the computations remain valid for an arbitrary N if we take for q the quantity $q = (R_1/R_2)^N$). Thus we have to make the following choice: both negative and positive vortices are unstable for low angular velocities of a rotating vessel; so which ones should be given preference and why? In the previous analysis, we stated that, if there is no stable solution of the equation for dF/dr_1, the emergence of circulation around the inner cylinder is assumed to be advantageous from the energy point of view. We shall study the justification for such a statement.

Let us consider expression (5) for free energy. Since the second variation of free energy is negative for any sign of vortices, the root is a maximum. At the right end (for $r_1 = R_2$), the values of the flow function F_1 corresponding to a positive vortex and of the flow function F_{-1} corresponding to a negative vortex coincide (Fig. 2). At the left end (for $r_1 = R_1$), the difference between the free energies F_1 and F_{-1} can be presented in the form

$$F_{-1} - F_1 = \pi\rho_s\gamma^2\left[\frac{2\omega}{\gamma}(R_2^2 - R_1^2)\right]. \tag{10}$$

The absolute values of these quantities can be obtained by calculating the limiting values of F_1 and F_{-1} for

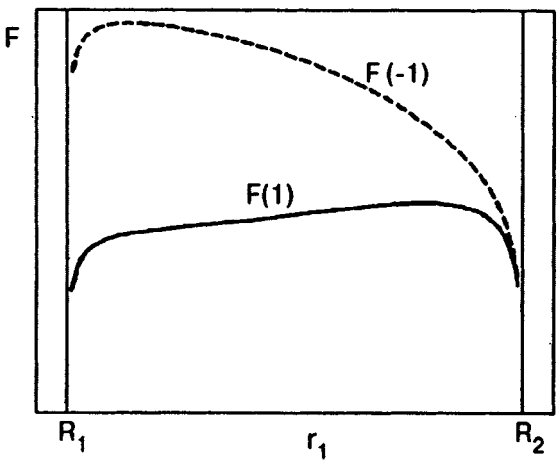

FIG. 2. Qualitative dependence of the free energy on the vortex position r_1 for a positive ($F(1)$) and negative ($F(-1)$) vortex.

$r_1 \to R_{1,2}$ by putting $r_1 = R_2 - \varepsilon$ or $r_1 = R_1 + \varepsilon$ and expanding the sigma-functions in the small parameter ε. These limits are defined as

$$F_{1|_{r_1=R_1+\varepsilon}} \approx \pi\rho_s\gamma^2\left\{\frac{1}{2}+\ln\frac{2\varepsilon}{a}\right\},$$

$$F_{1|_{r_1=R_2-\varepsilon}} \approx \pi\rho_s\gamma^2\left\{\frac{1}{2}+\ln\frac{2\varepsilon}{a}+\ln\frac{R_2}{R_1}-\frac{\omega}{\gamma}(R_2^2-R_1^2)\right\}. \tag{11}$$

At the right end, $F_{-1} = F_1$, while at the left end the sign of the last term is reversed. At $r_1 = R_2$, we find that $F = 0$ if we put $\varepsilon = a/2$ and disregard the term 1/2. However, it should be recalled that the accuracy of the obtained formulas (disregarding deviations of the vortex core shape from cylindrical) deteriorates sharply near the walls. Hence these values of free energy can hardly be called limiting values. However, for the same assumptions concerning ε, we obtain from formula (11)

$$F_1 = \pi\rho_s\gamma^2\left\{\ln\frac{R_2}{R_1}-\frac{\omega}{\gamma}(R_2^2-R_1^2)\right\}.$$

This is just the expression for free energy of a liquid in the presence of a circulation quantum (see Ref. 7 or formula (12) below). Thus, as a vortex descends to the inner cylinder, the free energy is transformed (with a slight error) into the free energy of a superfluid liquid without vortices but with a circulation.

The free energy curves are presented schematically in Fig. 2.

The real values of the maximum energy are of the order of $\gamma^2 \sim 10^{-8}$ (a more detailed estimate of this maximum will be obtained below). If for some reasons (hydrodynamic instability, thermal fluctuations, mechanical vibrations, etc.)[2] a vortex is detached from the wall and falls into unstable equilibrium, its deviation from this position leads to the emergence of a force that draws the vortex from the equilibrium position.

We shall show that the magnitude of this force is proportional to the second variation of the free energy (8). For this purpose, we use the expression for the friction force exerted on a vortex by the normal component and reverting to the equilibrium position if equilibrium is stable or drawing it from the equilibrium position in the opposite case. The equation of motion for the ith vortex filament displaced from equilibrium has the form[2]

$$\gamma\left[(\mathbf{v}_n-\mathbf{v}_{s,e})_i \times \frac{d\,\delta\mathbf{r}_i}{dt}\right] = \zeta_3\rho_s(\mathbf{v}_{s,e}-\mathbf{v}_n)_i^2\hat{e}_z\,.$$

Here, $\delta\mathbf{r}_i$ is the deviation of the vortex filament from the equilibrium position, ζ_3 the bulk viscosity, $\mathbf{v}_{s,e}$ the velocity generated in the vortex core by all the remaining vortices and images (i.e., the velocity of the vortex itself), and $\hat{e}_z$ the unit vector of the axis perpendicular to the plane of the ring (rotational axis). Calculating these expressions in cylindrical coordinates, we obtain a scalar equation (radial component) for one vortex filament:

$$\frac{d(\delta r_1)}{dt} = -\frac{\zeta_3\rho_s}{\gamma}\left[\omega r_1 - \frac{\gamma}{2r_1} - \frac{\gamma}{r_1}\,\mathrm{Im}\,\zeta\left(2i\,\ln\frac{r_1}{R_1}\right) + \frac{2\gamma\eta}{\pi r_1}\ln\frac{r_1}{R_1}\right].$$

In the equilibrium position $r_1 = \tilde{r}_1$, the right-hand side is equal to zero. For $r_1 = \tilde{r}_1 + \delta r_1$, we can obtain an equation for δr_1 by expanding all terms in the small parameter $\delta r_1/\tilde{r}_1$:

$$\frac{d(\delta r_1)}{dt} = -\zeta_3\rho_s\left[\frac{\omega}{\gamma}+\frac{1}{2\tilde{r}_1^2}+\frac{1}{\tilde{r}_1^2}\left(\mathrm{Im}\,\zeta\left(2i\,\ln\frac{\tilde{r}_1}{R_1}\right) - 2\,\mathrm{Re}\,\zeta'\left(2i\,\ln\frac{\tilde{r}_1}{R_1}\right)\right) + \frac{2\eta}{\pi\tilde{r}_1^2}\left(1-\ln\frac{\tilde{r}_1}{R_1}\right)\right]\delta r_1\,.$$

It can be seen easily that the brackets contain just the second variation of the free energy (7) (except for a dimensional factor). It was shown earlier that this quantity is always negative for both positive and negative vortices. Hence vortices displaced from the equilibrium always move away from this position.

A positive vortex detached from the outer wall and crossing the energy barrier approaches the inner wall and merges with its image, while a negative vortex detached from the inner wall drifts towards the outer wall. According to formula (10), however, the free energy F_1 for $r_1 = R_1$ is lower than the free energy F_{-1} for $r_1 = R_2$. This means that the detachment of a positive vortex from the outer wall is energetically more advantageous than the emergence of a negative vortex at the inner wall. Such a detachment leads to the emergence of a circulation around the inner cylinder with the same sign as the angular velocity of the rotating vessel. Thus, all previous arguments remain valid (see Ref. 7), and we can write for free energy the expression obtained above:

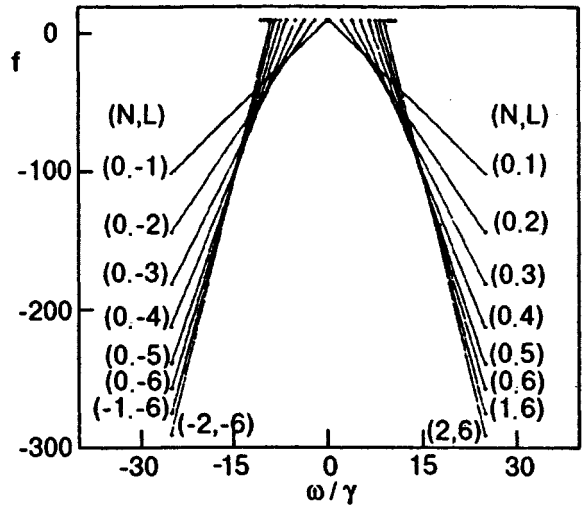

FIG. 3. Dimensionless free energy $f=F/(\pi\gamma^2\rho_s)$ as a function of ω/γ for various values of L and N for a ring with dimensions $R_1=0.1$ cm and $R_2=1.5$ cm.

$$F=\pi\gamma^2\rho_{s,0}\left\{\frac{N}{2}+L^2\ln\frac{R_2}{R_1}-\frac{\omega}{\gamma}L(R_2^2-R_1^2)\right.$$
$$+2LN\ln\frac{R_2}{r_1}-N\ln\frac{a}{r_1}+N\,\mathrm{Re}\ln\sigma\left(2i\ln\frac{r_1}{R_2}\right)$$
$$\left.+\frac{2\eta N}{\omega_1}\ln^2\left(\frac{r_1}{R_2}\right)-\frac{\omega}{\gamma}N(R_2^2-r_1^2)\right\}. \qquad (12)$$

However, the flow pattern is reversed completely for the vessel rotated in the opposite direction. In this case, negative-intensity vortices are formed, and the velocity circulation around the inner cylinder is also negative. This becomes obvious from the expression for free energy in which the last term (which plays a leading role in this analysis) depends on the ratio ω/γ. The total ''energy spectrum'' corresponding to negative and positive rotational velocities has the form shown in Fig. 3. It can be seen that rotation of a vessel filled with superfluid helium always leads to the emergence of vortices having the same direction (sign) as the angular velocity of the rotating vessel.

ENERGY BARRIER AS A FUNCTION OF ANGULAR VELOCITY

It was shown above that detachment of a positive vortex from the outer wall decreases the free energy. However, in order to appear in the vicinity of the inner wall, the vortex must overcome an energy barrier whose height is equal to the free energy at the maximum. To calculate this value, we must know the equilibrium position r_1 of the vortex [i.e., the solution of Eq. (6)] and the angular velocity corresponding to the emergence of the vortex. The problem is complicated by the fact that the root r_1 of Eq. (6) cannot be expressed analytically in terms of the parameters R_1 and R_2 of the ring, but is the solution of a complex equation containing infinite series. The expression for free energy is equally complex [see formula (5)]. Of course, this obstacle can be overcome in numerical computations, but it is not possible to obtain exact analytic expressions in the general case.

In some limiting cases, however, we can obtain approximate expressions for r_1 and free energy, which are more graphic and can provide valuable information.

In particular, for rings with a small inner radius (we shall call them ''broad''), we obtain the following approximate expression for the most complex term in the free energy:

$$S=\mathrm{Re}\ln\sigma\left(2i\ln\frac{r_1}{R_2}\right)+\frac{2\eta}{\omega_1}\ln^2\frac{r_1}{R_2}.$$

Calculations show that the first vortex in such rings appears near the outer wall (this is true for rings with $R_1/R_2<0.05$). In this case, the quantity $\lambda=R_2-r_1$ i small, and we can introduce a small parameter $\varepsilon=\lambda/R_2$. Expanding all expressions appearing in S and free energy in this small parameter, we obtain

$$S=\ln\frac{2\omega_1}{\pi\theta_1'(0)}+\ln\left|\theta_1\left(i\ln\frac{r_1}{R_2}\right)\right|=\ln\frac{2q^{1/4}}{\theta_1'(0)}$$
$$+\ln\left|\left[\frac{r_1^2-R_2^2}{R_2r_1}-q^2\frac{r_1^6-R_2^6}{R_2^3r_1^3}+q^6\frac{r_1^{10}-R_2^{10}}{R_2^5r_1^5}-\ldots\right]\right|$$
$$\approx\ln\frac{2q^{1/4}}{\theta_1'(0)}+\ln 2\varepsilon+\ln(1-3q^2+5q^6+\ldots).$$

Taking into account the expansion of $\theta_1'(0)$ in q,[6] we can present S in the form

$$S=\ln 2\varepsilon+O(\varepsilon).$$

This gives

$$F_1\approx\pi\gamma^2\rho_s\left\{\ln\frac{2R_2\varepsilon\sqrt{e}}{a}-\frac{\omega}{\gamma}R_2^2 2\varepsilon\right\}. \qquad (13)$$

For ''narrow rings'' ($2d=R_2-R_1\ll R_2$), the denominator q is not small. However, we can use the homogeneity condition for σ-functions[6] (''halfperiod reversal'', which was carried out while studying narrow rings in Ref. 7):

$$\sigma(iz|i\omega_1,i\omega_2)=i\sigma(z|\omega_1,\omega_2).$$

For such a substitution, the denominator

$$q=\exp\left(\frac{i\pi\omega_2}{\omega_1}\right)=\exp\left(-\frac{\pi^2}{\ln(R_2/R_1)}\right)$$

is small even for quite ''broad'' rings (for example, its value is of the order of 10^{-3} for the ratio $R_2/R_1\simeq 5$). In this case, the series used for expressing the σ-function will converge so rapidly that one can confine to just the first term in the expansion. Computing this series, we obtain the following approximate expression for free energy:

$$F_1\approx\pi\gamma^2\rho_s\left\{\ln\frac{2r_1\sqrt{e}}{a}+\frac{\ln^2(r_1/R_2)}{\ln(R_2/R_1)}\right.$$
$$\left.+\ln\left|\sin\frac{\pi\ln(r_1/R_2)}{\ln(R_2/R_1)}\right|-\frac{\omega}{\gamma}(R_2^2-r_1^2)\right\}.$$

This expression is valid for all rings with a small q^2. Hence we can easily calculate ω/γ for which F_1 vanishes.

Computer calculations show that in any case, the root is larger than $R=(R_1+R_2)/2$. This means that, as in the case of broad rings, $r_1=R_2-\lambda$. For narrow rings, the value of λ is close to d. Hence the ratio $\varepsilon=\lambda/R_2$ is also small, and all quantities can be expanded in the small parameter ε. This gives

$$\sin\frac{\pi\ln(r_1/R_2)}{\ln(R_2/R_1)}\approx\sin\frac{\pi\ln(1-\varepsilon)}{\ln(1-2\varepsilon)}\approx\sin\frac{\pi}{2}\left(1-\frac{\varepsilon}{2}\right)$$
$$\approx 1-\frac{\pi^2\varepsilon^{12}}{16}.$$

In this case, the free energy assumes the form

$$F_1\approx\pi\gamma^2\rho_s\left\{\ln\frac{2R_2\sqrt{e}}{a}-\frac{3}{2}\,\varepsilon-\frac{\omega}{\gamma}\,R_2^2 2\varepsilon\right\}.$$

In general, we can disregard terms of the order of ε, and present the energy barrier through a very simple relation

$$F_1\approx\pi\gamma^2\rho_s\left\{\ln\frac{2R_2\sqrt{e}}{a}-\frac{\omega}{\gamma}\,R_2^2 2\varepsilon\right\}. \tag{14}$$

Thus, the main contribution to free energy for both narrow and broad rings comes from the logarithm of the relatively large quantity $2R_2\sqrt{e}/a$ (the small factor ε is added to the numerator for broad rings). Due to the presence of the small quantity a in the denominator, this logarithm is of the order of 20, and hence the energy barrier is found to be of the order of $2\cdot10^{-7}$ erg in dimensional units (it is found that this barrier is practically independent of the inner radius for a fixed outer radius).

From formulas (13) and (14), we can easily calculate the angular velocity for which the energy barrier vanishes:

$$\frac{\omega}{\gamma}=\frac{1}{2\varepsilon}\ln\frac{2R_2\sqrt{e}}{a}$$

(for broad rings, we must add ε to the numerator of the logarithm).

Although we must assume in a rigorous analysis that the root of Eq. (6) depends on ω (it approaches the outer wall with increasing ω), even a qualitative analysis shows that the angular velocity at which the energy barrier vanishes is much higher than the theoretical velocity ω_0 at which the emergence of the first (unstable) vortex becomes advantageous from the energy point of view. This means that the probability of emergence of a vortex for $\omega=\omega_0$ is low.

This probability can be estimated by calculating the quantity

$$P=\exp\left(-\frac{F_1}{k_BT}\right)\frac{2\pi r_1}{a}.$$

Here F_1 is the height of the energy barrier being overcome, and T the temperature.[10] The exponential factor is determined by the frequency of collisions with the potential barrier, for which we can take the ratio of the circumference of the circle containing the vortex to the vortex radius.

TABLE I. Angular velocities corresponding to the emergence of the first vortex remark.

R_1, cm	ω_0, s^{-1}	ω_c, s^{-1}
1.10	$4.7\cdot10^{-5}$	$4.7\cdot10^{-3}$
1.20	$4.4\cdot10^{-5}$	$6.3\cdot10^{-3}$
1.30	$4.1\cdot10^{-5}$	$9.5\cdot10^{-3}$
1.35	$3.9\cdot10^{-5}$	$1.3\cdot10^{-2}$
1.40	$3.8\cdot10^{-5}$	$1.9\cdot10^{-2}$
1.45	$3.6\cdot10^{-5}$	$3.8\cdot10^{-2}$

Note. The outer radius $R_2=1.5$ cm.

Since $F_1\sim10^{-7}$ erg, $P\simeq\exp(-10^{-9})$ at $T\simeq1$ K, which is several orders of magnitude smaller than the second factor in the expression for P (the vortex radius is of the order of 10^{-8} cm). Thus, the probability of formation of a vortex for $\omega=\omega_0$ is practically equal to zero. In actual practice, circulation around the inner cylinder appears at velocities much higher than ω_0.

With increasing angular velocity, the barrier height F_1 decreases. But since the contribution from the second term which is proportional to ω is not as large as from the first term, F_1 becomes equal to zero for angular velocities much higher than ω_0. The real angular velocities ω_c at which the first vortex appears must exceed the theoretical value ω_0 by a factor of about 100 (see Table I). Although the absolute value of the angular velocity still remains quite small, this difference can be probably detected experimentally.

RELATION BETWEEN ANGULAR VELOCITY AND NUMBER OF VORTICES

The family of straight lines presented in Fig. 3 generally depends on three parameters, viz., r_1, L, and N. However, for a quite large number of vortices, the equilibrium position of the vortex chain lies practically at the middle of the gap for rings of all sizes, i.e.,

$$r_1=(R_2+R_1)/2,$$

while the angular velocity of the rotating vessel is connected with the number of vortices and the number of circulation quanta through a similar relation[8]

$$\frac{\omega}{\gamma}\,r_1^2=L+\frac{N}{2}. \tag{15}$$

While deriving the above relation, we have disregarded the terms

$$N\left[\left(\frac{R_1}{r_1}\right)^{2N}-\left(\frac{r_1}{R_2}\right)^{2N}\right].$$

We can estimate the number of vortices N for which these terms are several orders of magnitude smaller than the remaining terms $(L+N/2)$. For a fixed radius of the outer cylinder $R_2=1.5$ cm, the discarded terms are of the order of 10^{-3} for the following pairs of values of R_1 and N:

R_1, cm	0.1	0.3	0.5	1.0	1.2
N	$\geqslant 8$	$\geqslant 10$	$\geqslant 12$	$\geqslant 28$	$\geqslant 50$.

For large values of R_1, the number of circulation quanta L around the inner cylinder becomes very large, and hence the real values of N for which formula (15) is valid are much smaller than those mentioned above.

Using the expression for r_1 and formula (15), we can make the family of lines $F_{N,L}$ *one parametric* (although these lines will no longer be straight) and try to find the envelope of this family. For this purpose, we first derive an approximate expression for the term containing the σ-function:

$$S_N \equiv \mathrm{Re}\ \ln \sigma\left(2i\ \ln\frac{r_1}{R_1}\right)+\frac{2\eta}{\omega_1}\ln^2\left(\frac{r_1}{R_1}\right)$$
$$=\ln\frac{2}{N}+\mathrm{Re}\ \ln\frac{\theta_1(iN\ \ln(r_1/R_1))}{\theta_1'(0)}=\ln\frac{2}{N\theta_1'(0)}$$
$$+\ln\left[2q^{1/4}\sum_{n=0}^{\infty}(-1)^n q^{n(n+1)}\sinh\ N(2n+1)\ln\frac{r_1}{R_1}\right]$$
$$\approx\ln\frac{2}{N}+\ln\sinh\ N\ln\frac{r_1}{R_1}\approx\ln\frac{1}{N}+N\ln\frac{r_1}{R_1}.$$

This gives

$$F\approx\pi\gamma^2\rho_s\left\{\left(-L(R_2^2-R_1^2)-N(R_2^2-r_1^2)\right)\frac{\omega}{\gamma}\right.$$
$$+\left[L^2\ln\frac{R_2}{R_1}+2LN\ln\frac{R_2}{r_1}-N\ln\frac{aN}{r_1}\right.$$
$$\left.\left.+N^2\ln\frac{R_1R_2}{r_1^2}+N^2\ln\frac{r_1}{R_1}\right]\right\}. \qquad (16)$$

Substituting $L=(\omega/\gamma)r_1^2-N/2$ and grouping terms in powers of ω/γ, we obtain

$$F_{N,L}=-\left(\frac{\omega}{\gamma}\right)^2 r_1^2\left[R_2^2-R_1^2-r_1^2\ln\frac{R_2}{R_1}\right]$$
$$-\frac{\omega}{\gamma}N\left[\frac{R_1^2}{2}+\frac{R_2^2}{2}-r_1^2+r_1^2\ln\frac{r_1^2}{R_1R_2}\right]$$
$$+\frac{N^2}{4}\ln\frac{R_2}{R_1}-N\ln\frac{aN}{r_1}. \qquad (17)$$

It should be recalled that the free energy (17) should be treated as a function ω/γ, i.e., we should take ω/γ for the argument x, and $F_{N,L}$ for y. In order to obtain an equation for the envelope, we differentiate (17) with respect to the parameter N.[9]

$$\frac{\omega}{\gamma}\left[\frac{R_1^2}{2}+\frac{R_2^2}{2}-r_1^2+r_1^2\ln\frac{r_1^2}{R_1R_2}\right]=\frac{N}{2}\ln\frac{R_2}{R_1}-\ln\frac{aN}{r_1}-1. \qquad (18)$$

Together with Eq. (17), this expression gives the equation for the envelope of a one-parametric family of curves $F_{N,L}$. Although this equation cannot be derived explicitly (it is impossible to eliminate N in the analytic form), we observe that formula (18) can be treated as a quite simple relation between the number of vortices and the angular velocity of a rotating vessel: by specifying the number N of vortices, we can determine the corresponding angular velocity, and vice versa. The accuracy of this expression is determined by the order of the discarded terms in formulas (15) and (16).

The author thanks I. E. Tarapov for raising interesting questions at the seminar in the Department of Mechanics, which stimulated this research. Thanks are also due to S. I. Shevchenko for a discussion of the results and for helpful comments.

[1)]Note that while solving Eq. (6) with the right-hand side obtained from the condition $F_1<F_0$, we have no roots at all, since the right-hand side grows more rapidly than the left-hand side near the boundary $r=R_2$. However, it is obvious that a root always exists for a *fixed* ω, and this root is close to R_2. Figure 1 shows the plot of $(\omega/\gamma)r_1^2$ for the value of ω obtained from the condition $F_{1,0}<F_{0,0}$ in the preceding analysis.[7]

[1] R. Milne-Thomson, *Theoretical Hydrodynamics*, London (1960).
[2] C. Patterman, *Superfluid Hydrodynamics*, North-Holland, Amsterdam (1976).
[3] R. J. Donnelly and M. M. La Mar, J. Fluid Mech. **186**, 162 (1988).
[4] L. D. Landau and E. M. Lifshitz, Fluid Mech.-Sov. Res. , (1986).
[5] A. D. Tyuptsov and T. I. Zueva,Mat. Fiz., Analiz, Geomet. **1**, 529 (1994).
[6] M. Abramowitz and I. A. Stegun, Handbook of Mathematical Functions, Dover, New York (1965).
[7] A. D. Tyuptsov and T. I. Zueva, Fiz. Nizk. Temp. **20**, 1116 (1994) [Low Temp. Phys. **20**, 877 (1994)].
[8] T. I. Zueva, Fiz. Nizk. Temp. **22**, 1100 (1996) [Low Temp. Phys. **22**, 841 (1996)].
[9] G. M. Fikhtengol'ts, *A Course on Differential and Integral Calculus* [in Russian], Vol. 1, Nauka, Moscow (1969).
[10] D. R. Tilley and J. Tilley, *Superfluidity and Superconductivity*, Van Nostrand, New York (1974).

Translated by R. S. Wadhwa

Carrier transport in quasi-one-dimensional electron systems over liquid helium under strong localization conditions

Hideki Yayama and Akihisa Tomokiyo

Department of Physics, Faculty of Science, Kyushu University, Fukuoka 810, Japan

O. I. Kirichek, I. B. Berkutov, and Yu. Z. Kovdrya

*B. Verkin Institute for Low Temperature Physics and Engineering, National Academy of Sciences of the Ukraine, 310164 Kharkov, Ukraine**

(Submitted May 26, 1997)
Fiz. Nizk. Temp. **23**, 1172–1177 (November 1997)

The conductivity of carriers in a quasi-one-dimensional electron system over liquid helium is measured in the temperature interval $0.5-1.9$ K in confining electric fields up to 4 kV/cm at a frequency of 1.1 MHz. Quasi-one-dimensional channels were created by using an optical diffraction grating covered with a thin helium layer. The carrier conductivity decreases exponentially with temperature T, and the activation energy is of the order of a few degrees, thus pointing towards localization of electrons in a quasi-one-dimensional electron system. As the thickness of the helium layer covering the grating is increased, a departure from a mono exponential dependence is observed at $T<0.8$ K, which indicates that quantum effects begin to play an active role in electron mobility at these temperatures. An analysis of the obtained results leads to the assumption that under localization conditions, quasi-one-dimensional electron systems may contain two branches of the optical mode of plasma oscillations, viz., a high-frequency branch associated with electron oscillations in potential wells, and a low-frequency branch associated with the oscillations of the electron-dimple complex with a large effective mass.
[S1063-777X(97)00311-3]

The behavior of charge carriers in quasi-one-dimensional (Q1D) and one-dimensional (1D) electron systems over liquid helium is very interesting because of the possibility of realization of conducting channels with small transverse dimensions, containing one to ten electrons.[1] Surface electrons (SE) over liquid helium form an extremely pure and homogeneous low-dimensional electron system, and it can be expected that Q1D and 1D electron systems employing SE will also be homogeneous and perfect. Quasi-one-dimensional conducting channels over liquid helium were created experimentally by using the surface undulations of liquid helium flowing under the action of capillary forces into the grooves of the profiled substrate.[2,3] Under the action of a confining electric field, electrons are displaced towards the bottom of the groove and can move freely only in one direction. A distinguishing feature of such channels is that the depth of the liquid in the grooves of the profiled substrate reach values $\sim 10^{-4}$ cm and the roughnesses of the substrate have no effect on the behavior of the electron. Transfer measurements in such quasi-one-dimensional systems have shown that the mobility of electrons in Q1D channels may become close to the electron mobility in bulk helium.[4–6] However, experimental results obtained by increasing the separation H between the bulk helium surface and the upper plane of the substrate, i.e. by decreasing the radius of curvature of the liquid in the substrate grooves, indicate that the mobility of charge carriers decreases, and its temperature dependence begins to differ strongly from the analogous dependence for SE over bulk helium. The obtained results were attributed to the localization of carriers in potential wells emerging in conducting channels under the influence of electrons localized over a thin helium film in the immediate vicinity of the grooves filled with the liquid.[2,4]

In this research, we have measured the conductivity of electrons over liquid helium in quasi-one-dimensional channels under strong localization conditions. Measurements were made in the temperature range 0.5-1.9 K in the electron density of states between 10^8 and 10^9 cm^{-2} at a frequency of 1.1 MHz. The experimental cell used for measurements is shown in Fig. 1a. A high-quality glass optical grating 1 of size 24.4×19.6 mm and thickness $d=0.8$ mm (Fig. 1b) was used to obtain quasi-one-dimensional liquid channels. The glass used to form the optical grating had a dielectric constant $\varepsilon\simeq 4$, and the number of grooves in one centimeter of the grating was 1670. The grating was mounted over electrodes A, B, and C which were held at zero potential. The size of the electrodes A, B, and C was 15.6×9.2, 2×9.2, and 15.6×9.2 mm, respectively. A negative voltage confining the electrons to the surface of the liquid helium wetting the substrate was applied to electrodes *2* and *3*. In order to produce an electron spot with a sharper electron density profile at the edge, a negative potential was applied to the shielding electrode *4*. Two opposite cuts of width ~ 1.2 mm were made on the electrodes 2 and 3 to ensure a free leakage of helium to the drift space of the experimental cell and to reduce the possible temperature gradient between the liquid helium film at the grating surface and bulk helium. The generator voltage was supplied to the electrode A, while the signal passing through the cell was recorded at the electrode C. For such a voltage supply, the drift electric field is

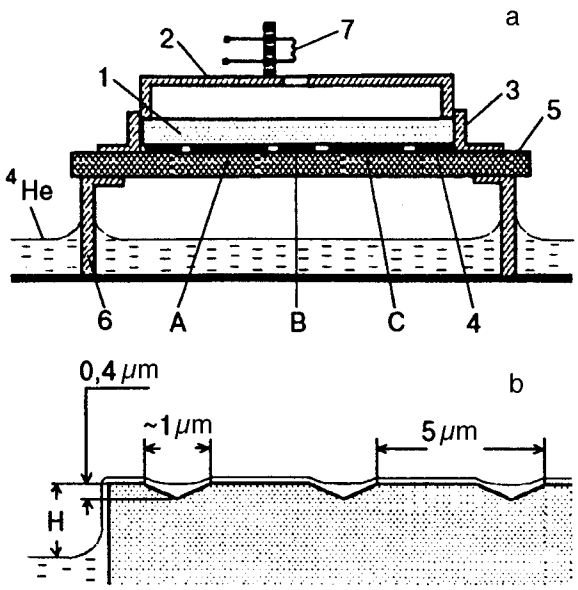

FIG. 1. (a) Schematic diagram of the measuring cell: optical grating *1*, confining electrodes (*2*, *3*), shielding electrode (*4*), foliated textolite glass (*5*), copper supports (*6*), incandescent filament (*7*), and measuring electrodes (A,B,C), (b) Optical grating profile.

directed along the liquid grooves. The electrode B was earthed.

The signal passing through the experimental cell was amplified by a wide-band preamplifier[1)] and detected by a phase-sensitive detector. In the experiments, we measured the phase shift $\Delta\varphi$ and the signal amplitude variation ΔU produced during charging of the measuring cell by electrons. Using the measured values of $\Delta\varphi$ and ΔU, we determined the real G_r and imaginary G_i components of the conductance of the cell. According to the computations made in Refs. 7, the values of G_r and G_i are defined by the real and imaginary components ρ_r and ρ_i of the electron layer resistance, as well as the frequency of plasma oscillations ω_p in the two-dimensional electron system.

Estimates reveal that, under the conditions of such measurements, we can disregard terms containing ρ_i in the expressions for G_r and G_i. In this case, the expressions for G_r and G_i assume the form

$$G_r=-n_se^2\sum_{q_n}\Lambda_{q_n}\frac{n_se^2\omega^2\rho_r}{m^2\tilde{\omega}_p^4+(n_se^2\omega\rho_r)^2}; \tag{1}$$

$$G_i=-n_se^2\sum_{q_n}\Lambda_{q_n}\frac{m\omega^2\omega_p}{m^2\tilde{\omega}_p^4+(n_se^2\omega\rho_r)^2}+g_0. \tag{2}$$

Here, e and m are the electron charge and mass, n_s is the average density of electrons in the conducting channels, ω the cyclic frequency, $\tilde{\omega}_p$ the plasma frequency in conducting channels, q_n the wave vector of plasma oscillations, and q_0 the conductance of the cell in the absence of electrons. Since the plasma wave in a quasi-one-dimensional system can propagate only in one direction, summation in Eqs. (1) and (2) is carried out over wave vectors of oscillations directed along the conducting channels. The quantities q_n are determined by the length L_x of the grooves. For a rectangular geometry and quasi-one-dimensional channels, the coefficient Λ_{q_n} was taken from Ref. 6.

The estimates obtained from an analysis of the experimental data show that for the values of H used in this work, the total resistance of all channels was quite large, and hence the condition $m\tilde{\omega}_p^2\ll n_se^2\omega\rho_r$ is satisfied. Moreover, experiments reveal that, during charging of the cell by electrons, the signal amplitude varies by just a few percent, while the phase shift turned out to be of the order of a few degrees. This means that we can disregard the contribution from electrons to G_i, and we can write $G_i\approx g_0$. In this case, the quantity tan $\Delta\varphi$, which is defined by the ratio of the quantities G_r and G_i, can be presented in the form

$$\tan\ \Delta\varphi\approx\Delta\varphi=-\frac{1}{g_0}\sum_{q_n}\Lambda_{q_n}\sigma, \tag{3}$$

where the quantity $\sigma=1/\rho_r$ corresponds to the conductivity of the channels over an area of 1 cm^2.

The electron density at the surface of liquid helium wetting the substrate was determined from the condition of complete charge saturation. Note that the signal from SE appears, as a rule, starting from a certain value $V_\perp$, thus pointing towards a slight initial charging of the substrate. The electron density in each experiment was determined by plotting the dependence of $\Delta\varphi$ on $V_\perp$. While recording this dependence, the liquid surface was charged each time at a new value of $V_\perp$ at which the quantity $\Delta\varphi$ was measured. The dependence of $\Delta\varphi$ on $V_\perp$ was practically linear. Upon a decrease in voltage, the curve $\Delta\varphi(V_\perp)$ was displaced, i.e., a slight hysteresis was observed. Unfortunately, a spread of about 30% was observed in the value of $\Delta\varphi$ in different experiments for the same values of H, $V_\perp$, and T. Such a spread is probably caused by the presence of a small number of impurities of solidified gases on the substrate, which could vary from experiment to experiment, by uncontrollable charging of the substrate, as well as by an uncertainty in determining the value of H. However, the results showed a very good reproducibility in the course of a single experiment. The total number of electrons over 1 cm^2 of the liquid surface was determined from the condition

$$n_0=\frac{V_\perp-V_\perp^k}{eC},$$

where $C=\varepsilon/4\pi d$.

Figure 2 shows typical temperature dependences of $\Delta\varphi$ and σ for values of H equal to 1.8 (curve *1*) and 0.8 mm (curve *2*). It can be seen that the smaller the value of H, the larger the value of σ, the dependence of σ on T being the steeper, the larger the value of H. An analysis of the experimental data shows that curve *1* can be described by the dependence

$$\sigma=\frac{\alpha}{T}\exp(-E/T), \tag{4}$$

where the coefficients α and E do not depend on temperature. For curve *1*, these quantities have the following values: $\alpha=(4\pm0.1)\cdot10^4\Omega^{-1}\cdot$K, $E=(6\pm0.2)$K. It can be seen that

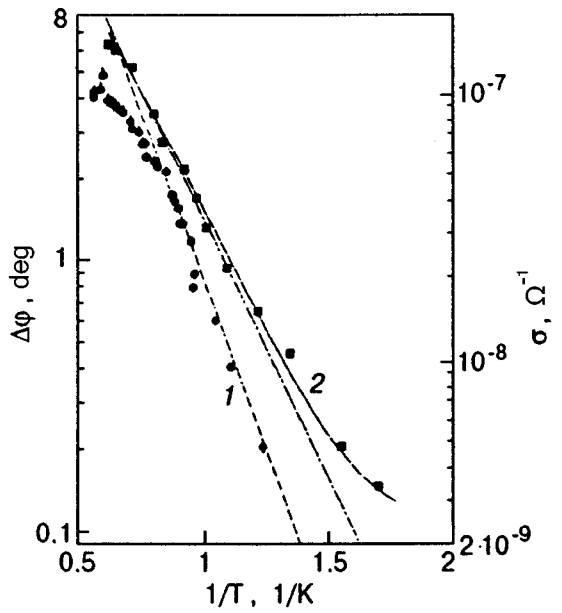

FIG. 2. Temperature dependences of the phase shift $\Delta\varphi$ of the signal transmitted through the experimental cell and electron conductivity σ in $Q1D$ channels for $n_s=6.7\cdot10^8$ cm^{-2}, $H=1.8$ (●) and 0.8 mm (■). The dotted and dashed curves correspond to the dependence $\sigma=(\alpha/T)\exp(-E/T)\Omega^{-1}$ with $\alpha=(4\pm0.1)\cdot10^{-4}\Omega^{-1}\cdot$K, $E=(6\pm0.2)$K; and $\alpha=(7.8\pm0.9)\times10^{-6}\Omega^{-1}\cdot$K, $E=(5.4\pm0.2)$K; respectively, while the solid cuve describes the dependence $\sigma=(\alpha/T)\exp(-E/T)+(\beta/T)\exp(-E_1/T)\Omega^{-1}$, $E=(5.4\pm0.2)$K, $E_1-0.05$ K. $\alpha=(7.8\pm0.9)\cdot10^{-6}\Omega^{-1}\cdot$K, $\beta=(4\pm0.5)\times10^{-10}\Omega^{-1}\cdot$K.

curve *2* displays a departure from the mono exponential dependence. An analysis of the data reveals that this curve can be described satisfactorily by the expression

$$\sigma=\frac{\alpha}{T}\exp(-E/T)+\frac{\beta}{T}\exp(-E_1/T) \tag{5}$$

with coefficients $\alpha=(7.8\pm0.9)\cdot10^{-6}\Omega^{-1}\cdot$K, $E=(5.4\pm0.2)$K, $\beta=(4\pm0.5)\cdot10^{-10}\Omega^{-1}\cdot$K, and $E_1\simeq0.05$ K.

The experimental dependences of σ on T indicate that carriers are localized in $Q1D$ channels. In the case of classical thermally activated motion of localized carriers, the conductivity is described by the following expression:

$$\sigma=\frac{n_s e^2\nu_0 a_0^2}{k_B T}\exp(-E/T), \tag{6}$$

where k_B is the Boltzmann constant, a_0 is the mean separation between potential wells in which the electrons are localized, ν_0 the electron vibrational frequency in potential wells, and E the height of the potential barrier.

The obtained results allow us to estimate the value of ν_0. For this purpose, we must know the values of n_s and a_0. During charging of the surface of helium covering the substrate, plane segments of the helium film are charged as well as the liquid channels. Our earlier calculations show[4] that, for a given value of H, the number density of electrons over a thin helium film is about double the value of electron density over the grooves with a thick helium layer. Knowing the total number of electrons over a unit area of helium surface and the relative areas of the thin helium film and liquid channels on the substrate, we can determine the value of n_s. Such calculations were made by using the condition of constant potential over the charged helium surface. Since the width of channels exceeds the mean separation between electrons insignificantly, this condition is not satisfied exactly, and the computation of n_s is approximate. The quantity a_0 defining the characteristic scale of variation of the potential relief in a liquid channel is determined by the mean separation between electrons localized over a thin helium film. Thus, knowing n_s and a_0 and using (6) with the corresponding activation energy E, we can determine the mean frequency ν_0 of electron oscillations in potential wells. For curves *1* and *2*, these frequencies are found to be $\sim1.0\cdot10^{11}$ s^{-1} and $\sim5\cdot10^{10}$ s^{-1}, respectively.

At temperatures T below 0.8 K, curve *2* exhibits a deviation from the monoexponential dependence. Two possible explanations can be given for this effect. The first one is associated with the assumption that two types of potential wells of different depths exist in Q1D channels. The number of carriers in deeper potential wells is larger than in shallower wells. At relatively high temperatures, carriers in deep potential wells play the main role in transport phenomena, while at low temperatures, when the mobility of such carriers becomes small, the main contribution to the conductivity comes from the electrons in shallower potential wells. Another possible reason behind the observed effect may be the emergence of quantum effects of electron tunneling from one potential well to another in the electron mobility at $T<0.8$ K.

A characteristic feature of the system under consideration is that there is a certain spread in the values of potential well parameters in $Q1D$ channels. This spread is probably not significant since at relatively high temperatures the data are described quite well by a single activation energy exponential. However, even a slight variation of the potential well parameters or a nonuniformity in their distribution along a channel can considerably affect the behavior of carrier conductivity in $Q1D$ channels. In particular, displacement of energy levels in potential wells may lead to tunneling if energy levels in adjacent potential wells coincide as a result of fluctuations. It should be borne in mind that electrons localized in $Q1D$ channels will form dimples (ripplon polarons) at the surface of liquid helium. The picture is further complicated due to the fact that the potential well may contain several potential levels.

Analyzing the diffusion D of ^{3}He impurities in crystals of solid helium, Kagan[8] showed that as the temperature is lowered, the emerging quantum effects make the dependence of D on T weaker than the dependence corresponding to the classical activation motion of particles. The effects observed by us in this work are similar to a certain extent to those observed in Ref. 8, with the only stipulation that the spread of potential well parameters in the present case may further complicate the picture. Finally, we observe that the transition of a particle from one potential well to another may involve absorption or emission of ripplons. Unfortunately, a theory of this effect does not exist at present, and a quantitative comparison of the experimental and theoretical data is not possible.

It was mentioned above that the condition $m\tilde{\omega}_p^2 \ll n_s e^2 \omega \rho_r$ is satisfied in our experiments. This relation allows us to estimate the upper limit of the quantity $\tilde{\omega}_p$ which turns out to be below ~ 1 GHz in the present case. This value one or two order of magnitude lower than the characteristic oscillation frequency ν_0 of electrons in a potential well. Such an estimate does not contradict the data of Ref. 6 where it is shown that the maximum value of $\tilde{\omega}_p$ for the grating used by the authors does not exceed ~ 900 MHz. The fact that $\tilde{\omega}_p$ is much smaller than ν_0 indicates that the electrons localized in potential wells form dimples at the surface of liquid helium,[9] and the effective mass m^* of an electron-dimple complex is much larger than the free electron mass.

It was shown by Chaplik[10] that one-dimensional electron systems contain a longitudinal branch of plasma oscillations with an energy-momentum relation

$$\omega_{\parallel} \approx \frac{2e^2 k}{ma} \ln \frac{1}{ka},$$

where k is the wave vector of oscillations, and a is the mean separation between electrons. According to what has been stated above, two optical modes of plasma oscillations may exist on the helium surface in $Q1D$ channels under localization conditions. The high-frequency mode is associated with electron oscillations, and its energy-momentum relation has the form

$$\omega_p^2 = (2\pi\nu_0)^2 + \omega_{\parallel}^2. \tag{7}$$

The low-frequency mode is associated with the oscillations of electron-dimple complexes, and its energy-momentum relation has the form

$$\tilde{\omega}_p^2(k) = \omega_\alpha^2 + \frac{2e^2 k}{m^* a} \ln \frac{1}{ka}, \tag{8}$$

where ω_α is the oscillation frequency of electron-dimple complexes in potential wells. In view of a spread in the potential well parameters, the plasma oscillation spectra (7) and (8) obviously have a certain dispersion. However, since the experimental data on conductivity in $Q1D$ channels are described correctly by an exponential relation (at least at $T > 0.8$ K), the potential well parameters do not differ significantly from one another, and it can be expected that dispersion in the spectra will not be significant. It should be quite interesting to carry out experimental observation of such plasma oscillation modes.

Thus, we have shown in the present work that, in quasi-one-dimensional electron systems over liquid helium, the electron conductivity under localization conditions decreases exponentially with temperature, the activation energy being of the order of several degrees. At $T < 0.8$ K, the $\sigma(T)$ dependence corresponding to small values of H shows a departure from the exponential law. This is apparently due to the existence of two types of carriers with different activation energies, or to the tunneling of electrons to the neighboring potential wells. It is predicted from an analysis of the experimental data that, under localization conditions, the $Q1D$ channels may contain two optical modes of plasma oscillations. One of these is a high-frequency mode with limiting frequency of electron oscillations in potential wells, while the second is the low-frequency mode whose limiting frequency is determined by oscillations of massive electron-dimple complexes in potential wells.

The authors are grateful to V. N. Grigor'ev for his interest in this research and for fruitful discussions of the results.

*E-mail: kovdrya@ilt.kharkov.ua

[1)]The authors are obliged to V. V. Dotsenko for his help in designing the measuring system.

[1] Yu. Z. Kovdrya and Yu. P. Monarkha, Fiz. Nizk. Temp. **12**, 1011 (1986) [Sov. J. Low Temp. Phys. **12**, 571 (1986)].
[2] Yu. Z. Kovdrya and V. A. Nikolaenko, Fiz. Nizk. Temp. **18**, 1278 (1992) [Sov. J. Low Temp. Phys. **18**, 894 (1992)].
[3] O. I. Kirichek, Yu. P. Monarkha, Yu. Z. Kovdrya, and V. N. Grigor'ev, Fiz. Nizk. Temp. **19**, 458 (1993) [Low Temp. Phys. **19**, 323 (1993)].
[4] Yu. Z. Kovdrya, V. A. Nikolaenko, and P. K. H. Sommerfeld, Czech. J. Phys. **46-S1**, 347 (1996).
[5] Hideki Yayama and Akihisa Tomokiyo, Czech. J. Phys. **46-S1**, 353 (1996).
[6] V. A. Nikolaenko, H. Yayama, Yu. Z. Kovdrya, and A. Tomokiyo, Fiz. Nizk. Temp. **23**, 642 (1997) [Low Temp. Phys. **23**, 482 (1997)].
[7] Yu. Z. Kovdrya, V. A. Nikolaenko, O. I. Kirichek *et al.*, J. Low Temp. Phys. **81**, 371 (1991).
[8] Yu. Kagan, J. Low Temp. Phys. **87**, 571 (1992).
[9] Yu. Z. Kovdrya, F. F. Mende, and V. A. Nikolaenko, Sov. J. Low Temp. Phys. **10**, 1129 (1984).
[10] A. B. Chaplik, Pis'ma Zh. Éksp. Teor. Fiz. **31**, 275 (1980) [JETP Lett. **31**, 252 (1980)].

Translated by R. S. Wadhwa

Resistive relaxation processes in oxygen-deficient single crystals of $YBa_2Cu_3O_{7-\delta}$

M. A. Obolenskii, A. V. Bondarenko, R. V. Vovk, and A. A. Prodan

Kharkov State University, 310077 Kharkov, Ukraine[*]

(Submitted March 11, 1997; revised May 14, 1997)
Fiz. Nizk. Temp. **23**, 1178–1182 (November 1997)

The effect of low-temperature annealing on the superconducting transition temperature and electrical resistance of single crystals of $YBa_2Cu_3O_{7-\delta}$ with an oxygen deficiency $\delta=0.5-0.6$ quenched from temperatures of 620–650 °C is considered. The transition temperature increases during annealing, while the resistance decreases. The isothermal relaxation of resistance is measured and used for estimating the activation energy of the relaxation process, which coincides with the activation energy of oxygen diffusion. The obtained results are attributed to oxygen ordering in Cu-O planes without changing its concentration. The observed step form of resistive transitions to the superconducting state is interpreted as the formation of clusters characterized by different oxygen concentrations and ordering. The cluster size is estimated.
 [S1063-777X(97)00411-8]

Studies of the superconducting[1,2] and optical[3,4] properties of $YBa_2Cu_3O_{7-\delta}$ single crystals with an oxygen deficiency $\delta\simeq 0.5-0.6$ quenched from high temperatures have shown that these properties depend not only on the oxygen index, but also on the annealing time at room temperature. For example, room temperature annealing causes an increase in the superconducting transition temperature T_c which may attain values up to 15 K depending on the oxygen index.[1,2] Optical investigations have shown[3,4] that annealing at room temperature causes an increase in the reflectivity single crystals, which was attributed to an increase in the carrier concentration.

Neutron diffraction studies[5] of ceramic samples of $YBa_2Cu_3O_{6.41}$ quenched from a temperature of 500 °C point towards a change in the lattice parameters during sample annealing at room temperature. However, no significant variation is observed in the occupancy of oxygen positions in Cu-O plane along **a** and **b**-axes.

The effect of room-temperature annealing on the transition temperature, carrier concentration, and lattice parameter variation of oxygen-deficient samples of $YBa_2Cu_3O_{7-\delta}$ is attributed to the ordering of oxygen atoms in the Cu-O plane without any change in the oxygen concentration in the sample.[5] Since the electrical resistance depends significantly on the carrier concentration and defect structure of the sample, a change in sample resistance must be observed during room-temperature annealing of the sample.

The present paper aims at studying the effect of room-temperature annealing on sample resistance in the ab-plane and on the superconducting transition temperature of $YBa_2Cu_3O_{7-\delta}$ single crystals with decreasing oxygen concentration after rapid cooling from 620–650 °C.

Single crystals of $YBa_2Cu_3O_{7-\delta}$ were grown by using the solution-melt technique in a gold crucible.[6] The crystals were annealed for two days in oxygen flow at temperatures 620–650 °C. After annealing, the crystals were cooled to room temperature in two-three minutes. The sample was mounted in a measuring cell and cooled to liquid helium temperature in about 15–20 minutes. All measurements of the temperature dependences of the sample resistance R were made during warming-up of the sample. The resistance was measured by the standard four-probe technique in a constant current $I=1$ mA. The temperature was measured by a platinum resistance thermometer.

The following sequence of measurements was adopted while studying the effect of room-temperature annealing on the superconducting transition temperature. After the first measurement of $R(T)$ just after mounting, the samples were held at room temperature for twenty hours before repeating the measurements. The samples were then held at room temperature for another three days, and measurements were made once again. The last series of $R(T)$ measurements was carried out after a further annealing for two weeks.

Figure 1 shows the results of measurements of transitions to the superconducting state for samples S1 and S2 with different transition temperatures. It can be seen that T_c increases with increasing room-temperature annealing time for crystals, while the remnant resistance $R_{\rm rem}$ decreases. It can also be seen that the main increase in transition temperature and decrease in remnant resistance occur at the initial stage of annealing, i.e., during the first day. Subsequent annealing for three days has no significant effect on the variation of transition temperature and of remnant resistance. Further annealing for two weeks does not change the transition temperature of the remnant resistance.

A characteristic feature of resistive transitions to the superconducting state is their step form. After room-temperature annealing, the steps on the resistive transitions are smoothed and sometimes vanish completely as, for example, in the case of sample S2.

The following sequence of measurements was adopted to study the effect of annealing on resistance. The sample was held at $T\simeq 620$ °C for a day, cooled to room temperature in 2–3 minutes, and mounted in the measuring cell for five

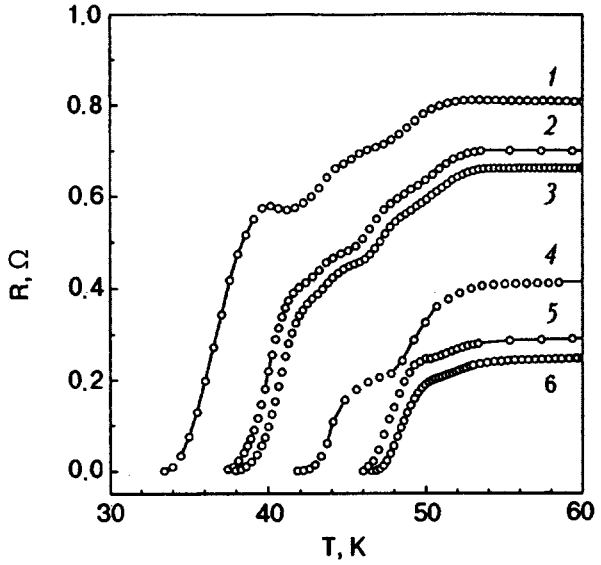

FIG. 1. Resistive transitions to superconducting state in single crystals *S*1 (curves *1–3*) and *S*2 (curves *4–6*). The dependences shown by curves *1* and *4* were obtained directly after thermal treatment of the crystal in oxygen flow, while the dependences shown by curves *2* and *5* were obtained after room-temperature annealing of the crystals for 20 hours. The dependences *3* and *6* correspond to annealing for four days.

minutes. After this the resistance $R(t)$ was measured as a function of time at a fixed temperature. Measurements were made at various temperatures between 240 and 320 K. During isothermal measurements, the temperature was kept constant to within 0.05 K.

The dependences $R(t)$ are presented in Fig. 2. It can be seen that the resistance decreases continuously with increasing annealing time, and the slope of the dependences $R(t)$ decreases rapidly with temperature. This points towards the thermal activation nature of the relaxation process. Using the method of variation of slope of resistance relaxation curves, we can determine the activation energy with the help of the expression[7]

$$U=\ln(\alpha_1/\alpha_2)/(1/T_2-1/T_1),$$

where α_1 and α_2 are the slopes of the $R(t)$ dependences measured at temperatures T_1 and T_2 and are determined for the same values of electrical resistance. The activation energy of resistance relaxation, determined from the measurement of $R(t)$ dependence at 295.3 and 305.8 K and for $R=0.44\Omega$ (curves *4* and *5* in Fig. 2a) is $1.1\cdot 10^4$ K. The value obtained by us coincides with the activation energy of oxygen diffusion in $YBa_2Cu_3O_{7-\delta}$ single crystals with a decreased oxygen concentration.[8,9] Hence the earlier assumption[1–5] about oxygen ordering in CuO planes during room-temperature annealing of $YBa_2Cu_3O_{7-\delta}$ single crystals quenched from 500 °C seems to be quite plausible.

It should also be observed that if the temperature is increased after the attainment of the equilibrium value of electrical resistance corresponding to a given temperature, and then reduced to its initial value, the equilibrium resistance value is restored only after the passage of a considerably longer time. This is shown graphically in Fig. 2b in which curve *1* corresponds to measurements at 289 K after the

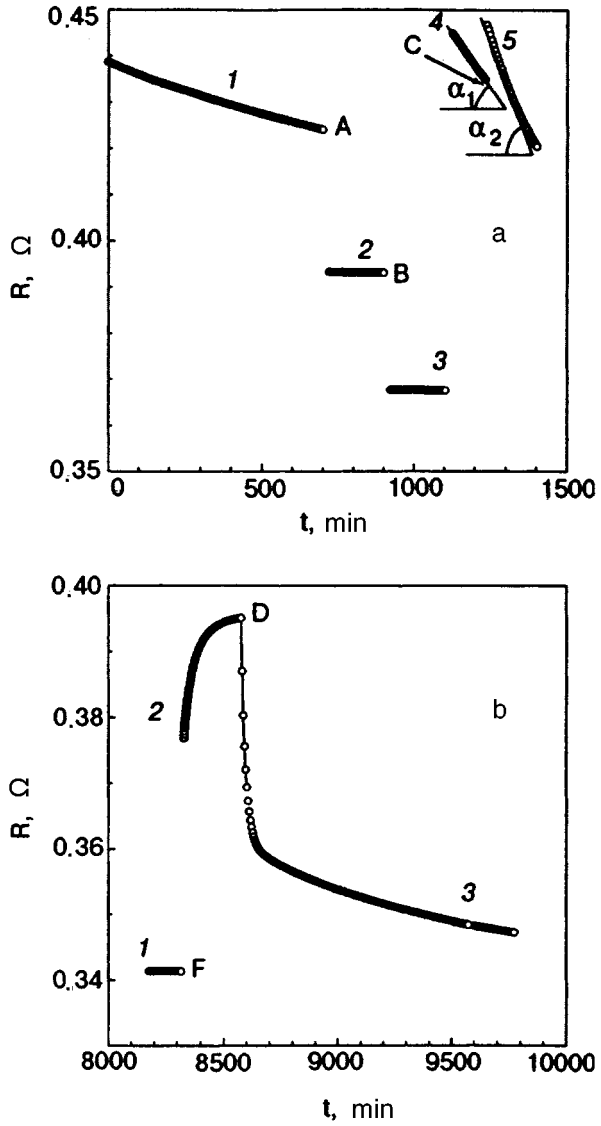

FIG. 2. Isothermal time dependences of electrical resistance measured at various temperatures *T*, (K: 279 (curve *1*), 257 (curve *2*), 239.4 (curve *3*), 295.3 (curve *4*), 305.6 (curve *5*). The temperature was varied at points *A*, *B*, and *C*: 289 (curve *1*), 320 (curve *2*), 289 (curve *3*). (a) and at points *F*, and *D* (**b**).

sample had been held at this temperature for two days. It can be seen that the resistance does not vary with time. The temperature was then increased to 320 K, the sample was held at this temperature for four hours (curve *2*), after which the temperature was again lowered to the initial value $T=289$ K. It can be seen that the resistance relaxes slowly to its equilibrium value (curve *3*). The equilibrium value $R(289\text{ K})=0.341\Omega$ was reached only after two days. It is also worth noting that the resistance value did not change subsequently as a result of isothermal holding of the sample at this temperature for two weeks.

Since the magnitudes of electrical resistance and superconducting transition temperature of $YBa_2Cu_3O_{7-\delta}$ single crystals are sensitive to the magnitude of the oxygen index as well as the spatial distribution of oxygen, the results obtained in this work can be attributed to saturation of the surface

layer of single crystals by oxygen, as well as the redistribution of oxygen in the bulk of the crystal. In the former case, the oxygen-enriched surface layer with a reduced resistivity and elevated T_c may shunt the bulk of the crystal. However, magnetization studies in $YBa_2Cu_3O_{6.45}$ single crystals reveal that the transition temperature increases throughout the entire volume of the crystal upon room-temperature annealing.[1] It is also worth noting that x-ray diffraction studies of monocrystalline[1] oxygen-deficient samples and neutron diffraction studies of polycrystalline samples[5] point towards a change in the crystal lattice parameters as a result of room-temperature annealing, as also towards an increase in orthorhombicity of the lattice. The occupancy of oxygen positions[5] and weight of the sample[1] do not vary upon annealing. The aggregate of these experimental data suggests that annealing causes structural changes over the entire volume of the samples without any change in the oxygen concentration. The decrease in the electrical resistance observed in by us points towards structural ordering during annealing, and the fact that the activation energy of resistance relaxation is equal to the activation energy of oxygen diffusion indicate that these changes are associated with the diffusive flow of oxygen. Hence we assume that the decrease in resistance and the increase in T_c observed during annealing are due to ordering of labile oxygen in Cu-O planes over the entire crystal volume, and not to the enrichment of surface layer of the crystals by oxygen. It can be seen from Fig. 2b that equilibrium distribution of oxygen depends on temperature and varies even when the temperature changes by just $\Delta T \simeq 30$ K. The reversibility of resistance after attainment of equilibrium value of indicates that the oxygen concentration in the crystals remains unchanged upon annealing at $T < 320$ K. This conclusion is in accord with those drawn in Refs. 1–5 from investigations of the effect of annealing in the temperature range 300–420 K on the optical, magnetic, and structural characteristics of oxygen-deficient mono- and polycrystalline samples of $YBa_2Cu_3O_{7-\delta}$.

The structure of $YBa_2Cu_3O_{7-\delta}$ for $\delta = 0$ is characterized by the presence of Cu-O chains. In other words, the oxygen positions O(1) are completely filled, while the O(5) positions are vacant. For an oxygen deficiency $\delta = 0.5$, the structure is characterized by an alternation of chains in which the O(1) positions are filled, and chains in which the O(1) positions are vacant. Such ordered structures can be realized for a stoichiometric ratio 1:0 and 1:1 of oxygen and vacancy concentration.[10,11] On the basis of experimental studies of various physical properties of $YBa_2Cu_3O_{7-\delta}$ with an oxygen deficit $\delta \leqslant 0.3$, Sukharevskii *et al.*[12] provided a justification for the emergence of a superconducting cluster whose structure is nearly ordered for oxygen-to-vacancy ratios 5:1, 4:1, 3:1, and 2:1. For example, it is assumed that for the ratio 5:1, the oxygen positions O(1) are vacant in every sixth chain, while in all other chains they are occupied.

For a nonstoichiometric ratio of oxygen to vacancy concentration, the oxygen-vacancy system can either be disordered, or contain a mixture of ordered clusters with different oxygen concentrations. It was mentioned above that an increase in T_c during room-temperature annealing of crystals[2] and an increase in carrier concentration upon a decrease in temperature from 150 to 20 °C[4] were interpreted as oxygen ordering in Cu-O planes. The decrease in electrical resistance during annealing observed by us also points towards ordering in the oxygen-vacancy system. Hence an ordered state in the oxygen-vacancy system can be expected at least at room temperature. The step form of resistive transitions observed by us probably points towards a nonstoichoimetric ratio of the oxygen and vacancy concentrations, leading to the formation of a mixture of different clusters. These clusters, which can be in the form of separate phases, are apparently characterized by different concentrations of oxygen and its ordering, and thus have different superconducting transition temperatures. The presence of steps also assumes the absence of percolation paths of current flow in the phase with a higher transition temperature. Otherwise this phase would shunt the low-temperature phase, and only the high-temperature phase would display a superconducting transition.

A typical feature of the effect of annealing is a change in the height of the steps in resistive transitions. This change is manifested most clearly in the *S*2 crystal. The height of the lower step in Fig. 1 (curve *4*) is $0.5R_N$, where R_N is the normal state resistance. On curves *5* and *6*, this height corresponds to $0.95R_N$ and $0.96R_N$, respectively. Such a large variation of the step height indicates a significant variation of the percolation paths after room-temperature annealing of the crystals, which may occur upon a change in the spatial distribution and the size of the low- and high-temperature phase clusters. The latter requires a diffusive flow of oxygen over a distance of the order of cluster size.

It is well known that saturation of $YBa_2Cu_3O_{7-\delta}$ crystals by oxygen requires an annealing in oxygen flow for one day at a temperature of 400 °C. Typical crystal size is $1 \times 1 \times 0.1$ mm and hence the distance $L_0 = (Dt)^{1/2}$ over which oxygen diffuses under the above-mentioned conditions is $0.1-1$ mm. Since the diffusion coefficient $D \sim \exp(-U/T)$ and the activation energy $U \simeq 1.1 \cdot 10^4$ K, we can estimate the distance over which oxygen can diffuse in one day at room temperature:

$$L \approx L_0\{[\exp(-U/300)]/\exp(-U/700)\}^{1/2} \approx 30-300 \text{ Å}.$$

Thus, the cluster size may attain values between 30 and 300 Å. This quantity is in reasonable agreement with the values of the length l of Cu-O chains in $YBa_2Cu_3O_{7-\delta}$ single crystals at room temperatures, obtained from neutron diffraction[13] ($l \simeq 50$ Å) and optical[4] ($l \simeq 300$ Å) experiments respectively.

It should also be observed that the decrease in resistance $\Delta R/R = 0.2-0.4$ observed by us during room-temperature annealing of crystals is in accord with an increase in the carrier concentration in Cu-O chains obtained from optical studies.[4]

The increase in the superconducting transition temperature during annealing of crystals at room temperature may be due to several reasons. Thus, the authors of Refs. 2, 5 associate the increase in T_c with a local ordering of oxygen, while the authors of Refs. 3, 4 believe that this is due to an

increase in carrier concentration. The increase in T_c may also be due to a change in the crystal lattice parameters and, among other things, in the separations Cu-O and Cu-Cu in the ab-plane.[5] This problem was discussed in details by us in Ref. 14.

Finally, it should be noted that the results obtained by us are in accord with the results of optical and magnetic investigations of oxygen-deficient crystals of $YBa_2Cu_3O_{7-\delta}$ quenched from high temperatures.[1–4] The activation energy of resistance relaxation is determined and is found to coincide with the activation energy of oxygen diffusion. The step form of superconducting transition is attributed to the cluster structure of crystals formed as a result of nonuniform distribution of oxygen in the Cu-O plane. The cluster size varies from 30 to 300 Å.

The authors are sincerely obliged to V. A. Shklovskii for his keen interest in this research and for a number of valuable comments.

This research was supported partially by the Ukrainian State Committee on Science and Technology under the project ''Term''.

*E-mail: Mikhail.A.Obolenskii@univer.kharkov.ua

[1] B. W. Veal, H. You, A. P. Paulikas *et al.*, Phys. Rev. B **42**, 4770 (1990).
[2] H. Claus, S. Yang, A. P. Paulikas *et al.*, Physica C **171**, 205 (1990).
[3] J. Kircher, M. Cardona, A. Zibold *et al.*, Phys. Rev. B **48**, 9684 (1993).
[4] K. Widder, A. Zibold, M. Merz *et al.*, Physica C **232**, 82 (1994).
[5] D. Jorgensen, S. Pei, P. Lightfoot *et al.*, Physica C **167**, 571 (1990).
[6] M. A. Obolenskii, A. V. Bondarenko, and M. O. Zubareva, Fiz. Nizk. Temp. **15**, 1152 (1989) **15**, 635 (1989).
[7] A. Damask and G. Dienes, *Point Defects in Metals*, New York (1963).
[8] J. Sabras, G. Peraudeau, R. Berjoan, and C. Monty, J. Less-Common Met. **164–165**, 239 (1990).
[9] J. R. LaGraff and D. A. Payne, Phys. Rev. B **47**, 3380 (1993).
[10] V. N. Molchanov, L. A. Muradyan, and V. I. Simonov, Pis'ma Zh. Éksp. Teor. Fiz. **49**, 222 (1989) [JETP Lett. **49**, 257 (1989)].
[11] R. Beyers, B. T. Ahn, G. Gorman *et al.*, Nature (London) **340**, 619 (1989).
[12] B. Ya. Sukharevskii, I. V. Zhikhareva, S. I. Khokhlova *et al.*, Preprint 91-10, Physicotechnical Inst., Donetsk (1991).
[13] F. Heimmaa, H. Lutgemeier, S. Pecker *et al.*, Appl. Magn. Reson. **3**, 689 (1992).
[14] D. D. Balla, A. V. Bondarenko, R. V. Vovk *et al.*, Fiz. Nizk. Temp. **23**, 1035 (1997) [Low Temp. Phys. **23**, 277 (1997)].

Translated by R. S. Wadhwa

Effect of high pressure on the phonon spectra of Bi2223 in Andreev junctions

V. M. Svistunov, V. B. Tarenkov, and A. I. D'yachenko

*A. Galkin Physicotechnical Institute, National Academy of Sciences of the Ukraine, 340114 Donetsk, Ukraine**

R. Aoki

Faculty of Engineering, Osaka University, Yamada-oka 2-1, Japan
(Submitted March 24, 1997; revised May 19, 1997)
Fiz. Nizk. Temp. 1183–1186 (November 1997)

A ''softening'' of the high-frequency modes of the phonon spectrum is detected under pressure. These modes correspond to breathing oxygen modes and to other vibrational modes of Cu–O. The obtained results explain the observed increase in the ratio $2\Delta/kT_c$ within the framework of the strong electron–phonon interaction model. © *1997 American Institute of Physics.* [S1063-777X(97)00511-2]

INTRODUCTION

The unusual symmetry of the order parameter in high-temperature superconductors suggests a non-phonon pairing mechanism. However, the electron–phonon interaction may play a significant role.[1–3] The phonon spectrum of cuprates extends to 100 mV, and previous investigations[1–5] have shown that a strong coupling exists between electrons and high-energy phonons. In the present paper, this fact is confirmed by experiments on elastic electron-phonon interaction (EPI) spectroscopy in Andreev-type $S–c–S$ point contacts under hydrostatic pressure (here S denotes a superconductor and c a normal constriction).

Tunnel studies of conventional superconductors under high pressures have proved convincingly that the departure of the ratio $R=2\Delta/kT_c$ from the universal BCS value $R=3.53$ is associated with a strong EPI.[6,7] There is no universal relation between $2\Delta_{\max}$ and T_c in anisotropic high-temperature superconductors ($\Delta_{\max}=\max(\Delta(\mathbf{k}))$. Nevertheless, EPI can make a significant contribution to the ratio $R=2\Delta_{\max}/kT_c$. As in the case of conventional superconductors, this contribution must be manifested under high pressures P since the phonon frequencies corresponding to the lower part of the boson spectrum of cuprates will affect the $R(P)$ dependence most significantly.

In order to single out this contribution, i.e. to reveal the role of EPI in high-temperature superconductivity, we must measure the ratio R and the phonon frequencies ω under pressure. For this purpose, the available Raman spectroscopy data[2] on $\omega(P)$ are not suitable since this method defines the phonon frequencies $\omega_{\mathbf{q}}$ for $\mathbf{q}=0$, i.e., at the center of the Brillouin zone. At the same time, the maximum contribution to superconductivity comes from phonons with large values of the vector $q\sim\pi/a$, a being the lattice constant. It is these phonons that are registered by the contact technique.[4,7] Hence the information on $\omega(P)$ obtained by this method reflects the electron–phonon interaction in superconductors more accurately.

The effect of pressure on the parameter $R=2\Delta/kT_c$ was studied by us earlier.[8] In the present paper, we shall present the results of complex studies of the Andreev reflection effect in $S–c–S$ junctions, which enable us to determine simultaneously the ratio $R=2\Delta/kT_c$ as well as the shift of the phonon frequency $\omega(P)$ under different pressures. It is well known[9] that a strong EPI results in a frequency dependence of the energy gap function $\Delta(\omega)$, while the dynamic conductivity G of an $S-c-N$ junction has the form

$$G=\frac{dI}{dV}=\frac{1}{R_N}\times\left\{1+\left|\frac{\Delta(\omega)}{\hbar\omega+[(\hbar\omega)^2-\Delta^2(\omega)]^{1/2}}\right|^2\right\}_{\omega=eV/\hbar}, \qquad (1)$$

where R_N is the junction resistance in the normal state. It follows from formula (1) that the data on the derivative dG/dV can provide information (as in the case of a tunnel junction)[1] on the electron–phonon interaction in a superconductor ($\alpha^2F(\omega)$ and $\Delta(\omega)$).[10] In $S–c–S$-type junctions, analogous singularities in the behavior of the conductivity σ caused by a strong EPI must be manifested at bias voltages $eV=\hbar\omega_1+2\Delta$, where ω_1 are the characteristic phonon frequencies of the density of states $F(\omega)$.

ANALYSIS OF EXPERIMENTAL RESULTS

The Andreev reflection was observed in bismuth cuprates (containing 95% $Bi_{1.6}Pb_{0.4}Sr_{1.8}Ca_{2.2}Cu_3O_x$(Bi2223) phase, $T_c=110$ K) prepared by solid-phase synthesis from chemically pure oxides. Bismuth ceramic plates of size $1\times0{,}1\times0.01$ cm were obtained by pressing the powder between steel anvils with copper wire props under pressures of 30–40 kbar. The initial diameter of the wires (0.25 mm) determined the finite plate thickness. Prepared plates with silver area elements for current and potential contacts were annealed at a temperature $T=845$ °C. The ceramic samples were pasted to a flexible steel substrate and covered with a layer of varnish. The substrate was bent until the formation of a microcrack in the ceramic, which was controlled by measuring the variation of the sample resistance. This led to the formation of a point contact of ''break junction'' type, which was either a tunnel junction ($R_N\sim50$–$100\ \Omega$) or an $S–c–S$-type junction with an ordinary conductivity ($R_N\sim1$–5Ω). Contacts with ordinary conductivity were

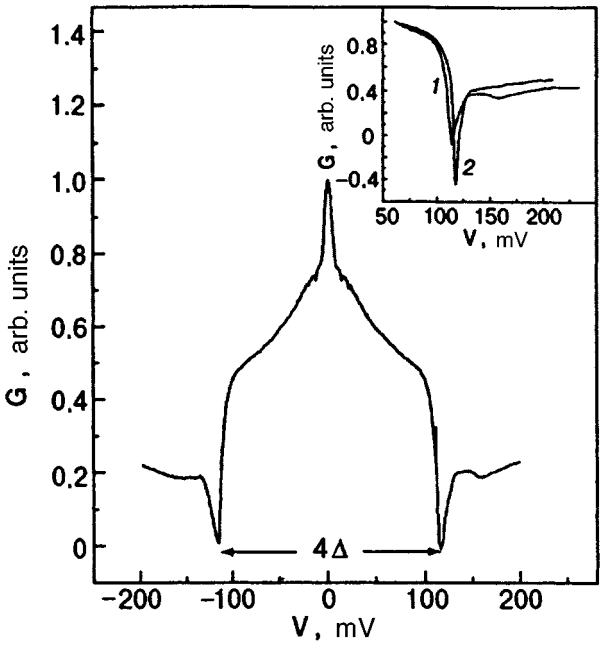

FIG. 1. Characteristic of the dynamic conductivity of an $S-c-S$ junction demonstrating the energy gap singularity for $eV=2\Delta$. The inset shows the variation of the gap with pressure: $P=0$, $2\Delta=114$ meV, $T_c=110$ K (curve *1*); $P=10$ kbar, $2\Delta=117$ meV, $T_c=111.5$ K (curve *2*).

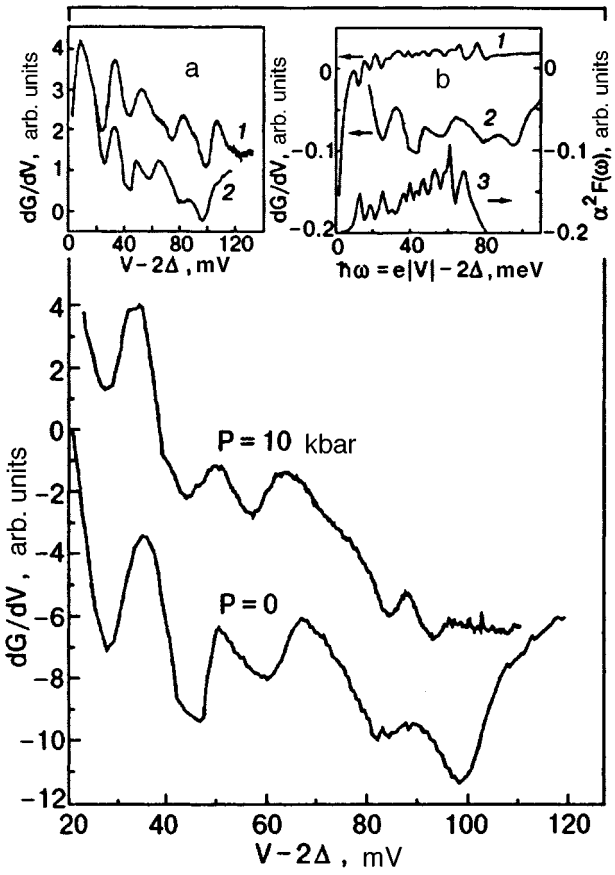

FIG. 2. Effect of pressure on Andreev reflection spectra $dG/dV=d^2I/dV^2$ in $S-c-S$ junctions. The inset (a) shows the derivatives of the conductivity of tunnel (curve *1*) and Andreev (curve *2*) junctions, while the inset (b) shows the theoretical dependence of dG/dV for an Andreev junction with Bi2212 (curve *1*) and the corresponding EPI function (curve *3*), as well as the experimental curve dG/dV for the phase Bi2223 (curve *2*).

found to be much more stable to pressure variations, and enabled a complete cycle of measurements under high pressures. Moreover, the superconductor energy gap in Andreev-type junctions was manifested much more strongly than in tunnel samples. This circumstance is quite significant for determining the variation $2\Delta/kT_c$.

Hydrostatic pressure up to 15 kbar was produced in a piston–cylinder chamber. The metallic behavior of the $S-c-S$ junction was controlled by measuring the temperature dependence of its resistance, as well as from the weak reaction of the junction conductivity to pressure. At low temperatures $T<T_c$, the current–voltage characteristics of $S-c-S$ samples had an excess current, which is a reliable index of junctions with direct (ordinary) conductivity.[4,10]

Figure 1 shows the $G(V)$ dependence of an $S-c-S$ junction displaying an energy gap at $eV=2\Delta=114$ meV($T=77$ K). A similar manifestation of the sum of energy gaps of an $S-c-S$ junction Nb–Nb was observed by Hoffmann *et al.*[11] As in Ref. 8, the temperature dependence $\Delta(T)$ corresponds to the BCS curve.

For bias voltages eV higher than 2Δ, the conductivity of $S-c-S$ samples displays singularities which can be interpreted as a reflection of the phonon structure of the metal oxide under consideration (Fig. 2). The spectroscopic nature of these singularities is confirmed by the fact that their position measured from the sum 2Δ of the energy gaps coincide for both tunnel and ordinary conductivity junctions (see inset a to Fig. 2). The peculiarities of the experimental curve are in accord with some peaks of the function $F(\omega)$ (see inset b to Fig. 2), although the experimental spectrum is more blurred. Moreover, according to Ref. 12, the phonon spectrum of Bi2223 ends in the region of 80 meV, while the Andreev reflection spectrum displays peculiarities at $eV-2\Delta=90$–95 meV. A similar result was also obtained for $S-I-S$ tunnel junctions (see inset a to Fig. 2). However, the parameter $2\Delta=2\Delta_{\max}=114$ meV for $S-c-S$ Andreev junctions is much larger than in tunnel junctions ($2\Delta=70$–84 meV).

Figure 2 shows the effect of a pressure of 10 kbar on the structure of the second derivative for one of the investigated $S-c-S$ Andreev junctions. It can be seen that the initial region of the phonon spectrum of Bi2223 does not vary much under pressure: $d\ln\omega/dP=(1-1.5)\cdot 10^{-3}\text{kbar}^{-1}$ (this is in accord with the Raman spectroscopy data).[2] The most significant variations occur in the high-frequency spectral region for $\hbar\omega=70$–95 meV, where the application of pressure causes a considerable decrease in the phonon energy: $d\ln\omega/dP=-6\times10^{-3}$ kbar^{-1}.

In order to find the general nature of the phonon structure peculiarities in Andreev reflection spectra in Bi2223 cuprates, calculations were made using formula (1) in which the complex gap parameters $\Delta(\omega)$ is obtained by exactly solving the Eliashberg equation for the phonon density of states $F(\omega)$ for Bi2223.[12] The effect of the high-frequency part of the boson spectrum (i.e., the nonphonon mechanism of high-temperature superconductivity) was formally taken into account by replacing the Coulomb pseudopotential μ^*

by $\mu^* - \lambda_p$, where λ_p is the effective constant of coupling with high-frequency bosons. The electron-phonon coupling constant $\alpha^2(\omega)$ in the function $g(\omega) = \alpha^2(\omega)F(\omega)$ was determined by using the method described by Aoki *et al.*,[13] while the EPI constant λ was chosen from the condition of matching the theoretical critical temperature with the experimental value of T_c. In particular, the theoretical values of the critical current and energy gap at $\lambda \approx 3.3$ and $\mu^* = 0.1$ ($\lambda_p = 0$) were $T_c = 110$ K and $\Delta = 27$ meV. When the nonphonon mechanism ($\lambda_p > 0$) is taken into account, the EPI constant decreases to values $\lambda = 1.63$ for $\lambda_p = 0.2$, but in this case the phonon structure in dG/dV is preserved. In the anisotropic case also, the main phonon singularities in dG/dV remain connected with a certain effective value of the energy gap.[14]

The departure from experimental values of the parameter Δ is not surprising since the superconducting Bi2223 under consideration has a high anisotropy $\Delta(\mathbf{k})$. However, the maximum value $\Delta_{\max}$ is always realized in the case of Andreev reflection, while the solution of Eliashberg's isotropic equations defines a certain effective mean value of the energy gap (this is the value recorded in tunnel junctions during diffusive scattering of electrons at the insulator–superconductor boundary).

Although the above calculations are of qualitative nature, they can be used to establish the general form of the spectrum of dG/dV and its variation under a pressure $P = 10$ kbar. The corresponding variation of the phonon spectrum was obtained by displacing the characteristic peaks in $F(\omega)$ by the experimentally determined quantity $\delta\omega(P)$. For the experimental value of $T_c(P) = 111.5$ K($P = 10$ kbar), we obtain the value $\lambda = 3.46$ (for $\mu^* = 0.1$ and $\lambda_p = 0$) (the experimental value of $2\Delta(P) = 117.5$ meV). Thus, in the strong (isotropic) EPI mechanism approximation, the change in the ratio $R = 2\Delta/kT_c$ under pressure was $\delta = [R(P) - R(0)]/R(0) = 0.018$, which is quite close to the experimental value $\delta = 0.017$ and to the value $\delta = 0.02$ obtained from the simple Geilikman–Kresin formula

$$\frac{2\Delta_{\max}}{kT_c} = C\left(1 + 5{,}3\left[\frac{T_c}{\omega_0}\right]^2 \ln\left[\frac{\omega_0}{T_c}\right]\right) \qquad (2)$$

for the characteristic breathing mode phonon frequency $\omega_0 = 75$ meV (in the BCS–Eliashberg theory, the constant $C = 3.53$). The obtained result justifies the application of formula (2) for anisotropic cuprate superconductors, where C is not a universal constant (the relation between this constant and the specific dependence $\Delta(\mathbf{k})$ is established, for example, in Ref. 15).

CONCLUSIONS

Experimental results show that in Bi2223 cuprates, the maximum influence of the pressure is experienced by high-frequency phonons associated with optical vibrations of oxygen atoms and their environment. These frequencies correspond to the energies 70–100 meV, especially to the breathing mode for $\hbar\omega = 70$–75 meV. Both tunnel and Andreev spectra display a singularity at $\hbar\omega \approx 95$ meV, although the theoretical phonon spectrum in Ref. 12 terminates at 80 meV. According to the data of inelastic neutron spectroscopy,[16] the function $F(\omega)$ in Bi2212 extends a little farther (up to 85 meV). For LaSrCuO, the edge of the phonon spectrum lies at the energy $\hbar\omega \approx 95$ meV.[17]

The theoretical data presented here can claim to be the result of a qualitative analysis only. However, it is obvious that the experimentally observed decrease of frequency in the upper part of the phonon spectrum can explain the discovered increase in the ratio $(2\Delta_{\max}/kT_c)(P)$. An agreement with the experiment is essentially reached by using a simple generalization of the Geilikman–Kresin formula (2), where $C = C(\mathbf{k})$ is a constant determined by the anisotropic pairing mechanism in cuprates. The characteristic phonon frequency ω_0 is the breathing mode whose energy decreases under pressure at a rate $d \ln \omega / dP = -6 \times 10^{-3}$ kbar^{-1}. This means that the observed increase in the ratio $2\Delta_{\max}/kT_c$ under pressure is due almost entirely to the strong electron–phonon interaction.

This research was supported by the Telecommunication Advancement Organization of Japan. One of the authors (V.M.S) wishes to thank Dr. C. Lobb of the Maryland Center for Superconductivity Research, USA, and Prof. G. Plitnik of the Frostburg University, USA, for fruitful discussions.

*E-mail: svistuno@sts.dipt.donetsk.ua

[1] V. M. Svistunov, M. A. Belogolovskii, and A. I. Khachaturov, Usp. Fiz. Nauk **163**, 61 (1993) 61 (1993) [Phys. Usp. **36**, 65 (1993)].
[2] A. P. Litvinchuk, C. Thompson, and M. Cardona, in *Physical Properties of High-Temperature Superconductors* (Ed. by D. M. Ginsberg), World Scientific, Singapore (1994).
[3] A. P. Litvinchuk and W. Reichardt, in *Physical Properties of High-Temperature Superconductors* (Ed. by D. M. Ginsberg), World Scientific, Singapore (1994).
[4] I. K. Yanson, Fiz. Nizk. Temp. **17**, 275 (1991) [Sov. J. Low Temp. Phys. **17**, 143 (1991)].
[5] R. Aoki, H. Murakami, T. Kita *et al.*, Phys. Rev. B **B219/220**, 172 (1996).
[6] A. A. Galkin and V. M. Svistunov, Phys. Status Solidi **26**, K55 (1968).
[7] V. M. Svistunov, M. A. Belogolovskii, and O. I. Chernyak, Usp. Fiz. Nauk **151**, 31 (1987) [Sov. Phys. Usp. **30**, 1 (1987)].
[8] V. Yu. Tarenkov, A. V. Abaleshev, A. I. D'yachenko *et al.*, Fiz. Nizk. Temp. **22**, 613 (1996) [Low Temp. Phys. **22**, 467 (1996)].
[9] A. I. Omel'yanchuk, S. I. Beloborod'ko, and I. O. Kulik, Fiz. Nizk. Temp. **14**, 1142 (1988) [Sov. J. Low Temp. Phys. **14**, 630 (1988)].
[10] A. V. Khotkevich, V. V. Khotkevich, I. K. Yanson, and G. V. Kamarchuk, Fiz. Nizk. Temp. **16**, 1198 (1990) [*sic*].
[11] O. Hoffmann Soerensen, B. Kofoed, N. F. Pedersen, and S. Shapiro, Phys. Rev. B **B9**, 3746 (1974).
[12] S. Mase and T. Yasuda, Solid State Commun. **68**, 655 (1988).
[13] R. Aoki, H. Murakami, and T. Kita, Physica C **C235-240**, 1891 (1994).
[14] A. I. D'yachenko and V. M. Svistunov, Fiz. Nizk. Temp. **22**, 547 (1996) [Low Temp. Phys. **22**, 421 (1996)].
[15] K. Langfeld and E. Frey, Phys. Rev. B **48**, 4176 (1993-II).
[16] B. Renker, F. Gompf, E. Gering, and D. Ewert, Phys. Rev. B **C162-164**, 462 (1989).
[17] B. Renker, F. Gompf, E. Gering *et al.*, Jpn. J. Appl. Phys., Part 2 **26**, 2143 (1987).

Translated by R. S. Wadhwa

Tunneling of nonequilibrium quasiparticles excited by x-ray quanta in a nonsymmetric superconducting tunnel detector

V. A. Andrianov, M. G. Kozin, S. A. Sergeev, and V. S. Shpinel

*D. Skobel'tsyn Research Institute of Nuclear Physics, Lomonosov State University, 119899 Moscow, Russia**

V. P. Koshelets and I. V. Abramova

Institute of Radioelectronics, Russian Academy of Sciences, 103907 Moscow, Russia
(Submitted March 11, 1997; revised June 9, 1997)
Fiz. Nizk. Temp. **23**, 1187–1194 (November 1997)

Pulse height distribution from nonsymmetric superconducting Nb/Al/AlO_x/Nb tunnel junction irradiated by x-ray quanta emitted by a ^{55}Fe source is studied. Signals of opposite polarity emerging as a result of absorption in different electrodes of the tunnel junction are observed at low bias voltages. This makes it possible to obtain amplitude spectra of essentially different shape for each electrode separately. The dependence of the maximum charge output on the bias voltage is analyzed. The diffusion coefficient, effective lifetime, and recombination probability for quasiparticles are obtained. It is found that the charge output increases with the magnetic field strength. © *1997 American Institute of Physics.* [S1063-777X(97)00611-7]

Detectors of x-ray and soft γ-quanta that are being developed on the basis of superconducting tunnel junctions (STJ) make it possible to lower the energy threshold for recording and to obtain a much higher energy resolution than for semiconducting detectors.[1,2] The values of energy resolution R attained for electrodes consisting of Nb and Al films are 36 eV for 6 keV,[3] the theoretical limit being approximately 4 eV. For detectors in which Ta films are used to increase the efficiency of radiation absorption, the best resolution for 6 keV is 68 eV.[4] However, the efficiency of STJ detectors that have been developed by now is low in view of their small size, and such detectors are used very rarely. Besides, some peculiarities in the operation of STJ detectors complicate their practical application. Among other things, radiation absorption in the lower and upper STJ electrodes usually leads to the emergence of pulses of the same polarity, but with different amplitudes, which complicates the shape of the obtained amplitude spectra. The improvement of STJ detectors necessitates a further study of physical processes taking place in various types of STJ upon the absorption of an energy quantum and excitation of quasiparticles.

In this research, we study a nonsymmetric tunnel junction Nb/Al/AlO_x/Nb. The shape of current-voltage characteristics (IVC) proved that the tunnel junction has a structure of the $S/I/S'$ type with different widths Δ_1 and Δ_2 of the superconducting gaps for the upper and lower electrodes. The STJ was irradiated by x-rays emitted by Mn and accompanied by the radioactive decay of ^{55}Fe. The amplitude spectra were measured at different temperatures in the interval 1.4–2.2 K. We studied the effect of the applied bias voltage, magnetic field applied for suppressing the Josephson current and Fiske resonances, and temperature on the shape of the spectra.

For small bias voltages $V_d < (\Delta_2 - \Delta_1)/e$ (e is the electron charge), pulsed of anomalous polarity emerging as a result of competition of the electron and hole channels of tunneling for nonequilibrium quasiparticles from the electrode with a larger superconducting gap were detected. Different polarities of pulses from the lower and upper electrodes made it possible to separate spectra and to analyze them for each electrode separately.

The spectra obtained for different electrodes differ significantly. The spectra were analyzed on the basis of the diffusion model taking into account the dependence of quasiparticle output on the coordinate of phonon absorption and under the assumption of the presence of quasiparticle traps in the electrodes.

Preliminary results of this research were reported earlier.[5]

SAMPLES AND APPARATUS

Tunnel junction Nb/Al/AlO_x/Nb were prepared at the Institute of Radioelectronics, Russian Academy of Sciences, by magnetron sputtering on a silicon substrate of thickness $\sim$0.4 mm. Schematic diagram of STJ is shown in Fig. 1. At first, a buffer layer of amorphous Al_2O_3 was deposited on the substrate, followed by a three-layer structure: the lower Nb film of thickness 2000 Å, a thin Al layer of thickness 60 Å, on which an insulating AlO_x layer of thickness 10–20 Å was created as a result of oxidation, and finally the upper Nb film of thickness 1000 Å. The deposition of the Nb current-carrying layer of thickness 3500 Å on the upper electrode increased its thickness to 4500 Å. The structure formation on the chip was carried out by the photolithographic and etching technique. The STJ had the shape of a square with the insulating barrier size 20×20 μm. The sizes of the lower and upper electrodes were larger than the size of the barrier by 20 and 10 μm respectively. The normal resistance R_N of the STJ was 3Ω.

In view of technological peculiarities, the Nb films had a small-grain structure and contained the Ar impurity since the sputtering was carried out in the Ar plasma. The residual resistance coefficient RRR of the films was close to 3.

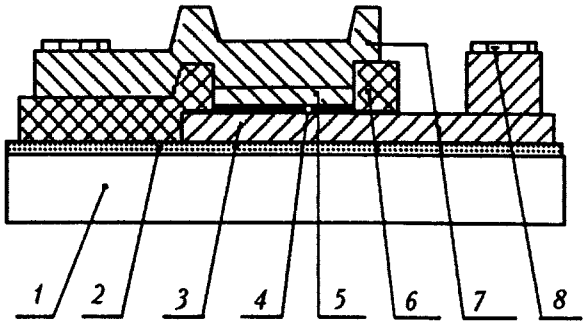

FIG. 1. Schematic cross section of a superconducting tunnel junction: silicon substrate (*1*), layer of amorphous Al_2O_3 (*2*), lower Nb electrode with leads (*3*), Al/AlO_x barrier layer (*4*), upper Nb electrode (*5*), insulating SiO_2 film (*6*), leads to the upper electrode (*7*), and Al/Au contact areas (*8*).

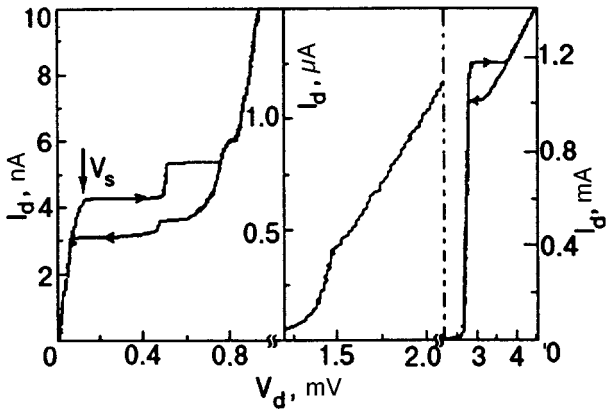

FIG. 2. Current-voltage characteristic of a STJ ($T=1.4$ K, $H=200$ Oe). Detector current I_d is laid on the ordinate axis in three measuring ranges.

The STJ was cooled to 4.2–1.4 K in a helium cryostat with evacuation of He vapor. The detector was exposed to x-rays with 5.89 keV of Mn K_α(88%) and 6.49 keV of Mn K_β(12%), accompanying the radioactive decay of ^{55}Fe. The intensity of the ^{55}Fe source was 0.8 μCi. The magnetic field of strength up to 900 Oe was created by a superconducting solenoid and was directed in the plane of the tunnel barrier along its face.

The signals from the STJ detector were supplied through a coaxial cable of length $\sim$1 m to a low-noise charge-sensitive preamplifier operating at room temperature. The bias voltage was supplied to the tunnel junction through a loading resistance of 50 kΩ, which ensured the conditions of pulse measuring close to the constant-voltage regime. The amplitude spectra were recorded by using a multichannel analyzer. The pulse shape was determined with the help of a digital oscillograph. A more detailed description of the samples and the setup is given in Ref. 5.

CURRENT-VOLTAGE CHARACTERISTICS

Figure 2 shows the IVC obtained at temperature $T=1.4$ K in a magnetic field $H=200$ Oe. The Josephson current was suppressed by the magnetic field. The current step at a voltage of 0.5 mV coincides with the first Fiske step. The IVC hysteresis at voltages below 0.5 mV is associated with the local current peak at a voltage $V_s=0.14$ mV (the IVC were measured in the constant-current mode). This peak is due to the difference in the superconducting gaps for the lower and upper electrodes of the STJ ($V_s=(\Delta_2-\Delta_1)/e$). The gap singularity on the IVC is observed at a voltage $V_g=2.74$ mV and corresponds to the sum of the gaps of the lower and upper electrodes ($V_g=(\Delta_2+\Delta_1)/e$). This gives the values of $\Delta_1=1.30$ meV and $\Delta_2=1.44$ meV.

Thin films are characterized by a smaller width of the superconducting gap ($\Delta_0=1.55$ meV) as compared with bulk Nb samples, which can be explained by the defect nature of Nb films and by the presence of the Al interlayer in the lower electrode. However, for small thicknesses of the Al layer ($\sim$50 Å), the decrease in the gap width associated with the proximity effect is small, and defectiveness of the film is a decisive factor in the decrease of the gap width. For this reason, the smaller value $\Delta_1=1.30$ meV in all probability corresponds to the upper electrode with a more defective small-grain structure. Such an identification of electrodes does not contradict the experimental data obtained by Golubov *et al.*[6] and is in accord with our results on the time of quasiparticle tunneling from different electrodes.

At $T=1.4$ K and for voltages across the junction smaller than $\sim$0.8 mV, the quasiparticle (thermal) current does not exceed a few nanoamperes. The temperature variation of this current in the interval 4.2-1.4 K follows the theoretical dependence[7] $I_d\sim\sqrt{T}\exp(-\Delta/kT)^E$ with $\Delta=1.34$ meV, indicating the smallness of leakage currents at $T\geqslant 1.4$ K and a high quality of the tunnel barrier. At voltages above $\sim$0.8 mV, the quasiparticle current increases abruptly (see Fig. 2), which was also observed by some authors[8,9] and was explained by two-particle tunneling processes.

X-RAY DETECTION

The absorption of radiation in STJ is usually responsible for the emergence of pulses whose polarity is determined by the sign of the applied voltage and corresponds to the enhancement of the quasiparticle current. However, at small bias voltages $V_d<V_s=\Delta_2-\Delta_1$, anomalous pulses with the opposite polarity were also observed by us along with the pulses of normal polarity. For $V_d>V_s$, no pulses with anomalous polarity were observed. The oscillograms of normal and anomalous pulses are shown in Fig. 3. The pulse front durations τ_f differ considerably and amount to approximately 0.3 μs for normal and 0.8 μs for anomalous pulses.

Figure 4 shows the pulse-height (amplitude) spectra for pulses from the ^{55}Fe source at $T=1.4$ K in a magnetic field $H=175$ Oe for different bias voltages V_d across the tunnel junction. The heights of pulses are normalized to output charge units. The electron noise level of the entire circuit (including STJ noises), which was determined with the help of a gage pulse generator, did not exceed $5\cdot 10^3 e$.

Figures 4a and b show the amplitude spectra for normal and anomalous pulses, measured at a voltage $V_d<V_s$ across the junction. The spectrum of pulses with the normal polarity (Fig. 4a) has a peak blurred on the side of small amplitudes, and a small step behind the peak, which correspond to the x-ray lines K_α and K_β of Mn, marked by arrows in the fig-

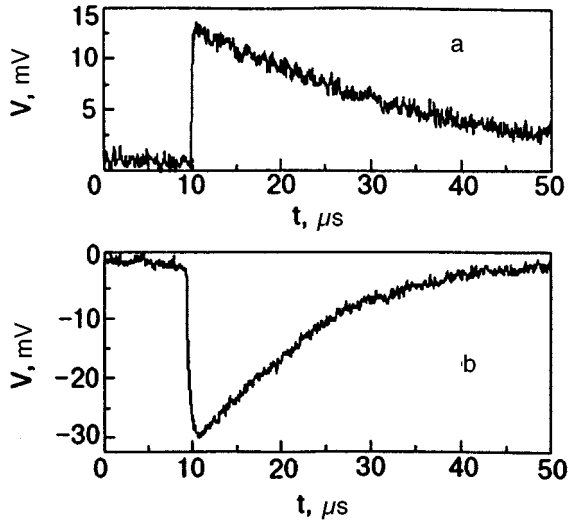

FIG. 3. Pulses from the STJ detector behind inverting charge-sensitive preamplifier for $V_d < V_s$: normal polarity, $\tau_f \simeq 0.3$ μs (a) and anomalous polarity, $\tau_f \simeq 0.8$ μs (b).

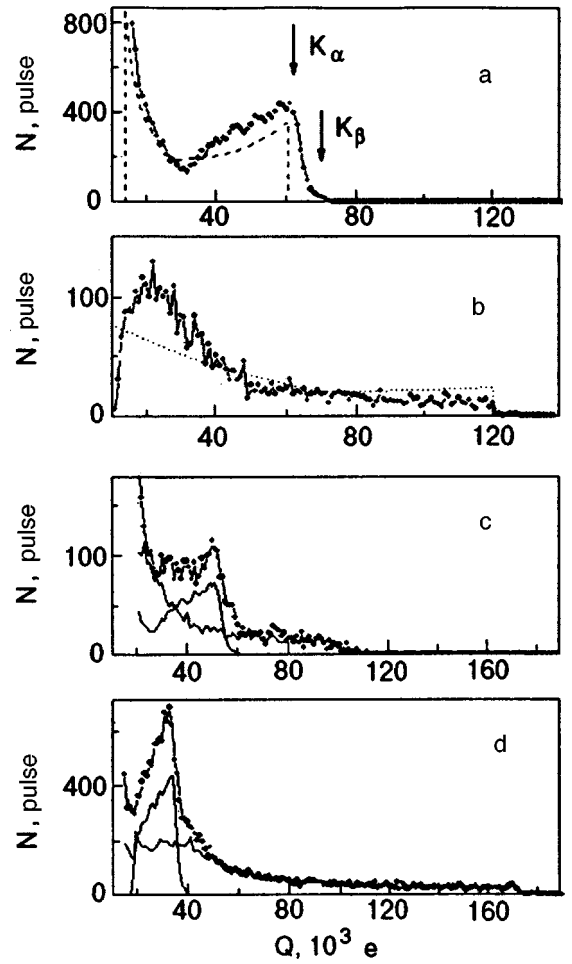

FIG. 4. Amplitude spectra of pulses for various voltages across the STJ: V_d, mV: 0.12, normal polarity (a), 0.07, anomalous polarity (b), 0.23 (c), and 0.75 (d). Dashed curve corresponds to calculations based on the diffusion model. Fine curves describe the decomposition in the spectra from the upper and lower electrodes.

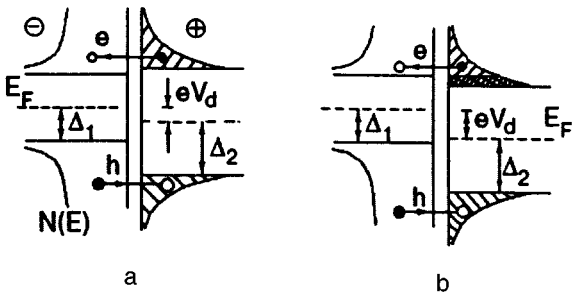

FIG. 5. Schematic diagram of tunneling of nonequilibrium quasiparticles in a nonsymmetric STJ. The electron and hole channels are denoted by e and h. The arrows indicate the direction of electron tunneling. Double hatching marks the states blocked for tunneling. Anomalous pulses are formed as a result of absorption of radiation in the electrode with a larger superconducting gap for $V_d < V_s = (\Delta_2 - \Delta_1)/e$; E_F is the Fermi level, Δ the superconducting gap, and V_d the bias voltage across the detector.

ure. Besides, a steep ascent is observed in the region of small amplitudes. The spectrum of anomalous pulses (Fig. 4b) differs considerably from the above spectrum. It contains a plateau in the region of large amplitudes and a broad peak at the beginning of the spectrum.

The emergence of pulses with opposite polarities for $V_d < V_s$ is associated with the radiation absorption in different electrodes of a nonsymmetric STJ. Tunneling of excess quasiparticles can take place through two (electron and hole) channels making opposite contributions to the resultant pulse (Fig. 5). The electron channel dominates for $V_d < V_s$ in the case of radiation absorption in the lower electrode with a larger superconducting gap in view of the difference in the densities of the final states, and the observed pulses have the anomalous polarity (Fig. 5a). As the voltage increases ($V_d > V_s$), the electron channel is blocked, and the hole channel of tunneling plays the major role. As a result, pulses acquire the normal polarity (Fig. 5b).

In the case when a quantum is absorbed in the electrode with a smaller gap (upper electrode), electron tunneling prevails at all values of voltage, and hence the pulses always have the positive polarity. For low voltages $V_d < V_s$, quasiparticle states near the gap boundary are blocked for tunneling. As the voltage increases from 0 to V_s, the blocking is gradually removed, and the tunnel current increases, reaching its maximum value for $V_d \approx V_s$. A further increase in the voltage leads to a suppression of the tunnel current due to a decrease in the density of the final states. Thus, the amplitude of pulses from the upper electrode must be a nonmonotonic function of the bias voltage.

Thus, for low voltages ($V_d < V_s$), the amplitude spectra of normal pulses (Fig. 4a) correspond to the absorption of radiation in the upper electrode with a smaller superconducting gap, while the spectra of pulses with the anomalous polarity (Fig. 4b) correspond to the lower electrode in the STJ.

When the voltage across the junction $V_d > V_s$, radiation absorption in the upper and lower electrodes leads to the formation of pulses with the same polarity, and the observed spectra are a superposition of the spectra from each of the electrodes. Figures 4c and d show typical spectra obtained for $V_d > V_s$. The sharp crest at the beginning of the ampli-

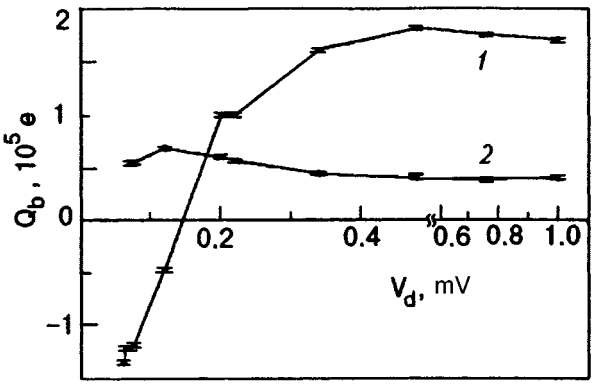

FIG. 6. Dependences of the boundary values of the output charge Q_d on the voltage across the junction for the lower (curve *1*) and upper (curve *2*) electrodes ($T=1.4$ K, $H=175$ Oe).

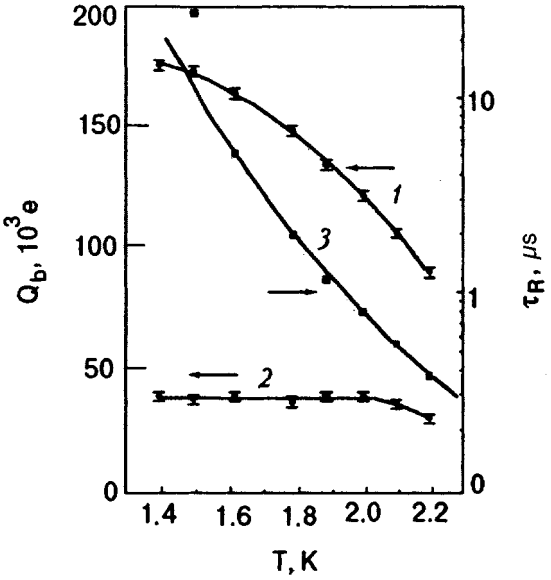

FIG. 7. Temperature dependences of the boundary values of the output charge Q_d for the lower (curve *1*) and upper (curve *2*) electrodes ($H=175$ Oe, $V_d=0.75$ mV), and temperature dependence of the recombination time τ_R (curve *3*).

tude spectra corresponds to the upper electrode, while the broad peak and the plateau in the region of large amplitudes correspond to the lower electrode. Figures 4c and d show the decomposition of spectra obtained by using the Phazan program.[10] In the decomposition, use was made of the spectra obtained at low (see Figs. 4a and b) voltages, whose scale on the abscissa axis varied in accordance with the change in the voltage for which the resultant spectrum was obtained.

An analysis of the duration of pulses measured at voltages larger than V_s also confirms the above decomposition of the spectra. Pulses with short ($\sim 0.3\ \mu$s) fronts had small amplitudes corresponding to the spectrum from the upper electrode, while the amplitudes of pulses with front of duration $\sim 0.8\ \mu$s corresponded to the plateau region in the spectrum from the lower electrode.

The results obtained by us show that a variation of the voltage across the junction virtually does not affect the shape of the spectra from each electrode, changing only the scale of the output charge. Figure 6 shows the dependence of the upper boundary Q_b of the spectra on the voltage across the tunnel junction for the upper and lower electrodes. In accordance with the diagram of tunneling (see Fig. 5), the boundary of the spectrum from the lower electrode passes through zero (curve 1), while Q_b for the upper electrode has a peak (curve 2). The obtained results coincide qualitatively with the voltage dependences of the tunneling probability, which were calculated by Golubov *et al.*[11]

DEPENDENCE OF SPECTRA ON TEMPERATURE AND MAGNETIC FIELD

The temperature dependence of amplitude spectra was measured in the interval 1.4–2.2 K. With increasing temperature, the spectra were gradually ''compressed''. Figure 7 shows the temperature dependence of the boundary output charge Q_b for the lower and upper electrodes (curves 1 and 2 respectively). It can be seen that a decrease in the output charge is mainly observed for the lower electrode, while for the upper electrode it becomes noticeable only at $T>2$ K.

The magnetic field also produced a significant effect on the amplitude spectra. Figure 8 shows the dependences of Q_b on the magnetic field strength for the spectra corresponding to the upper and lower electrodes for two samples No. 1 and No. 2 under investigation. The data were obtained from the spectra measured at $T=1.4$ K. It can be seen that in fields higher than ~ 100 Oe, the boundary of the spectrum for the lower electrode is displaced linearly, the boundary of the spectrum for the upper electrode remaining virtually unchanged. For the second sample, the charge output in the field 900 Oe increases almost by a factor of two.

DISCUSSION OF RESULTS

The analysis of the STJ Nb/Al/AlO_x/Nb revealed that nonsymmetric tunnel junctions under a low bias voltage permit the separation of the amplitude spectra corresponding to absorption of x-ray quanta in different electrodes. The pulses from the electrode with a larger gap width have anomalous polarity which does not correspond to the sign of the applied voltage. The obtained amplitude spectra and the time of signal growth in different electrodes of a STJ differ considerably.

Recently, the pulses with anomalous polarity were detected independently during the study of tunnel junctions with the help of a scanning electron microscope[12] and in the analysis of STJ having a more complex structure and containing Nb, Ta, and Al layers.[13] The possibility of the emergence of such pulses was theoretically predicted earlier by Golubov *et al.*[11]

When a quantum creates a photoelectron in an electrode, a cascade of quasiparticles and phonons is formed soon (in a few nanoseconds), which results in the creation of the initial cloud of excess quasiparticles with an energy equal to or slightly exceeding the energy Δ and nonequilibrium phonons with the energy approximately equal to 2Δ. The linear dimensions of this cloud must be of the order of magnitude of the region occupied by the track of the primary photoelectron

($\sim$500 Å in our case). Then excess quasiparticles diffuse over the volume of the electrode, which is accompanied by the processes of loss, recombination, and tunneling with time constants $\tau_{\rm loss}$, τ_R, and τ_T respectively. These constants determine the effective lifetime τ_d of quasiparticles:

$$\tau_d^{-1}=\tau_{\rm loss}^{-1}+\tau_R^{-1}+\tau_T^{-1}. \tag{1}$$

The time τ_d can be determined experimentally from the duration τ_f of the pulse front from the charge-sensitive preamplifier: $\tau_d=\tau_f/2.2$. For the junction under investigation, the time τ_d is equal to 0.13 μs for the upper and 0.36 μs for the lower electrode.

In order to estimate the characteristic tunneling time τ_T, we can use the expression[14]

$$Q_b=eN_0\,\frac{\tau_d}{\tau_T}, \tag{2}$$

where Q_b are the upper boundaries of spectra for $V_d \gg V_s$ and N_0 is the number of excess quasiparticles formed in Nb as a result of absorption of a quantum of energy 6 keV; $N_0=2.2\cdot 10^6$.[7]

Using the measured values of $Q_{b1}=4\cdot 10^4 e$ and $Q_{b2}=16\cdot 10^4 e$ for the upper and lower electrodes, we obtain $\tau_{T1}=7$ μs for the upper and $\tau_{T2}=5$ μs electrodes respectively. These values are much higher than the experimental lifetime of quasiparticles in STJ electrodes. According to our estimates, the recombination time τ_R at low temperatures ($\leqslant$1.4 K) is also much larger than τ_d. For this reason, the lifetime is determined by quasiparticle losses, i.e., capture of quasiparticles in traps, leakage through leads, and other possible processes.

The effect of diffusion on the shape of the observed spectra is determined by the relation between the linear size of the electrodes of the STJ and the diffusion length over the lifetime of nonequilibrium quasiparticles, $L_D=\sqrt{4D\tau_d}$, where D is the diffusion coefficient. In our case, the diffusion length and the size of the electrodes are approximately of the same order of magnitude. Consequently, the quasiparticle density distribution, and hence the output charge, are functions of the photon absorption coordinate. The nonuniformity of the charge output becomes even stronger due to the presence of large peripheral regions in the given structure of STJ, which have no direct contact with the tunnel barrier (''skirts'').

The diffusion equation in our case has the form

$$\frac{\partial n(\mathbf{r},t)}{\partial t}=D\nabla^2 n(\mathbf{r},t)-\frac{1}{\tau_d}\,n(\mathbf{r},t), \tag{3}$$

where $n(\mathbf{r},t)$ is the number density of quasiparticles as a function of the spatial coordinate and time.

Since diffusion lengths L_D are always much larger than the thickness of the electrodes, Eq. (3) should be considered for the two-dimensional case.

The charge Q of quasiparticles after tunneling is defined by the integral

$$Q=\frac{e}{\tau_T}\int_0^\infty dt\int_A n(\mathbf{r},t)\,d\mathbf{r}, \tag{4}$$

where the integration is carried out over the area A of the tunnel barrier.

The initial conditions are determined by the δ-function

$$n(\mathbf{r},t=0)=N_0\,\delta(\mathbf{r}-\mathbf{r}_0), \tag{5}$$

where $\mathbf{r}_0$ is the coordinate of quantum absorption.

The boundary conditions are determined by the probability of quasiparticle reflection at the electrode boundaries and must also take into account the possibility of quasiparticle loss through the leads.

We obtained an approximate solution of Eq. (3) in the one-dimensional case. The solution was presented in the form of a series expansion in Gaussians.[15] We varied the diffusion coefficient D, tunneling time τ_T, and the reflection coefficient R which changed from 1 (total reflection of quasiparticles) to -1 (perishing of quasiparticles at the boundary) and used the experimental values of τ_d. The final result of our calculations was in the form of distribution functions for the output charge, which were compared with the experimental spectra.

The results of calculations presented in Figs. 4a and b by dashed curves are in qualitative agreement with the experimental spectra except for the region of small amplitudes in the spectrum in Fig. 4b. The asymmetric peak in the spectrum for the upper electrode (Fig. 4a) and the plateau in the spectrum for the lower electrode (Fig. 4b) correspond to absorption of quanta in the central region of the electrodes. The spectral regions with small pulse amplitudes correspond to absorption in the ''skirts'' of the electrodes.

The calculated data are in agreement with the experimental results only for small values of the reflection coefficient R, indicating annihilation of quasiparticles along the perimeters of the electrodes. Taking into account the qualitative nature of the model used, we can state that this can also be an indication of quasiparticle perishing in the ''skirts''.

The results of calculations were used for estimating the diffusion coefficients: $D\simeq 1.5$ cm^2/s ($L_D=9$ μm) for the upper electrode and $D\simeq 2.1$ cm^2/s ($L_D=17$ μm) for the lower electrode. The diffusion coefficient is connected with the mean free path l_f of quasiparticles through the relation[16]

$$D=\frac{1}{3}\,v_F l_f\left(\frac{2kT}{\pi\Delta}\right)^{1/2}, \tag{6}$$

where v_F is the velocity of electrons on the Fermi surface, $v_F=0.57\cdot 10^8$ cm/s,[17] and k is the Boltzmann's constant.

This gives the values of $l_f=34$ and 48 Å for the upper and lower electrodes respectively. These values are slightly smaller than the size of crystallites (50–100 Å) in Nb electrodes.

The difference in the shape of the spectra for the lower and upper electrodes is primarily due to the difference in the diffusion length L_D in view of different values of the lifetime τ_d for quasiparticles. It was mentioned above that the value of τ_d is determined by losses. The most probable mechanism of losses is the capture of quasiparticles in traps which are regions with a lower value of the gap Δ, that are not in contact with the tunnel barrier, e.g., regions on the outer surfaces of the electrodes. At the same time, the traps in

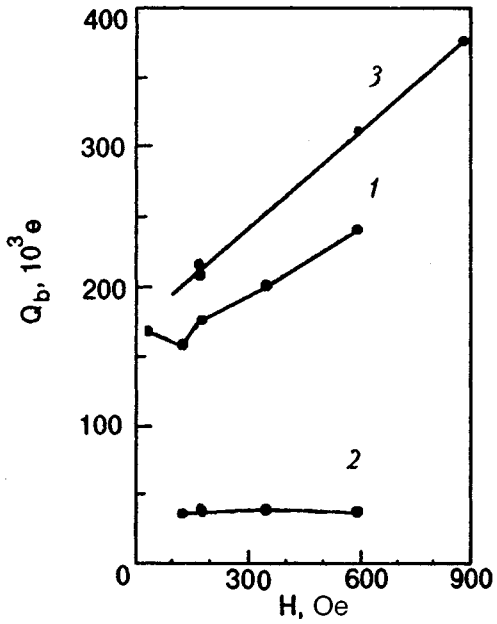

FIG. 8. Dependences of the boundary values of the output charge Q_d on the magnetic field for the lower (curve *1*) and upper (curve *2*) electrodes, and for the lower electrode of sample No. 2 (curve *3*) ($T=1.4$ K, $V_d=0.75$ mV).

contact with the barrier play a positive role since they reduce the probability of quasiparticle annihilation and ensure favorable conditions for quasiparticle tunneling.[14] It cannot be ruled out that the longer lifetime in the lower electrodes is due to the capture in such traps that are formed, for example, in the region adjoining the aluminum interlayer, or along grain boundaries.

Using the measured temperature dependence of the boundary charge Q_b (Fig. 7a), we can calculate the temperature dependence of the recombination time τ_R. For this purpose, we can use relation (2) for Q_b and relation (1) for the effective lifetime τ_d of quasiparticles, assuming that a decrease in recombination time plays the leading role in the case of heating. The values of τ_R calculated in this way for the lower electrode are presented in Fig. 7 (points on curve *3*). The obtained results confirm the exponential dependence of τ_R on temperature[16] for $\Delta=1.3$ meV.

The quasiparticle loss rate for the upper electrode is considerably higher ($\tau_{\text{loss}}\simeq 0.13\ \mu$s), and hence the boundary charge starts decreasing at much higher temperatures, when the values of $1/\tau_R$ becomes comparable with $1/\tau_{\text{loss}}$.

The most astonishing result of this research is the charge output increase with the magnetic field strength (Fig. 8). Such an effect of the magnetic field is observed only for one electrode, while for the other electrode this effect is insignificant. The magnetic field penetrates the surface layers of superconducting electrodes to the penetration depth λ, thus reducing the energy gap. In all probability, in the lower electrode, in which superconductivity is suppressed by the Al interlayer, the magnetic field caused a decrease in the gap width sufficient for the formation of a trap increasing the output of quasiparticles. The possibility of formation of a magnetic trap was considered in Ref. 18.

This research shows that the shape of the amplitude spectra of STJ detectors is determined to a considerable extent by diffusion of excess quasiparticles, in particular, by the relation between the diffusion length L_D and the linear dimensions of the electrodes. Peripheral regions (''skirts'') of the electrodes affect significantly the amplitude spectra and can be sources of additional losses of quasiparticles. Nonsymmetric STJ which make it possible to separate signals from different electrodes can be used for developing specific STJ detectors as well as in analysis of kinetics of nonequilibrium quasiparticles.

The authors are grateful to M. Yu. Kupriyanov for fruitful discussions, Yu. D. Zonnenberg and L. F. Nefedov for their help in preparing the setup.

*E-mail: andrva@srdlan.npi.msu.su

[1] V. S. Shpinel, V. A. Andrianov, and M. G. Kozin, Izv. Ross. Akad. Nauk, Ser. Fiz. **59**, 2 (1995).
[2] G. Charden, Nucl. Instrum. Methods Phys. Res. A **370**, 279 (1996).
[3] C. A. Mears, S. E. Labov, and A. T. Barfknecht, J. Low Temp. Phys. **93**, 561 (1993).
[4] F. S. Porter, D. van Vechten, M. G. Blamire, and E. C. G. Kirk, IEEE Trans. Appl. Supercond. **5**, 3026 (1995).
[5] V. A. Andrianov, M. G. Kozin, L. F. Nefedov *et al.*, Izv. Ross. Akad. Nauk, Ser. Fiz. **60**, 186 (1996).
[6] A. A. Golubov, E. P. Houwman, V. M. Krasnov *et al.*, J. Phys. (Paris) IV, Colloque C6, Suppl. J. Phys. (Paris) III **4**, C6-273 (1994).
[7] N. Rando, A. Peacock, A. van Dordrecht *et al.*, Nucl. Instrum. Methods Phys. Res. A **313**, 173 (1992).
[8] C. L. Foden, N. Rando, A. van Dordrecht *et al.*, Phys. Rev. B **47**, 3316 (1993).
[9] R. Christiano, L. Frunzio, R. Monaco *et al.*, Phys. Rev. B **49**, 429 (1994).
[10] V. S. Rusakov and N. I. Chistyakova, in *Abstr. Latin American Conf. on Applications of the Mössbauer Effect*, Buenos Aires (1992).
[11] A. A. Golubov, E. P. Houwman, J. G. Gijsbertsen *et al.*, Phys. Rev. B **49**, 12953 (1994).
[12] S. Lemke, J. Martin, J. B. le Grand *et al.*, Nucl. Instrum. Methods Phys. Res. A **370**, 119 (1996).
[13] M. Gutche, P. Hettl, J. Jochum *et al.*, Nucl. Instrum. Methods Phys. Res. A **370**, 91 (1996).
[14] N. E. Booth, P. L. Brink, R. J. Gaitskel *et al.*, J. Low Temp. Phys. **93**, 521 (1993).
[15] B. M. Budak, A. A. Samarskii, and A. N. Tikhonov, *Problems in Mathematical Physics* [in Russian], Nauka, Moscow (1972).
[16] B. Ivlev, G. Pepe, and U. Scotti di Uccio, Nucl. Instrum. Methods Phys. Res. A **300**, 127 (1991).
[17] H. W. Weber, E. Seidl, C. Laa *et al.*, Phys. Rev. B **44**, 7585 (1991).
[18] E. P. Houwman, A. A. Golubov, J. G. Gijsbertsen *et al.*, J. Low Temp. Phys. **93**, 677 (1993).

Translated by R. S. Wadhwa

Dipole magnet model for $CsDy(MoO_4)_2$

A. I. Anders and V. S. Bondarenko

B. Verkin Institute for Low Temperature Physics and Engineering, National Academy of Sciences of the Ukraine, 310164 Kharkov, Ukraine[*]

S. B. Bordovsky

Kharkov State University, 310024 Kharkov, Ukraine

A. Feger and A. Orendacheva

Faculty of Science, P. J. Safarik University, 04154 Kosice, Slovakia
(Submitted February 24, 1997; revised June 13, 1997)
Fiz. Nizk. Temp. **23**, 1195–1201 (November 1997)

The energy of the ordered state of the rare-earth subsystem of $CsDy(MoO_4)_2$ is calculated in the pure dipole approximation, and the magnetic configuration corresponding to the ground state is determined. The temperature dependence of the magnetic heat capacity is calculated in the temperature range $T>T_N$, and a good agreement with the experiment is observed.
 [S1063-777X(97)00711-1]

INTRODUCTION

In the theory and practice of magnetism, most magnetic systems are described in the exchange approximation in which the dipole-dipole interaction is taken into account as a correction. The reverse situation has not been given much consideration although a large number of magnetically concentrated compounds and, in particular, rare-earth insulators including those used as working substance for adiabatic demagnetization behave like pure dipole systems. This is due to a considerable value for the one-site magnetic moment of rare-earth (RE) ions and a comparatively large atomic separation in the lattice, which effectively decrease the exchange interaction in the system.

Studies of the compounds $KEr(MoO_4)_2$[1,2] and $CsGd(MoO_4)_2$,[3] which belong to the group of alkali-earth double molybdates, indicate that their main magnetic properties can be described in the pure dipole approximation.

According to the results of earlier investigations of electron paramagnetic resonance[4] and magnetic heat capacity,[5] the allied compound $CsDy(MoO_4)_2$ can also be treated as a dipole magnet. Indeed, the considerable value ($\sim 10\,\mu_B$) of one-site magnetic moments of Dy^{3+} ions in this crystal, a low value of the temperature of transition to the magnetically ordered state ($T_N=1.294$ K), which is comparable with the energy of dipole-dipole interactions in the system, as well as the close nature of temperature dependence of heat capacity near T_N and the heat capacity of a two-dimensional Ising magnet, point towards the dominating contribution from dipole-dipole interaction to the general pattern of spin-spin interactions in this case also.

The present work aims at describing the magnetic properties of $CsDy(MoO_4)_2$ in the dipole approximation. We shall determine the spin configuration corresponding to the ground state in the magnetically ordered phase, obtain the energy relations characterizing the ionic interaction, and calculate the temperature dependence of the magnetic heat capacity above the magnetic ordering point.

MAGNETIC STRUCTURE OF THE GROUND STATE OF $CsDy(MoO_4)_2$

At room temperature, the crystallographic structure of $CsDy(MoO_4)_2$ corresponds to the space group D_{2h}^3 with the parameters $a=9.51$ Å, $b=7.97$ Å, and $c=5.05$ Å of the unit cell which contains two structural units of this compound.

In terms of the unit cell parameters, the coordinates of the RE ions are $x=0$, $y=0.25$, and $z=0$ (Fig. 1).

With decreasing temperature, the crystal undergoes structural phase transitions, among which the first-order phase transition occurring at $T\simeq 40$ K is studied most extensively. Hence, in the helium temperature range in which we are interested, the volume of the unit cell is at least doubled. This is accompanied by a decrease in its symmetry and the formation of nonequivalent centers to be occupied by RE ions.[6] However, this nonequivalence is manifested in the EPR spectrum of $CsDy(MoO_4)_2$ in symmetric rotations of the effective g-factor (relative to the rhombic axes) characterizing the resonant absorption at the lowest Kramers doublet of the ground energy level ${}^6H_{15/2}$ of the Dy^{3+} ions, which is split by the crystal field. The extremal values of the effective g- factor are found to be the same for both centers, while the angles of rotation of the principal tensor axes are not large and amount to $\pm 10°$ and $\pm 5°$ in the ab and bc planes of the rhombic phase.

In view of such an insignificant difference in the parameters of the RE lattice sites, we can treat them as magnetically equivalent in the first approximation. In turn, during an analysis of the magnetic structure, this circumstances allows us to consider a unit cell containing one RE site and having

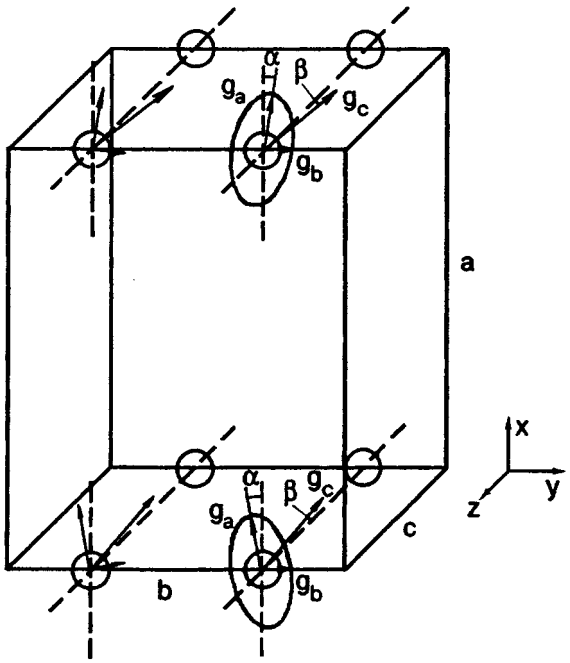

FIG. 1. Arrangement of Dy^{3+} ions in a $CsDY(MoO_4)_2$ unit cell. The arrows indicate possible directions of the axes of g-tensors of nonequivalent centers.

half the volume in the case under consideration due to a halving of the parameter b.

The method of determining the magnetic structure of the ground state for one ion per unit cell was proposed by Luttinger and Tisza for classical dipole systems,[7] and generalized by Niemeyer for quantum systems.[8] This technique was used actively for determining the minimum dipole energy of several paramagnetic salts,[8,9] as well as the molybdates mentioned above.

The essence of the method lies in the following. The Hamiltonian of interactions of magnetic moments lying at the sites i and j of the crystal lattice can be written in the form

$$H_D=\sum_{i<j}\ \frac{1}{r_{ij}^3}\left[\mu_i\mu_j-3\frac{(\mu_i\mathbf{r}_{ij})\cdot(\mu_j\mathbf{r}_{ij})}{r_{ij}^2}\right], \tag{1}$$

where r_{ij} is the radius vector connecting the sites i and j. Taking into consideration the connection between the components of magnetic moment and spin

$$\mu_i^\alpha=\sum_\beta\ \mu_B g_i^{\alpha\beta}S_i^\beta,\alpha,\quad \beta=x,y,z, \tag{2}$$

where μ_B is the Bohr magneton, we can represent Hamiltonian (1) in the form

$$H_D=\sum_{i<j}\ \sum_{\alpha,\beta}\ P_{ij}^{\alpha\beta}S_i^\alpha S_j^\beta, \tag{3}$$

where

$$P_{ij}^{\alpha\beta}=\sum_{\varepsilon,\lambda,\nu}\ \frac{\mu_B^2}{r_{ij}^3}\left(g_i^{\varepsilon\alpha}g_j^{\varepsilon\beta}-3\frac{g_i^{\alpha\lambda}g_j^{\beta\nu}r_{ij}^\lambda r_{ij}^\nu}{r_{ij}^2}\right). \tag{4}$$

The tensor $\hat{g}$ is diagonal in the coordinate system of the unit cell and is independent of the position of the sites i and j.

According to Niemeyer's theorem, the magnetic structure of the ground state for one ion per unit cell must correspond to one of the eight possible versions with the minimum energy of the moment μ_i in the field of the surrounding moments. Figure 2 shows the ferromagnetic structure 1FM, the antiferromagnetic Neel structure 2AF, and six types of layered antiferromagnetic structures.

Calculation of the eigenvalues of the dipole-dipole interaction energy of these states involves the use of the third-order matrices

$$A_k=\sum_{i<j}\ q(k)P_{ij}^{\alpha\beta},\quad k=1,...,8, \tag{5}$$

which assume the following form if Eqs. (3) and (4) are taken into account:

$$A_k=\sum_{l,m,n}\ q(k)\times\begin{pmatrix} g_x^2\dfrac{r^2-3x^2}{r^5} & -3\dfrac{g_xg_yxy}{r^5} & -3\dfrac{g_xg_zxz}{r^5}\\ -3\dfrac{g_xg_yxy}{r^5} & g_y^2\dfrac{r^2-3y^2}{r^5} & -3\dfrac{g_yg_zyz}{r^5}\\ -3\dfrac{g_xg_zxz}{r^5} & -3\dfrac{g_yg_zyz}{r^5} & g_z^2\dfrac{r^2-3z^2}{r^5}\end{pmatrix}, \tag{6}$$

where $\mathbf{r}\equiv\{x,y,z\}=\{la,mb/2,nc\}$. According to Fig. 2, the configurational component $q(k)$ can be represented in the form

$$\begin{aligned} &q(1)=1;\quad q(5)=(-1)^n;\\ &q(2)=(-1)^{l+m+n};\quad q(6)=(-1)^{l+n};\\ &q(3)=(-1)^m;\quad q(7)=(-1)^{m+n};\\ &q(4)=(-1)^l;\quad q(8)=(-1)^{l+m}. \end{aligned} \tag{7}$$

Since $\langle(S^\alpha)^2\rangle=S(S+1)/3$, the energy eigenvalues for Hamiltonian (3) have the form

$$E_k^\alpha=\frac{1}{3}\,\mu_B^2S(S+1)\varepsilon_k^\alpha, \tag{8}$$

where ε_k^α are the eigenvalues of the matrix A_k, which were calculated through a direct summation of the elements of matrix (6) over a sphere of radius 475 Å, thus ensuring a maximum error of 0.1% for moderate computing time.[1)] In this case, we used the lattice parameters of the high-temperature phase of $CsDy(MoO_4)_2$ since dilatometric studies[10] show that the difference in lattice parameters at 4.2 and 300 K do not exceed 0.1%. The results of computations are presented in Table I and shown schematically in Fig. 3.

The minimum energy value for $E_8=-1.3390$ K corresponds to the configuration 8AF with the magnetic moments directed along the c-axes and for the maximum value of projection of the effective g-factor ($g_a=3.7$, $g_b=1$, $g_c=13.4$).[4] The configuration 3AF for which the moments are also oriented along the c-axis has an energy value very close to the 8AF configuration. The difference in the energy char-

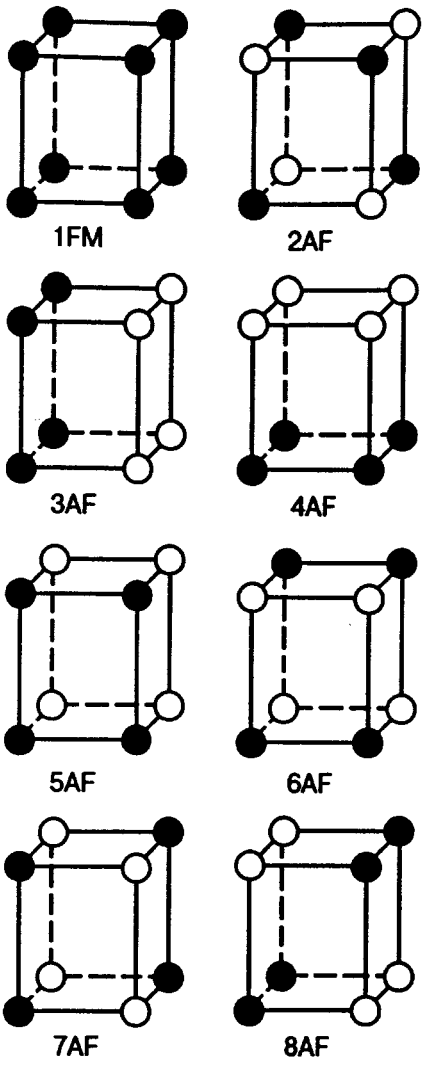

FIG. 2. Niemeyer's ordered magnetic structures[8] (black and white sites correspond to opposite directions of moments).

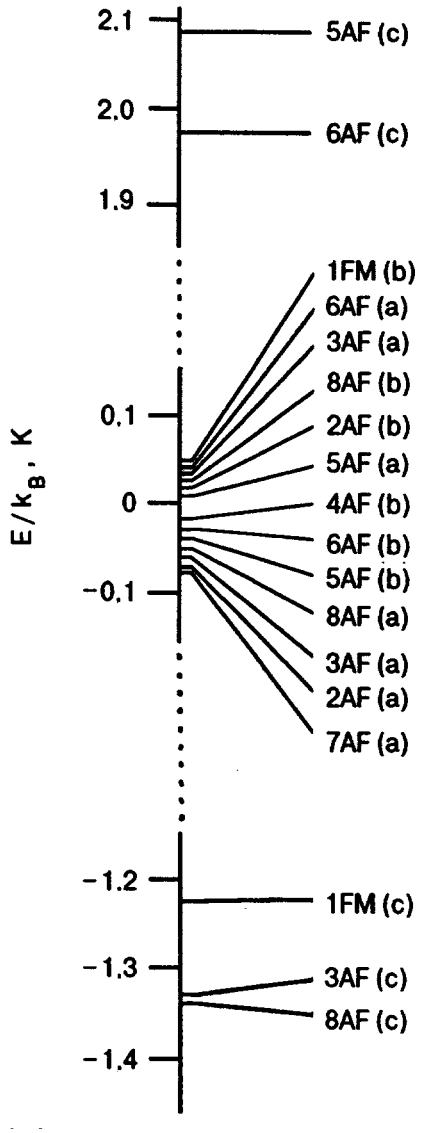

FIG. 3. Energy scale of magnetic configurations of the ordered state of $CsDy(MoO_4)_2$. The directions of magnetic moments are indicated in brackets.

acteristics of these states is quite insignificant: $E_3 - E_8 = 0.0044$ K. This quantity may serve as an estimate for the coupling between chains in the ground state of $CsDy(MoO_4)_2$, which is much lower than the binding energy $E_8 = 1.339$ K in the chain.

The configuration 1FM lies higher on the energy scale, its energy exceeding the ground state energy by ~ 0.11 K for moments oriented along the c-axis. The crystals of $CsDy(MoO_4)_2$ are usually in the form of thin plates (the a-axis is perpendicular to the plane of the plate). Hence, while calculating the energy of the purely ferromagnetic structure 1FM. We take the demagnetizing factor into consideration only along the a-axis; this changes the energy of the system by $\Delta E = 2\pi\mu_B^2 g_a^2 S^2 n_0$, which amounts to $\Delta E = 0.0667$ K for a density $n_0 = 4.98 \times 10^{21}$ cm^{-3} of Dy^{3+} ions in $CsDy(MoO_4)_2$.

TABLE I. Energy eigenvalues of spin configurations of the ordered state of $CsDy(MoO_4)_2$ with different directions of magnetic moments.

Magnetic configuration	Energy, K		
	E_a/k_B	E_b/k_B	E_c/k_B
1FM	1.1048	0.0488	−1.2285
2AF	−0.0702	0.0101	−0.3041
3AF	−0.0543	0.0130	−1.3346
4AF	0.2657	−0.0069	−0.8322
5AF	0.0059	−0.0143	2.0852
6AF	0.0150	−0.0134	1.9751
7AF	−0.0709	1.0733	−0.3011
8AF	−0.0522	0.0123	−1.3390

Results of our computations show that the energy of antiferromagnetic structures with the moments oriented at right angles to the ''easy'' axis c is higher than the energy of the ferromagnetic structure 1FM with the momenta directed along the c-axis (Fig. 3). This means that, in an external magnetic field $\mathbf{H} \| \mathbf{c}$, the system in the ground state must bypass the energetically disadvantageous spin-flop state, giving way to a metamagnetic phase transition to the ferromagnetic phase. In this case, the transition field will be defined by the

difference in the energies of the phases 1FM ($\boldsymbol{\mu}\|\mathbf{c}$) and 8AF ($\boldsymbol{\mu}\|\mathbf{c}$), which amounts to

$$H=k_B(E_1-E_8)/g_c\mu_B S=245.4 \text{ Oe}.$$

The experimental results[11] on the dependence of magnetization of $CsDy(MoO_4)_2$ on external magnetic field obtained at $T\simeq 0.5$ K show a sharp increase in the magnetic moment at $H_c\simeq 300$ Oe for $\mathbf{H}\|\mathbf{c}$ to the nominal value which remains unchanged upon a further increase in the field up to ~ 50 kOe. Such a behavior of magnetization is in qualitative agreement with our conclusion about the metamagnetic phase transition in this system.

MAGNETIC HEAT CAPACITY

The quantitative analysis of the heat capacity of a magnetic system can be used for verification of the interaction model chosen by us for describing the properties of the crystal under consideration. The method of high-temperature expansion of the distribution function is frequently used for this purpose. In spite of the fact that computation of higher-order terms in the expansion becomes quite cumbersome, this method has been used extensively for describing magnetic heat capacity and magnetic susceptibility of a number of systems with dominating dipole-dipole interaction even at temperatures close to T_N.[12,13] A satisfactory agreement with the experiment was obtained by taking into account the first two or three terms in the expansion.

For dipole systems with Hamiltonian (3), the expansion of the partition function

$$Z=\mathrm{Tr}(e^{-H_D/k_BT}) \tag{9}$$

in powers of reciprocal temperature leads to a series of the type

$$Z=\mathrm{Tr}\sum_{n=0}^{\infty}\frac{1}{n!}\left(-\frac{H_D}{k_BT}\right)^n. \tag{10}$$

Taking into account the relation between the Gibbs potential $G(T)=-k_BT\ln Z$ and the heat capacity $c_m=-T(\partial^2 G/\partial T^2)_{H=0}$, we can obtain an expression for $c_m(T)$ also in the form of a series in powers of the reciprocal temperature:

$$\frac{c_m}{R}=\sum_{n=2}^{\infty}(-1)^n\frac{b_n}{T^n}, \tag{11}$$

where R is the universal gas constant. The general form of coefficients b_2 and b_3 for dipole systems is presented in Refs. 12, 13.

According to the results of EPR experiments,[4] $CsDy(MoO_4)_2$ is characterized by a significant anisotropy of the g-factor ($g_c \gg g_a, g_b$). Hence while calculating the coefficients b_n in the case considered by us, we can disregard terms containing $(g_b^2)^n$ and $(g_a g_b)^n$. The expressions for b_2 and b_3 used by us for computing heat capacity are presented in the Appendix.

Figure 4 shows the temperature dependence of the magnetic heat capacity $c_m(T)$ for $T>T_N$, obtained by subtracting the lattice contribution c_{tot}[5]: from the total heat capacity c_{lat}. $c_m=c_{\mathrm{tot}}-c_{\mathrm{lat}}$. The solid curve corresponds to the value

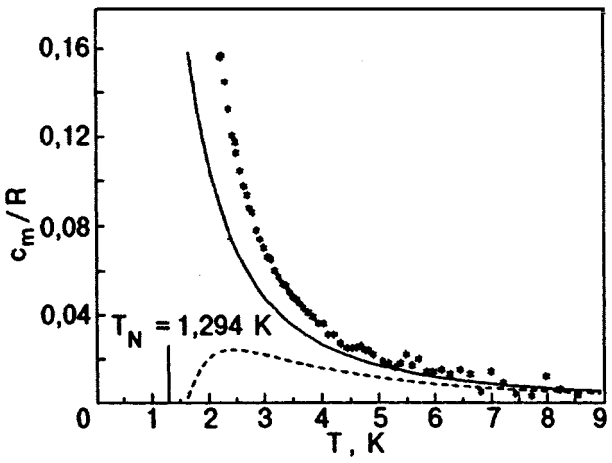

FIG. 4. Temperature dependence of the magnetic heat capacity of $CsDy(MoO_4)_2$: experiment (*); calculations taking into account the first term of the expansion (11) (solid curve), and the first two terms of the expansion (dashed curve).

of c_m calculated by using formula (11) taking into account only the term with b_2. The inclusion of the second term with the coefficient b_3 does not improve agreement with the experimental values since this term appears with a negative sign in the expansion (11). It can be assumed that the experimental values can be described better by taking into account terms with b_4 as well as higher-order terms. However, the problem becomes much more cumbersome due to a complex form of the coefficients b_n and a large number of lattice sums. However, the theoretical curve is in quite good agreement with the experimental data if we take into account only the first term of the expansion (11) into consideration.

CONCLUSIONS

As in the case of previously studied alkali-earth double molybdates $KEr(MoO_4)_2$ and $CsGd(MoO_4)_2$ with a large magnetic moment of rare-earth ions, the main magnetic properties of $CsDy(MoO_4)_2$ may be described by assuming a predominantly dipole-dipole nature of spin-spin interactions in the system. The available computational methods allow us to choose the magnetic configuration of the ground state in the magnetically ordered phase of a dipole magnetic and use the energy estimate to predict its main properties. Among other things, the magnetic structure of $CsDy(MoO_4)_2$ in the ground state consists of ferromagnetic chains of Dy^{3+} ions arranged and oriented along the c-axis of the crystal with the maximum value of the g-factor projection. The magnetic moments of adjacent chains are antiparallel to each other.

Note that for a configuration corresponding to the ground state, the computational technique used by us, which is essentially a mean-field method, leads to an energy value close to the value T_N for the crystal expressed in kelvins, which serves as a measure of internal interactions in the system.

The coupling energy between the chains is much lower than the binding energy of magnetic moments in a chain. Together with a fairly stable minimum for orientations of the moments $\mu\|\mathbf{c}$, this allows us to consider $CsDy(MoO_4)_2$ as a

quasi-one-dimensional Ising magnet which is characterized by a metamagnetic phase transition in an external magnetic field oriented in the direction of the moments. Experimental studies of magnetization of a crystal qualitatively support this conclusion.

Finally, we can describe the magnetic component of the heat capacity of $CsDy(MoO_4)_2$ without introducing any additional types of ionic interactions. All this confirms the qualitative applicability of the dipole model of a magnet for the system under consideration.

APPENDIX

Since $\mathrm{Tr}(H_D^2)$ for systems with purely dipole-dipole interaction contains only terms of the type $\sum_{ij} P_{ij}^{\alpha\beta} P_{ij}^{\alpha\beta}$, while $\mathrm{Tr}(H_D^3)$ contains only terms of the type $\sum_{ij,jk,ki} P_{ij}^{\alpha\beta} P_{jk}^{\alpha\beta} P_{ki}^{\alpha\beta}$ and $\sum_{ij} P_{ij}^{\alpha\beta} P_{ij}^{\alpha\beta} P_{ij}^{\alpha\beta}$, the coefficients b_2 and b_3 can be represented in the form

$$b_2 = \frac{1}{18k^2} S^2(S+1)^2 \mu_B^2 \{ g_x^4 (S_1 - 6S_3 + 9S_7) + g_z^4 (S_1 - 6S_4 + 9S_8) + 18 g_z^2 (g_x^2 S_9 + g_y^2 S_{10}) \};$$

$$b_3 = \frac{1}{6k^2} S^2(S+1)^2 \mu_B^2 \{ g_x^6 (S_2 - 9S_5 + 27(S_{11} - S_{13})) + g_z^6 [S_2 - 9S_6 + 27(S_{12} - S_{14})] - 54 g_z^3 (g_x^3 S_{15} + g_y^3 S_{16}) \} + \frac{1}{9k^3} S^3(S+1)^3 \mu_B^3 \{ g_x^6 [S_{17} - 3(2S_{18} + S_{20}) + 9(2S_{22} + S_{24}) - 27 S_{26}] + g_z^6 [S_{17} - 3(2S_{19} + S_{21}) + 9(2S_{23} + S_{25}) - 27 S_{27}] - 54 g_z^3 (g_x^3 S_{28} + g_y^3 S_{29}) \},$$

where S_n are lattice sums of the following types:

$$S_1 = \sum_{ij} \frac{1}{r_{ij}^6}; \quad S_2 = \sum_{ij} \frac{1}{r_{ij}^9}; \quad S_3 = \sum_{ij} \frac{x_{ij}^2}{r_{ij}^8};$$

$$S_4 = \sum_{ij} \frac{z_{ij}^2}{r_{ij}^8}; \quad S_5 = \sum_{ij} \frac{x_{ij}^2}{r_{ij}^{11}}; \quad S_6 = \sum_{ij} \frac{z_{ij}^2}{r_{ij}^{11}};$$

$$S_7 = \sum_{ij} \frac{x_{ij}^4}{r_{ij}^{10}}; \quad S_8 = \sum_{ij} \frac{z_{ij}^4}{r_{ij}^{10}}; \quad S_9 = \sum_{ij} \frac{x_{ij}^2 z_{ij}^2}{r_{ij}^{10}};$$

$$S_{10} = \sum_{ij} \frac{y_{ij}^2 z_{ij}^2}{r_{ij}^{10}}; \quad S_{11} = \sum_{ij} \frac{x_{ij}^4}{r_{ij}^{13}}; \quad S_{12} = \sum_{ij} \frac{z_{ij}^4}{r_{ij}^{13}};$$

$$S_{13} = \sum_{ij} \frac{x_{ij}^6}{r_{ij}^{15}}; \quad S_{14} = \sum_{ij} \frac{z_{ij}^6}{r_{ij}^{15}}; \quad S_{15} = \sum_{ij} \frac{x_{ij}^3 z_{ij}^3}{r_{ij}^{15}};$$

$$S_{16} = \sum_{ij} \frac{y_{ij}^3 z_{ij}^3}{r_{ij}^{15}}; \quad S_{17} = \sum_{ij,jk,ki} \frac{1}{r_{ij}^3 r_{jk}^3 r_{ki}^3};$$

$$S_{18} = \sum_{ij,jk,ki} \frac{x_{ij}^2}{r_{ij}^5 r_{jk}^3 r_{ki}^3}; \quad S_{19} = \sum_{ij,jk,ki} \frac{z_{ij}^2}{r_{ij}^5 r_{jk}^3 r_{ki}^3};$$

$$S_{20} = \sum_{ij,jk,ki} \frac{x_{jk}^2}{r_{ij}^3 r_{jk}^5 r_{ki}^3}; \quad S_{21} = \sum_{ij,jk,ki} \frac{z_{jk}^2}{r_{ij}^3 r_{jk}^5 r_{ki}^3};$$

$$S_{22} = \sum_{ij,jk,ki} \frac{x_{ij}^2 x_{jk}^2}{r_{ij}^5 r_{jk}^5 r_{ki}^3}; \quad S_{23} = \sum_{ij,jk,ki} \frac{z_{ij}^2 z_{jk}^2}{r_{ij}^5 r_{jk}^5 r_{ki}^3};$$

$$S_{24} = \sum_{ij,jk,ki} \frac{x_{ij}^2 x_{ki}^2}{r_{ij}^5 r_{jk}^3 r_{ki}^5}; \quad S_{25} = \sum_{ij,jk,ki} \frac{z_{ij}^2 z_{ki}^2}{r_{ij}^5 r_{jk}^3 r_{ki}^5};$$

$$S_{26} = \sum_{ij,jk,ki} \frac{x_{ij}^2 x_{jk}^2 x_{ki}^2}{r_{ij}^5 r_{jk}^5 r_{ki}^5}; \quad S_{27} = \sum_{ij,jk,ki} \frac{z_{ij}^2 z_{jk}^2 z_{ki}^2}{r_{ij}^5 r_{jk}^5 r_{ki}^5};$$

$$S_{28} = \sum_{ij,jk,ki} \frac{x_{ij} x_{jk} x_{ki} z_{ij} z_{jk} z_{ki}}{r_{ij}^5 r_{jk}^5 r_{ki}^5};$$

$$S_{29} = \sum_{ij,jk,ki} \frac{y_{ij} y_{jk} y_{ki} z_{ij} z_{jk} z_{ki}}{r_{ij}^5 r_{jk}^5 r_{ki}^5}.$$

Numerical values of S_n were obtained through direct summation with increasing number of coordination spheres participating in the summation. The computer program terminated the computational process when the difference between the results of preceding and succeeding summations was less than 1% of the preceding value of the sum.

*E-mail: aanders@ilt.kharkov.ua

[1)]A preliminary analysis of the convergence of eigenvalues ε_k^α upon an increase in the number of coordination spheres participating in the summation shows that even a doubling of the radius in this case changes the value of ε_k^α by not more than 0.1% of its initial value. Hence this estimate is used for the error in the results of computation of ε_k^α.

[1] A. G. Anders, S. V. Volotskii, and O. È Zubkov, Fiz. Nizk. Temp. **20**, 131 (1994) [Low Temp. Phys. **20**, 105 (1994)].
[2] A. G. Anders, S. V. Volotskii, and O. E. Zubkov, Fiz. Nizk. Temp. **20**, 137 (1994) [Low Temp. Phys. **20**, 110 (1994)].
[3] A. G. Anders, S. V. Volotskii, and S. V. Startsev, *et al.* Fiz. Nizk. Temp. **21**, 52 (1995) [Low Temp. Phys. **21**, 38 (1995)].
[4] A. G. Anders and V. S. Bondarenko, Fiz. Nizk. Temp. **22**, 1042 (1996) [Low Temp. Phys. **22**, 799 (1996)].
[5] P. Stefanyi, A. Orendaheva, A. Feger, *et al.*, Fiz. Nizk. Temp. **15**, 1105 (1989) [Sov. J. Low Temp. Phys. **15**, 615 (1989)].
[6] N. M. Nesterenko, V. I. Fomin, V. I. Kut'ko, and A. I. Zvyagin, Preprint No. 26–82, Inst. Low Temp. Phys. and Eng., Kharkov (1982).
[7] J. M. Luttinger and L. Tisza, Phys. Rev. **70**, 954 (1946).
[8] T. Niemeyer, Physica (Utrecht) **57**, 281 (1972).
[9] J. M. Daniels and J. Felsteiner, Can. J. Phys. **42**, 1469 (1964).
[10] S. B. Feodos'ev, E. S. Syrkin, I. A. Gospodarev, *et al.*, Fiz. Tverd. Tela (Leningrad) **31**, 186 (1989) [Sov. Phys. Solid State **31**, 102 (1989)].
[11] A. S. Chernyi, Ph.D. Thesis, Kharkov (1994).
[12] S. Wong, S. T. Dembinski, and W. Opechowski, Physica 42, 565 (1969).
[13] E. Lagendijk, H. W. L. Blote, and W. J. Huiskamp, Physica **61**, 220 (1972).
[14] C. D. Marquart, Proc. Phys. Soc. London **92**, 650 (1967).
[15] P. H. E. Meijer and D. J. O'Keeffe, Phys. Rev. B **1**, 3786 (1970).

Translated by R. S. Wadhwa

Effect of pressure on the phase diagrams and dynamic properties of easy-plane antiferromagnets

Yu. N. Mitsay, Yu. A. Fridman, G. A. Bairamaliyeva, and C. N. Alexeev

Simferopol State University, 333036, Simferopol, Yaltinskaya st., 4
(Submitted March 19, 1997; revised May 22, 1997)
Fiz. Nizk. Temp. **23**, 1202–1210 (November 1997)

Phase diagrams and dynamic properties of strongly anisotropic, easy-plane antiferromagnets in the presence of external pressure are studied. It is demonstrated that the phase with tensorial order parameter is possible in the system. Spectra of bound magnetoelastic waves are studied in the vicinity of the phase transition points. © *1997 American Institute of Physics.* [S1063-777X(97)00811-6]

INTRODUCTION

Special attention has recently been focused on the study of peculiarities of the behavior of easy-plane magnets with one-ion anisotropy.[1–3] Systems with the energy of uniaxial anisotropy comparable or greater than the energy of the exchange interaction have attracted considerable interest. First of all, it is connected with the fact that such magnets are low-temperature magnets. They are[4,5] $NiSiF_6 \cdot 6H_2O$, $NiZrF_6 \cdot 6H_2O$, $FeSiF_6 \cdot 6H_2O$, $CsFeCl_3$, and some others. The behavior of these magnets in a transverse magnetic field has been studied extensively[1,3] and interesting peculiarities of their properties, such as the emergence of the quadruple phase (QU) and discontinuity of phase diagrams when the value of the magnetic ion spin is greater than unity, have been revealed. The dynamical properties of such systems have also been studied extensively in the vicinity of the orientational phase transition (OPT).

However, the behavior of such magnets in a longitudinal field (parallel to the basic plane) has been studied insufficiently since investigations of this case were limited to small anisotropy ($\beta \ll J$, where β is the constant of one-ion anisotropy, and J is the exchange constant).[6] The influence of mechanical boundary conditions on the properties of strongly anisotropic easy-plane magnets and spectra of elementary excitations with allowance for magnetoelastic interaction have virtually been ignored in those studies.

In this study we have focused our attention on these factors.

PHASE DIAGRAM OF A STRONGLY ANISOTROPIC EASY-PLANE ANTIFERROMAGNET

The system under study is a strongly anisotropic ($\beta \gg J$) antiferromagnet with the Dzyaloshinskii's exchange. The resulting magnetic momentum lies in the easy plane (XY), as does the applied external magnetic field. Let us determine the influence of the external pressure on the static and dynamic properties of the magnet. We assume that the external pressure is applied parallel to the easy plane. As we shall see, this is the most interesting case.

The Hamiltonian of the system has the form

$$\begin{aligned}\mathscr{H}_0 = & -H\sum_{n_i} S^x_{n_i} + \frac{\beta}{2}\sum_n (S^z_{n_i})^2 + \sum_{n_1,n_2}\{J(n_1-n_2) \\ & \times \mathbf{S}_{n_1}\mathbf{S}_{n_2} - D(n_1-n_2)[\mathbf{S}_{n_1}\times\mathbf{S}_{n_2}]_z\} \\ & + \nu\sum_{n_i} S^j_{n_i} S^k_{n_i} u_{jk}(n_i) + \int dr\left\{\frac{\lambda+\eta}{2}(u^2_{xx}+u^2_{yy}+u^2_{zz})\right. \\ & + \eta(u^2_{xy}+u^2_{xz}+u^2_{yz}) + \lambda(u_{xx}u_{yy}+u_{yy}u_{zz} \\ & \left. + u_{xx}u_{zz}) - Pu_{xx}\right\}, \end{aligned} \tag{1}$$

where $S^\alpha_{n_i}$ is the spin operator at site n of the ith sublattice, $D(n_1-n_2)<0$ the Dzyaloshinskii's exchange, ν is the constant of magnetoelastic (ME) exchange, λ and η are the elasticity moduli, $u_{jk}(n_i)$ is the deformation tensor, $J(n_1-n_2)>0$ is the exchange integral, P is the external pressure, and H is the external magnetic field.

In (1) the first three terms describe the magnetic subsystem, the fifth term describes the elastic subsystem, and the fourth term describes the ME exchange. Further investigations are carried out in a low-temperature limit ($T \ll T_N$, T_N is the Néel temperature) since in this case it is possible to make all calculations analytically. Without lack of generality we can assume the magnetic ion spin to be $S=1$. The orientation of the sublattice magnetic momenta for the system described by (1) can be represented as shown in Fig. 1.

Rotate the coordinate system around the axis (perpendicular to the plane of Fig. 1) so that the new quantization axis ξ_i would be parallel to the vector of magnetization of the ith sublattice. In this local coordinate system define the new spin operators $S^\xi_{n_i}$, $S^\eta_{n_i}$; and $S^\zeta_{n_i}$ as follows:

$$\begin{aligned} S^x_{n_i} &= S^\xi_{n_i}\cos\theta_i + (-1)^{i+1}S^\eta_{n_i}\sin\theta_i, \\ S^y_{n_i} &= (-1)^{i+1}S^\xi_{n_i}\sin\theta_i + S^\eta_{n_i}\cos\theta_i, \\ S^z_{n_i} &= S^\zeta_{n_i}, \quad \psi = \frac{\theta_1+\theta_2}{2}, \quad \varphi = \frac{\theta_1-\theta_2}{2}. \end{aligned} \tag{2}$$

We carry out further calculations with use of the Hubbard's operators,[3,6] which make it possible to exactly take into account the one-ion and ME exchange. These operators are built on eigenfunctions of the one-site Hamiltonian

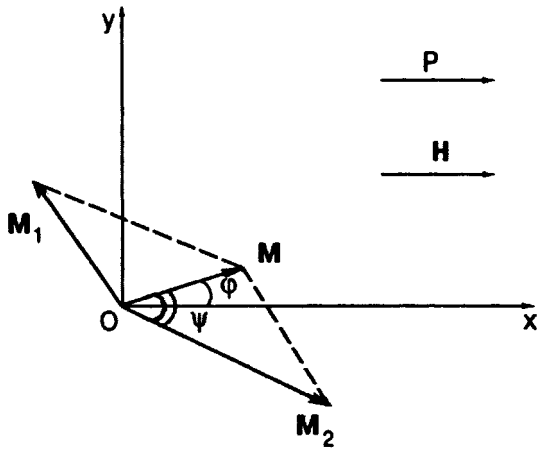

FIG. 1. Orientation of the sublattice magnetic momenta.

$\mathscr{H}_0(n_i)$. After separation of the mean field in the exchange part of (1) and transition to local operators (2) the one-site Hamiltonian assumes the form

$$\mathscr{H}_0=-\sum_{n_i} H_i S^{\xi}_{n_i}+\sum_{n_i}(-1)^{i+1}\overline{H_i}(S^+_{n_i}+S^-_{n_i})$$
$$-\frac{\beta}{8}\sum_{n_i}\{(S^+_{n_i})^2+(S^-_{n_i})^2-S^+_{n_i}S^-_{n_i}-S^-_{n_i}S^+_{n_i}\}$$
$$+\frac{\nu}{2}\sum_{n_i}\Big\{(u^i_{xx}+u^i_{yy}-u^i_{zz}-A_i+B_i)(S^+_{n_i})^2+2A_i(S^{\xi}_{n_i})^2$$
$$+\frac{1}{2}(u^i_{xx}+u^i_{yy}+u^i_{zz}-A_i)(S^+_{n_i}S^-_{n_i}+S^-_{n_i}S^+_{n_i})$$
$$+(C^i_1+C^i_2)(S^+_{n_i}S^{\xi}_{n_i}+S^{\xi}_{n_i}S^+_{n_i})+\text{e.g.}\Big\}. \tag{3}$$

Here we denote

$$S^{\pm}_{n_i}=S^{\eta}_{n_i}\pm iS^{\xi}_{n_i},\quad \langle S^{\zeta}_{n_i}\rangle=\langle S^{\zeta}_{n_2}\rangle=\langle S^{\zeta}\rangle,$$
$$H_i=H\cos\theta_i-\langle S^{\zeta}\rangle[J_0\cos 2\psi+D_0\sin 2\psi],$$
$$\overline{H_i}=\frac{1}{2}\{H\sin\theta_i-\langle S^{\zeta}\rangle[J_0\sin 2\psi-D_0\cos 2\psi]\},$$
$$A_i=u^i_{xx}\cos^2\theta_i+u^i_{yy}\sin^2\theta_i+(-1)^{i+1}u^i_{xy}\sin 2\theta_i,$$
$$B_i=-2i\{u^i_{yz}\cos\theta_i+(-1)^{i+1}u^i_{xz}\sin\theta_i\},$$
$$C^i_1=(-1)^i(u^i_{xx}-u^i_{yy})\sin 2\theta_i+2u^i_{xy}\cos 2\theta_i,$$
$$C^i_2=-2i\{u^i_{xz}\cos\theta_i+(-1)^{i+1}u_{yz}\sin\theta_i\}, \tag{3a}$$

where J_0 is the zero Fourier component of the exchange integral, and D_0 is the zero Fourier component of the Dzyaloshinskii exchange. Here

$$J_0=\sum_n J(n).$$

Solving the one-ion problem with the Hamiltonian (3)

$$\mathscr{H}_0(n_i)\psi_{n_i}(M)=E^i_M\psi_{n_i}(M),$$

we determine the eigenvalues and eigenfunctions of $\mathscr{H}_0$ (M is the magnetic quantum number. For $S=1$ $M=-1, 0, 1$):

$$E^i_{1,-1}=\frac{\beta}{4}+\frac{\nu/2}{H_i^2+4\overline{H_i^2}}\{(u^i_{xx}+u^i_{yy})(H_i^2+8\overline{H_i^2})+u^i_{zz}$$
$$\times(H_i^2+4\overline{H_i^2})+A_i(H_i^2-4\overline{H_i^2})+(-1)^{i+1}2C^i_1H_i\overline{H_i}\}$$
$$\mp\Big\{\frac{\beta^2}{16}+H^2+4\overline{H_i^2}-\frac{\nu\beta/4}{H_i^2+4\overline{H_i^2}}(u^i_{xx}+u^i_{yy})H_i^2-u^i_{zz}$$
$$\times(H_i^2+4\overline{H_i^2})-A_i(H_i^2-4\overline{H_i^2})+(-1)^{i+1}2C^i_1H_i\overline{H_i}$$
$$+\left(\frac{\nu/2}{H_i^2+4\overline{H_i^2}}\right)^2[(u^i_{xx}+u^i_{yy})H_i^2-u^i_{zz}(H_i^2+4\overline{H_i^2})$$
$$-A_i(H_i^2-4\overline{H_i^2})+(-1)^{i+1}2C^i_1H_i\overline{H_i}]^2\Big\}^{1/2}, \tag{4}$$

$$E^i_0=\frac{\beta}{2}+\frac{\nu}{H_i^2+4\overline{H_i^2}}\{(u^i_{xx}+u^i_{yy})H_i^2+u^i_{zz}(H_i^2+4\overline{H_i^2})$$
$$-A_i(H_i^2-4\overline{H_i^2})+(-1)^{i+1}2C^i_1H_i\overline{H_i}\}.$$

The Hubbard's operators are built on eigenfunctions by standard rules[9] $Y^{M'M}_{n_i}=|\psi_{n_i}(M')\rangle|\langle\psi_{n_i}(M)|$ and describe the transition of a magnetic ion state M to state M'. These operators are related to spin operators through familiar relations.[9]

From the condition of free energy density minimum

$$\mathscr{F}=\mathscr{F}_0-T\ln Z, \tag{5}$$

where $\mathscr{F}_0$ is the free energy of an elastics subsystem which is determined by the last term in (1)

$$Z=\sum_M \exp(-E_M/T)$$

and Z is the partition sum. Determine the equilibrium (spontaneous) deformations $u^{(0)}_{jk}(n_i)$. They appear to be

$$u^{(0)i}_{xx}=\frac{b^i_1(\eta+2\lambda)-\lambda(b^i_2+b^i_3)}{\eta(\eta+3\lambda)},$$

$$u^{(0)i}_{yy}=\frac{b^i_2(\eta+2\lambda)-\lambda(b^i_1+b^i_3)}{\eta(\eta+3\lambda)},$$

$$u^{(0)i}_{zz}=\frac{b^i_3(\eta+2\lambda)-\lambda(b^i_1+b^i_2)}{\eta(\eta+3\lambda)},$$

$$u^{(0)i}_{xz}=u^{(0)i}_{yz}=0,$$

$$u_{xy}^{(0)i}=\frac{(-1)^{i+1}}{2\eta}\,\frac{\nu(H_i^2-4\overline{H_i^2})\sin^2(\psi+(-1)^{i+1}\varphi)-4H_i\overline{H_i}\cos(\psi+(-1)^{i+1}\varphi)}{H_i^2+4\overline{H_i^2}}$$
$$\times\left\{\cosh\frac{\kappa_i^0}{T}+\frac{\beta}{\kappa_i^0}\sinh\frac{\kappa_i^0}{T}-\exp(-\beta/4T)\right\}\Big/\ Z_i^{(0)}, \tag{6}$$

where

$$b_1^i=-P-\frac{\nu}{Z_i^{(0)}}\left\{\left[1-\frac{(H_i\cos(\psi+(-1)^{i+1}\varphi)+2\overline{H_i}\sin(\psi+(-1)^{i+1}\varphi))^2}{H_i^2+4\overline{H_i^2}}\right]\cosh\frac{\kappa_i^0}{T}\right.$$
$$\left.-\frac{[H_i\sin(\psi+(-1)^{i+1}\varphi)-2\overline{H_i}\cos(\psi+(-1)^{i+1}\varphi)]^2}{H_i^2+4\overline{H_i^2}}\left(\frac{\beta}{4\kappa_i^0}\sinh\frac{\kappa_i^0}{T}\,\mathrm{e}^{-\beta/4T}\right)\right\},$$
$$b_2^i=-\frac{\nu}{Z_i^0}\left\{\left[1+\frac{(H_i\sin(\psi+(-1)^{i+1}\varphi)+2\overline{H_i}\cos(\psi+(-1)^{i+1}\varphi))^2}{H_i^2+4\overline{H_i^2}}\right]\cosh\frac{\kappa_i^0}{T}\right.$$
$$\left.-\frac{(H_i\cos(\psi+(-1)^{i+1}\varphi)+2\overline{H_i}\sin(\psi+(-1)^{i+1}\varphi))^2}{H_i^2+4\overline{H_i^2}}\left(\frac{\beta}{4\kappa_i^0}\cosh\frac{\kappa_i^0}{T}-\mathrm{e}^{-\beta/4T}\right)\right\}, \tag{7}$$
$$b_3^i=-\frac{\nu}{Z_i^{(0)}}\left\{\cosh\frac{\kappa_i^0}{T}+\frac{\beta}{4\kappa_i^0}\sinh\frac{\kappa_i^0}{T}+\mathrm{e}^{-\beta/4T}\right\},$$
$$Z_i^{(0)}=2\cosh\frac{\kappa_i^0}{T}+\mathrm{e}^{-\beta/4T},\quad \kappa_i^0=\left\{H_i^2+4\overline{H_i^2}+\frac{\beta^2}{16}\right\}^{1/2}.$$

As is evident from (4) and (6), the energy level corresponding to the ground state is E, whose analytical expression in our approximation is

$$E_1^i=-\frac{H_i^2+4\overline{H_i^2}}{\beta}-\frac{\nu P}{\eta}+\frac{2\nu P}{\eta}\,\frac{H_i\overline{H_i}}{H_i^2+4\overline{H_i^2}}$$
$$\times\sin 2(\psi+(-1)^{i+1}\varphi). \tag{8}$$

In (8) the terms proportional to ν^2/η are rather cumbersome and we will omit them here. Near the phase-transition lines these expressions are important and we take them explicitly into account.

In this case the free energy density can be represented in the form

$$\mathscr{F}^i=\mathscr{F}_0^i+E_1^i,$$
$$\mathscr{F}_0^i=\frac{\lambda+\eta}{2}(H_i^2+u_{yy}^2+u_{zz}^2)+\eta(u_{xy}^2+u_{xz}^2+u_{yz}^2)$$
$$+\lambda(u_{xx}u_{yy}+u_{xx}u_{zz}+u_{yy}u_{zz})+Pu_{xx}. \tag{9}$$

Using (9), we determine the phases in which the system under study may exist. Suppose that the system has such values of field H and pressure P that the mean magnetization at the sites is oriented as shown in Fig. 1. With an increase in the field to a certain value H_{c2} (at constant pressure), the vector of mean magnetization is oriented along the direction of the magnetic field H. In this case the angle $\varphi=0$ and ψ is determined from the condition of free energy density minimum (9). This condition leads to that in a phase with $\psi=0$, $H_i=0$ from which it is easy to obtain

$$\cos\psi=\frac{H+\langle S^\xi\rangle|D_0|}{2J_0\langle S^\xi\rangle}.$$

One can demonstrate that in the H_{c2} vicinity the mean sublattice magnetization approximately equals unity, $\langle S^\xi\rangle=1$. The phase which is realized at $H\geqslant H_{c2}$ is called the FM1 phase. We determine the value of H_{c2} from the ME wave spectra.

A further increase of the field leads to the fact that the vector $\mathbf{M}=\mathbf{M}_1+\mathbf{M}_2$ orients along the direction of the field (i.e., $\varphi=\psi=0$) as well as vectors of sublattice magnetization. Such configuration occurs at $H\geqslant H_{c3}$, where $H_{c3}=2J_0-|D_0|$.

The phase realized at $H\geqslant H_{c3}$ is called the FM2 phase. Of most interest is the case of small fields in which the so-called quadruple (QU) phase is realized. In this phase the magnetic vector order parameter equals zero.[7]

For our system it means that the mean sublattice magnetization and the mean magnetization at the site equal zero. It is well known[7] that for easy-plane ferromagnets in a transverse magnetic field the realization of a QU phase is accompanied by the inversion of energy levels; i.e., the E_0 level becomes the lowest level. In the system under investigation there is no such inversion and the QU phase is realized due to certain purely quantum effects.

Let us discuss this question in detail. Let us assume that in a certain field the system undergoes a transition to the QU phase. The magnetic phase realized in fields $H_{c2}\leqslant H\leqslant H_{c1}$ is called the QFM phase (quadruple ferromagnet). In our geometry the pressure plays the role of an effective anisotropy

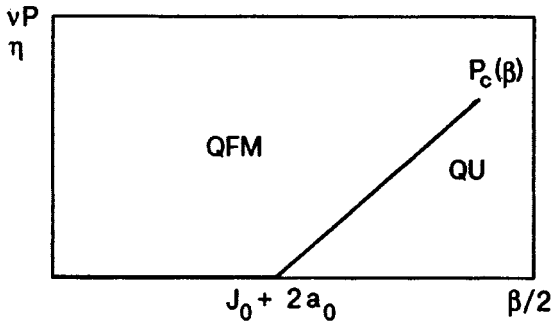

FIG. 2. Phase diagram of an easy-plane AFM in the plane (P,β).

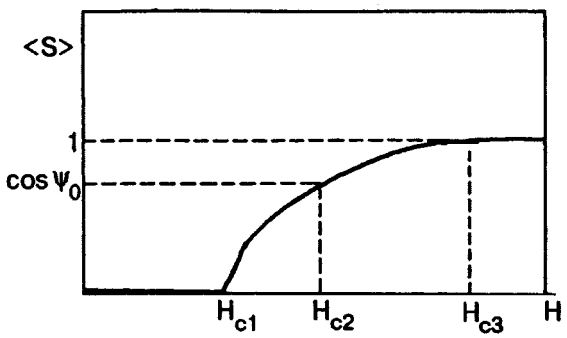

FIG. 3. Dependence of the sublattice magnetization on the external magnetic field.

with the easy magnetization axis (EMA) parallel to the OY axis.[6] At fields close to the field of the QFM-QU phase transition, as follows from the analysis of the free energy density[9] its minimum corresponds to values of the angles and is close to the following: $\varphi=\pi/2$, $\psi=0$; i.e., the vector of mean magnetization at the site the vectors of the sublattice mean magnetization tend to ''turn'' along the ''effective'' EMA. For mean magnetization of sublattices we obtain

$$\langle S^{\xi}_{n_i}\rangle = 4\frac{H}{\beta}\cos(\psi+(-1)^{2(i+1)}\varphi). \tag{10}$$

At $P=0$ and $H=0$ the system is in the QU phase since this result may be interpreted in the following way: there is no distinct axis in the system and all the directions in the basic plane (XY) are equal. Therefore, magnetizations at different sites may be directed arbitrarily and their average equals zero. This situation is similar to the one in which the QU phase is realized in strongly anisotropic easy-plane ferromagnets.[7]

As is evident, the ground state of an AFM at $P=0$ and $H=0$ corresponds to the eigenvector $|1\rangle$ of the S^{ξ} operator:

$$\psi_{n_i}(1)=|1\rangle.$$

With increasing pressure the mean magnetization should be turned along the axis of the ''effective'' anisotropy (OY). The ground state of an AFM is a superposition of the eigenvectors $|1\rangle$ and $|-1\rangle$ of the S^{ζ} operator: $\psi_{n_i}(1)=\cos\delta_i|1\rangle+\sin\delta_i|-1\rangle$. Such superposition of the vectors $|1\rangle$ and $|-1\rangle$ leads to the quantum redaction of the spin. This effect is characteristic of easy-axis magnets in a magnetic field perpendicular to an easy axis. In our case this effect is caused by the presence of an external pressure, which plays the role of uniaxial anisotropy.

In the AFM under study the two described quantum effects account for the existence of the QU phase. It turns out that the QU phase exists up to pressures determined by the formula

$$\frac{\nu P_c}{\eta}=\frac{\beta}{2}-J_0-2a_0, \tag{11}$$

where

$$a_0=\nu^2/2\eta.$$

This expression can be obtained by investigating the existence domain of a phase with nonzero mean magnetization.

In Fig. 2 we show the phase diagram at $H=0$ in the plane (P,β). The field of QFM-QU phase transition (H_{c1}) can be determined from the ME wave spectra. The behavior of angles and sublattice magnetization as a function of external magnetic field is shown in Figs. 3 and 4, where we denote

$$\psi_0=\frac{D_0}{4J_0}+\left(\frac{D_0^2}{16J_0^2}+\frac{d_0}{2J_0}\right)^{1/2}, \quad d_0=P\nu/\eta.$$

SPECTRA OF BOUND ME WAVES

The dynamic properties of magnets have several special features in the vicinity of orientational phase transitions. It is well known that allowance for the ME interactions leads to hybridization of elementary excitation.[3,6] Although the ME exchange is weak in the vicinity of OPT, precisely this pa-

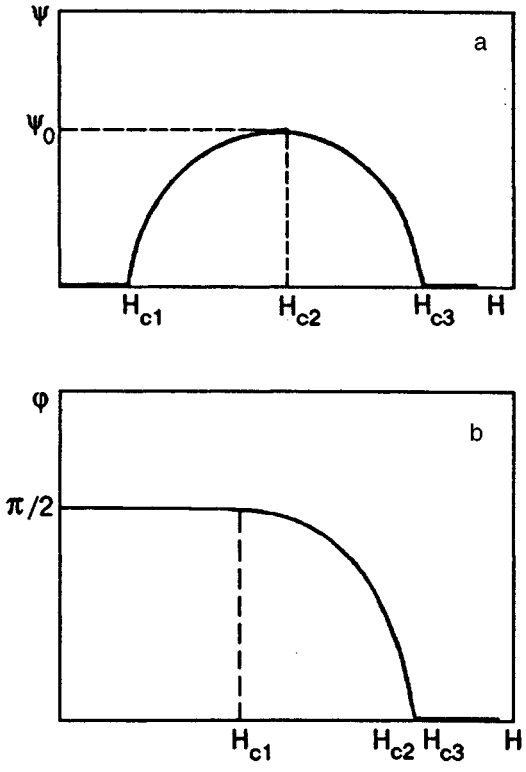

FIG. 4. Dependence of the angles of sublattice orientation on the external magnetic field.

rameter plays the decisive role in the dynamics of a system.[3,6] To investigate this question we represent the deformation tensor as a sum of two terms: spontaneous deformations $u_{jk}^{(0)}(n_i)$, which are determined by (6), and the dynamic term $u_{jk}^{(1)}(n_i)$, which corresponds to the lattice oscillations. The latter may be written in terms of phonon operators as follows[18]:

$$u_{jk}^{(1)i}=\frac{i}{2}\sum_{q,\lambda}\frac{\exp(iqn_i)}{(2mN\omega_\lambda(q))^{1/2}}(b_{q,\lambda}+b_{-q,\lambda}^{+})(e_\lambda^j(q)q_k + e_\lambda^k(q)q_j),$$

where $e_\lambda(q)$ is the unit vector of a phonon polarization, $\lambda = l,\ t,\ \tau$; m is the mass of a magnetic ion, N is the number of sites in a lattice, $\omega_\lambda(q)=c_\lambda q$ is the dispersion of a free phonon, and c_λ is the velocity of polarized sound.

After separation in the one-site Hamiltonian (3) of a part proportional to $u_{jk}^{(1)}(n_i)$ and its quantization in accordance with the given formula it is possible to write the Hamiltonian describing the processes of magnon-phonon transformations:

$$\mathscr{H}_{\rm tr}=\sum_{n_i}\left\{\sum_M \mathscr{P}_M J_{n_i}^M+\sum_\alpha \mathscr{P}_\alpha^i Y_{n_i}^\alpha\right\},$$

where

$$\mathscr{P}_{m(\alpha)}^{\ i}=\frac{1}{\sqrt{N}}\sum_{q,\lambda}(b_{q,\lambda}+b_{q,\lambda}^{+})T_{n_i}^{M(\alpha)}(q,\lambda),$$

α are the root vectors[6,9], and $T_{n_i}^{M(\alpha)}(q,\lambda)$ are the amplitudes of transformations.

Further, we consider the simplest and the most interesting case in which the wave vector is parallel to an external field H. In such geometry the only nonzero components of the unit vector of phonon polarization are $e_l^x(q)$, $e_t^y(q)$, and $e_\tau^z(q)$ and the corresponding amplitudes of transformation have the form

$$T_{n_i}^{1-1}(q,l)=T_{n_j}^{-11}(q,l)=\frac{i\nu}{2}T_{n_j}^0(q,l)qe_l^x\left(\frac{H_j}{\kappa_j^0}\cos 2\delta_i - \frac{\beta}{4\kappa_i^0}\sin 2\delta_i\right)\sin^2\psi,$$

$$T_{n_j}^{10}(q,l)=T_{n_j}^{01}(q,l)=(-1)^{j+1}\frac{i\nu}{4}T_{n_j}^0(q,l)qe_l^x(\gamma_\perp^j(\alpha_1) - \gamma_\perp^j(\alpha_2))\sin 2\psi,$$

$$T_{n_j}^{-10}(q,l)=T_{n_j}^{0-1}(q,l)=(-1)^{j+1}\frac{i\nu}{4}T_{n_j}^0(q,l)qe_l^x(\gamma_\perp^j(\alpha_5) - \gamma_\perp^j(\alpha_6))\sin 2\psi,$$

$$T_{n_j}^{1-1}(q,t)=T_{n_j}^{-11}(q,t)=-\frac{i\nu}{4}T_{n_j}^0(q,t)qe_t^y\left(\frac{H_i}{\kappa_j^0}\cos 2\delta_j - \frac{\beta}{4\kappa_j^0}\sin 2\delta_j\right)\sin 2\psi, \qquad (12)$$

$$T_{n_j}^{10}(q,t)=T_{n_j}^{01}(q,t)=(-1)^{j+1}\frac{i\nu}{4}T_{n_j}^0(q,t)qe_t^y(\gamma_\perp^j(\alpha_1) - \gamma_\perp^j(\alpha_2))\cos 2\psi,$$

$$T_{n_j}^{-10}(q,t)=T_{n_j}^{0-1}(q,t)=(-1)^{j+1}\frac{i\nu}{4}T_{n_j}^0(q,t)qe_t^y(\gamma_\perp^j(\alpha_5) - \gamma_\perp^j(\alpha_6))\cos 2\psi,$$

$$T_{n_j}^{1-1}(q,\tau)=-T_{n_j}^{1-1}(q,\tau)=(-1)^j\frac{\nu}{2}T_{n_j}^0(q,\tau)qe_\tau^z\sin\psi,$$

$$T_{n_j}^{10}(q,\tau)=-T_{n_j}^{01}(q,\tau)=\frac{\nu}{4}T_{n_j}^0(q,\tau)qe_\tau^z(\gamma_\perp^j(\alpha_1) + \gamma_\perp^j(\alpha_2))\cos\psi,$$

$$T_{n_j}^{-10}(q,\tau)=-T_{n_j}^{0-1}(q,\tau)=\frac{\nu}{4}T_{n_j}^0(q,\tau)qe_\tau^z(\gamma_\perp^j(\alpha_5) + \gamma_\perp^j(\alpha_6))\cos\psi,$$

$$T_{n_j}^0(q,\lambda)=\exp(iqn_j)/\sqrt{2m\omega_\lambda(q)}.$$

The functions $\gamma_\perp^j(\alpha)$ in (12) are determined from the relation between the spin operators and the Hubbard operators[6] and in the given geometry $\gamma_\perp^j(\alpha)\ \gamma_\parallel^j(\alpha)=0$ for all α, n is the number of the site, and j is the number of the sublattice.

The spectra of ME waves are determined by the poles of a full Green's function

$$G^{\alpha\alpha'}(n,\tau;n',\tau')=-\langle\hat{T}\tilde{Y}_n^\alpha(\tau)\tilde{Y}_{n'}^{-\alpha}(\tau')\rangle,$$

where $\hat{T}$ is the time-ordering operator, and $Y_n^\alpha(\tau)$ are the Hubbard operators in the Heisenberg representation.

The Fourier transform of the Green's function to be found is related to the irreducible transform by the Larkin part $\Sigma_{jj}^{\alpha\alpha'}(k,\omega_n)$ and the amplitudes of transformation $T_j^\alpha(k,\lambda)$ are related by the Larkin-type equation

$$G_{jj'}^{\alpha\alpha'}(k,\omega_n)=\Sigma_{jj'}^{\alpha\alpha'}(k,\omega_n)+(\Sigma_j^\alpha(k,\omega_n)v(k)\mathbf{P}_{j'}^{\alpha}(k,\omega_n) + \Sigma_{jj_1}^{\alpha\alpha_1}(k,\omega_n)T_{j_1}^{\alpha_1}(k,\lambda)D_\lambda(k,\omega_n)T_{j_2}^{\alpha_2} \times(-k,\lambda)G_{j_2j'}^{\alpha_2\alpha'}(k,\omega_n). \qquad (13)$$

In (13) $D_\lambda(k,\omega_n)=2\omega_\lambda(k)/(\omega_n^2-\omega_\lambda^2(k))$ is the Green's function of a λ-polarized free phonon, and $\Sigma_j^\alpha(k,\omega_n)$ is the six-dimensional vector, which in the block notation has the form

$$\Sigma_j^\alpha(k,\omega_n)=(\Sigma_{j1}^\alpha(k,\omega_n),\Sigma_{2j}^\alpha(k,\omega_n)),$$

where the three-dimensional vectors $\Sigma_{jj'}^{\alpha}(k,\omega_n)$ have the form

$$\Sigma_{jj'}^{\alpha}(k,\omega_n)=\Sigma_{\alpha_t}c_{j'}(-\alpha_1)\Sigma_{jj'}^{\alpha\alpha_1}(k,\omega_n),$$

$$c_j(\alpha)=(\gamma_{\|}^{j}(\alpha),\quad \gamma_{\perp}^{j}(\alpha),\quad \gamma_{\perp}^{*j}(-\alpha)).$$

The six-dimensional matrix is $\hat{V}(k)=\sigma^1\otimes V$, and σ^1 is the Pauli matrix

$$V=\begin{pmatrix} V^{\zeta\xi} & -V^{+\xi} & -V^{+\xi} \\ V^{+\xi} & V^{++} & V^{+-} \\ V^{+\xi} & V^{+-} & V^{++} \end{pmatrix}$$

$$V^{\zeta\xi}(n-n')=J(n-\dot{n}')\cos 2\psi+D(n-n')\sin 2\psi,$$

$$V^{++}(n-n')=\frac{1}{4}\{V^{\xi\xi}(n-n')-J(n-n')\},$$

$$V^{+-}(n-n')=\frac{1}{4}\{V^{\xi\xi}(n-n')+J(n-n')\},$$

$$V^{+\xi}(n-n')=\frac{1}{2}\{J(n-n')\sin 2\psi-D(n-n')\cos 2\psi\}.$$

The six-dimensional vectors $\mathbf{P}_{j'}^{\alpha}(k,\omega_n)$ can also be represented in a block notation

$$\mathbf{P}_{j'}^{\dot{\alpha}}(k,\omega_n)=(P_{j1}^{\alpha}(k,\omega_n),\quad P_{2j}^{\alpha}(k,\omega_n)),$$

while the three-dimensional vectors $\mathbf{P}_{jj'}^{\alpha}(k,\omega_n)$ are determined by the relation

$$\mathbf{P}_{jj'}^{\alpha}(k,\omega_n)=\sum_{\alpha_1}\ \mathbf{c}_j(\alpha_1)G_{jj'}^{\alpha\alpha_1}(k,\omega_n).$$

Equation (13) can be solved due to the ''split'' dependence on index α. Finally, the dispersion relation in the mean-field approximation for the ME waves has the form

$$\{1-(y_2-y_3)^2\}\{1-(y_2+y_3)^2\}=0, \tag{14}$$

where

$$\begin{aligned} y_2(k,\omega_n)=&-V^{++}(k)\Big\{b(\alpha)G_0^{\alpha}(\omega_n)|\gamma_{\perp}(\alpha)|^2 \\ &+\frac{D_{\lambda}(k,\omega_n)}{1-Q_{\lambda\lambda'}D_{\lambda}(k,\omega_n)}\,b(\alpha)b(\beta)G_0^{\alpha}(\omega_n) \\ &\times\gamma_{\perp}(\alpha)\gamma_{\perp}^{*}(\beta)T^{\alpha}(k,\lambda)T^{\beta}(-k,\lambda')\Big\}, \end{aligned} \tag{15}$$

$$\begin{aligned} y_3(k,\omega_n)=&-V^{+-}(k)\Big\{b(\alpha)G_0^{\alpha}(\omega_n)\gamma_{\perp}(\alpha)\gamma_{\perp}(-\alpha) \\ &+\frac{D_{\lambda}(k,\omega_n)}{1-Q_{\lambda\lambda'}D_{\lambda}(k,\omega_n)}\,b(\alpha)b(\beta)G_0^{\alpha}(\omega_n) \\ &\times G_0^{\beta}(\omega_n)\gamma_{\perp}(\alpha)\gamma_{\perp}(-\beta)T^{-\alpha}(k,\lambda)T^{-\beta} \\ &\times(-k,\lambda')\Big\}, \end{aligned}$$

$$Q_{\lambda\lambda'}=T_j^{\alpha}(-k,\lambda')\Sigma_{jj'}^{\alpha\alpha'}(k,\omega_n)T_{j'}^{-\alpha'}(k,\lambda).$$

Here we sum over α, β, λ, and λ'.

As is evident from the analysis of (14) in the QFM phase, the transverse polarized ME waves (τ and t) ''become entangled'', while the equation for the longitudinally polarized wave splits out (1) and its spectra has the form

$$\omega_1^2(k)=\omega_l^2(k)(1-a_0/J_0).$$

However, in the vicinity of the OPT QFM-FM phase and QFM-QU phase it is possible to uncouple Eq. (14) with respect to polarizations. Let us consider the dynamics of a system in the vicinity of the QFM-FM1 phase transition. In this case (see above) $\varphi=0$, $\cos 2\psi\approx -1$, and $\cos\psi\approx 0$, while the mean sublattice magnetization is $\langle S_i^{\xi}\rangle\approx 1$. It follows from (12) that the only nonzero amplitudes of transformations are $T^{10}(k,t)$ and $T^{01}(k,t)$ and only t-polarized phonons interact with the magnetic subsystem. The equation $1-(y_2+y_3)^2=0$ decomposes in the vicinity of the QFM-FMI transition into three equations, each describing quasiphonon oscillations of certain polarization. The solutions of these equations are

$$\begin{aligned} &\omega_{\mathrm{I}}^2(k)=\omega_l^2(k)(1-a_0/J_0), \\ &\omega_{\mathrm{II}}^2(k)=\omega_{\tau}^2(k)(1-a_0/4J_0), \\ &\omega_{\mathrm{III}}^2(k)=\omega_t^2(k)\,\frac{\alpha k^2+[(H^2+H|D_0|)/2J_0]-d_0}{\alpha k^2+a_0+[(H^2+H|D_0|)/2J_0]-d_0}. \end{aligned} \tag{16}$$

From the condition $[(H^2+H|D_0|)/2J_0]-d_0=0$ we determine the field of a QFM-FM1 phase transition

$$H_{c2}=-\frac{|D_0|}{2}+\left(\frac{D_0^2}{4}-2d_0J_0\right)^{1/2}. \tag{17}$$

It follows from (16) that at the point of OPT in a long-wave limit ($\alpha k^2\ll a_0$) the spectrum of t-polarized quasiphonons softens:

$$\begin{aligned} &\omega_{\mathrm{I}}(k)\approx\omega_l(k), \\ &\omega_{\mathrm{II}}(k)\approx\omega_{\tau}(k), \\ &\omega_{\mathrm{III}}^2(k)=\omega_t^2(k)\,\frac{\alpha k^2}{a_0}, \end{aligned} \tag{18}$$

while the spectrum of quasimagnons is determined by the expression

$$\mathscr{E}^2(k)=2J_0(\alpha k^2+a_0). \tag{19}$$

Thus t-polarized phonons strongly interact with magnons in the vicinity of the OPT (QFM-FM1). Their spectrum softens while in quasimagnon spectrum the ME gap appears.

The value of the gap, as follows from (19), is

$$\omega_{me}=\sqrt{2J_0a_0}. \tag{20}$$

The results (18)–(20) obtained by us precisely coincide with the results for slightly anisotropic AFM.[6]

Of special interest is the dynamics of a system in the vicinity of the OPT QFM-QU phase since this case has not been investigated previously.

As we have noticed above, near the point under study $\varphi=\pi/2$ and $\psi=0$, while the mean sublattice magnetization equals zero: $\langle S^{\zeta}\rangle\approx 0$. Hence $V^{++}=0$ and therefore y_2 equals zero (15). The dispersion relation (14) has a more simple form:

$$1-y_3^2=0. \tag{21}$$

It should be noted that in this situation $T^{10}(k,\tau)$ and $T^{01}(k,\tau)$ amplitudes of transformation differ from zero $T^{10}(k,t)\approx T^{01}(k)\approx 0$ by virtue of infinitesimally small H/β ratio. Equation (21) accordingly splits into equations, each of which describes quasiphonon oscillations of certain polarization. These equations have the solutions

$$\omega_{\rm I}^2(k)=\omega_l^2(k),$$

$$\omega_{\rm II}^2(k)=\omega_\tau^2(k)\,\frac{\alpha k^2+H_{c1}^2-H^2}{\alpha k^2+H_{c1}^2-H^2+2a_0},$$

$$\omega_{\rm III}^2(k)\approx\omega_t^2(k), \tag{22}$$

where

$$H_{c1}=\sqrt{\beta/2(\beta/2-d_0-2a_0-J_0)}.$$

Here H_{c1} is the field of a OPT QFM-QU. At the point of a transition in a long-wave limit ($\alpha k^2\ll a_0$) the spectrum of τ-polarized quasiphonons softens:

$$\omega_{\rm II}^2(k)=\omega_\tau^2(k)\,\alpha k^2/2a_0, \tag{23}$$

while in the spectrum of quasimagnons

$$\mathscr{E}^2(k)=(\alpha k^2+2a_0)(2J_0+2a_0), \tag{24}$$

the ME gap appears

$$\omega_{me}=2\sqrt{J_0a_0}. \tag{25}$$

As is evident from the relations (18) and (23), in the vicinity of the point of OPT QFM-QU phase the soft mode is a τ-polarized quasiphonon mode, while at the point of OPT QFM-QU phase a t-polarized quasiphonon mode is a soft mode. Therefore, in the QFM phase (at $H_{c2}<H<H_{c1}$) two transversely polarized modes interact with the magnon branch.

Note that the value of ME gap in the spectrum of quasimagnons in the QU-phase is $\sqrt{2}$ times larger than the gap in the vicinity of a transition to the FM1 phase. Besides, as follows from (20) and (25), the ME gap suffers the so-called exchange amplification characteristic of antiferromagnets.

From the condition $H_{c1}<H_{c2}$ we obtain the value of a one-ion anisotropy constant at which the above-described effects are realized

$$\beta>J_0+d_0+2a_0+\{(J_0+d_0+2a_0)^2+D_0^2+4d_0 -4|D_0|\sqrt{D_0^2/4+J_0d_0}\}^{1/2}.$$

CONCLUSIONS

As we have noted recently, anisotropic magnets have attracted considerable attention. Peculiarities of their behavior were studied in many papers.[1–3] However, the influence of mechanical boundary conditions on the properties of such systems was virtually neglected. In the present paper it is demonstrated that the presence of mechanical boundary conditions (external pressure P) leads to a series of specific features in the behavior of easy-plane AFM.

In particular, these peculiarities exhibit themselves in the QU phase. We show that this phase is formed due to the presence of two quantum effects, one of which is characteristic only of the easy-plane magnets and the other is characteristic of the easy-axis magnets.

Quite interesting is the effect involving the change of polarization of the soft mode, which softens in the transition from H_{c1} to H_{c2}.

[1] V. G. Borisenko and Yu. V. Pereverzev, Fiz. Nizk. Temp. **11**, 730 (1985).
[2] W. G. Bos, T. O. Khassen, N. J. Poulis, and R. L. Carlin, Magn. Magn. Mater. **15–18**, 464 (1980).
[3] Yu. N. Mitsay and Yu. A. Fridman, Ukr. Fiz. Zh. **35**, 459 (1990).
[4] F. J. Varret, Phys. Chem. Solids **37**, 257 (1976).
[5] E. A. Zavadsii, Thesis of a report, Makhachkala (1984), p. 131.
[6] Yu. N. Mitsay and Yu. A. Fridman, Ukr. Fiz. Zh. **35**, 5 (1990).
[7] F. N. Onufriyeva, Fiz. Tverd. Tela (Leningrad) **26**, 145 (1984).
[8] L. D. Landau and E. M. Lifshitz, Statistical Physics, Nauka, Moskow (1976).
[9] R. O. Zaltsev, Zh. Éksp. Teor. Fiz. **63**, 207 (1975).

This article was published in English in the original Russian journal. It was edited by S. J. Amoretty.

Faraday rotation in conductors with magnetoimpurity electron states

A. M. Ermolaev and G. I. Rashba

Kharkov State University, 310077 Kharkov, Ukraine
(Submitted April 22, 1997; revised June 2, 1997)
Fiz. Nizk. Temp. **23**, 1211–1214 (November 1997)

The high-frequency Hall conductivity for metals and degenerate semiconductors with magnetoimpurity electron states is calculated. The effect of these states both on Faraday rotation angle and on magnetic circular dichroism is considered. Additional maxima and minima on the frequency dependence of Faraday angle, which are associated with the magnetoimpurity electron states, are observed. © *1997 American Institute of Physics.* [S1063-777X(97)00911-0]

Crystals in a magnetic field have a circular anisotropy caused by nonequivalence of rotational directions in a plane perpendicular to the magnetic field. This anisotropy causes a difference in the velocities of electromagnetic waves having opposite circular polarizations and propagating in the magnetic field direction, as well as a difference in the coefficients of absorption of these waves. As a result, the polarization plane of a linearly polarized radiation passing through a crystal turns through a certain (Faraday) angle, while the linearly polarized radiation becomes elliptically polarized.[1]

The practical significance of the Faraday effect is associated with the possibility of using it as a method for studying the structure of solids. For example, the Faraday effect can be used to determine reliably an important band parameter in semiconductors, viz., the effective mass of conduction electrons, and to draw conclusions about the properties of energy bands and electron impurity states.[2] Faraday rotation at optical transitions from bound states of donor impurities in semiconductors was considered in Refs. 3 and 4, where it was shown that bound electrons make a strong contribution to the Faraday rotation in weak as well as strong magnetic fields. If the electron and impurity concentrations are commensurate, the contribution of rotation at donor electrons may be comparable with the Faraday rotation at free carriers.

Impurities are manifested in two ways in low-temperature magneto-optical effects. On one hand, they confine the mean free path of conduction electrons and hinder the formation of closed stable electron orbits as well as resonance absorption. This effect is usually taken into consideration by introducing a constant ν, i.e., the electron collision frequency. This is true for the case when electrons undergo only potential scattering at the impurity atoms. At the same time, electron-impurity scattering may contain resonances corresponding to local and quasilocal states,[5] which are accompanied by a sharp increase in the electron density of states at local and quasilocal levels. This leads to the formation of new optical absorption resonances associated with electron transitions between impurity and band states. Virtual bound states of electrons[6] are a special case of impurity states. These correspond to d-resonances in the scattering of electrons by transition metal impurities in a nonmagnetic matrix. The corresponding resonant levels may lie below the Fermi boundary. (Al-Cr, Al-Fe, Al-Cu), as well as above it (Al-V).[7] New optical absorption bands associated with these states have been observed experimentally.[7,8]

The magnetoimpurity states[9,10] formed as a result of the combined action of the attractive potential of impurity atoms and a magnetic field on electrons are a specific case of impurity states of electrons. The impurity perturbation partially removes the degeneracy in the position of the Larmor ''orbit'' center and splits one or several sublevels from each Landau level. This results in the emergence of a large number of optical absorption resonances associated with electron transitions between Landau levels and magnetoimpurity levels.[10,11] Magnetoimpurity states of electrons have been observed experimentally and are responsible for the creation of beats in the de Haas-van Alphen effect in bismuth with Te and Se impurities.[9,12] They also cause new optical absorption resonances in semiconductors Si and Ge with neutral impurity atoms.[11]

In this work, we shall consider the effect of magnetoimpurity states of electrons in metals, semimetals, and degenerate semiconductors on the Faraday effect and circular magnetic dichroism. We use the model of a conductor described in Refs. 9, 10, 13. Among other things, it is assumed that the mean separation between point impurity atoms is larger than the radius of the bound state of an electron, while the electromagnetic field frequency ω is much higher than the electron collision frequency.

It is well known[2,3] that the angle of rotation of the light polarization plane parallel to the z-axis and to the wave vector is determined by the difference in the refractive indices n_- and n_+ for circularly right-and left-polarized waves. In the case of weak absorption, this difference is proportional to the real component of the Hall conductivity σ_{xy}:

$$\theta = \frac{\omega(n_- - n_+)}{2c} = \frac{2\pi \ \mathrm{Re}\ \sigma_{xy}}{nc}, \tag{1}$$

where $n=(n_+ + n_-)(1/2)$ and c is the velocity of light in vacuum. The magnetic circular dichroism is determined by the quantity Δ proportional to the difference in the absorption coefficients $k_\pm$ of circularly polarized waves or to the imaginary component of the Hall conductivity[2]:

$$\Delta = \frac{\omega(k_- - k_+)}{2c} = \frac{2\pi \ \mathrm{Im}\ \sigma_{xy}}{nc}. \tag{2}$$

In the approximation linear in the concentration of impurity atoms, the high-frequency conductivity tensor can be written in the form $\sigma = \sigma_0 + \delta\sigma$, where σ_0 is determined only by potential scattering of conduction electrons by impurity atoms, and $\delta\sigma$ is the contribution from magnetoimpurity states.[10] This gives $\theta = \theta_0 + \delta\theta$, where θ_0 is the known contribution due to rotation at free carriers taking into account potential electron-impurity scattering, while $\delta\theta$ takes into account magnetoimpurity states.

The method of calculation of high-frequency Hall conductivity of metals with magnetoimpurity electron states was described in Refs. 10 and 13. Near the frequencies of resonant transitions of electrons between Landau levels and magnetoimpurity levels, it contains the contribution

$$\delta\sigma_{xy}^{(s)} = i\,\frac{e^2 n_e}{m\omega_s^-}\,\alpha_s^-\left(\frac{\omega_s^-}{\omega_s^- - \omega - i\Gamma}\right)^{1/2}, \tag{3}$$

where

$$\alpha_s^- = 2\,\frac{n_i}{n_e}\,\frac{\Omega}{\omega_s^-}\left(\frac{\omega_0}{\omega_s^-}\right)^{3/2} \times \sum_k \left[f(\varepsilon_k^r - \omega_s^-) - f(\varepsilon_k^r)\right] \times \left[\frac{k-s}{(1+\Omega/\omega_s^-)^2} - \frac{k-s+1}{(1-\Omega/\omega_s^-)^2}\right] \tag{4}$$

is the oscillator force of a resonant transition. Here m and e are the effective mass and charge of the electron, n_e and n_i the number densities of electrons and impurity atoms, $\omega_s^- = s\Omega - \omega_0$ are the resonance frequencies (Ω is the cyclotron frequency and ω_0 the separation between the Landau level and the magnetoimpurity level split from it, $s = 1,2,...$), f is the Fermi function, and ε_k^r and Γ are the position and width of the kth magnetoimpurity level. Summation in formula (4) is carried out over the magnetoimpurity levels participating in transitions at frequency ω_s^-. The difference in the Fermi functions is associated with the Pauli exclusion principle. Here and below, the quantum constant is assumed to be equal to unity.

Taking (3) and (4) into account, we obtain from (1) the contribution of magnetoimpurity states to the Faraday angle:

$$\delta\theta_s^- = \frac{2\pi e^2 n_e}{mcn\omega_s^-}\,\alpha_s^-\ \mathrm{Re}\left(\frac{\omega_s^-}{\omega - \omega_s^- + i\Gamma}\right)^{1/2}. \tag{5}$$

This formula shows that the Faraday angle as a function of ω has asymmetric peaks at resonance frequencies ω_s^-, which are shifted towards high frequencies. In the case of electron transitions from magnetoimpurity levels to above-lying Landau levels, we can write this correction in the vicinity of resonance frequencies $\omega_s^+ = s\Omega + \omega_0$ ($s = 0,1,...$) in the form

$$\delta\theta_s^+ = -\,\frac{2\pi e^2 n_e}{mcn\omega_s^+}\,\alpha_s^+\ \mathrm{Re}\left(\frac{\omega_s^+}{\omega_s^+ - \omega - i\Gamma}\right)^{1/2}, \tag{6}$$

where the oscillator force now has the form[10,13]

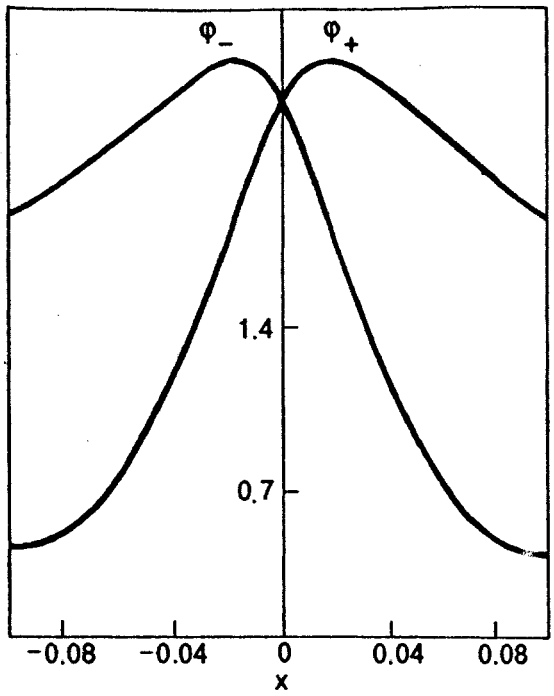

FIG. 1. Frequency dependence (7) of the Faraday angle $\varphi_\pm$ as a function of $x = \omega/\omega_\pm - 1$ near the resonance frequencies $\omega_\pm$.

$$\alpha_s^+ = 2\,\frac{n_i}{n_e}\,\frac{\Omega}{\omega_s^+}\left(\frac{\omega_0}{\omega_s^+}\right)^{3/2} \sum_k \left[f(\varepsilon_k^r) - f(\varepsilon_k^r + \omega_s^+)\right] \times \left[\frac{k+s}{(1-\Omega/\omega_s^+)^2} - \frac{k+s+1}{(1+\Omega/\omega_s^+)^2}\right].$$

Expression (6) leads to the emergence of asymmetric peaks on the frequency dependence of the Faraday angle. The minima lie at frequencies ω_s^+ and are shifted towards low frequencies.

Figure 1 shows the results of calculation of the quantity

$$\varphi_\pm = |\,\delta\theta_\pm|\,\frac{mcn\omega_\pm}{2\pi e^2 n_e \alpha_\pm} \tag{7}$$

as a function of $x = \omega/\omega_\pm - 1$ in the vicinity of resonance frequencies $\omega_\pm = \Omega \pm \omega_0$. We have used the value of the parameter $\gamma_\pm = \Gamma/\omega_\pm = 0.02$ typical of semimetals and degenerate semiconductors with donor impurities in a magnetic field of induction $B = 50$ T. If we substitute into (7) the InSb parameters $m = 3.2\times10^{-32}$ kg, $n_e = 10^{21}$ m^{-3}, $n = 3$, 4, and also $n_i/n_e = 0.002$, $\omega_0/\Omega = 0.04$, the maximum value of the correction to the Faraday angle due to magnetoimpurity levels is $|\delta\theta_\pm^{\max}| = 0.2$. The ratio of this value to the maximum Faraday angle in the absence of magnetoimpurity states is 25%.

The corrections to Δ due to magnetoimpurity states of electrons is found to be negative. It leads to asymmetric minima on the frequency dependence of Δ. The minimum at ω_s^- is displaced towards low frequencies and that at ω_s^+ towards high frequencies. For the above values of parameters, this correction is equal to 0.2.

The authors are grateful to V. K. Miloslavskii for fruitful discussions of the results.

[1] L. D. Landau and E. M. Lifshitz, *Electrodynamics of Continuous Media* [in Russian], Nauka, Moscow (1992).
[2] F. F. Sizov and Yu. I. Ukhanov, *Magnetooptical Faraday and Fogt Effects in Semiconductors* [in Russian], Naukova Dumka, Kiev (1979).
[3] I. M. Boswarva, R. E. Howard, and A. B. Lidiard, Proc. R. Soc. London **A269**, 125 (1962).
[4] E. Haga, J. Phys. Soc. Jpn. **20**, 735 (1965).
[5] I. M. Lifshits, S. A. Gredeskul, and L. A. Pastur, *Introduction to the Theory of Disordered Systems*, Wiley, New York (1988).
[6] *Theory of Ferromagnetism of Metals and Alloys* [in Russian] (ed. by S. V. Vonsovskii), Izd. Inostr. Lit., Moscow (1963).
[7] P. Ziesche and G. Lehmann, (Eds.) *Ergelnisse in dev Electronea Theorie der Metalle*, Akademie-Verlag, Berlin (1983).
[8] M. M. Noskov, *Optical and Magnetooptical Properties of Metals* [in Russian], Sverdlovsk (1983).
[9] A. M. Ermolaev and M. I. Kaganov, Pis'ma Zh. Éksp. Teor. Fiz. **6**, 984 (1967) [JETP Lett. **6**, 395 (1967)].
[10] E. A. Kaner and A. M. Ermolaev, Zh. Éksp. Teor. Fiz. **92**, 2245 (1987) [Sov. Phys. JETP **65**, 1266 (1987)].
[11] S. P. Andreev, Usp. Phys. Nauk **143**, 213 (1984) [Sov. Phys. Usp. **27**, 431 (1984)].
[12] N. B. Brandt and L. G. Lyubutina, Zh. Eksp. Teor. Phys. **52**, 686 (1967) [Sov. Phys. JETP **25**, 450 (1967)].
[13] N. V. Gleizer, A. M. Ermolaev, and G. I. Rashba, Fiz. Nizk. Temp **20**, 1169 (1994) [Low Temp. Phys. **20**, 919 (1994)].

Translated by R. S. Wadhwa

Vibrational modes of a terminated atomic chain

E. Ya. Glushko and V. A. Khrisanov

*State Pedagogical Institute, 324086 Krivoi Rog, Ukraine**
(Submitted April 21, 1997; revised June 28, 1997)
Fiz. Nizk. Temp. **23**, 1215–1222 (November 1997)

A complex terminated molecular chain adsorbed at the surface is analyzed without taking into account periodic boundary conditions and translational invariance approximation. The solution of the motion equation is a standing wave. The dispersion equation for band modes is obtained and conditions for the existence of localized states are investigated. The constructed parametric diagrams make it possible to evaluate vibrational bands and local modes (if they exist) for $(SN)_x$ and C-C samples. It is proposed that excitations of local and band modes of adsorbed molecules can be used for low temperature laser cleaning of the surface and for molecular engineering purposes. © *1997 American Institute of Physics.* [S1063-777X(97)01011-6]

INTRODUCTION

The problem of small vibrations of a linear atomic chain is traditionally affiliated to exactly solvable problems forming the basis of the dynamic theory of crystal lattices.[1–3] Periodic boundary conditions (PBC) used in this approximation as well as the assumption concerning the independence of the vibrational phase of the unit cell number[4,5] make it possible to obtain an analytic solution for dispersion of band mode frequencies for simple chains. A transition to the description of real (including terminated) systems is made by taking into account more accurately the interaction between atoms, its quantum-mechanical nature in the PBC approximation, and the condition of translational invariance (TI) of the solution.[6] The arguments in favor of the PBC approximation put forth starting from Born and *Karman* are based on the independence of bulk properties (electron and phonon spectra) of the state of the boundary for one- or three-dimensional crystals of large size, which is well known from experiments (see, for example, Ref. 5). A theoretical proof of the smallness of the density perturbation for normal vibrations, which is introduced by cyclic boundary conditions in the case of bulk crystals was obtained by Ledermann.[7] Lifshits and Rozentsveig[8] carried out a more complete analysis of the effect of free surface on the vibrational states of a semi-infinite crystal by using the method of regular perturbations. More general relations were obtained for local states split from continuous bands. However, PBC become inapplicable (even for band states) in the case of small or mesoscopic crystals in view of the fact that the effect of boundaries on the bulk states cannot be eliminated in principle in such systems. The grounds for application of the PBC method in an analysis of local states (their frequencies, conditions of splitting from bands, and amplitude distribution) are still less solid. Local states can be obtained approximately for a semi-terminated chain by introducing a complex wave number whose imaginary component is responsible a decrease in the amplitude of a local vibrational mode with increasing distance from the boundary.[4,9] On the other hand, an accurate analysis involves the solution of a finite system of coupled dynamic equations, in which the equations of motion for boundary atoms differ from those for other atoms in view of a special position of these atoms. In such an approach, the phases of atomic displacements are determined by matching conditions and ''perceive'' the remoteness of their ''host'' from the lattice boundary.

The mechanism of the influence of boundaries on the electron spectrum of a periodic system was clarified in Ref. 10: the eigenstates in an infinitely large system have the form of standing waves due to the inevitable presence of the reflected wave (see also Ref. 11) and do not possess translational invariance. The same effect can be expected for the problem on vibrational modes in a terminated chain, which can be essentially treated as a single large molecule. The distribution of mode amplitudes in such a system is essential for understanding of thermodynamic and optical properties, as well as adsorption and desorption conditions. Finite atomic and molecular chains play an important role in modern microelectronics as an element of ultrasmall semiconducting devices[12]: bridges, switches, elements of optical memory, etc. Electronic, phonon, and optical properties of linear chains and superstructures are being intensely studied both experimentally[13] and theoretically.[14,15] Among scarce publications which are not confined to the PBC and TI approximations, we can mention the paper by Syrkin and Feodos'ev,[16] in which exact analytic expressions for integral characteristics (heat capacity, spectral shift function, and spectral density) of a monatomic linear chain are considered by using the Peresada method of Jacobi matrices.

In the present paper, the exact solution of the classical problem on vibrational modes in a complex harmonic chain containing an arbitrary number N of unit cells is obtained without using the TI and PBC approximations. It is shown that for $N \gg 1$, the positions of the edges of the acoustic and optical bands of states virtually coincide with the results obtained in the TI and PBC approximations, but local vibrational states and mode amplitude distribution in the chain

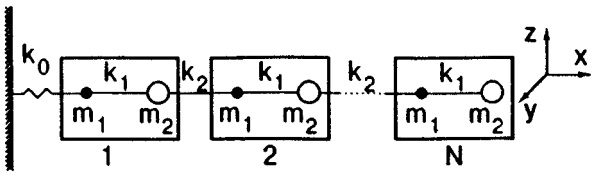

FIG. 1. Schematic diagram of a model chain.

differ radically. The mode amplitude distribution in band states resembles the pattern of standing waves in a cavity with absorbing walls. In the case of a diatomic chain, the dispersion equations are obtained for band and local states, and the phase diagrams as well as conditions of local mode splitting are analyzed for various ratios of elastic constants and atomic masses. The parameters of the $(SN)_x$ and C-C chains are evaluated. The possibility of selective effect on individual regions of linear molecules in the low-temperature experiments are considered.

DESCRIPTION OF THE MODEL

Let us consider a linear diatomic chain containing N identical cells. The atomic masses in each cell will be denoted by m_1 and m_2. The longitudinal interaction between the atoms of a cell is described by a force constant k_1, while the interaction between cells is described by the force constant k_2. We assume that there is a surface with which the first atom of the chain is linked, while the last atom remains free (Fig. 1). The coupling of the chain with the surface changes the force constants near the first atom. Assuming that interaction takes place only between nearest neighbors, we can consider that only the constant of coupling of the chain with the surface (denoted by k_0) will be modified. The transverse degrees of freedom of the linear chain are described by other sets of force constants (k_0',k_1',k_2') and (k_0'',k_1'',k_2''). In the case of small vibrations, the problem is solved independently for each vibrational branch in view of separatibility of the interaction potential. The resultant spectrum is obtained as a result of combination of three solutions obtained in a similar way.

EXACT SOLUTION OF THE PROBLEM OF SMALL VIBRATIONS OF A TERMINATED LINEAR CHAIN

Let us consider longitudinal vibrations of the adsorbed model chain shown in Fig. 1. We write the system of classical equations of motion in the harmonic approximation:

$$m_\alpha \ddot{x}_\alpha = k_\alpha x_{\alpha-1} - (k_\alpha + k_{\alpha+1}) x_\alpha + k_{\alpha+1} x_{\alpha+1},$$
$$\alpha = 1,...,2N, \tag{1}$$

where x_α is the displacement of the αth atom from its equilibrium position under the following conditions:

$$x_0 = 0 \quad k_{2N+1} = 0, \tag{2}$$

which indicate that the surface is stationary and the last atom is free. We shall seek the solution of system (1) in the form

$$x_\alpha = x_{0\alpha} e^{i\omega t}, \tag{3}$$

where $x_{0\alpha}$ is the amplitude of vibrations of the αth atom. Note that x_α does not possess translational invariance in view of the finite size of the linear crystal.

The condition for the existence of a nonzero solution of system (1) is the equality of its determinant to zero. Taking into account (3), we obtain

$$\begin{vmatrix} b_2^* & b_3 & 0 & 0 & \cdots & & & & \\ a_1 & a_2 & a_3 & 0 & \cdots & & & & \\ 0 & b_1 & b_2 & b_3 & \cdots & & & & \\ \cdots & \cdots & \cdots & \cdots & \cdots & \cdots & \cdots & \cdots & \cdots \\ & & & & \cdots & a_1 & a_2 & a_3 & 0 \\ & & & & \cdots & 0 & b_1 & b_2 & b_3 \\ & & & & \cdots & 0 & 0 & a_1 & a_2^* \end{vmatrix} = 0. \tag{4}$$

The order of determinant (4) is $2N$. The left-hand side of (4) can be represented as the product of matrices

$$(D, -D')\hat{\Lambda}^n \begin{pmatrix} A_1 \\ B_1 \end{pmatrix} = 0, \quad n = N-2 \tag{5}$$

with the matrix elements

$$D = \begin{vmatrix} b_2^* & b_3 \\ a_1 & a_2 \end{vmatrix}, \quad D' = \begin{vmatrix} b_2^* & 0 \\ a_1 & a_3 \end{vmatrix},$$
$$A_1 = \begin{vmatrix} b_2 & b_3 \\ a_1 & a_2^* \end{vmatrix}, \quad B_1 = \begin{vmatrix} b_1 & b_3 \\ 0 & a_2^* \end{vmatrix},$$
$$C = \begin{vmatrix} b_2 & b_3 \\ a_1 & a_2 \end{vmatrix}, \quad C' = \begin{vmatrix} b_2 & 0 \\ a_1 & a_3 \end{vmatrix},$$
$$Q = \begin{vmatrix} b_1 & b_3 \\ 0 & a_2 \end{vmatrix}, \quad R = \begin{vmatrix} b_1 & 0 \\ 0 & a_3 \end{vmatrix},$$
$$\hat{\Lambda} = \begin{pmatrix} C & -C' \\ Q & -R \end{pmatrix}, \tag{6}$$

and

$$a_2^* = \omega_{12}^2 - \omega^2; \quad b_2^* = \omega_0^2 + \omega_{11}^2 - \omega^2;$$
$$a_1 = -\omega_{12}^2; \quad a_2 = \omega_{12}^2 + \omega_{22}^2 - \omega^2; \quad a_3 = -\omega_{22}^2;$$
$$b_1 = -\omega_{21}^2; \quad b_2 = \omega_{11}^2 + \omega_{21}^2 - \omega^2; \quad b_3 = -\omega_{11}^2,$$

where $\omega_{ij}^2 = k_i/m_j$, $i,j = 1,2$; $\omega_0^2 = k_0/m_1$.

Equation (5) has an exact solution if we represent the matrix $\hat{\Lambda}$ in the form of the sum of two matrices $\hat{X}_1$ and $\hat{X}_2$ which possess the properties of orthogonality

$$\hat{X}_1 \cdot \hat{X}_2 = \hat{0} \tag{7}$$

and reproducibility

$$\hat{X}_i^2 = \alpha_i \hat{X}_i, \quad i = 1,2. \tag{8}$$

It can easily be verified that the matrices

$$\hat{X}_1 = \begin{pmatrix} 1 & x \\ y & xy \end{pmatrix}, \quad \hat{X}_2 = \begin{pmatrix} 1 & z \\ -1/x & -z/x \end{pmatrix} \tag{9}$$

satisfy conditions (7) and (8). In this case, the transfer matrix can be written in the form

$$\hat{\Lambda}=h(\hat{X}_1+\hat{X}_2), \tag{10}$$

where $h=C/2$, and the coefficients α_i in (8) are defined as

$$\alpha_1=1+xy, \quad \alpha_2=1-z/x. \tag{11}$$

Taking (10) into account, we obtain the following formula for the nth-order matrix $\hat{\Lambda}$:

$$\hat{\Lambda}^n=h^n\left(\alpha_1^{n-1}\hat{X}_1+\frac{\alpha_1^{n-1}-\alpha_2^{n-1}}{\alpha_1-\alpha_2}\hat{X}_1\hat{X}_2+\alpha_2^{n-1}\hat{X}_2\right). \tag{12}$$

A slightly different approach for deriving (12) is described in Ref. 20. The components of the matrices $\hat{X}_1$ and $\hat{X}_2$ can be determined by comparing Eqs. (6), (9), and (10):

$$\begin{cases} x=-\dfrac{C+R}{2Q}+\left[\left(\dfrac{C+R}{2Q}\right)^2-\dfrac{C'}{Q}\right]^{1/2} \\ y=-\dfrac{C+R}{2C'}+\left[\left(\dfrac{C+R}{2C'}\right)^2-\dfrac{Q}{C'}\right]^{1/2}+2\dfrac{Q}{C} \\ z=\dfrac{C+R}{2Q}+\left[\left(\dfrac{C+R}{2Q}\right)^2-\dfrac{C'}{Q}\right]^{1/2}-2\dfrac{C'}{C} \end{cases}.$$

After summing up the matrices in the parentheses on the right-hand side of (12), we obtain

$$\hat{\Lambda}^n=\frac{h^{n-1}}{\alpha_1-\alpha_2}\hat{V}. \tag{13}$$

Here $\hat{V}$ is a matrix with the components v_{ij}:

$$v_{11}=-L_1\alpha_1^n+L_2\alpha_2^n, \quad v_{12}=-C'(\alpha_1^n-\alpha_2^n),$$
$$v_{21}=Q(\alpha_1^n-\alpha_2^n), \quad v_{22}=L_2\alpha_1^n-L_1\alpha_2^n, \tag{14}$$

where

$$L_1=C'/x, \quad L_2=Qx,$$
$$\alpha_1=(C+L_2)/h, \quad \alpha_2=(C+L_1)/h. \tag{15}$$

Taking into account (14) and (15), we can write the general dispersion equation (5) in the form

$$\frac{1}{x(L_2-L_1)}[(C+L_2)^n(A_1+B_1x)(DC'+D'L_2) - (C+L_1)^n(D'+Dx)(C'B_1+A_1L_2)]=0. \tag{16}$$

The quantities $C+L_1$ and $C+L_2$ are conjugate, which follows from (15) and (13):

$$C+L_2=\beta+\xi\sqrt{g}, \quad C+L_1=\beta-\xi\sqrt{g}, \tag{17}$$

where $\beta=(C-R)/2$, $\xi=\operatorname{sgn} Q$, $g=(C+R)^2/4-C'Q$. Noting that $x(L_2-L_1)\neq 0$ and taking (17) into account, we obtained from (16) the generalized dispersion equation for vibrational modes of a linear chain:

$$(\beta+\xi\sqrt{g})^n(A_1L_1+B_1C')(DC'+D'L_2) - (\beta-\xi\sqrt{g})^n(D'L_1+DC')(C'B_1+A_1L_2)=0. \tag{18}$$

Equation (18) has a structure coinciding with the structure of dispersion equations for electronic states in a terminated periodic system of potential wells as well as for electromagnetic oscillatory modes of a terminated structure of alternating layers with different permittivities.[10] The type of solutions of Eq. (18) is determined by the sign of the function g. Delocalized states distributed over a chain are compactly located in frequency intervals where $g<0$. In our case, these intervals correspond to acoustic and optical modes. Positive values of g correspond to frequency regions in which only local states can exist.

For frequencies belonging to the acoustic or optical band, the expressions $\beta+\xi\sqrt{g}$ and $\beta-\xi\sqrt{g}$ are complex conjugate:

$$\beta\pm\xi\sqrt{g}=e^{\pm i\phi}. \tag{19}$$

Since x also becomes a complex quantity, we have

$$x=|x|e^{i\varphi}, \tag{20}$$

where $|x|=\sqrt{C'/Q}$, $\cos\varphi=-\xi(C+R)/\sqrt{4C'Q}$, $0<\varphi<\pi$. Substituting (19) and (20) into the generalized dispersion equation (18), we obtain the dispersion equation for band vibrational modes:

$$\sin(n\phi+\psi)=0, \tag{21}$$

where

$$\psi=\arccos(p_1/\sqrt{p_1^2+p_2^2}), 0<\psi<\pi,$$
$$\phi=\arccos\beta, \quad 0<\phi<\pi,$$
$$p_1=\frac{A_1D'}{|x|}+B_1D|x|+(B_1D'+A_1D)\cos\varphi,$$
$$p_2=(B_1D'-A_1D)\sin\varphi.$$

It follows from (21) that for $N\gg 1$ the chain ends affect the mode spectrum of band states weakly since the additional phase $\psi\in[0,\pi]$. For sufficiently long chains, the exact result (21) coincides with that obtained by using the TI and PBC approaches,[4] the only difference being that the number of band modes is reduced by the number of split local modes. Figure 2 shows the band relief calculated by formula (21) for $k_0=k_2$. It can be seen that the acoustic and optical bands merge for $m_1/m_2=k_1/k_2=1$. As the inequivalence of atoms becomes stronger, the forbidden gap is broadened, and the optical vibration band becomes narrower. In the frequency range where $g>0$, Eq. (18) describes the boundary local states split from the bands to the forbidden gap. In the case of a long chain ($N\gg 1$), the dispersion equation (18) for local states is simplified. The frequencies of local modes are determined by zeros of the first term in (18) for $\xi\beta>0$ and by zeros of the second term for $\xi\beta<0$.

LOCAL MODES AND AMPLITUDE DISTRIBUTION

The general dispersion equation (18) allows us to formulate the condition of splitting of local states from band edges for long chains. The requirement $g=0$ gives

$$A_1D-B_1D'=0. \tag{22}$$

Analyzing this equation, we find that a local state splits from the top of the optical band for the following relation between model parameters:

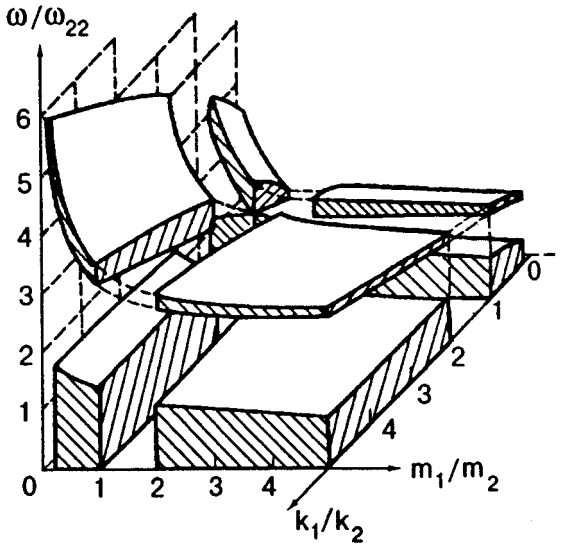

FIG. 2. Band relief of a diatomic chain for $k_0=k_2$ as a function of relative parameters of the model. Band states are hatched, local states are not shown ($\omega_{22}^2=k_2/m_2$).

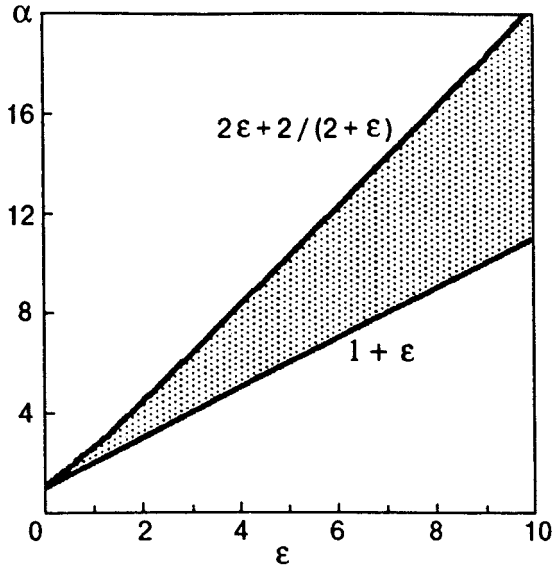

FIG. 3. Region of existence of local states above the optical band for various ratios of the parameters $\varepsilon=m_1/m_2$ and $\alpha=k_0/k_2$.

$$2\zeta(1+\varepsilon-\alpha)+\alpha=0. \tag{23}$$

The condition for the splitting of local states from the bottom of the optical band and from the top of the acoustic band has the form

$$\zeta(1+\varepsilon-\alpha)(1\pm\sigma)+3\alpha-8=0, \tag{24}$$

where the plus sign corresponds to splitting from the bottom of the optical band and the minus sign from the top of the acoustic band. Here

$$\zeta=\frac{(\varepsilon+1)(\gamma+1)}{\varepsilon\gamma}, \quad \sigma=\left(1-\frac{16}{\varepsilon\gamma\zeta^2}\right)^{1/2},$$

$$\varepsilon=\frac{m_1}{m_2}, \quad \gamma=\frac{k_1}{k_2}, \quad \alpha=\frac{k_0}{k_2}.$$

Relations (23) and (24) allow us to determine the regions of existence of local states on the diagrams of model parameters. Obviously, for chains with any parameters ε and γ, we can always find a value of α for which a local superoptical state is formed. On the (γ,α) plane, the region of localization lies above the straight line $\alpha=1$. The region of splitting of local states from the top of the optical band on the diagram of parameters (ε,α) lies between the straight lines $\alpha=1+\varepsilon$ and $\alpha=2\varepsilon+2/(\varepsilon+2)$ (Fig. 3).

Let us consider various cases of coupling between an atomic chain and the surface.

1. If a heavy atom ($m_1/m_2>1$) is coupled with the surface, the forbidden band contains a level which does not depend on the coupling with the surface. Its position is determined by the ratio k_1/k_2. For $k_1/k_2>1$, the level lies near the bottom of the optical band the closer to it, the larger the ratio k_1/k_2. For $k_1/k_2<1$, the level occupies a position near the acoustic band in a similar manner. For $k_1=k_2$, the level is localized at the middle of the forbidden gap. Moreover, as the rigidity of the coupling between the chain and the surface increases, a level splits from the acoustic band approaches the optical band upon an increase in k_0. The ratio k_1/k_2 determines the form of this approach: the level approaches the bottom of the optical band asymptotically for $k_1/k_1>1$ (Fig. 4a), while for $k_1/k_2<1$ the local state rapidly reaches the optical band and vanishes (Fig. 4b). In both cases, an increase in the rigidity of coupling between the chain and the surface leads to the splitting of a local state in the band above the optical band of the spectrum. The superoptical mode is formed rapidly as the local state moves away from the band edge in a narrow region near the free end of the chain. For certain values of the parameters m_1/m_2 and k_1/k_2, the region of localization of vibrations with a superoptical frequency can be shifted from one end of the linear chain to the other upon an increase in the coupling rigidity k_0 and can even be distributed over both ends of the chain. Such a phenomenon is observed, for example, for $m_1=m_2$ and $k_1=k_2$, when the ratio k_0/k_2 increases from 2 to 5. For $k_1/k_2>1$, a rigidly adsorbed chain has three local modes, while such a number of local modes can be observed for $k_1/k_2<1$ only in a very narrow band of values of k_0.

2. If a light atom is coupled with the surface, the forbidden gap can contain, in accordance with (24), not more than one local state (Fig. 5). For $k_1/k_2>1$ and a rigid coupling k_0, a local level lies near the acoustic band the closer to it, the closer the ratio k_1/k_2 of coupling constants to unity. Another local level is observed above the optical band. A chain weakly coupled with the surface has only one local state in the forbidden band, which moves away from the optical band as the coupling with the surface becomes weaker and weaker (Fig. 5a). For $k_1=k_2$, no local state is split from the acoustic band, and when the coupling constant k_1 and k_2 are such that $k_1/k_2<1$, the diagram contains only the upper local branch whose slope is smaller than in the case when $k_1/k_2>1$ (Fig. 5b). Thus, in the case of a rigid coupling of a chain with a surface through any of the two atoms. i.e., for any ratio m_1/m_2, the frequency spectrum contains a strongly localized superoptical vibrational mode.

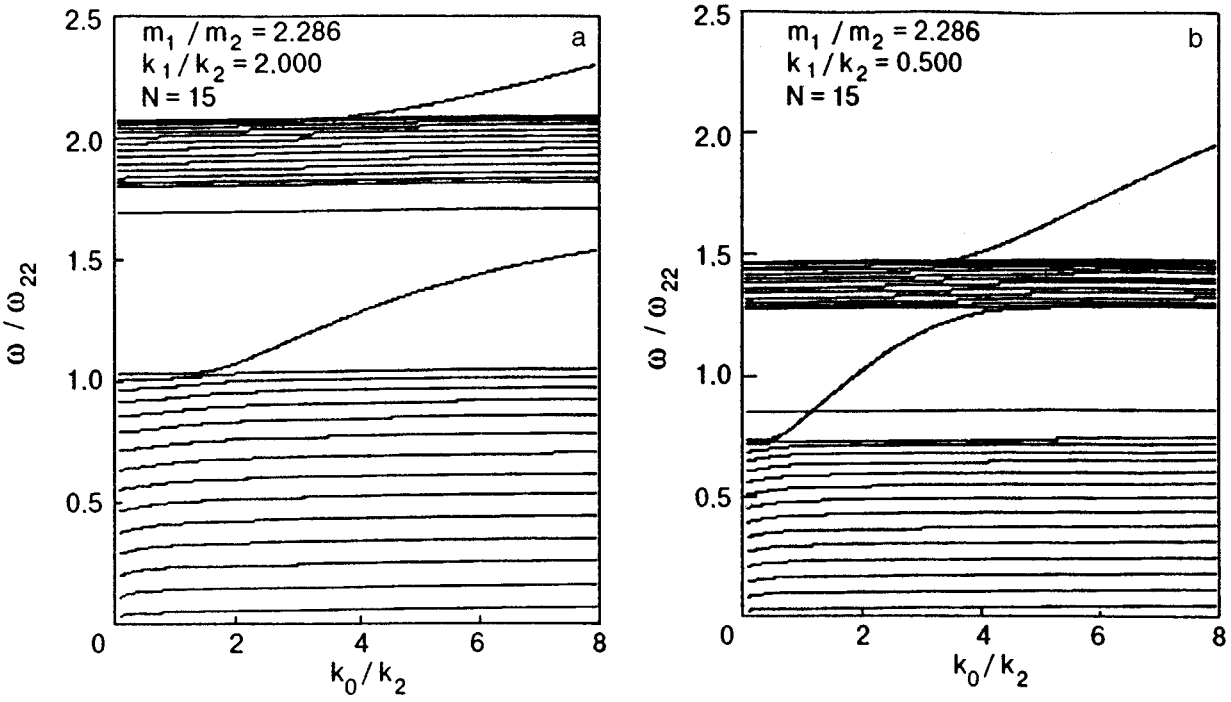

FIG. 4. Diagram of local states for a coupling with the surface through a heavy atom: strong (a) and weak (b) coupling of the atom with the chain.

Irrespective of the rigidity of coupling of a chain with a surface, the frequency spectra for chains coupled with the surface through a heavy atom always contains at least one local vibration, while the spectra of chains coupled through a light atom are characterized by a range of values of the coupling constant k_0, in which not a single local state is formed. For example, for $m_1/m_2=0.5$ and $k_1/k_2=0.9$, no local states are formed for values of the ratio k_0/k_2 from the range from 1.0 and 1.5. Irrespective of the type of the atom linking a chain with the surface, all the local vibrations depicted in Figs. 4 and 5 are formed at the right (free) end of the chain.

The second part of the problem on vibrations of a terminated chain for the amplitudes $x_{0\alpha}$ of vibrational modes also has an exact solution. The substitution of mode frequencies into (1) leads to a nonhomogeneous system of $2N-1$ linear equations which can be solved by the Kramer method. The

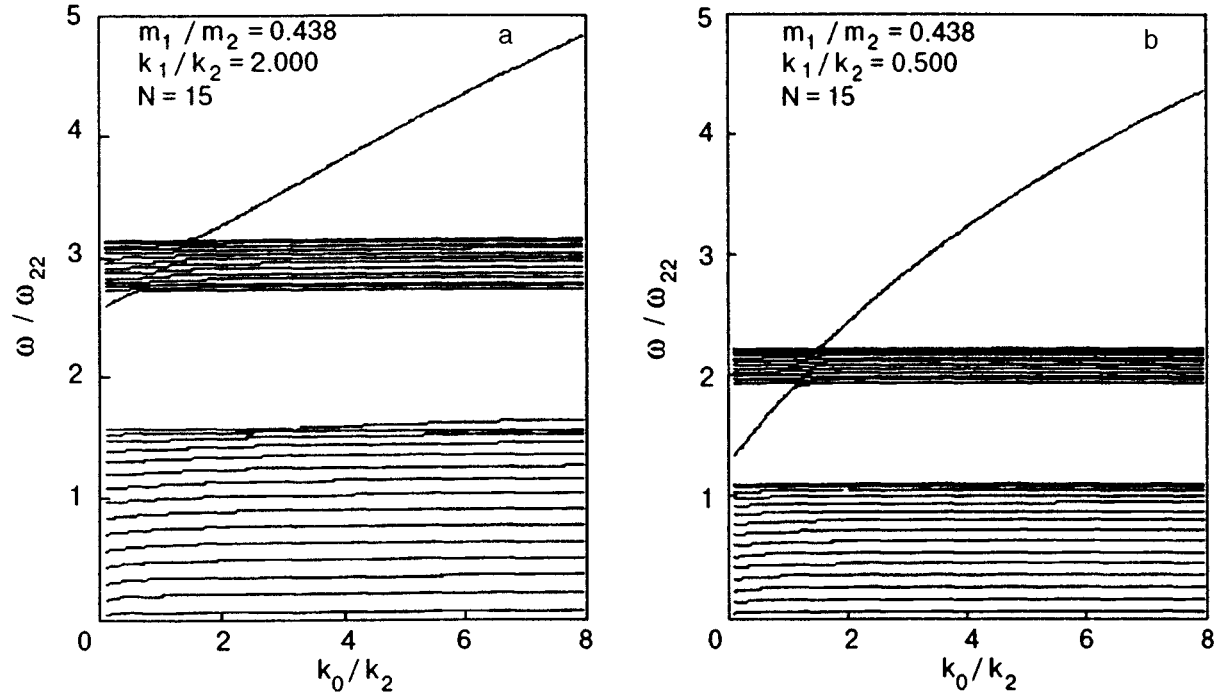

FIG. 5. Diagram of local states for a coupling with the surface through a light atom: strong (a) and weak (b) coupling of the atom with the chain.

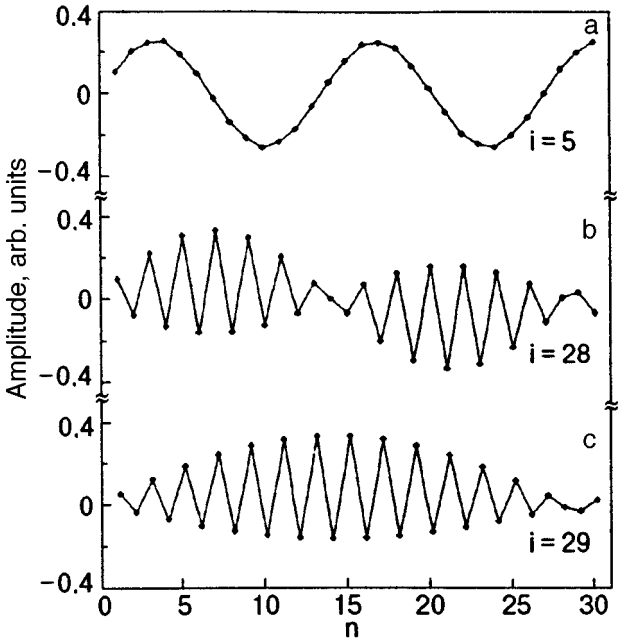

FIG. 6. Distribution of mode amplitudes in arbitrary units over a chain of 30 atoms. The atoms are marked by dots and connected by straight lines for better visualization: fifth mode from the bottom of the acoustic band (a) and modes near the top of the optical band (b) and (c).

convolution of the determinants appearing in this case is carried out according to the above procedure (7)–(13) (see also Ref. 10). Analytic expressions for $x_{0\alpha}$ are found to be real-valued both for band and for local modes.

The distribution of mode amplitudes of band states in a linear chain is shown in Fig. 6. The chain contains 30 atoms. The state with the number $i=5$ corresponds to the fifth level lying in the acoustic band, while the state with the number $i=29$ corresponds to the boundary of the optical band. The complete frequency spectrum also includes a local vibration with a frequency lying above the optical band. The chain is coupled with the surface through a light atom. The results of calculations definitely confirm the fact that band vibrational modes in terminated oscillatory systems do not possess translational invariance, and the amplitude $x_{0\alpha}$ in (3) depends strongly on the position of an atom in the chain. The splitting of a local mode at one end of the chain is accompanied by a suppression of amplitudes of the nearest band modes in this region (Fig. 6c). Analytic expressions for the amplitudes of local vibrations indicate their exponential decrease from the edge.

CONCLUSION

This research determines the limits of applicability of the constant-phase and PBC approximations which are traditionally used in vibrational problems.[1–9,21] The obtained analytic results indicate an extremely weak dependence of delocalized mode frequencies of periodic structures with $N \gg 1$ on the choice of the boundary conditions as well as on the type of TI assumptions concerning the phase of vibrations. If we are speaking of local modes, these approximations at least distort their frequency. Exact distributions of mode amplitudes of all types differ in principle from those obtained in the constant-phase approximation: they have the form of standing waves in a periodic structure with semipermeable walls. In this case, the well-known oscillatory theorem on the relation between the number of nodes in the amplitude distribution function in a mode and the serial number of this mode holds well.

The information about the position of a local vibrational mode of an adsorbed chain of atoms can be important for practical purposes of laser cleaning of surfaces under controlled low-temperature desorption.[17] In the course of fine cleaning, optical radiation is spent on ''heating'' of the surface local mode only right to the rupture of the bond and following desorption. On the other hand, the emergence of desorbed molecules at a certain laser frequency in low-temperature experiments makes it possible to determine the elastic constant of coupling between a linear molecule and a surface from parametric diagrams (see Figs. 4 and 5).

Selective excitation of band modes of an adsorbed chain at low temperatures makes it possible to preserve a definite sequence of antinodes and nodes in its linear structure for subsequent restriction or another action on the system.

We obtained approximate estimates of frequencies and amplitudes of vibrations for an $(SN)_x$ crystal whose structure is formed by weakly interacting chains. We considered an individual chain as a one-dimensional lattice with two atoms in a unit cell with the same coupling constants ($k_1=k_2$). Proceeding from the energy of dissociation of the S-N bond[19] and assuming that the ratio of the energy of a vibrational quantum of S-N to the energy of dissociation of the S-N bond is the same as for C-H,[17] we find that the S-N coupling constant $k=1.43$ mdyne/Å. In this case, the optical spectrum lies in the band $(1-1.3)\cdot 10^{14}$ s^{-1}, while the acoustic spectrum occupies the frequency range $(0.3-7.4)\cdot 10^{13}$ s^{-1}. The vibrational amplitudes of upper modes in the acoustic and optical bands are 0.10 and 0.13 Å, respectively, for the average length of the S-N bond of 1.61 Å.[18]

For a C=C=C chain, the acoustic band width is estimated as $1.3\cdot 10^{14}$ s^{-1}, which gives approximately 3.3 mdyne/Å for the elastic coupling constant.

*E-mail: eyagl@kpi.dp.ua

[1] M. Born and Huang Kun, *Dynamic Theory of Crystal Lattices*, Oxford (1954).
[2] A. M. Kosevich, *Fundamentals of Crystal Lattice Dynamics* [in Russian], Nauka, Moscow (1972).
[3] J. Reissland, *The Physics of Phonons*, Benjamin/Cummings, London (1973).
[4] R. L. Bjork, Phys. Rev. **105**, 456 (1957).
[5] A. I. Anselm, *Introduction to the Theory of Semiconductors* [in Russian], Nauka, Moscow (1971).
[6] A. I. Kitaigorodskii, *Molecular Crystals* [in Russian], Nauka, Moscow (1971).
[7] W. Ledermann, Proc. Roy. Soc. **182**, 362 (1944).
[8] I. M. Lifshits and L. N. Rozentsveig, Zh. Éksp. Teor. Fiz. **18**, 1012 (1948); L. N. Rozentsveig, in *Proceedings of Phys. Dept. of Phys. Math. Faculty*, Kharkov State Univ. [in Russian], vol. **2, p.** 19 (1950).
[9] F. G. Bass, V. L. Fal'ko, and S. I. Khankina, Ukr. Fiz. Zh. **38**, 901 (1993).
[10] E. Ya. Glushko, Fiz. Tverd. Tela (St. Peterburg) **38**, 2051 (1996) [Solid State Phys. **38**, 1132 (1996)]; Opt. Spektr. **82**, 331 (1997); [Opt. Spectrosc. **82**, 304 (1997)].
[11] E. Ya. Glushko and V. N. Evteev, Ukr. Fiz. Zh. **40**, 719 (1995).

[12] *Proceedings of the IInd NATO Conf.* ''Quantum Dot Materials for Nonlinear Optics Applications''. Bressanone, Italy (1996).
[13] R. M. Friend, Physica Scr. **66**, 9 (1996).
[14] O. A. Zhikol and V. O. Cheranovskii, Fz. Nizk. Temp. **22**, 793 (1996) [Low Temp. Phys. **22**, 787 (1996)].
[15] Q. V. Usatenko, Fiz. Tverd. Tela (Leningrad) **33**,1665 (1991) [Sov. Phys. Solid State **33**, 937 (1991)].
[16] E. S. Syrkin and S. B. Feodos'ev, Fiz. Nikz. Temp. **20**,586 (1994) [Low Temp. Phys. **20**, 463 (1994)].
[17] A. Zewail, Phys. Today, November issue , 27 (1980).
[18] M. Pope and E. Swenberg, *Electronic Processes in Organic Crystals*, Oxford Univ. Press, Oxford (USA) (1982).
[19] V. V. Nekrasov, *Fundamentals of General Chemistry* [in Russian], Khimiya, Moscow (1963).
[20] V. V. Ul'yanov, *Problems in Quantum Mechanics and Quantum Statistics* [in Russian], Vishcha Shkola, Kharkov (1980).
[21] L. I. Mandelshtam, *Lectures on Oscillations* [in Russian], Izd. Akad. Nauk SSSR, Moscow (1955).

Translated by R. S. Wadhwa

Magnetoplasma waves in inversion layers with local electron states

N. V. Gleizer, A. M. Ermolaev, and Babak Haghighi

Kharkov State University, 310077 Kharkov, Ukraine
(Submitted April 15, 1997)
Fiz. Nizk. Temp. **23**, 1223–1228 (November 1997)

The spectrum and damping factor of plasma and magnetoplasma waves in a two-dimensional electron gas at low temperatures are calculated, taking into account local electron states at impurity atoms. It is shown that localization of electrons decreases the frequency of long-wave plasmons and rearranges the magnetoplasma spectrum in the vicinity of resonant frequencies of electron transitions between the Landau levels and local levels. As a result, the plasma absorption peak is displaced towards low frequencies, and the magnetoplasma peak splits. The characteristics of plasmons and magnetoplasmons are calculated for parameters of the inversion layer at the boundary between silicon and silicon dioxide. © *1997 American Institute of Physics.* [S1063-777X(97)01111-0]

1. INTRODUCTION

Two-dimensional plasmons in the inversion layer at the boundary between silicon and silicon dioxide at low temperatures were observed for the first time by Allen *et al.*[1] who excited plasma waves by linearly polarized infrared radiation incident on the grating deposited on the surface of a semitransparent shutter.[1,2] Since the wavelength of the radiation is much larger than the thickness of the inversion layer, the latter can be treated as a conducting plane $z=0$ with a two-dimensional conductivity tensor. The calculations[2] made in the approximation of an infinitely large conductivity of the shutter without taking into account delay effects proved that the plasmon frequency can be written in the form

$$\omega_p(q)=\left\{\frac{4\pi e^2 n q}{m}\left[\varepsilon_s \coth(qd_s)+\varepsilon_d \coth(qd_d)\right]^{-1}\right\}^{1/2}, \tag{1}$$

where m and e are the electron mass and charge, n is the electron number density in the inversion layer, ε_s and ε_d are the static permittivities of the semiconductor and the insulator, d_s and d_d their thicknesses, and $\mathbf{q}$ is the two-dimensional wave vector. Collisionless damping of long-wave plasmons in a two-dimensional degenerate electron gas is not observed. Their damping is mainly determined by collision of electrons with impurity atoms. The damping of such plasmons is mainly determined by collisions of electrons with impurity atoms. The damping factor is equal to $\nu/2$, where ν is the collision frequency determined by the potential electron-impurity scattering. The absorption of the electromagnetic radiation by the inversion layer is determined by the real component of the quantity $\overline{\sigma}(q,\omega)=\sigma(q,\omega)/\varepsilon(q,\omega)$, where σ and ε are the conductivity and permittivity of the two-dimensional electron gas, which are functions of the wave vector $\mathbf{q}$ and frequency ω.[2] In the vicinity of frequency (1), we have

$$\mathrm{Re}\ \overline{\sigma}(q,\omega)=\frac{e^2 n \gamma_q}{2m}\left[(\omega-\omega_q)^2+\gamma_q^2\right]^{-1}. \tag{2}$$

where ω_q is the spectrum of plasmons (1) and γ_q is the damping factor. This expression shows that plasma waves are manifested in the presence of a clear peak on the curve describing the frequency dependence of absorption, which is superimposed on the high-frequency Drude background[2]

$$\mathrm{Re}\ \overline{\sigma}=e^2 n \nu/(m\omega^2).$$

In a magnetic field perpendicular to the inversion layer, plasma resonance is transformed into magnetoplasma resonance. Such a resonance was observed for the first time by Theis *et al.*[3] and is manifested in the presence of a peak on the dependence of absorption P on the magnetic field strength or radiation frequency. The peak lies at the magnetoplasmon frequency[2]

$$\omega_q^{(0)}=\left[\omega_c^2+\omega_p^2(q)\right]^{1/2}, \tag{3}$$

where ω_c is the cyclotron frequency of electrons. The peak width is given by

$$\gamma_q^{(0)}=\frac{\nu}{2}\left(1+\omega_c^2/\omega_q^{(0)2}\right). \tag{4}$$

In the vicinity of the peak, the real component of $\overline{\sigma}$ is given by formula (2) as in the absence of the field, but ω_q and γ_q are defined by (3) and (4).

It was noted in Refs. 1–3 that the experimentally observed properties of plasmons and magnetoplasmons in the inversion layer at the $Si-SiO_2$ boundary are satisfactorily described by the classical formulas (1)–(4) only for a large electron number density. In the case of a low density ($n<10^{16}$ m^{-2}), deviations from the classical theory of conductivity of a two-dimensional electron gas become significant. For example, Allen *et al.*[1] noted that the plasma peak on the $P(\omega)$ curve for low electron densities is shifted from the value predicted by formula (1) towards low frequencies. According to Allen *et al.*,[1] such a displacement is due to an increase in the effective mass m or electron localization. Theis *et al.*[3] proved that for small n the magnetoplasma peak splits into two peaks. One of them lies below the peak described by formula (3), while the other peak lies above it. In order to explain this phenomenon, the effects associated with a nonlocal nature of conductivity of a two-dimensional elec-

tron gas in a magnetic field were taken into account.[2,4] The conductivity contains a correction of the order of $(ql)^2$ (l is the magnetic length) with a resonance at a frequency $2\omega_c$. The interaction of a magnetoplasmon with the subharmonic structure of the cyclotron resonance leads to magnetoplasmon peak splitting.[4] It was noted in Refs. 2, 4, however, that this interaction is too weak to be responsible for the observed splitting. For this reason, the problem of the plasma absorption line in inversion layers cannot be regarded as solved completely.

In the present paper, we consider the effect of local electron states in the field of impurity atoms on the spectrum and absorption of plasmons and magnetoplasmons in a two-dimensional electron gas. We used the model and the computational method described in Refs. 5, 6. It will be shown that electron localization leads to a displacement of the plasma peak on the $P(\omega)$ curve towards the low-frequency region. The inclusion of resonant transitions of electrons between Landau levels and local levels causes a rearrangement of magnetoplasmon spectrum in the vicinity of resonant frequencies similar to the crossover in the theory of coupled waves.[7] This leads to the splitting of the magnetoplasmon peak mentioned above.

In Sec. 2, we consider the properties of magnetoplasmons near the frequency $\omega_+=\omega_c+\omega_0$ of resonant electron transitions from a local level to the Landau level lying above it (ω_0 is the separation between a Landau level and the local level split from it by an attracting impurity). The neighborhood of the frequency $\omega_-=\omega_c-\omega_0$ corresponding to transitions from a Landau level to a local level will be analyzed in Sec. 3. The spectrum and damping of plasmons taking into account electron localization in zero magnetic field are considered in Sec. 4. The obtained results are summarized in Conclusion, where the theoretical results are compared with experimental data.

2. EFFECT OF LOCAL ELECTRON STATES ON THE PROPERTIES OF TWO-DIMENSIONAL MAGNETOPLASMONS

It was proved in Ref. 6 that local electron states in a quantizing magnetic field perpendicular to the inversion layer are manifested in the presence of resonant terms in the tensor or high-frequency conductivity of a two-dimensional electron gas. For example, the transverse conductivity σ_{xx} in the vicinity of the frequency $\omega_+=\omega_c+\omega_0$ corresponding to electron transitions between a local level and a Landau level contains the term

$$\delta\sigma=i\,\frac{e^2n\alpha_+\omega_+}{m\omega}\,(\omega-\omega_++i\Gamma)^{-1}, \tag{5}$$

where

$$\alpha_+=\frac{n_iNr_{N-1}}{2\pi mn\omega_0^2\omega_+l^4}\,[1+(1+N^{-1})(1+2\omega_c/\omega_0)^{-2}]$$
$$\times[f(\varepsilon_{N-1}^l)-f(\varepsilon_N)] \tag{6}$$

is the oscillator force of a resonant transition and Γ the width of the local level labeled by $N-1$ and participating in transitions. Here n_i is the number density of impurity atoms, r_N the residue of the amplitude of the electron-impurity scattering at the pole $\varepsilon_N^l-i\Gamma$,[6] and f the Fermi function; the quantum constant is assumed to be equal to unity. The difference in the Fermi functions in (6) takes into account the Pauli exclusion principle in electron transitions from the local level ε_{N-1}^l to the Landau level ε_N. We assume that the Fermi boundary ε_F of two-dimensional electrons lies between the levels ε_{N-1} and ε_N^l, and $ql\ll 1$. In this case, the expression for the oscillator force contains only one term (6), and spatial dispersion of conductivity (5) can be neglected.

Expression (5) must be taken into account in the dispersion equation for magnetoplasma waves[2]:

$$\varepsilon(q,\omega)=1+\frac{4\pi iq}{\omega}\,\sigma_{xx}(q,\omega)$$
$$\times(\varepsilon_s\coth qd_s+\varepsilon_d\coth qd_s)^{-1}=0. \tag{7}$$

This equation can be written in the form

$$1-A_+(x^2-\omega_c^2/\omega_+^2)^{-1}=\alpha_+A_+x^{-2}(x-1)^{-1}, \tag{8}$$

where

$$x=\omega/\omega_+,$$
$$A_+=4\pi e^2nq[m\omega_+^2(\varepsilon_s\coth qd_s+\varepsilon_d\coth qd_d)]^{-1}. \tag{9}$$

In the absence of local levels ($\alpha_+\to 0$), the solution of Eq. (8) is the function (3). The inclusion of electron localization leads to a rearrangement of themagnetoplasmon spectrum in the vicinity of frequency ω_+. As a matter of fact, the straight line $\omega=\omega_+$ intersects the dispersion curve (3) at the point

$$q_0=\frac{m\omega_0^2}{4\pi e^2n}\left(1+2\frac{\omega_c}{\omega_0}\right)(\varepsilon_s+\varepsilon_d),$$

where we assume that $qd_s\gg 1$ and $qd_d\gg 1$. Consequently, in the vicinity of this point we have a crossover situation similar to that observed in the spectrum of a lattice with quasilocal vibrations.[7] Equation (8) has two real positive roots x_1 and x_2, one of which lies below the magnetoplasmon frequency (3), while the other lies above this frequency. Figure 1 shows the results of numerical solution of the dispersion equation (8) for values of parameters of the inversion layer at the Si-SiO_2 boundary in a magnetic field of induction $B=0.1$ T. The dashed curve describes the function (3), while the lower and upper curves present x_1 and x_2 as functions of the ratio of the wave number q to the Fermi wave number k_F. The following values of parameters are used: $m=0.2m_0$ (m_0 is the free electron mass), $\omega_0/\omega_c=0.1$, $n=10^{16}$ m^{-2}, $\varepsilon_s+\varepsilon_d=15$, and $n_i/n_l=0.1$. In this case, $N=196$, which allows us to neglect the effect of magnetic field on the scattering amplitude residue. In zero field, it is given by[6]

$$r=2\pi|\varepsilon_l|/m,$$

where ε_l is the position of the local level in the field of an attracting impurity. The residue r is obtained for $\varepsilon_F/|\varepsilon_l|=2$. For such values of parameters, we have $q_0=1.5\times 10^2$ m^{-1} and $\omega_+=9.8\times 10^{10}$ s^{-1}.

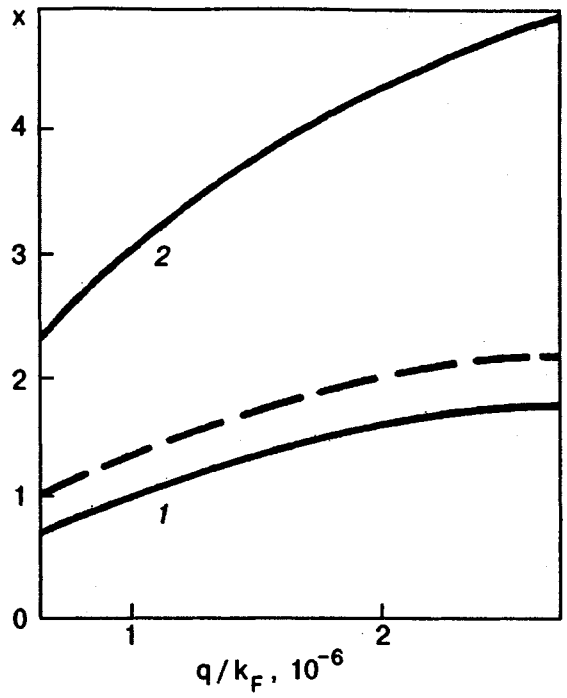

FIG. 1. Splitting of the dispersion curve (3) (dashed curve) of magnetoplasmons into the low-frequency (curve *1*) and high-frequency (curve *2*) branches in a magnetic field $B=0.1$ T.

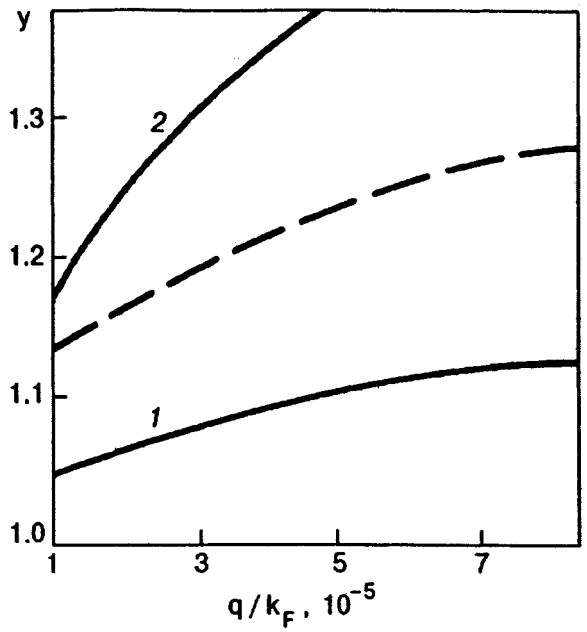

FIG. 2. Low-frequency (curve *1*) and high-frequency (curve *2*) branches of the magnetoplasmon spectrum in the vicinity of frequency ω_- in a magnetic field $B=1$ T. The dashed curve corresponds to spectrum (3) in the absence of local levels.

The damping factor for magnetoplasmons with the spectrum $\omega_q^{(i)}$ ($i=1,2$ is the number of the branch) is given by $\gamma_q^{(i)}=\gamma_q^0+\delta\gamma_q^{(i)}$, where

$$\delta\gamma_q^{(i)}=\frac{\omega_0^4\alpha_+}{2\omega_+^2}\,(1+2\omega_c/\omega_0)^2\Gamma[(\omega_q^{(i)}-\omega_+)^2+\Gamma^2]^{-1}. \tag{10}$$

The term (10) in the decrement, which is associated with the local level, has a peak at the frequency ω_+ of electron transitions from the local level ε_{N-1}^l to the Landau level ε_N.

The existence of two roots of the dispersion equation (8) indicates that the plasma peak on the curve describing the frequency dependence of absorption of electromagnetic radiation splits into two peaks. In the vicinity of the ith peak, the absorption is proportional to

$$\mathrm{Re}\ \overline{\sigma_i}(q,\omega)=\frac{m(\varepsilon_s+\varepsilon_d)^2\gamma_q^{(i)}}{32\pi^2e^2nq^2}\,(\omega_q^{(i)2}-\omega_c^2)^2 \times[(\omega-\omega_q^{(i)})^2+\gamma_q^{(i)2}]^{-1}. \tag{11}$$

The position of the peak of (11) is determined by the energy-momentum relation $\omega_q^{(i)}$ for magnetoplasmons, and the peak width is determined by the damping factor $\gamma_q^{(i)}$.

3. MAGNETOPLASMONS IN THE VICINITY OF FREQUENCY $\omega_-=\omega_c-\omega_0$

In the vicinity of frequency $\omega_-=\omega_c-\omega_0$, the conductivity of resonant transition of electrons from a Landau level to the neighboring local level differs from (5) in the resonance frequency and oscillator force.[6] The latter quantity is defined as

$$\alpha_-=\frac{n_iNr_N}{2\pi mn\omega_0^2\omega_-l^4}\,[1+(1-N^{-1})(1-2\omega_c/\omega_0)^{-2}] \times[f(\varepsilon_{N-1})-f(\varepsilon_N^l)],$$

where N is the number of the local level participating in transitions.

The dispersion equation (7) for magnetoplasma waves in the vicinity of frequency ω_- can be obtained from Eq. (8) by replacing the subscript ''+'' by ''−''. This equation has two roots $y_{1,2}=\omega_{1,2}/\omega_-$ lying below and above (3). Figure 2 shows the solution of the dispersion equation for the values of parameters used in Sec. 2 and for $B=1$ T. In this case, $N=20$, and the residue r_N should be calculated by taking into account the magnetic field. For $\omega_0\ll\omega_c$, it is given by[6]

$$r=2\pi(l\omega_0)^2.$$

The contribution of the local level to the damping factor for magnetoplasmons can be obtained from formula (10) by replacing the subscript ''+'' by ''−'' and by changing the sign of ω_c. This leads to a peak against the background of a smooth dependence of the damping factor (4) on the plasmon frequency. The position of the peak is determined by the resonance frequency ω_-, and its width by the broadening of the local level. The ratio of the maximum value of decrement (10) to (4) is equal to 3.3 for all values of parameters indicated in Sec. 2 and for $\nu=\Gamma=10^{11}\ \mathrm{s}^{-1}$.

As in Sec. 2, the magnetoplasma peak on the curve describing the frequency dependence of absorption splits into two peaks. The absorption in the vicinity of the peak is proportional to expression (11) in which we must substitute the

frequency $\omega_q^{(i)}$ and the damping factor $\gamma_q^{(i)}$ of magnetoplasma waves obtained in this section. The ratio of the maximum absorption to the background

$$\mathrm{Re}\ \overline{\sigma} = \frac{e^2 n \nu}{m} (\omega^2 + \omega_c^2)(\omega^2 - \omega_c^2)^{-2}$$

is $k_1 = 0.02$ for the low-frequency branch and $k_2 = 21.4$ for the high-frequency branch in Fig. 2. It should be noted that this ratio for magnetoplasmons in the absence of electron localization is $k_0 = 0.6$. The calculations were made for the above values of parameters and for $q = 10^4\ \mathrm{m}^{-1}$. In this case, $\omega_p = 3.2 \times 10^{10}\ \mathrm{s}^{-1}$, $\omega_q^{(0)} = 9.5 \times 10^{11}\ \mathrm{s}^{-1}$, and $\omega_- = 8 \times 10^{11}\ \mathrm{s}^{-1}$.

4. PLASMA WAVES IN ZERO MAGNETIC FIELD

We assume that the energy spectrum of two-dimensional electrons contains only one local level $\varepsilon_l = -\omega_g$ split by an attracting impurity from the lower edge of the conduction band. Owing to the local level, the imaginary component of the high-frequency conductivity of the degenerate electron gas contains the contribution[6]

$$\mathrm{Im}\ \delta\sigma = \frac{e^2 r n_i}{\pi \omega^3} (\varepsilon_l + \omega) \times \ln \left| \frac{\varepsilon_F - \varepsilon_l - \omega}{\varepsilon_F - \varepsilon_l} \right| - (\omega \to -\omega), \tag{12}$$

in which $(\omega \to -\omega)$ denotes the term differing from the previous one in the sign of frequency. Taking into account (12), we can write the dispersion equation (7) in the form

$$1 - b u^{-2} = c \varphi_a(u), \tag{13}$$

where

$$u = \omega/(\varepsilon_F + \omega_g);$$

$$\varphi_a(u) = u^{-4} \left[u \ln \left| \frac{1-u}{1+u} \right| - a \ln \left| 1 - u^2 \right| \right];$$

$$a = (1 + \varepsilon_F/\omega_g)^{-1},$$

$$b = 4\pi e^2 n q [m(\varepsilon_F + \omega_g)^2 (\varepsilon_s + \varepsilon_d)]^{-1},$$

$$c = 2b \frac{n_i}{n} (1 + \varepsilon_F/\omega_g)^{-1}.$$

Figure 3 shows the solution of the dispersion equation (13) for long-wave plasmons in a degenerate electron gas for the above values of parameters. It can be seen that the inclusion of electron localization reduces the plasmon frequency. Such an effect was observed[1] in the inversion layer at the Si-SiO_2 boundary for a low electron density. The separation between the dispersion curves in Fig. 3 is

$$\Delta u = \frac{n_i}{n} b^{1/2} (1 + 2\varepsilon_F/\omega_g)(1 + \varepsilon_F/\omega_g)^{-2}.$$

This leads to the relative deviation of the plasmon frequency from (1), i.e., $\Delta\omega/\omega = 0.06$.

The damping factor for plasmons with the energy-momentum relation ω_q is given by

$$\gamma_q = \frac{\nu}{2} + \frac{m\omega_q^2}{2e^2 n} \mathrm{Re}\ \delta\sigma(\omega_q), \tag{14}$$

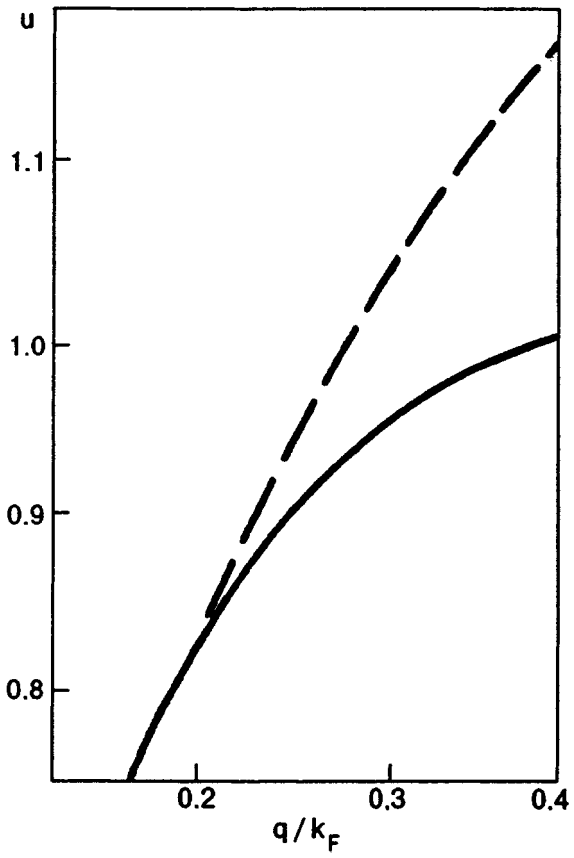

FIG. 3. Dispersion of plasmons taking into account the local level. The dashed curve is the dispersion curve (*1*) in the absence of electron localization.

where

$$\mathrm{Re}\ \delta\sigma(\omega) = \frac{e^2 r n_i}{\omega^3} \Theta(\varepsilon_l + \omega)(\varepsilon_l + \omega) \times [f(\varepsilon_l) - f(\varepsilon_l + \omega)] + (\omega \to -\omega),$$

and Θ is the Heaviside function. Formula (14) shows that the contribution $\delta\gamma$ to the damping factor from the local level has a frequency threshold ω_g for activation of localized electrons. Near the threshold, $\delta\gamma \propto \omega - \omega_g$. This threshold is shifted upon cooling to the point $\varepsilon_F + \omega_g$ in accordance with the Pauli principle. For $q/k_F = 0.04$ and the values of parameters given in Sec. 2, the relative value of the peak of the decrement (14) is $2\delta\gamma/\nu = 6$.

Plasma absorption taking into account the local level is given by formula (2) into which the energy-momentum relation and the damping factor of plasmons obtained in this section should be substituted. For $q/k_F = 0.04$, $n = 0.4 \times 10^{16}\ \mathrm{m}^{-2}$, and $\nu = 0.5 \times 10^{12}\ \mathrm{s}^{-1}$, the relative height of the plasma peak is $(\omega_q/\nu)^2 = 70$.

CONCLUSIONS

In this paper, we considered the effect of electron localization in the field of isolated impurity atoms on the spectrum and damping of plasma and magnetoplasma waves in a two-dimensional electron gas. We also considered the plasma absorption of electromagnetic radiation incident on

the electron layer. It was proved that electron localization reduces the frequency of long-wave plasmons as compared to its value in the absence of local levels. Such a decrease was observed by Allen *et al.*[1] who studied plasmons in the inversion layer at the boundary between Si and SiO_2 and explained the freezing out of charge carriers to local levels. But this is not the only effect observed in this case. Ionization of electrons localized at impurities by an electromagnetic field is accompanied by the emergence of a noticeable contribution to the high-frequency conductivity, which must be taken into account in the dispersion equation for plasmons. This also leads to a decrease in the plasmon frequency, which is manifested in a shift of the plasma peak on the curve describing the frequency dependence of absorption towards the low-frequency region. The estimate of the displacement given in Sec. 4 is in satisfactory agreement with the experimentally obtained estimate,[1] but the theory predicts an elevated value of the peak height.

In a quantizing magnetic field perpendicular to the electron layer, a system of local levels alternating with Landau levels is formed. Electron transitions between these levels, which are induced by the magnetic field, lead to resonant corrections to the conductivity of the two-dimensional electron gas. A rearrangement of the magnetoplasmon spectrum similar to the crossover in the theory of coupled waves is observed in the vicinity of the resonant transitions frequencies. As a result, the magnetoplasma peak on the frequency dependence of absorption splits into two peaks. Such a splitting was observed by Theis *et al.*[3] who studied the dependence of absorption on the magnetic field in the inversion layers at the $Si\text{-}SiO_2$ boundary. According to calculations, for a fixed radiation frequency ω (following Ref. 3, we put $\omega = 3.7$ meV), the resonant fields B_1 and B_2 for which absorption has the maximum value are $B_1 = 6.88$ T and $B_2 = 5.69$ T. The positions of the peaks and their separation $\Delta B = 1.2$ T are in good agreement with the experimental data.[3] However, the theory gives higher heights of the peaks as in the case of zero magnetic field. This is apparently due to the existence of mechanisms of electron scattering in inversion layers, which were not taken into account in this research.

[1] S. J. Allen, Jr., D. C. Tsui, and R. A. Logan, Phys. Rev. Lett. **38**, 980 (1977).
[2] T. Ando, A. Fowler, and F. Stern, *Electronic Properties of Two-Dimensional Systems*, American Physical Society, New York (1982).
[3] T. N. Theis, J. P. Kotthaus, and P. J. Stiles, Solid State Commun. **24**, 273 (1977).
[4] T. Ando, Solid State Commun. **27**, 895 (1978).
[5] È. A. Kaner and A. M. Ermolaev, Zh. Éksp. Teor. Fiz. **92**, 2245 (1987) [Sov. Phys. JETP **65**, 1266 (1987)].
[6] N. V. Gleizer and A. M. Ermolaev, Fiz. Nizk. Temp. **23**, 73 (1997) [Low Temp. Phys. **23**, 55 (1997)].
[7] A. M. Kosevich, *The Theory of Crystal Lattice* [in Russian], Vishcha Shkola, Kharkov (1988).

Translated by R. S. Wadhwa

Verification of the theory of Brownian motion of a particle through a potential barrier in a viscous medium during experimental study of dislocation acoustic relaxation in normal and superconducting niobium

V. D. Natsik and P. P. Pal-Val

*B. Verkin Institute for Low Temperature Physics and Engineering, National Academy of Sciences of the Ukraine, 310164 Kharkov, Ukraine**

(Submitted May 28, 1997)
Fiz. Nizk. Temp. **23**, 1229–1242 (November 1997)

The Kramers theory (1940) describing a thermally activated escape of a particle from a potential well in a viscous medium is used for explaining the acoustic absorption peak discovered by Kramer and Bauer (1967) in niobium in the liquid helium temperature range. It is shown that the properties of the peak observed in experiments correspond to the model of resonant interaction of acoustic vibrations with dislocation kink chains. Kinks, viz., pseudoparticle excitations on dislocation lines, perform diffusive drift in the second-order Peierls relief under the action of acoustic vibrations, experiencing simultaneously viscous drag exerted by conduction electrons. The possibility of a sharp controllable change in electron viscosity during a superconducting transition can be used for verifying the conclusions of the Kramers theory in experimental investigations of the dislocation contribution to attenuation of sound. It is found that at low temperatures, the conditions for the observation of the anomaly predicted by Kramers are created for kinks in niobium: the diffusion mobility of particles increases with the dynamic drag coefficient. This circumstance makes it possible to explain one of the most interesting properties of the Kramer–Bauer peak which could not be interpreted correctly till now, i.e., the displacement of the peak towards low temperatures during a magnetic field induced transition of *Nb* from the superconducting to the normal state. The possibilities of observation of quantum diffusion of kinks in acoustic experiments are also considered briefly. [S1063-777X(97)01211-5]

INTRODUCTION

Thermally activated motion of quasi- and pseudoparticles through potential energy barriers is of utmost importance for many branches of physical kinetics. In 1940, Kramers[1] was the first to pay attention to the important and nontrivial role of the viscosity of the medium in contact with moving particles in processes of this type. He described one-dimensional Brownian movement of a particle in a complex potential relief (Fig. 1a), which is activated by thermal forces exerted by a thermodynamically equilibrium medium and calculated the mean time in which the particle, which was initially trapped by the potential well A, escapes through the barrier B. Following the basic concepts of the classical theory of Brownian movement, Kramers assumed that the action of the medium on the particle can be presented as the sum of two components: viscous drag and fast thermal impacts. The main result obtained by Kramers was the conclusion that the time during which the particle escapes from the potential well is a nonmonotonic function of the drag coefficient. It was found that in the case of a high viscosity of the medium, the increase in the drag coefficient slows down the emergence of the particle from the well. At the same time, in the other limiting case of a low-viscosity medium, the opposite effect is observed: the increase in the drag coefficient accelerated the particle escape from the well. This conclusion is not trivial and even unexpected to a certain extent: the first case is intuitively clear, while the second appears as a paradox and can be regarded as a peculiar anomaly.

The Kramers analysis as well as the theory of Brownian movement on the whole are based on phenomenological assumptions concerning specific correlation properties of a random force describing the interaction of a particle with a medium. The correctness of these assumptions for a specific physical situation is not obvious as a rule. For this reason, physical experiments aimed at the verification of nontrivial predictions of the theory of Brownian movement (like the conclusion concerning the nonmonotonic dependence of the time of emergence of a damped particle from a potential well on the damping constant) are of special interest.

The Kramers theory was developed to clarify the kinetics of chemical reactions and of decay of heavy atomic nuclei, which were urgent at that time, on the basis of the liquid-drop model of the nucleus. To our knowledge, no attempts were made to verify experimentally the above conclusion concerning the role of viscosity in such type of reactions. It is also difficult to estimate the possibility of a controllable change in viscosity during the measurements of reaction rates in experiments made in the above fields of science. In this paper, we consider an interesting possibility of experimental verification of the Kramers theory while studying dynamic dislocation processes occurring in metallic

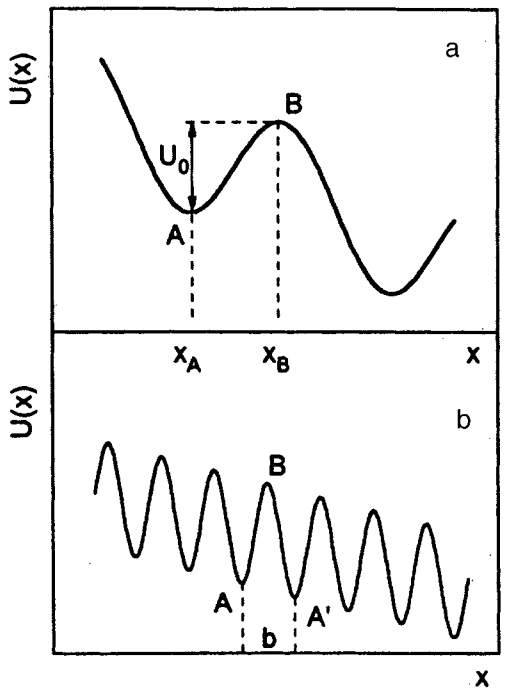

FIG. 1. Two types of potential reliefs in which Brownian movement of particles is considered: a solitary potential well of a finite depth (a) and the sum of a periodic crystal relief and a potential field of constant intensity (b).

superconductors at temperatures below the superconducting transition temperature T_c.

Bcc metals are the most effective objects of investigation, which can be used for solving the problem formulated above. Among these metals, niobium which has a relatively high superconducting transition temperature $T_c = 9.3$ K can be singled out since the potentialities of experiments with this metal are much richer. A typical element in the dislocation structure of bcc metals is a set of dislocations whose lines lie in extended rectilinear valleys of the lattice potential relief (first-order Peierls relief).[2] A special action on such dislocations can lead to the creation of pseudoparticle excitations (kinks) connecting two rectilinear segments of a dislocation line, which lie in neighboring valleys of the Peierls relief.[3,4] One-dimensional motion of kinks along a dislocation line involves the overcoming of another system of lattice potential barriers, viz., second-order Peierls relief. In addition, moving kinks experience the action of viscous friction due to scattering of phonons and conduction electrons at dislocations.[4–6] In metals with standard electron parameters, the electronic component plays the leading role in damping of the motion of a dislocation line in the temperature range $T \leqslant 10$ K.[5,6] Thus, a thermally activated motion of a kink (pseudoparticle) through second-order Peierls barriers in a viscous electronic medium corresponds completely to the process considered by Kramers. The advantage of the superconductor used for verifying the conclusion of the Kramers theory about the role of viscosity lies in the possibility of a controllable change in the electron drag coefficient for a kink: at $T < T_c$, the electron damping of dislocations can be varied considerably by a transition of the metal from the superconducting to the normal state, induced by an applied magnetic field.[7,8]

The experimental study of the kinetics of formation and motion of dislocation kinks is based on the application of acoustic spectroscopy.[3,4,9] By varying the vibrational frequency and temperature of samples, we can create conditions for a resonant interaction of sound with kinks. A detailed analysis of such resonances makes it possible to obtain rich information on the dynamic and kinetic characteristics of kinks as well as on the parameters of potential barriers overcome by kinks. For a fixed frequency of vibrations, each such resonance corresponds to a peak on the temperature dependence of sound absorption. In 1967, Kramer and Bauer[10] who studied the low-temperature acoustic properties of niobium at a frequency $\sim 10^5$ Hz observed a new absorption peak localized in the temperature region near 3 K and changing its position on the temperature axis upon a change in the vibrational frequency as well as upon a superconducting transition. Later, the existence of such a peak was confirmed by some other authors.[11–15] In a recent publication,[15] the properties of the Kramer–Bauer peak were analyzed in detail, and it was proved that most of these properties can be described by using the model of resonant interaction of sound with dislocation kink chains performing a thermally activated diffusion in a second-order Peierls relief.

However, the explanation of the behavior of the peak in the superconducting state proposed in Ref. 15 appeared as slightly artificial since it was based on the assumption about a significant change in the lattice potential barrier for dislocations in niobium upon a superconducting transition. This assumption does not contradict the existing ideas about a relation between the lattice and electronic properties of transition bcc metals, but other experimental confirmations of the assumption have not been obtained.

A dissatisfaction remaining in connection with this problem after the previous publication[15] stimulated a more detailed analysis of changes in the diffusion mobility of dislocation kinks which can appear upon a considerable change in the electron viscosity. It was found that the dislocation and electronic parameters of niobium have values permitting the realization of the anomalous dependence of diffusion mobility of a particle (kink in our case) on the drag coefficient predicted by Kramers: the inclusion of this circumstance makes it possible to provide a universal description of the behavior of the Kramer–Bauer peak in the normal as well as superconducting state without any additional assumptions. This publication is devoted to the description of details of such an analysis and to a substantiation of the above conclusion.

In Sec. 1, the basic concepts of the Kramers theory[1] are formulated in the form convenient for the application of the theory to a description of the Brownian movement of dislocation kinks.

In Sec. 2, the experimental data obtained by different authors who studied the Kramer–Bauer acoustic relaxation peak in normal and superconducting niobium are systematized. The basic concepts of the dislocation model proposed in Ref. 15 and used for explaining the physical nature of the peak are also described briefly.

In Sec. 3, the contribution of the ensemble of dislocation kinks to the logarithmic decrement of sample vibrations is analyzed. The analysis is based on the application of the results of the Kramers theory to the description of the Brownian movement of a kink through the barriers of a second-order Peierls relief.

In Sec. 4, the conclusions of the theory are compared with the experimental data obtained from the study of the Kramer–Bauer peak. It is shown that the application of the Kramers theory makes it possible to describe all the main peculiarities of the peak.

1. KRAMERS THEORY

Kramers[1] studied a one-dimensional motion of a particle under the action of the resultant of two independent forces $f(x)$ and $f_S(t)$. The first term $f(x)=-dU(x)/dx$ describes the action of the potential field $U(x)$ on the particle (Fig. 1a), while the second term $f_S(t)$ is a random force associated with the thermal motion of a thermodynamically equilibrium medium in which the particle moves. The time variation of the dynamic variables of the particle, viz., the momentum $p(t)$ and coordinate $x(t)$, obeys the Hamilton classical equations

$$\begin{cases} \dot{p}=f(x)+f_S(t) \\ m\dot{x}=p, \end{cases} \tag{1}$$

where m is the mass of the particle, and the dot denotes the time derivative. As a result of the action of a random force $f_S(t)$, the time variation of the dynamic variables becomes random also. For this reason, it is more convenient to describe the motion of the particle by using the distribution function $\rho(p,x,t)$ for the mapping point (p,x) in the phase space. In the general case, the function $\rho(p,x,t)$ must satisfy the kinetic equation

$$\left(\frac{\partial}{\partial t}+f(x)\,\frac{\partial}{\partial p}+\frac{p}{m}\,\frac{\partial}{\partial x}\right)\rho=\hat{L}_S(\rho), \tag{2}$$

in which the left-hand side is determined by the motion of the particle in the phase space in the absence of the medium, and $(\hat{L})_S(\rho)$ is a functional (collision integral) describing the change in the distribution function under the action of the medium.

We can obtain the explicit form of the operator $\hat{L}$ only by specifying the statistical properties of the random force $f_S(t)$ and by establishing its relation with temperature and dissipative parameters of the medium. Kramers proceeded from the assumption that the random process $f_S(t)$ has a short correlation time τ: on one hand, the values of $f_S(t)$ and $f_S(t+\tau)$ are regarded as statistically independent, and on the other hand, the momentum

$$p_\tau=\int_t^{t+\tau} f_S(t')dt'$$

transferred to the particle during this time can be regarded as very small. The quantity p_τ defined in this way is independent of time t; moreover, it is assumed that p_τ has a thermodynamically equilibrium distribution function determined by the properties of the medium. A formal expression of these assumptions is the equality

$$\overline{(p_\tau)^n}=\mu_n\tau, \quad n=1,2,3,..., \tag{3}$$

where the bar indicates statistical averaging, and the coefficients μ_n do not depend on time t explicitly, but can be functions of the variables p and x as well as of the parameters of the medium. Using equality (3), we can write the collision integral in the form of a series in the moments of the transferred momentum:

$$\hat{L}_S(\rho)=-\frac{\partial}{\partial p}(\mu_1\rho)+\frac{1}{2}\,\frac{\partial^2}{\partial p^2}(\mu_2\rho)+\dots\,. \tag{4}$$

The next step is the establishment of the relation between the coefficients μ_1 and μ_2 and physical parameters of the medium. This problem can be solved by analyzing two limiting cases for which the distribution function $\rho(p,x,t)$ can be written easily from simple physical considerations.[1)] The first is the stabilized motion of a particle with a constant average momentum $\overline{p}=p_0=\text{const}$ under the action of the uniform potential $U(x)=-f_0x$, where f_0 is a constant force. It is well known that such a motion can be described by characterizing the interaction of the particle with the medium through the viscous drag coefficient β:

$$\begin{cases} \beta V=f_0, \\ \overline{x}=Vt; \end{cases} \tag{5}$$

where $V=\dot{\overline{x}}=m^{-1}\overline{p}$ is the average velocity of the steady-state motion. If we neglect dispersion of momentum and coordinate and are interested only in the change in their mean values, we can put in correspondence with motion (5) a distribution function of the form

$$\rho(p,x,t)=\text{const}\cdot\delta(p-mV)\,\delta(x-Vt), \tag{6}$$

where $\delta(x)$ is the Dirac delta function. It can easily be verified that Eq. (2) permits such a form of diffusion in the phase space if we retain only the first term in the collision integral (4) and put

$$\mu_1=-\frac{\beta}{m}\,p. \tag{7}$$

in it.

The other limiting case is the steady state of a particle in a potential well with infinitely high walls. $U(-\infty)=U(\infty)=\infty$. In this case, the function $\rho(p,x,t)$ must coincide with the equilibrium Boltzmann's distribution

$$\rho_B(p,x)=\text{const}\cdot\exp\left(-\frac{E(p,x)}{kT}\right),$$

$$E=\frac{p^2}{2m}+U(x). \tag{8}$$

In order to describe dispersion of momentum and coordinate in the collision integral (4) typical of distribution (8), we must retain both terms. In this case, the function (8) satisfied Eq. (2) if we put, in addition to (7),

$$\mu_2=2\beta kT. \tag{9}$$

The retainment of only two terms in the collision integral and the choice of the coefficients μ_1 and μ_2 in the form (7) and (9) are in complete agreement with the classical pattern of Brownian movement proposed by Einstein. In this approximation, diffusion of the mapping point of a particle in the two-dimensional phase space is described by solutions of a partial differential equation of the Focker–Planck type:

$$\frac{\partial}{\partial t}\rho=\frac{dU(x)}{dx}\frac{\partial}{\partial p}\rho-\frac{p}{m}\frac{\partial}{\partial x}\rho+\frac{\beta}{m}\frac{\partial}{\partial p}\left(p\rho+mkT\frac{\partial}{\partial p}\rho\right). \tag{10}$$

It should be noted that in the derivation of this equation, the drag coefficient β and the temperature T were introduced as two separate characteristics of the medium, which, however, does not rule out a possible temperature dependence $\beta(T)$.

The solution of the problem of the emergence of a particle from the well A of a potential relief $U(x)$ we are interested in (see Fig. 1a) is reduced to the search of a solution of Eq. (10) satisfying the initial condition of the form $\rho(p,x,t)=\text{const}\cdot\delta(p)\delta(x-x_A)$. Considering the low-temperature limit in which $kT\ll U_0$, Kramers proved that the temperature dependence of the average frequency ν of emergence of the particle from the well A through the barrier B without taking into account the reverse process can be described by an expression resembling in form the Arrhenius classical law for the rates of chemical reactions:

$$\nu=\nu_0(\beta,T)\exp\left(-\frac{U_0}{kT}\right). \tag{11}$$

However, the preexponential factor $\nu_0(\beta,T)$ in this expression remains a complex function of the parameters β and T. We can obtain explicitly only the asymptotic forms of the function $\nu_0(\beta,T)$ in the limits of low ($\beta\to\infty$) and high ($\beta\to 0$) viscosity. In each of these cases, diffusion in the two-dimensional phase space (p,x) can be reduced to a one-dimensional problem. For large values of the drag coefficient, diffusion flow along the spatial coordinate x plays the leading role, while the role of the effective diffusion coefficient d_x is played by a quantity inversely proportional to the drag coefficient β:

$$d_x=mkT/\beta.$$

In the case of small drag, the emergence of a particle from a well id determined by one-dimensional diffusion along the energy coordinate $I(E)=\oint p\,dx$, where the integration is carried out along the contour of constant energy $E(p,x)=E$ (I is the adiabatic invariant for undamped motion of the particle in the potential well A). In this case, the role of effective diffusion coefficient d_I is played by a quantity proportional to the drag coefficient β:

$$d_I=\frac{\beta kTI}{m}\frac{dI}{dE}.$$

Kramers also obtained an estimate for the characteristic value of the drag coefficient β_0 separating the above-mentioned asymptotic forms:

$$\beta_0=\frac{kT}{2\pi U_0}(mU_A'')^{1/2}=\frac{m\nu_A kT}{U_0}. \tag{12}$$

Here and below, we will use in addition to the barrier height U_0 its differential characteristics $U_{A,B}''$ and the frequencies $\nu_{A,B}$ of undamped motion of the particle near the bottom of the well and the top of the barrier, corresponding to these characteristics:

$$U_{A,B}''=\left|\frac{d^2U(x)}{dx^2}\right|_{x=x_A,x_B},\quad \nu_{A,B}=\frac{1}{2\pi}\left(\frac{U_{A,B}''}{m}\right)^{1/2}. \tag{13}$$

Ultimately, Kramers proved that the dependence $\nu_0(\beta,T)$ can be correctly described by a relatively simple interpolation formula for any values of the viscosity of the medium:

$$\nu_0(\beta,T)\cong\begin{cases}\beta U_0/(mkT), & \beta<\beta_0;\\ \nu_A\{[1+(\beta/(4\pi m\nu_B))^2]^{1/2}-\beta/(4\pi m\nu_B)\}, & \beta>\beta_0.\end{cases} \tag{14}$$

Thus, the theory predicts a nonmonotonic dependence of the reaction rate (11) on the viscosity of the medium: the linear increase in the preexponential factor in (11) for small values of $\beta<\beta_0$ is transformed into a broad peak in the region $\beta_0<\beta<4\pi m\nu_B$. As the viscosity increases further, the preexponential factor decreases according to the law $\nu_0\approx 2\pi m\nu_A\nu_B\beta^{-1}$. The anomaly described by the upper line of formula (14), i.e., the increase in the reaction rate with the viscosity of the medium, is a consequence of the specific nature of diffusion of the mapping point along the energy coordinate.

Concluding this section, let us consider a more complex diffusion underlying many kinetic phenomena in crystals. In the physics of crystals, it is often necessary to describe macroscopic diffusion flows for which the elementary process of activated transition of a particle through an individual barrier considered by Kramers is repeated many times in space (diffusion of impurities, electrons, polarons, elements of a dislocation line, etc. in a periodic potential relief of the crystal lattice). In such cases, the problem involves the calculation of a macroscopic diffusion flux or macroscopic mean values of the particle displacement $u=\langle\overline{x}\rangle$ and velocity $\dot{u}=\langle\overline{\dot{x}}\rangle$ in a potential of the form

$$U(x)=U_p(x)-f_0x, \tag{15}$$

where $U_p(x)=U_p(x+b)$ is a periodic (with period b) lattice potential and f_0 is a constant force applied to the particle (Fig. 1b). The operation of averaging $\langle\ldots\rangle$ presumes the evaluation of average values of the relevant quantities over time intervals much longer than the time ν^{-1} of emergence of a particle from an individual well. According to the well-known concepts of the diffusion theory in crystals,[16] a macroscopic diffusion flux is characterized by the spatial diffusion coefficient D, which is connected (in the case of one-dimensional processes) with length b and frequency ν of an elementary jump through the relation $D=b^2\nu$. In the linear approximation ($bf_0\ll kT$), the average velocity $\dot{u}$ of diffu-

sion drift, which is acquired by a particle under the action of the constant force f_0, is determined by the Einstein relations[16,17]

$$\beta_d \dot{u} = f_0, \quad \beta_d = \frac{kT}{D} = \frac{kT}{b^2 \nu}. \tag{16}$$

Relations (16) are also valid in the case when a particle experiences the action of a periodic (in time) force $f(t)$ if the characteristic frequency of force variation remains smaller than the frequency ν of diffusion jumps.

It should be noted that in problems of the type under investigation, the role of the medium the interaction with which is determined by the particle drag coefficient β is played by the ensemble of quasiparticles (phonons, conduction electrons, etc.) in the crystal, which are scattered at a particle or pseudoparticle undergoing diffusion. Henceforth, we will call this phenomenon the dynamic drag (or first-order damping). At the same time, relations (16) show that the steady-state diffusion drift of a particle in the crystal relief under the action of the constant force f_0 is also formally equivalent to its motion in a viscous medium with the drag coefficient β_d. This drag describes actual dissipation of mechanical energy $f_0 x$ of the particle, accompanying random activated wandering in the lattice; such a process can be called diffusive drag (or second-order damping). Formulas (11), (14), and (16) describe the relation between the diffusive (β_d) and dynamic (β) drag of the particle:

$$\beta_d = \frac{kT}{b^2 \nu_0(\beta, T)} \exp\left(\frac{U_0}{kT}\right). \tag{17}$$

Such a relation is not universal: for a large dynamic viscosity, β_d is proportional to β, while in the opposite limiting case β_d is inversely proportional to β. There also exists a large interval of β values for which $\nu_0 \approx \nu_a$, and the value of β_d is virtually independent of β. It should also be noted that the temperature dependences of the dynamic $\beta(T)$ and diffusive $\beta_d(T)$ viscosities differ qualitatively. As a rule, $\beta(T)$ decreases with temperature: the phonon viscosity as a result of the decrease in the density of thermal phonons, and electron viscosity in the superconductor due to Cooper pairing of electrons. On the contrary, $\beta_d(T)$ increases exponentially upon cooling in accordance with (17), and the temperature dependence $\beta(T)$ can only suppress or enhance this increase.

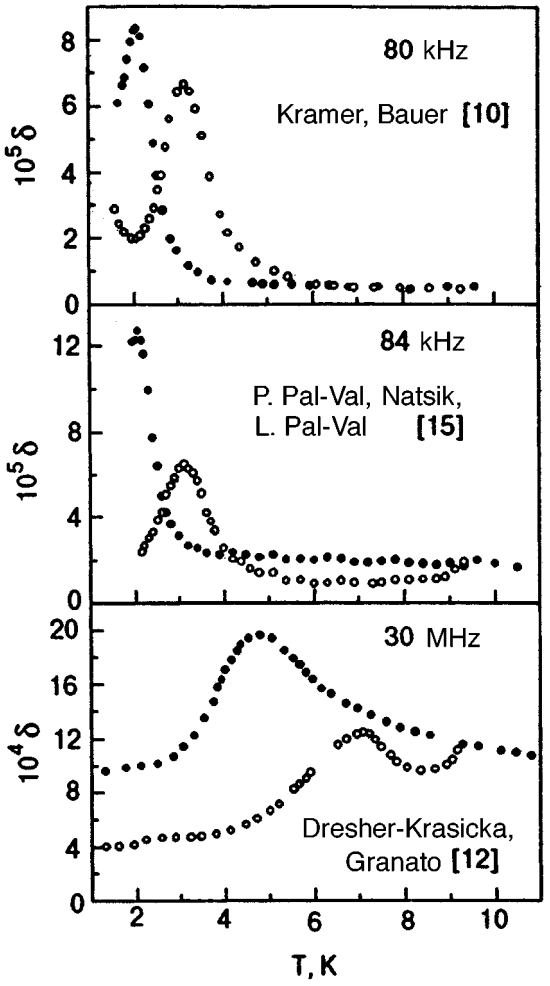

FIG. 2. Low-temperature peaks of acoustic relaxation in Nb in the normal (●) and superconducting (○) states for various ultrasonic frequencies according to data obtained in Refs. 10, 12, 15.

2. KRAMER–BAUER PEAK

Kramer and Bauer,[10] and subsequently a number of other authors[11–15] who studied experimentally the acoustic properties of niobium in the liquid helium temperature range, observed an absorption peak of the relaxation type (Fig. 2). They used in experiments a wide range of acoustic and ultrasonic frequencies from $2 \cdot 10^4$ to $7 \cdot 10^7$ Hz and observed a systematic displacement of the peak temperature T_p towards high temperatures upon an increase in the vibrational frequency (see Table I).

The measurements were mainly made on samples in the superconducting state since the peak was localized below $T_c \simeq 9.3$ K in all cases. In some cases, the samples were transformed into the normal state during measurements[10,12,14,15] by applying a magnetic field of a supercritical magnitude $H > H_{c2} \simeq 5$ kOe, which resulted in a displacement of the peak towards low temperatures (see Fig. 2 and Table I). The presence of the peak and its reaction to the superconducting transition can also explain[18] the anomalies in the field dependences of acoustic absorption in Nb in

TABLE I. Frequency dependence of the Kramer–Bauer peak temperature in the normal and superconducting states.

Cyclic frequency ω, s^{-1}	Peak temperature T_p, K		Reference
	n-state	*s*-state	
$1.3 \cdot 10^5$	–	2.62	13
$4.6 \cdot 10^5$	–	3.14	13
$5.0 \cdot 10^5$	2.08	3.24	10
$5.3 \cdot 10^5$	2.05	3.15	14, 15
$1.5 \cdot 10^6$	2.37	3.75	10
$6.3 \cdot 10^7$	–	6.3	11
$1.9 \cdot 10^8$	4.7	7	12
$1.9 \cdot 10^8$	–	7.15	11
$3.1 \cdot 10^8$	–	7.5	11
$4.4 \cdot 10^8$	–	7.8	11

a mixed state for $H_{c1}<H<H_{c2}$, which were detected in Refs. 18–21.

It was found in Refs. 10–15 that the peak is affected not only by the superconducting transition, but also some other factors characterizing the structural state of the samples (single crystals, polycrystals, grain size, impurity composition, and preliminary plastic deformation) as well as the experimental conditions (the rate of sample cooling to helium temperatures). In Ref. 15 devoted to a generalization of various experimental observations, we noted the following most significant peculiarities in the acoustic absorption in Nb at helium temperatures:

1. All the absorption peaks listed in Table I have the same physical origin and are due to the action of a system of identical thermally activated relaxators in Nb samples.
2. The linear response of relaxators to acoustic excitation of the samples corresponds to the model of a standard linear body with a single characteristic frequency of relaxation.
3. The temperature dependence of the characteristic relaxation frequency is described qualitatively by the Arrhenius relation (11), and the empirical values of the parameters appearing in this relation have values of the order of $U_0 \sim (2-3)\cdot 10^{-3}$ eV and $\nu_0 \sim 10^{10}-10^{11}$ s^{-1}.
4. The transition of the samples from the normal to the superconducting state leads to a considerable decrease in the relaxation frequency, which is formally equivalent to an increase in the activation energy by $\delta U \sim 1\cdot 10^{-3}$ eV.
5. The relaxators responsible for the Kramer–Bauer peak are formed in the samples as a result of action of thermoelastic stresses upon rapid cooling; in the case of a slow cooling, no peak is observed.
6. An increase in the impurity concentration in the samples facilitates the accumulation of relaxators upon rapid cooling.

Having analyzed all possible mechanisms of the emergence of above singularities critically, we proposed[15] a simple dislocation model for their explanation. This model is based on electron microscopic data on the dislocation structure of bcc metals,[2] on the concepts of dislocation kinks existing in the theory of dislocations and on their dynamic properties,[3,4,9] and on the results of computer simulation of the motion of an individual kink in bcc metals through second-order Peierls barriers.[22] The basic concepts of the model are illustrated in Figs. 3 and 4. We assume that the initial Nb samples contain a mesh of screw dislocations of the slip system ⟨111⟩{011}, consisting of rectilinear segments L_N lying in the valleys of the first-order Peierls relief (Fig. 3a). In the case of rapid cooling of the sample, thermoelastic stresses bend the segments between the nodes of the mesh and form a system of kinks at them (Fig. 3b). After temperature stabilization, thermoelastic stresses disappear, but kinks are preserved at dislocations owing to the drag effect of impurities which hamper the returning of the segments to the initial linear configurations (Fig. 3c). Under the action of

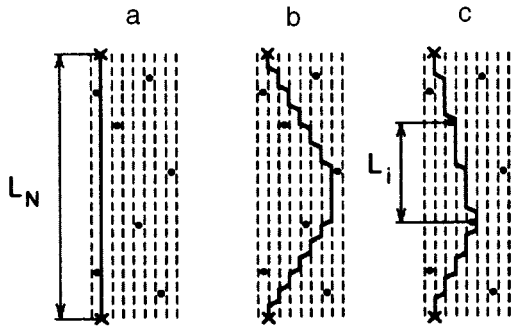

FIG. 3. Dislocation model[15] used for interpreting the Kramer–Bauer peak: various configurations of a dislocation line (solid curve) in a first-order Peierls relief (before (a), during (b) and after rapid cooling of the samples (c); dashed lines show minima of the relief, crosses indicate the nodes of dislocation mesh, and dark circles correspond to impurity atoms.

small periodic mechanical stresses accompanying acoustic vibration of the sample, kinks move along the dislocation, overcoming second-order Peierls barriers $U_p(x)$ (Fig. 4b). The contribution from kink chains L_i bounded by impurity atoms (Fig. 4c) to the response of the sample to acoustic excitation becomes resonant under certain condition, causing the formation of the absorption peak. The shape of the peak and its position on the temperature axis are determined by the temperature dependence of the mobility of kinks in the relief $U_p(x)$.

3. INTERACTION OF ACOUSTIC VIBRATIONS WITH DISLOCATION KINKS

An individual kink connecting two linear segments of a dislocation line, which are located in neighboring valleys of the Peierls relief (Fig. 4a), is characterized by the width λ_k and effective mass m_k. In the simple case of a sinusoidal relief, these quantities are defined as[23]

$$\lambda_k = a\left(\frac{2C}{\pi a b \sigma_P}\right)^{1/2}, \quad m_k = \frac{4aM}{\pi^2}\left(\frac{\pi a b \sigma_P}{2C}\right)^{1/2}, \tag{18}$$

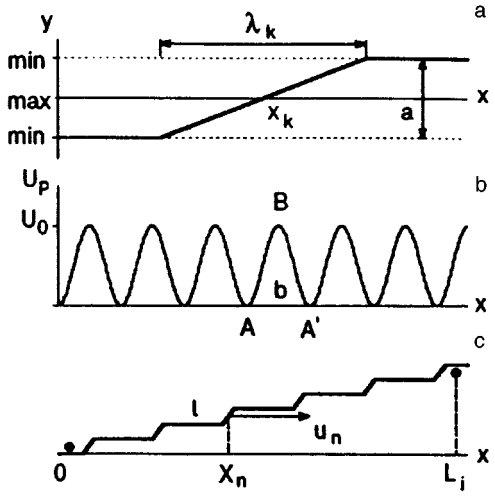

FIG. 4. Kinks on a dislocation line[15]: and individual kink and its geometrical parameters (a), Second-order Peierls relief for a kink (b), and a kink chain bounded by impurity atoms (●) (c).

where C and M are the linear densities of eigenenergy and effective mass of the dislocation, σ_p the Peierls stress, a the Peierls relief period, and b the magnitude of the Burgers vector of the dislocation. The one-dimensional motion of the kink along the peak of the relief (the x-axis in Fig. 4a) is equivalent to the motion of a particle of mass m_k is we choose the coordinate x_k of the center of the kink as the coordinate of such a pseudoparticle. The kinks moves in the periodic second-order potential $U_P(x)=U_P(x+b)$ of the Peierls relief (Fig. 4b), and the total potential energy of the kink in the presence of a shear stress $\sigma(x,t)$ in the dislocation slip plane has the form

$$U_p(x,t)=U_P(x)-ab\int \sigma(x,t)dx. \tag{19}$$

The role of the thermostat-medium in which the motion of the kink takes place is played by the system of conduction electrons and the system of thermal phonons. The scattering of electrons and phonons at a kink moving at a constant average velocity $\bar{\dot{x}}=V_k=\text{const}$ leads to the emergence of the viscous drag force βV_k,[4–6] and the drag coefficient is the sum of the electron and phonon components.

Let us consider the interaction of the acoustic field with an individual kink chain L_i bounded by impurity atoms (Fig. 4c). For a large length L_N of the initial segment and not very high concentrations of impurities $b/L_N \ll c \ll b/\lambda$, the segments L_i contain a large number N_i of kinks separated by linear segments $l=L_i/N_i+1 \gg \lambda_k$. The kinks interact with one another through long-range forces of the Coulomb type,[3] and hence form equidistant chains $X_n=nl$ $(n=1,2,...,N_i)$ in the absence of stresses $(\sigma=0)$. If the shear stress component $\sigma(x,t)=\sigma_0(x)\exp(i\omega t)$ acting in the region of location of the chain (ω is the cyclic frequency of vibrations) has a small amplitude $ab^2|\sigma_0| \ll U_0$, the chain performs small forced vibrations in which an individual kink with number n performs diffusion drift in the relief (19), being displaced from the equilibrium position X_n by $|\bar{x}_{kn}-X_n| \geqslant b$.

Under real experimental conditions, $\omega \leqslant 10^8\ \text{s}^{-1} \ll \nu_A$, and the acoustic wavelength is $2\pi s/\omega \geqslant 10^{-2}\ \text{cm} \gg L_i$ (s is the velocity of sound). These inequalities allow us to assume that the stress σ_0 is uniform over the length L_i. Under the action of a uniform force $f_\sigma=ab\sigma_0\exp(i\omega t)$ varying slowly with time, individual kinks perform diffusive drift in the relief $U_P(x)$ considered at the end of Sec. 1. Such a motion can be described conveniently by using average displacements $u_n(t)=\langle \bar{x}_{kn}\rangle - X_n$ which satisfy the inequalities max $|u_n| \gg b$ and $|u_{n+1}-u_n| \ll l$. In the case of diffusive drift of a kink, the average force of inertia $m_k\ddot{u}_n \sim m_k\omega^2 u_n$ is negligibly small as compared to the diffusive drag force $\beta_d\dot{u}_n \sim \omega\beta_d u_n (m_k\omega \ll \beta_d)$. For this reason, the collective movement of a kink chain is determined by the balance of drag forces $\beta_d\dot{u}_n$, the force f_{nn} of interaction between kinks, and the driving force f_σ:

$$\beta_d\dot{u}_n+\sum_{n'} f_{nn'}=ab\sigma_0 e^{i\omega t}. \tag{20}$$

It was shown in the monograph[3] that in the case of small vibrations of a chain containing a large number N_i of kinks, the force $\sum_n fnn'$ can be approximated by the formula

$$\sum_{n'} f_{nn'} \cong \frac{\pi^2 a^2 C_k}{lL_i^2}u_n,$$

where C_k is the effective linear tensile force in the kink chain (by the order of magnitude, $2C_k \sim 2C \sim Gb^2$, where G is the shear modulus). Consequently, the kink chain under the action of a varying stress performs forced vibrations equivalent to the vibrations of an overdamped oscillator:

$$u_n(t)=\frac{\sigma_0 b l^3(N_i+1)^2}{\pi^2 a C_k}\frac{e^{i\omega t}}{1+i\omega\tau_{di}},$$

$$\tau_{di}=\frac{\beta_d l^3(N_i+1)^2}{\pi^2 a^2 C_k}. \tag{21}$$

Using formula (21), we can easily calculate the energy w_i dissipated by the kink chain L_i over the period of vibrations $2\pi/\omega$:

$$w_i=\sum_{n=1}^{N_i 2\pi/\omega}\int_0 dt\ \text{Re}\ f_\sigma(t)\text{Re}\ \dot{u}_n(t)$$

$$=\frac{\sigma_0^2 b^2 l^3 N_i(N_i+1)^2}{\pi C_k}\frac{\omega\tau_{di}}{1+\omega^2\tau_{di}^2}. \tag{22}$$

In real samples, the parameters N_i and l are random quantities. Let us introduce the average number ρ_k of dislocation kinks per unit volume and the dimensionless parameter

$$\kappa=\overline{\left(\frac{l}{a}\right)^3(N_i+1)^2}=\overline{\left[\frac{L_i^3}{a^3(N_i+1)}\right]}, \tag{23}$$

where the bar indicates statistical averaging over the ensemble of kinks. In addition, the sample contains several equivalent slip systems with dislocations of the type under investigation, and hence we can characterize their interaction with an individual mode of elastic vibrations of the sample by introducing the average orientational factor χ defined by the relation $2W_0M_e\chi=\sigma_0^2$, where M_e is the elastic modulus corresponding to the given vibrational mode and W_0 the energy of vibrations averaged over the period. Calculating the mean energy dissipated in a unit volume of the sample by using formula (22), we obtain the following expression for the logarithmic decrement of the individual vibrational mode:

$$\delta=\frac{\overline{\Sigma_{L_i}w_i}}{2W_0}=\frac{\chi M_e b^2 a^3 \kappa\rho_k}{\pi C_k}\frac{\omega\tau_d}{1+\omega^2\tau_d^2}, \tag{24}$$

$$\tau_d=\frac{a\kappa\beta_d}{\pi^2 C_k}=\frac{a\kappa kT}{\pi^2 b^2 C_k \nu_0(\beta,t)}\exp\left(\frac{U_0}{kT}\right). \tag{25}$$

While deriving the expression for the relaxation time τ_d, we have used formula (17) for the diffusion drag coefficient β_d.

Formulas (24) and (25) provide an exhaustive description of the contribution of dislocation kinks to the internal friction of the sample. These formulas contain the parameters

ρ_k and κ characterizing the distribution of kinks over the sample volume as well as the parameters U_0 and $\nu_0(\beta,T)$ characterizing the interaction of an individual kink with the second-order Peierls relief and quasiparticles (electrons and phonons). The temperature dependence of decrement $\delta(T)$ might acquire peaks located at the points $T_p(\omega)$ on the temperature scale, which are defined by the equation

$$\omega\tau_d(T_p)=1. \tag{26}$$

In the cases when the frequency $\nu_0(\beta,T)$ appearing in formula (25) strongly depends on the dynamic drag coefficient β for kinks, the position T_p of absorption peaks on the temperature axis also becomes sensitive to the value of the coefficient β and to the form of its temperature dependence.

4. THEORY AND EXPERIMENT

According to the results of computer simulation of the motion of a kink on a screw dislocation of the slip system $\langle 111\rangle\{011\}$ in bcc metals, the typical heights U_0 of the second-order Peierls barriers are of the order of 10^{-3} eV.[22] For such values of activation energy and reasonable values of the parameters appearing in the preexponential factor of formula (25), the peak on the temperature dependence of decrement (24) falls in the region of helium temperatures. The peak height

$$\delta_m=\delta(T_p)=\frac{\chi M_e b^2 a^3 \kappa\rho_k}{2\pi C_k} \tag{27}$$

is proportional to the parameters κ and ρ_k characterizing the kink distribution in the sample. Thus, the model formulated in Sec. 2 and formulas (24) and (25) corresponding to it provide a qualitative description for most of properties of the Kramer–Bauer peak, which are listed in that section. An additional analysis is required only for the effect of displacement of the peak during a superconducting transition.

Analyzing Eq. (26) connecting the peak temperature T_p with the vibrational frequency ω,[15] we assumed that the dependence of relaxation time τ_d on the dynamic drag coefficient β is insignificant and put $\nu_0=\nu_A$ in formula (25). In this case, Eq. (26) can be written in the form

$$\ln\,\omega T_p=-\ln\,\alpha-\frac{U_0}{kT_p}, \tag{28}$$

$$\alpha=\frac{a\kappa k}{\pi^2 b^2 C_k \nu_A}. \tag{29}$$

A comparison of experimental results given in Table I with formula (28) is illustrated in Fig. 5. For the normal (n) state, the position of the peak on the temperature axis is in good agreement with formula (28), but for the superconducting (s) state the agreement is much worse. Besides, the slopes of straight lines for the normal and superconducting states differ considerably, which indicates (under the assumptions made above) the effect of the superconducting transition on the height of Peierls barriers for kinks: $U_{0n}\simeq 2.15$ meV and $U_{0s}\simeq 3.23$ meV.

Here we will consider the possibility of another explanation of the effect of the superconducting transition of the Kramer-Bauer peak, that is based on an analysis of the dependence $\nu_0(\beta,T)$ of frequency in formula (25) on the electron drag coefficient for kinks, which decreases abruptly upon such a transition.[5] According to the conclusions drawn by Kramers, a considerable dependence of frequency $\nu_0(\beta,T)$ on the coefficient β can be observed only when certain inequalities connecting the dynamic drag coefficient β, the kink mass m_k, and the parameters of the relief $U_p(x)$ are satisfied (see formula (14)). In order to obtain semiquantitative estimates, we assume that the relief $U_p(x)$ has a sinusoidal shape

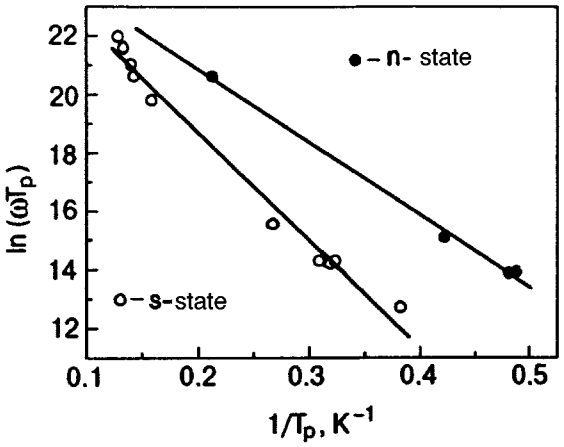

FIG. 5. A comparison of experimental data (Table I) on the frequency dependence of the Kramer–Bauer peak temperature $T_p(\omega)$ with formula (28).[15]

$$U_p(x)=\frac{U_0}{2}\left(1-\cos\frac{2\pi}{b}x\right), \tag{30}$$

and estimate the barrier heights by using the values of the relief $U_0\sim(2-3)\cdot 10^{-3}$ eV obtained from Fig. 5. We will also use the standard estimates of the continual theory of dislocations, i.e., $2C\sim Gb^2$ and $2M\sim\rho b^2$ (ρ is the density of the crystal) and assume that the relation $\sigma_p\sim 10^{-2}G$ typical of most of bcc metals is satisfied for Nb. For the slip system in Nb under consideration, $a=3.3\times10^{-8}$ cm, $b=2.9\times10^{-8}$ cm, $G=3.9\times10^{11}$ dyne/cm^2, and the Nb density $\rho=8.6$ g/cm^3. Using these estimates and formulas (12), (13), and (30), we obtain the order-of-magnitude estimates for several important parameters appearing in formula (14):

$$m_k\sim10^{-23}\text{ g},\quad \nu_A=\nu_B\sim5\times10^{11}\text{ s}^{-1},$$

$$\beta_0(T\sim5\text{ K})\sim10^{-12}\text{ g}\times\text{s}^{-1}. \tag{31}$$

Going over to the estimate of the drag coefficient β for kinks, we note that elastic scattering of conduction electrons and thermal phonons at kinks plays the leading role in the dynamic drag of kinks in bcc metals in the helium temperature region.[4,5] Using the results presented in the reviews,[4,5] we can write the following expression to the total contribution of electrons and phonons to the coefficient β at $T<10$ K:

$$\beta=\beta_e+\beta_{\rm ph}=\frac{a}{\lambda_k}\left[q_e abp_F n_e\gamma_{n,s}(T)+q_{\rm ph}\frac{\hbar b}{a^3}\left(\frac{T}{\Theta}\right)^{9/2}\right];$$

$$\gamma_n(T)\equiv 1, \quad \gamma_s(T)=2\left[1+\exp\frac{\Delta(T)}{kT}\right]^{-1}. \tag{32}$$

Here p_F and n_e are the Fermi momentum and the number density of conduction electrons respectively, $\gamma_{n,s}(T)$ is a function describing the change in the number of electron excitations upon a transition of the metal from the normal to the superconducting state, $\Delta(T)$ the energy gap of the superconductor, Θ the Debye temperature, and q_e and $q_{\rm ph}$ are numerical coefficients whose exact values are determined by details of scattering of electrons and phonons at the dislocation core. The available theories give only rough estimates for the coefficients q_e and $q_{\rm ph}$ (with an order-of-magnitude spread in values): $q_e\sim 10^{-1}$ and $q_{\rm ph}\sim 5\times 10^5$.

In the case of Nb, $\Theta\simeq 275$ K, $p_F\simeq 10^{-19}$ g·cm/s, and $n_e\simeq 10^{23}$ cm^{-3}. Using this values, we can easily find that the electron component in the drag coefficient in the normal state has the value $\beta_{en}\sim 10^{-13}$ g·s^{-1} and is much larger than the phonon component $\beta_{\rm ph}<10^{-14}$ g·s^{-1} at temperatures $T<10$ K under consideration. In the superconducting state, the electron component of drag decreases abruptly (exponentially) with temperature. The phonon component also decreases, but according to a power law. Consequently, there exists a temperature T_0 below which $\beta_{es}(T)<\beta_{\rm ph}(T)$. The temperature T_0 is determined by the condition of equality of the electron and phonon components of drag in the superconducting state, which can be written in the form of the equation

$$\gamma_s(T_0)=q\left(\frac{T_0}{\Theta}\right)^{9/2}, \quad q=\frac{\hbar q_{\rm ph}}{q_e p_F n_e a^4}. \tag{33}$$

Unfortunately, the value of the parameter q can be estimated only to within two orders of magnitude in view of a large indeterminacy in the parameters $q_{\rm ph}$ and q_e: $q\sim 10^5-10^7$. Taking into account this indeterminacy and using the value of the gap width for Nb $\Delta(0)\simeq 1.5\times 10^{-3}$ eV,[24] we can easily obtain the estimate $T_0\sim(1-3)$K.

The above analysis shows that for temperatures of interest, the dynamic drag coefficients for kinks satisfies the inequality $\beta<\beta_0$, and hence we must use the expression in the upper line of formula (14) for the frequency factor $\nu_0(\beta,T)$. In the temperature range $T_0<T<T_c$, the phonon component in formula (32) can be neglected, which leads to the following expression for the relaxation time τ_d:

$$\tau_d(T)=\frac{\eta T^2}{\gamma_{n,s}(T)}\exp\left(\frac{U_0}{kT}\right), \tag{34a}$$

$$\eta=\frac{k^2 m_k a\kappa}{\pi^2 b^2 C_k U_0 \beta_{en}}. \tag{34b}$$

Formula (34a) provides a natural explanation for the effect of an increase of the activation energy for the Kramer–Bauer peak upon a transition of Nb to the superconducting state: at low temperatures, $\Delta(T)\gg kT$, and the temperature dependence of relaxation time in the superconducting state acquired the form

$$\tau_d(T)\cong\frac{\eta T^2}{2}\exp\left(\frac{U_0+\Delta}{kT}\right).$$

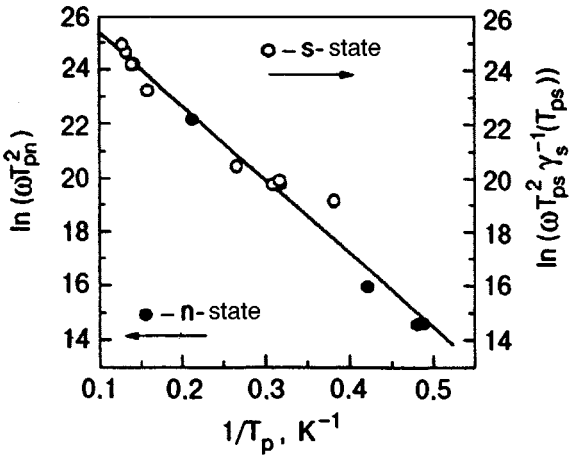

FIG. 6. A comparison of experimental data (Table I) on the frequency dependence of the Kramer–Bauer peak temperature $T_p(\omega)$ with formulas (35). The values of the function $\gamma_s(T)$ are calculated by using the data on the value of the gap $\Delta(T)$ for Nb, presented in the review in Ref. 24.

It should be noted that the order of magnitude of the quantity Δ corresponds to the activation energy jump determined from the change in the slopes of the straight lines in Fig. 5. However, in the present case, the effect is not associated with a change in the lattice parameters of Nb upon a superconducting transition, but is a consequence of the anomalous effect of viscosity on the Brownian movement of particles (dislocation kinks in our case) predicted by Kramers.

The application of formula (34a) allows us to write Eq. (26) defining the peak temperature T_p in the form

$$\ln\,\omega T_{pn}^2=-\ln\,\eta-\frac{U_0}{kT_{pn}}; \tag{35a}$$

for the normal state and

$$\ln\frac{\omega T_{ps}^2}{\gamma_s(T_{ps})}=-\ln\,\eta-\frac{U_0}{kT_{ps}}, \tag{35b}$$

for the superconducting state. Figure 6 illustrates good agreement between formulas (35) and experimental results given in Table I. It can be seen from the figure that the values of T_p recorded experimentally in the normal (T_{pn}) and in the superconducting (T_{ps}) states lead to identical values of the barrier height $U_0\simeq 2.4\times 10^{-3}$ eV and the parameter $\eta\simeq 1.5\times 10^{-12}$s·K^{-2}.

An important circumstance supporting the applicability of the above consideration to a description of the Kramer-Bauer peak is the correlation of the temperatures T_{ps} with the magnitude and temperature dependence of the energy gap $\Delta(T)$ of Nb, which are determined from independent experiments.[24]

Using the empirical estimates of the parameters of the theory obtained above, the experimental values of $\delta_m\sim 10^4$, and formulas (27) and (34b), we can also obtain the order-of-magnitude estimates for the parameters characterizing the kink distribution in the samples: $\kappa\sim 10^5$ and $\rho_k\sim 10^{14}$ cm^{-3}.

Thus, the dislocation model described in Sec. 2 together with the Kramers theory of activated motion of a particle

through a potential barrier as well as the theory of electron dislocation drag provide a satisfactory semiquantitative description of all the peculiarities of the Kramer–Bauer peak detected in experiments. It should be noted, however, that the point $T_{ps}=2.62$ K in Fig. 6 deviates noticeably from the straight line described by Eq. (35b). The most plausible reason behind such a deviation is apparently the role of the phonon component in the dynamic drag coefficient for kinks in the s-state, which increases upon cooling. In order to describe this deviation quantitatively, we must put $q\sim 10^7$ in Eq. (33) and the corresponding value of $T_0\simeq 3$ K. However, an unambiguous interpretation of this deviation requires the experimental detection of the peak in the s-state at lower temperatures, which is possible only for vibrations with a cyclic frequency $\lesssim 10^4$ s^{-1}.

Concluding this section, it is also appropriate to discuss the considerations[25] concerning the possibility of the effect of quantum properties of dislocation kinks on the properties of the Kramer–Bauer peak. According to general laws of quantum statistics, there must be a characteristic temperature T_q below which the diffusion of kinks in the relief $U_P(x)$ will be determined not only by the thermally activated transition of kinks through the barriers U_0, but also by the possibility of under-the-barrier passage (quantum tunneling). A detailed discussion of tunneling of kinks through the barriers of the second-order Peierls relief and estimates of the temperature T_q were given by Petukhov[26]:

$$kT_q \cong \frac{\hbar}{b}\left(\frac{U_0}{2m_k}\right)^{1/2} = \hbar\nu_A . \tag{36}$$

According to conclusions drawn in Ref. 26, the diffusion of kinks at $T>T_q$ is thermally activated, and a transition to the purely quantum limit occurs at $T<0.5T_q$. In the temperature interval $(0.5\text{-}1)T_q$, diffusion is determined by the joint effect of quantum tunneling and thermal activation. Substituting the parameters of kink in Nb into (36) leads to the estimate $T_q\sim 3$ K. Consequently, we can expect a significant influence of quantum effects on the Kramer–Bauer peak in experiments at frequencies $\omega<10^4$ s^{-1}, for which the temperature of the peak is shifted below 2 K. A theoretical description of such effects should be based of a quantum analog of the Kramers theory.

CONCLUSIONS

1. This research aims at theoretical interpretation of the acoustic absorption peak discovered for the first time by Kramer and Bauer,[10] who studied niobium at liquid helium temperatures, and observed later by some other authors.[11–15] The main attention was paid to an analysis of the most interesting peculiarity of the peak, i.e., its shift towards low temperature upon a transition of Nb from the superconducting to the normal state, induced by a magnetic field.
2. The analysis is based on the model of resonant interaction of acoustic vibrations with kink chains at screw dislocations of the slip system $\langle 111\rangle\{011\}$, which was proposed by us earlier,[15] and on the application of the results obtained by Kramers,[1] who describes the kinetics of a thermally activated emergence of a particle from a potential well taking into account of the force of viscous friction acting on it, for describing kink diffusion in the lattice potential relief (second-order Peierls relief). When kinks move along dislocations in a metal at low temperatures, the drag is mainly due to their interaction with conduction electrons. For this reason, a transition of the metal to the superconducting state (as well as the reverse transition), which changes significantly the viscosity of the electron gas, is also accompanied by a strong controllable change in the drag coefficients for kinks. This creates unique premises for experimental verification of the conclusions of the Kramers theory concerning the role of viscosity in activated motion of particles.
3. The basic concepts of the Kramers theory are presented in this paper in the form convenient for application to a description of diffusion of dislocation kinks. The main properties of the Kramer–Bauer peak recorded experimentally are systematized, and the data characterizing the dependence of the temperature of the peak on the vibrational frequency in the normal and superconducting states are tabulated.
4. It is shown that the conditions for observing the nontrivial kinetic effect predicted by Kramers, i.e., the increase in the diffusion mobility of particles with the drag coefficients, are satisfied for kinks in Nb in the helium temperature range. Owing to this effect, the relaxation time (the characteristic diffusion time) for dislocation kink chains in the superconducting state is much longer than in the normal state, which caused the experimentally observed displacement of the dislocation absorption peak towards low temperatures upon a transition of Nb from the superconducting to the normal state.
5. According to the conclusions of the theory, the displacement of the Kramer–Bauer peak as a result of a superconducting transition must correlate with the temperature dependence of the energy gap of the superconductor. The use of gap values obtained from independent experiments[24] in the analysis of the properties of the peak confirms these conclusions. This circumstance is a sound argument in favor of the adequacy of the theory and experiments.
6. A comparison of experimental data with the results of the theory makes it possible to obtain empirical estimates for a number of parameters characterizing kinks at dislocations of the system $\langle 111\rangle\{011\}$ in Nb: the orders of magnitude of the kink mass, second-order Peierls barrier height, electron and phonon drag coefficients for a kink, and the volume density of kinks.
7. An approximate estimate of the characteristic temperature (2–3 K) below which kink diffusion in the lattice relief in Nb can acquire quantum-mechanical features is obtained. Quantum diffusion of kinks should be studied by acoustic spectroscopy methods at vibrational frequencies of $\lesssim 10^4$ Hz.

This research was partly supported by the Ukrainian

State Foundation for Fundamental Studies (project No. 2.4/156 ''Bion'') and by the International Soros Program Supporting Education in Science (grant No. SPU 072042).

*E-mail: palval@ilt.kharkov.ua

[1)]The considerations described below differ slightly from the Kramers' considerations.

[1] H. A. Kramers, Physica **7**, 284 (1940).
[2] L. P. Kubin, Comments Condens. Matter Phys. **14**, 67 (1988).
[3] J. Hirt and I. Lote, *The Theory of Dislocations* [Russian transl.], Atomizdat, Moscow (1972).
[4] A. Seeger and P. Schiller, in *Physical Acoustics, Principles and Methods* Principles and Methods (ed. by W. Masou), vol. 3, Academic Press, New York (1966).
[5] M. I. Kaganov, V. Ya. Kravchenko, and V. D. Natsik, Usp. Fiz. Nauk **111**, 655 (1973) [Sov. Phys. Usp. **16**, 878 (1973)].
[6] V. I. Al'shits and V. L. Indenbom, Usp. Fiz. Nauk **115**, 3 (1975) [Sov. Phys. Usp. **18**, 1 (1975)].
[7] V. I. Startsev, in *Dislocations in Solids*, North-Holland, Amsterdam, New York, Oxford (1983).
[8] V. I. Startsev, V. Ya. Il'ichev, and V. V. Pustovalov, *Plasticity and Strength of Metals and Alloys at Low Temperatures* [in Russian], Metallurgiya, Moscow (1975).
[9] G. Alefeld, J. Appl. Phys. **36**, 2633 (1965).
[10] E. J. Kramer and C. L. Bauer, Phys. Rev. **163**, 407 (1967).
[11] K. F. Huang, A. V. Granato, and H. K. Brinbaum, Phys. Rev. B **32**, 2178 (1985).
[12] E. Dresher-Krasicka and A. V. Granato, J. Phys. (Paris) **46**, 1073 (1985).
[13] G. Cannelli, R. Cantelli, and F. Cordero, Phys. Rev. B **34**, 7721 (1986).
[14] P. P. Pal-Val, V. D. Natsik, H.-J. Kaufmann, and A. S. Sologubenko, Mater. Sci. Forum **119–121**, 117 (1993).
[15] P. P. Pal-Val, V. D. Natsik, and L. N. Pal-Val, Fiz. Nizk. Temp. **21**, 647 (1995) [Low Temp. Phys. **21**, 505 (1995)].
[16] J. Manning, *Diffusion Kinetics for Atoms in Crystals*, Princeton University Press, Princeton (USA) (1968).
[17] C. V. Heer, *Statistical Mechanics. Kinetic Theory and Statistic Processes*, Acad. Press, New York-London (1972).
[18] P. P. Pal-Val, V. D. Natsik, L. N. Pal-Val, and T. V. Kustova, Phys. Status Solidi A **157**, 311 (1996).
[19] E. M. Forgan and C. E. Gough, Phys. Lett. **21**, 133 (1966).
[20] M. Gottlieb, M. Garbuni, and S. K. Johnes, in *Physical Acoustics, Principles and Methods* (ed. by W. Masou and R. Thupston), vol. 7, Academic Press, New York (1968–1970).
[21] J. Dominec and K. Misek, J. Phys. (France) **48**, C8-489 (1987).
[22] O. V. Klyavin, N. P. Likhodeev, and A. N. Orlov, Fiz. Tverd. Tela (Leningrad) **27**, 3388 (1985) [Sov. Phys. Solid State **27**, 2039 (1985)].
[23] A. M. Kosevich, *Dislocations in the Theory of Elasticity* [in Russian], Naukova Dumka, Kiev (1978).
[24] R. Meservey and B. B. Schwartz, in *Superconductivity*, vol. 1, Marcel Dekker, Inc., New York (1969).
[25] E. B. Hermida, A. Seeger, and W. Ulfert, J. Phys. (Paris) IV **IV 6**, C8-175 (1996).
[26] B. V. Petukhov, Crystallogr. Rep. **40**, 433 (1995).

Translated by R. S. Wadhwa

Hamiltonian formalism in the theory of quadruple magnet

A. A. Isayev

*National Science Center ''Kharkov Physicotechnical Institute,'' 310108 Kharkov, Ukraine**
(Submitted April 18, 1997; revised June 5, 1997)
Fiz. Nizk. Temp. **23**, 1243–1246 (November 1997)

Poisson brackets are obtained for dynamic variables of a quadrupole magnet, i.e., the spin density and the matrix of the quadruple moments. The starting point for the analysis is the derivation of the kinematic component of the Lagrangean of the system. Equations of motion are derived, and the number of Goldstone and activation modes is determined for the case when the energy functional is invariant to spin rotations. © *1997 American Institute of Physics.* [S1063-777X(97)01311-X]

1. POISSON BRACKETS FOR A QUADRUPLE MAGNET

The description of magnets in which tensor interactions[1] (higher-order exchange interactions and one-ion anisotropy) exist along with ordinary spin-spin interactions necessitates the application of not only dipole (spin) degrees of freedom, but also multipole (quadrupole, octupole, etc.) degrees of freedom.[2] This is due to the fact that the replacement of tensor interactions by certain effective fields which can be expressed only through magnetization and the application of uncoupling of the type $\langle (s^i)^m \rangle \to \langle s^i \rangle^m$ are possible only when tensor interactions are weak. Even in the simple case when the spin $S=1$, the matrix of the quadruple moment must be used along with the spin variable. Such dynamics, which includes tensor degrees of freedom, can differ significantly from the orientational dynamics for magnetization described by the Landau–Lifshitz equations.

This communication aims at the development of the Hamilton approach to the theory of a quadrupole magnet. The Hamilton approach is known to be an effective method for deriving nonlinear dynamic equations which take into account the symmetry properties of the Hamiltonian automatically.[3] Being a phenomenological formalism, it is simpler and more clear from the physical point of view than the microscopic approach which, as a rule, depends on the model used.[2] The Hamilton approach is based on Poisson brackets (PB) of dynamic variables of the system. In the continual limit, the dynamic variables of a quadrupole magnet include the spin density $s_\alpha(x)$ and the matrix $f_{\alpha\beta}(x)$ of the quadrupole moment. Poisson brackets can be obtained in several different ways.[4] We shall follow the approach developed in Ref. 5, according to which the form of the kinematic component of the Lagrangean of the system

$$L_k = \int d^3x F_\alpha(x;\varphi)\varphi_\alpha(x) \equiv \int d^3x \mathscr{L}_k(x)$$

(φ_α are dynamic variables and $F_\alpha(x;\varphi(x'))$ is a certain functional of the variables φ_α) and variations of dynamic variables which leave the kinematic component invariant play a decisive role for determining the PB structure. For this reason, we shall consider the derivation of the functional $\mathscr{L}_k(x)$ in the case of a quadrupole magnet.

In Ref. 6, the kinematic component of the Lagrangean for a magnet with complete breaking of symmetry relative to spin rotations was written in the form

$$\mathscr{L}_k(x) = -s_\alpha(x)\omega_\alpha(x), \quad \omega_\alpha = \frac{1}{2}\varepsilon_{\alpha\beta\gamma}\tilde{a}_{\gamma\mu}\dot{a}_{\mu\beta}, \tag{1}$$

where a id the real matrix of rotations in the spin space ($a\tilde{a}=1$). Using the kinematic component (1), we can obtain PB for the variables $s_\alpha(x)$ and $a_{\alpha\beta}(x)$. Differentiating the condition of orthogonality of the matrix a with respect to time, we obtain

$$\dot{a}\tilde{a} + a\dot{\tilde{a}} = 0. \tag{2}$$

Modifying the density of the kinematic component $\mathscr{L}_k$ of the Lagrangean taking into account the limitation (2), we obtain

$$\mathscr{L}_k \to \mathscr{L}_k = \mathscr{L}_k + \frac{1}{2} f_{\alpha\beta}(\dot{a}\tilde{a} + a\dot{\tilde{a}})_{\alpha\beta}. \tag{3}$$

Here the quantities $f_{\alpha\beta}$ play the role of Lagrangean multipliers (it will be shown below that the matrix $f_{\alpha\beta}$ has the meaning of the matrix of the quadrupole moment). Assuming that the matrix $f_{\alpha\beta}$ is symmetric ($f=\tilde{f}$), we transform expression (3) to the form

$$\mathscr{L}_k = c_{\alpha\beta}\, a_{\beta\alpha}, \tag{4}$$

where

$$c_{\alpha\beta} = \left(f_{\alpha\rho} - \frac{1}{2}\varepsilon_{\alpha\rho\nu} s_\nu \right) a^{-1}_{\rho\beta}, \quad \tilde{f} = f. \tag{5}$$

Henceforth, we shall assume that a is the matrix of an arbitrary linear transformation. In fact, we extend the set of dynamic variables. A new set of variables corresponding to the density of the kinematic component (4) includes the spin density $s_\alpha(x)$, the matrix $a_{\alpha\beta}(x)$ of an arbitrary linear transformation, and the Lagrangean multipliers $f_{\alpha\beta}(x)$. The PB for the initial set of variables $s_\alpha(x), a_{\alpha\beta}(x)$ (where $a_{\alpha\beta}$ is the rotation matrix) will form the subalgebra of PB for the ex-

tended set of variables. Also, the new set of variables will be used to obtain the subalgebra of PB corresponding to a quadrupole magnet.

The density of the kinematic component (4) has the standard form known from classical mechanics. Consequently, we can immediately write the PB for the variables a and c:

$$\{a_{\alpha\beta}(x),a_{\mu\nu}(x')\}=\{c_{\alpha\beta}(x),c_{\mu\nu}(x')\}=0,$$
$$\{a_{\alpha\beta}(x),c_{\mu\nu}(x')\}=\delta_{\alpha\nu}\delta_{\beta\mu}\delta(x-x'). \tag{6}$$

For further analysis, it is convenient to introduce the tensor $g_{\alpha\beta}$:

$$g_{\alpha\beta}=c_{\alpha\nu}\,a_{\nu\beta}. \tag{7}$$

It follows from (5) that in this case we have

$$g_{\alpha\beta}=f_{\alpha\beta}-\frac{1}{2}\,\varepsilon_{\alpha\beta\gamma}s_\gamma.$$

In turn, the spin density can be expressed in terms of the antisymmetric component of $g_{\alpha\beta}$:

$$s_\alpha(x)=\varepsilon_{\alpha\beta\gamma}g^a_{\gamma\beta}(x),\quad g^a_{\mu\nu}\equiv\frac{1}{2}\,(g_{\mu\nu}-g_{\nu\mu}), \tag{8}$$

and the matrix $f_{\alpha\beta}$ is expressed in terms of the symmetric component of $g_{\alpha\beta}$:

$$f_{\alpha\beta}=g^s_{\alpha\beta},\quad g^s_{\alpha\beta}\equiv\frac{1}{2}\,(g_{\alpha\beta}+g_{\beta\alpha}). \tag{9}$$

Taking into account the definition (7) of the matrix $g_{\alpha\beta}$ and formulas (6), we can easily obtain the following algebra for the variables $a_{\alpha\beta}(x)$ and $g_{\alpha\beta}(x)$:

$$\{a_{\alpha\beta}(x),g_{\mu\nu}(x')\}=\delta_{\beta\mu}a_{\alpha\nu}(x)\,\delta(x-x'),$$
$$\{g_{\alpha\beta}(x),g_{\mu\nu}(x')\}=(g_{\alpha\nu}(x)\,\delta_{\beta\mu}-g_{\mu\beta}(x)\,\delta_{\alpha\nu})\,\delta(x-x'). \tag{10}$$

The variables $s_\alpha(x)$ and $f_{\alpha\beta}(x)$ are connected with the variables $g_{\alpha\beta}(x)$ through relations (8) and (9). Using these expressions and (10), we can obtain PB for the dynamic variables $s_\alpha(x)$, $a_{\alpha\beta}(x)$, and $f_{\alpha\beta}(x)$:

$$\{f_{\alpha\beta}(x),f_{\mu\nu}(x')\}=\frac{1}{4}\,(\varepsilon_{\alpha\gamma\nu}\delta_{\beta\mu}+\varepsilon_{\beta\gamma\mu}\delta_{\alpha\nu}+\varepsilon_{\beta\gamma\nu}\delta_{\alpha\mu}$$
$$+\varepsilon_{\alpha\gamma\mu}\delta_{\beta\nu})s_\gamma(x)\,\delta(x-x'),$$
$$\{s_\alpha(x),f_{\beta\gamma}(x')\}=(\varepsilon_{\alpha\beta\rho}f_{\gamma\rho}(x)+\varepsilon_{\alpha\gamma\rho}f_{\beta\rho}(x))\,\delta(x-x'),$$
$$\{s_\alpha(x),s_\beta(x')\}=\varepsilon_{\alpha\beta\gamma}s_\gamma(x)\,\delta(x-x'), \tag{11}$$

$$\{a_{\alpha\beta}(x),s_\mu(x')\}=\varepsilon_{\beta\mu\rho}a_{\alpha\rho}(x)\,\delta(x-x'),$$
$$\{a_{\alpha\beta}(x),a_{\mu\nu}(x')\}=0,$$
$$\{a_{\alpha\beta}(x),f_{\mu\nu}(x')\}=\frac{1}{2}\,(\delta_{\beta\mu}a_{\alpha\nu}(x)+\delta_{\beta\nu}a_{\alpha\mu}(x))\,\delta(x-x'). \tag{12}$$

The first three formulas in (11) define the subalgebra of the dynamic variables s and f. We shall give a physical interpretation of this subalgebra, by replacing the dynamic variables s_α and $f_{\alpha\beta}$ by the operators $\hat{s}_\alpha$ and $\hat{f}_{\alpha\beta}$ and the PB $\{...,...\}$ by the commutators $(1/i)[\ldots,\ldots]$ according to the general rules of quantum mechanics. Then relations (11) assume the form

$$[\hat{f}_{\alpha\beta}(x),\hat{f}_{\mu\nu}(x')]=\frac{i}{4}\,(\varepsilon_{\alpha\gamma\nu}\delta_{\beta\mu}+\varepsilon_{\beta\gamma\mu}\delta_{\alpha\nu}+\varepsilon_{\beta\gamma\nu}\delta_{\alpha\mu}$$
$$+\varepsilon_{\alpha\gamma\mu}\delta_{\beta\nu})\hat{s}_\gamma(x)\,\delta(x-x'),$$
$$[\hat{s}_\alpha(x),\hat{f}_{\beta\gamma}(x')]=i(\varepsilon_{\alpha\beta\rho}\hat{f}_{\gamma\rho}(x)+\varepsilon_{\alpha\gamma\rho}\hat{f}_{\beta\rho}(x))\,\delta(x-x'),$$
$$[\hat{s}_\alpha(x),\hat{s}_\beta(x')]=i\varepsilon_{\alpha\beta\gamma}\hat{s}_\gamma(x)\,\delta(x-x').$$

We can easily explicate this algebra in the language of spin matrices corresponding to the spin $S=1[(s_\alpha)_{\mu\nu}=i\varepsilon_{\alpha\mu\nu}]$, namely,

$$\hat{f}_{\alpha\beta}=\frac{1}{2}\left(\hat{s}_\alpha\hat{s}_\beta+\hat{s}_\beta\hat{s}_\alpha-\frac{2}{3}\,\delta_{\alpha\beta}\hat{s}^2\right). \tag{13}$$

Since $\hat{f}_{\alpha\beta}$ is the operator of the quadrupole moment (see Ref. 7), we shall assume that the quantity $f_{\alpha\beta}$ appearing in formulas (11) is the matrix of the quadrupole moment of spin $S=1$, and $\mathrm{Tr}f=f_{\alpha\alpha}=0$ (relation $f_{\alpha\alpha}=0$ together with subalgebra (11)). Using the PB (11), we obtain dynamic equations for the quantities s_α and $f_{\alpha\beta}$:

$$\dot{s}_\alpha(x)=\varepsilon_{\alpha\beta\gamma}\,\frac{\delta H}{\delta s_\beta(x)}\,s_\gamma(x)+2\varepsilon_{\alpha\beta\rho}f_{\mu\rho}(x)\,\frac{\delta H}{\delta f_{\mu\beta}(x)},$$
$$\dot{f}_{\alpha\beta}(x)=\frac{1}{2}\,\frac{\delta H}{\delta f_{\gamma\nu}(x)}\,(\delta_{\gamma\beta}\varepsilon_{\nu\mu\alpha}+\delta_{\alpha\nu}\,\varepsilon_{\gamma\beta\mu})s_\mu(x)$$
$$+(\varepsilon_{\beta\gamma\rho}f_{\alpha\rho}(x)+\varepsilon_{\alpha\gamma\rho}f_{\beta\rho}(x))\,\frac{\delta H}{\delta s_\gamma(x)}. \tag{14}$$

These equations describe ''ideal hydrodynamics'' of a quadrupole magnet and are valid in the low-temperature region ($T\ll T_c$), in which we can neglect relaxation processes. It follows from Eqs. (14) that the main condition $s^2=\mathrm{const}$ of the orientational dynamics is not satisfied for a quadrupole magnet in the general case. Instead, we have two new independent conserved quantities

$$I_1=\mathrm{Tr}\;f^2-\frac{1}{2}\,s^2\equiv\mathrm{Tr}\;g^2,$$
$$I_2=\mathrm{Tr}\;f^3+\frac{3}{4}\,s_\alpha f_{\alpha\beta}s_\beta\equiv\mathrm{Tr}\;g^3, \tag{15}$$

whose PB with the variables s_α and $f_{\alpha\beta}$ are equal to zero. Since the conservation of the quantities I_1 and I_2 is not associated with a specific structure of the Hamiltonian and is only due to the structure of PB (11), relations (15) can be regarded as kinematic constraints. For this reason, the number of independent dynamic variables is actually equal to six[8–10] and not to eight. From the general algebra (11) and (12), we can single out the subalgebra of dynamic variables $a_{\alpha\beta}$ and s_α (the quantities $f_{\alpha\beta}$ do not appear in this subalgebra), which is compatible with the additional condition $a\tilde{a}=1$. This subalgebra determines the low-frequency dynamics of a many-sublattice magnet.[11]

It should be noted that quantum-mechanical dynamics of a quadrupole magnet with the spin $S=1$ was studied by

many authors (see, for example, the review in Ref. 2 and the literature cited therein). In the case of pure states, this dynamics can be described in terms of four independent variables. In the general case, the complete set of mean values of eight operators $\hat{s}_\alpha, \hat{f}_{\alpha\beta}$ forming the Lie algebra SU(3) and taking into account two kinematic operator identities should be used.

2. SPECTRUM OF COLLECTIVE OSCILLATIONS

The calculation of the spectrum of collective oscillations involves the determination of the corresponding equilibrium values of the spin density s^0 and quadrupole moment f^0 by minimizing the energy functional $H(s,f)$ followed by a linearization of the dynamic equations (14) in the vicinity of the obtained values s^0 and f^0. As a rule, this is a complicated procedure. Here, we shall formulate a few symmetry considerations which make it possible to draw general conclusions concerning the form of possible oscillations in the system.

Let us consider uniform spin rotations described by the matrix c, i.e.,

$$s \to s' = cs, \quad f \to f' = cf\,\tilde{c}, \tag{16}$$

and assume that the energy functional $H(s,f)$ is invariant to transformations (16):

$$H(s,f) = H(s',f'). \tag{17}$$

If in this case the functional $H(s,f)$ attains its minimum value for $s = s^0$ and $f = f^0$, the minimum is degenerate, the degeneracy being described by the transformation

$$s^0 \to s = cs^0, \quad f^0 \to f = cf^0\tilde{c}. \tag{18}$$

The order parameter of a quadrupole magnet is represented by the spin density s_α and the matrix of the quadrupole moment $f_{\alpha\beta}$ or, which is the same, by the traceless matrix $g_{\alpha\beta}$, and is therefore eight-dimensional. According to Monastyrsky,[12] the space of the order parameter as a manifold is a factor-space SO(3)/H, where SO(3) is the group of three-dimensional rotations and H the subgroup of rotations preserving $g^0_{\alpha\beta} \equiv f^0_{\alpha\beta} - (1/2)\,\varepsilon_{\alpha\beta\gamma} s^0_\gamma$: $cg^0\tilde{c} = g^0$. In addition to the trivial identity transformation, the SO(3) group has a nontrivial subgroup, viz., the continuous group of two-dimensional rotations SO(2). Consequently, the space of the order parameter can be either the SO(3) group, or the sphere $S^2 = \mathrm{SO(3)/SO(2)}$. The former case corresponds to a biaxial quadrupole magnet, while the latter indicates the existence of a certain preferred direction and corresponds to a uniaxial quadrupole magnet.

Let us first consider the former case. We assume that the energy functional has a minimum in the class of solutions belonging to SO(3). In this case, displacements of the point of minimum can be of two types. First, these can be three-dimensional displacements in a space tangential to the initial point of minimum. Since these displacements do not draw the minimum from the stationary SO(3) orbit, the three vibrational branches corresponding to these displacements are Goldstone branches. Second, there exist five types of displacements which pull the minimum from the SO(3) orbit; in view of the existence of two kinematic constraints, only three of these displacements are independent. These displacements correspond to three activation branches. Thus, for a biaxial quadrupole magnet with the energy functional invariant to spin rotations, we have three Goldstone and three activation vibrational modes.

Let us now consider a uniaxial quadruple magnet. In this case, the energy minimum belongs to the steady-state S^2 orbit, and there are two types of displacements in a space tangential to this orbit, corresponding to two Goldstone vibrational branches. In addition, there are six displacements in a space transverse to the steady-state orbit, which draw the minimum from the S^2 orbit. Four of these displacements are independent, which corresponds to four activation modes. Thus, two Goldstone and four activation vibrational branches exist for a uniaxial quadrupole magnet.

It should be noted that a symmetry analysis similar to that considered above was used for describing and classifying intrinsic modes in the B-phase of ^{3}He (Ref. 13) and in nematic liquid crystals.[14] In particular, Golo and Ketterson[13] explained the ''real squashing'' of the mode ($J = 2_+$) in experiments of propagation of zeroth sound in $^3\mathrm{He}-B$ on the basis of the theory of representations of the SO(3) group.

The author is grateful to S. V. Peletminsky and M. Yu. Kovalevsky for fruitful discussions.

*E-mail: isayev@kipt.kharkov.ua

[1] È. L. Nagaev, *Magnets with Complex Exchange Interactions* [in Russian], Nauka, Moscow (1988).
[2] V. M. Loktev and V. S. Ostrovskii, Fiz. Nizk. Temp. **20**, 983 (1994) [Low Temp. Phys. **20**, 775 (1994)].
[3] L. A. Takhtadzhyan and L. D. Faddeev, *Hamiltonian Approach in the Soliton Theory* [in Russian], Nauka, Moscow (1986).
[4] I. E. Dzyaloshinskii and G. E. Volovick, Ann. Phys. **125**, 67 (1980).
[5] A. A. Isayev, M. Yu. Kovalevsky, and S. V. Peletminsky, Teor. Mekh. Fiz. **102**, 283 (1995); Preprint ICTP IC/94/329 (1994).
[6] M. Yu. Kovalevsky, S. V. Peletminsky, and A. L. Shishkin, Ukr. Fiz. Zh. **36**, 245 (1991).
[7] L. D. Landau and E. M. Lifshitz, *Quantum Mechanics* [in Russian], Nauka, Moscow (1989).
[8] F. T. Hioe and J. H. Eberly, Phys. Rev. Lett. **47**, 838 (1981).
[9] S. I. Orfanidis, Phys. Lett. **A75B**, 304 (1980).
[10] R. Sasaki and Th. N. Ruijgrok, Physica A **113**, 388 (1982).
[11] A. A. Isayev and S. V. Peletminsky, Teor. Mekh. Fiz. **102**, 470 (1995).
[12] M. I. Monastyrsky, *Topology and Gauge Fields and Condensed Media*, Plenum Press, London (1992).
[13] V. L. Golo and J. B. Ketterson, Phys. Rev. B **45**, 2516 (1992).
[14] V. L. Golo and E. I. Kats, Zh. Éksp. Teor. Fiz. **103**, 857 (1993) [JETP **76**, 420 (1993)].

Translated by R. S. Wadhwa

The behavior of the paramagnetic susceptibility of a $2D$ metal during transitions between normal, pseudogap, and superconducting phases

V. P. Gusynin, V. M. Loktev, S. G. Shaparov

*N. N. Bogoliubov Institute of Theoretical Physics, National Academy of Sciences of the Ukraine, 252143 Kiev, Ukraine**

(Submitted May 23, 1997; revised July 1, 1997)
Fiz. Nizk. Temp. **23**, 1247–1249 (November 1997)

The paramagnetic susceptibility of a $2D$ metal with an arbitrary charge carrier density is calculated. It is shown that the temperature dependence of the susceptibility displays a clearly manifested nonmonotonisity upon a transition from the normal to an ''abnormal'' (also nonsuperconducting) phase whose one-particle spectrum contains a pseudogap. © *1997 American Institute of Physics.* [S1063-777X(97)01411-4]

1. Phenomena occurring in high-temperature superconductors (HTS materials) upon a change in the concentration n_f of mobile charge carriers (holes) in them remain vital problems in solid state physics. Although the relation between doping and magnetic, conducting, and superconducting properties of these compounds has been established reliably, the reasons behind the observed correlations remain unclear. Essentially, the following main tendency should be mentioned: the lower the concentration n_f in cuprate (CuO_2) layers, the stronger the deviations in the properties of HTS materials from the predictions of the theory of a normal Fermi liquid on one hand and the BCS theory of superconductivity on the other hand. For this reason, the concepts of underdoped and overdoped states (modes) in which the behavior of various HTS parameters differ qualitatively have been introduced and used widely (see the reviews in Refs. 1–3 and Ref. 4).

For example, a transition from the normal to the superconducting state in underdoped samples is accompanied with a decrease in the density of quasiparticle states which is not typical of the normal Fermi liquid. It is important that this decrease starts long before the temperature T attains its critical value T_c. The behavior of the heat capacity[5] and the ARPES spectrum[6,7] confirm this effect directly. This decrease is interpreted (see Ref. 4) as an opening of a pseudogap in the electron spectrum of cuprates. According to Pines,[3] the reasons behind the emergence of the pseudogap form a key problem in the HTS theory.

At the same time, other characteristics (the NMR relaxation time and the Knight shift[8]) indicate that the uniform magnetic susceptibility $\chi(T)$ of the normal phase decreases upon cooling at a value of T much higher than T_c, which also contradicts the Fermi-liquid behavior according to which

$$\chi(T)=\chi_{\text{Pauli}}\equiv\frac{1}{\pi}\,\mu_B^2 m$$

in the region $T>T_c$ (here μ_B is the Bohr magneton and m the effective mass of the carrier). According to an alternative point of view (see reviews in Refs. 3, 9, and 10), the main changes occur not in the delocalized subsystem (charge carriers), but in the localized subsystem (spins of Cu^{2+} ions) in which a spin gap can emerge upon a decrease in the magnetic correlation length in view of the fact that the CuO_2 planes contain lattice site magnetic moments. Some critical remarks concerning this hypothesis were formulated in Ref. 1.

It was proved recently[11,12] (by using a simple model of a $2D$ superconductor with an arbitrary n_f) that a pseudogap in the one-electron spectrum and the corresponding pseudogap phase emerge in metallic systems with a lowered dimensionality. In the approximation used, the pseudogap phase is formed self-consistently at a certain temperature T_ρ which for all n_f is higher than T_c ($\equiv T_{\text{BKT}}$ in the $2D$ case, T_{BKT} being the Berezinskii–Kosterlitz–Thouless temperature).

This communication aims at the calculation of the paramagnetic susceptibility (PMS) of a $2D$ metal undergoing a transition from the normal to the pseudogap phase, and then to the superconducting phase (BKT in our case) with singlet pairing. The unexpected result of this research was that the PMS clearly ''perceives'' the transition to the pseudogap (nonsuperconducting) phase, while the transition to the superconducting phase occurs smoothly.

2. The density of the Hamiltonian H^* for $2D$ fermions in an external magnetic field[1)] has the form

$$\begin{aligned}\mathscr{H}(x)=&-\psi_\sigma^+(x)\left(\frac{\nabla^2}{2m}+\mu\right)\psi_\sigma(x)\\&-V\psi_\uparrow^+(x)\psi_\downarrow^+(x)\psi_\downarrow(x)\psi_\uparrow(x)\\&-\mu_B H[\psi_\uparrow^+(x)\psi_\uparrow(x)-\psi_\downarrow^+(x)\psi_\downarrow(x)],\end{aligned}\qquad(1)$$

where all notations are the same as in Ref. 11.

Without considering the details of calculations (which are virtually the same as in Ref. 11), we note that, since the field term in (1) has a diagonal form in spin indices, the general expressions for the statistical sum Z and the thermodynamic potential Ω preserve their form, the only difference being that the one-particle Green's function through which these quantities are defined becomes a function of the field:

$$G(i\omega_n,\mathbf{k})=\frac{(i\omega_n+\mu_B H)\hat{I}+\tau_3\xi(\mathbf{k})-\tau_1\rho}{(i\omega_n+\mu_B H)^2-\xi^2(\mathbf{k})-\rho^2}\,e^{i\omega_n\tau_3\delta},$$

$$\delta\to+0.\qquad(2)$$

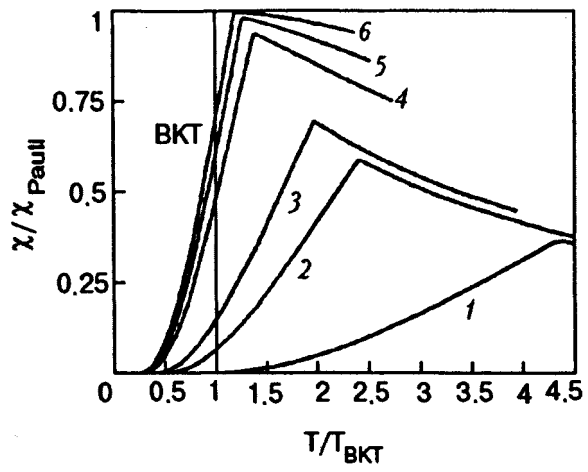

FIG. 1. Temperature dependence of PMS for different values of n_f determined by the value of the ratio $\varepsilon_F/\varepsilon_b$ (ε_b is the energy of a two-particle bound state[1,11]): 0.2 (curve *1*), 0.6 (curve *2*), 1 (curve *3*), 5 (curve *4*), 10 (curve *5*), and 20 (curve *6*).

Thus, Ω is also a function of H, which allows us to calculate directly the required PMS by using the well-known relation

$$\chi(T)=\frac{1}{v}\left.\frac{\partial^2\Omega}{\partial H^2}\right|_{H\to 0}. \tag{3}$$

The final expression for (3) taking into account (2) is simple and has the form

$$\chi(T)=\frac{1}{2}\,\chi_{\text{Pauli}}\int_{-\mu/2T}^{\infty} dx\,\cosh^{-2}\sqrt{x^2+\rho^2/4T^2}. \tag{4}$$

It can easily be verified that if the modulus of the order parameter $\rho=0$ (normal phase), integral (4) can easily be evaluated, and the PMS acquires the form typical for an ideal $2D$ Fermi gas[13]:

$$\chi(T)=\chi_{\text{Pauli}}[1+\exp(-\mu/T)]^{-1}.$$

The results of numerical solution of the self-consistent system of equations for ρ, μ, and T_{BKT} (and also for T_ρ on the critical line $\rho\to 0$), which was derived in Ref. 11, make it possible to calculate $\chi(T)$ directly by using (4) (see Fig. 1). It can be seen that, if the PMS has a sharp kink at $T=T_\rho$, the point of transition to the superconducting state on the $\chi(T)$ curve is actually not manifested. Such a behavior corresponds qualitatively to the situation observed for HTS materials (see Refs. 3 and 14), in which the uniform PMS (as well as other observable parameters) experiences the most noticeable change at a certain temperature $T_*>T_c$. If we assume that this temperature corresponds to the formation of a pseudogap (or ρ, which is actually the same), we must identify T_ρ and T_*. Thus, the temperature T_* introduced empirically by some authors acquires a clear physical meaning.

The curves depicted in Fig. 1 correspond to the disregard of fluctuations of ρ and vortex configurations of the angle θ, which is more or less justified only for phases in which $\rho\neq 0$. However, in the normal phase the fluctuations of the order parameter (and not only of its phase) are significant even for relatively high n_f and can make a contribution to the PMS (which is also negative) in the region $T>T_\rho$.[15] In the given case, we neglect this contribution in order to emphasize the difference in the behavior of the PMS at the points T_{BKT} (i.e., T_c) and T_ρ.

Moreover, our calculations proved (see Fig. 1) that the higher the value of n_f, the relatively smaller the width of the region of the pseudogap phase, which is also in satisfactory agreement with the pattern following from the experiments.[4,14] As regards the thermodynamics of the phase transition from the normal to the pseudogap phase, it must be studied only by taking into account the damping of the excitations present in the system, which requires a special analysis (naturally, including a more complete analysis of the contribution from fluctuations). It should also be borne in mind that this transition does not lower the symmetry spontaneously and hence cannot be regarded as a true phase transition. The only thing that can be stated is that the value of ρ starts increasing rapidly at the point T_ρ (if $T<T_\rho$), while above this temperature the value of ρ decreases quite slowly.

However, the potentialities of the simple model used for obtaining the results described above should not be overestimated, although these results are in good agreement with the conclusions drawn on the basis of experiments. The model not only disregards the three-dimensional nature of real HTS materials (this effect is weak, but is essential for T_c), but also ignores such an important circumstance as the presence of localized spins which strongly interact with charge carriers[1] and make their own significant contribution to the PMS, not to mention the possible formation (see Ref. 1) of an anisotropic order parameter. However, these (and some other) factors cannot be studied simultaneously and consistently so far.

*E-mail: vloktev@gluk.apc.org

[1)]The direction of the field is insignificant for subsequent calculation; it should be noted, however, that if the field lies in the plane of motion of fermions, the diamagnetic contribution to the total magnetic susceptibility is ruled out automatically.

[1] V. M. Loktev, Fiz. Nizk. Temp. **22**, 3 (1996) [Low Temp. Phys. **22**, 1 (1996)].
[2] B. G. Levi, Physics Today **49**, 17 (1996).
[3] D. Pines, Tr. J. Physics **20**, 535 (1996).
[4] *Proc. of the 10th Anniversary of HTS Workshop on Physics, Materials, and Applications* (Texas, Houston, March 12–16, 1996), World Scientific, Singapore (1996).
[5] J. W. Loram, K. A. Murza, J. R. Cooper, and W. Y. Liang, Phys. Rev. Lett. **71**, 1740 (1993).
[6] Y. Fukuzumi, K. Mizuhashi, K. Tanaka, and S. Ushida, Phys. Rev. Lett. **76**, 684 (1996).
[7] D. S. Marshall, D. S. Dessau, A. G. Loeser *et al.*, Phys. Rev. Lett. **76**, 4841 (1996).
[8] H. Alloul, T. Ohno, and P. Mendels, Phys. Rev. Lett. **63**, 1700 (1989).
[9] V. Barzykin and D. Pines, Phys. Rev. B **52**, 13585 (1995).
[10] D. Scalapino, Tr. J. Physics **20**, 560 (1996).
[11] V. P. Gushynin, V. M. Loktev, and S. G. Sharapov, Fiz. Nizk. Temp. **23**, 816 (1997) [Low Temp. Phys. **23**, 612 (1997)].
[12] V. M. Loktev, S. G. Sharapov, and V. N. Turkowski, Preprint, Cond-mat/9703070.
[13] M. A. Kvasnikov, *Thermodynamics and Statistical Physics* [in Russian], Izd. MGU, Moscow (1991).
[14] C. Berthier, M. H. Julien, M. Horvatic, and Y. Berthier, J. Phys. (Paris) **6**, 2205 (1996).
[15] V. M. Loktev and S. G. Sharapov, Fiz. Nizk. Temp. **23**, 180 (1997) [Low Temp. Phys. **23**, 132 (1997)].

Translated by R. S. Wadhwa

Temperature dependence of the dislocation component of the modulus defect in deformed bcc metals

P. P. Pal-Val

*B. Verkin Institute for Low Temperature Physics and Engineering, National Academy of Sciences of the Ukraine, 310164 Kharkov, Ukraine**

(Submitted July 31, 1997)
Fiz. Nizk. Temp. **23**, 1250–1255 (November 1997)

Experimental data on temperature dependences of the dislocation component of the modulus defect are obtained for some bcc metals (Mo, Fe, and Nb) of different purity and orientation. Measurements are made at frequencies $\omega/2\pi \simeq 90$ kHz in the temperature range 6–300 K. It is found that the modulus defect in Mo and Fe single crystals increases monotonically with temperature starting from 6 K. The increase in the modulus defect becomes stronger in temperature intervals in which relaxation peaks were observed earlier on the temperature dependences of absorption. It is shown that such a behavior of the modulus defect is due to some thermally activated dislocation processes with a broad distribution of activation parameters, which occur in the given temperature range. In contrast to Mo and Fe, Nb shows no temperature dependence of the modulus defect up to 170–200 K, but at higher temperatures it increases rapidly. The existence of a broad temperature region in which the modulus defect is constant indicates that thermally activated processes with a relaxation time close to the reciprocal cyclic frequency $1/\omega$ are either absent or suppressed considerably in this temperature range.
 [S1063-777X(97)01511-9]

INTRODUCTION

The total strain in a mechanically loaded real crystal is the sum of the elastic and inelastic components. The inelastic component is determined to a considerable extent by the mobility of structural defects (above all, dislocations) contained in the crystal. The main difference between the elastic and inelastic strain components is that elastic deformation occurs ''instantaneously,'' while inelastic deformation is a function of time. This is due to a certain relaxation time τ characterizing the mobility of crystal structure defects. By definition, the elastic modulus is the ratio of the applied stress to the total strain of the crystal. In view of the presence of the relaxing strain component, we distinguish between two limiting values of elastic moduli: unrelaxed modulus E_U (i.e., the elastic modulus at the instant of application of a load, when the inelastic component of strain is zero), and relaxed modulus E_R (i.e., the modulus measured in a time interval exceeding τ considerably, when the inelastic strain has the maximum value). The quantity $(E_U-E_R)/E_U \equiv \Delta$ is known as the maximum defect of modulus. If we apply a periodic load of frequency ω to the crystal, the dynamic elastic modulus measured in experiments will have an intermediate value $E_R<E<E_U$, i.e., a certain intermediate defect of modulus $\Delta E/E$ will be observed. In the approximation of a linear standard rigid body, this quantity can be expressed in the form (see, for example, Ref. 1)

$$\frac{\Delta E}{E} \equiv \frac{E_U-E}{E_U} = \Delta \frac{1}{1+\omega^2\tau^2}. \tag{1}$$

The value of Δ is determined by the number of microscopic relaxators of various types and by their individual contribution to inelastic deformation under given experimental conditions, in particular, at a given temperature. In the general case, we are dealing with a complex superposition of contributions from different microrelaxators, and a special choice of experimental conditions is required for the objects of interest to make the dominating contributions. This problem has a relatively simple solution when we analyze the dislocation contribution to dynamic moduli. At first, thoroughly annealed samples are investigated, which are subsequently subjected to plastic deformation, and repeated measurements are made. On the contrary, in other experiments the deformed samples are studied first, and then dislocations contained in them are fined by irradiation or annealing. If deformation is carried out mainly due to slip, the change in elastic moduli can be attributed to changes in the dislocation structure of the crystals, i.e., the creation of new dislocations and untrapping of the initial dislocations. To our knowledge, the authors of all publications in this field assumed (explicitly or implicitly) in an analysis of experimental data that the dislocation contribution to inelastic strain in annealed (or irradiated) samples is equal to zero. In this case, formula (1) can be written in the form

$$\left(\frac{\Delta E}{E}\right)_d \cong \frac{E_0-E_\varepsilon}{E_0} = \Delta_d \frac{1}{1+\omega^2\tau_d^2}, \tag{2}$$

where E_0 is the measured dynamic elastic modulus in annealed (or irradiated) samples, E_ε the dynamic elastic modulus in deformed samples, and the subscript d indicates the dislocation nature of the relaxation under investigation.

Dynamic dislocation effects are usually described qualitatively and quantitatively on the basis of the string model of dislocation proposed by Granato and Lücke[2] as well as the kink model of dislocations developed by Seeger and subsequently by other researchers.[3–5] Several dislocation processes making contributions to additional dislocation-

TABLE I. Basic parameters of samples.

Metal	Orientation	Impurities, 10^{-4} wt. %	RRR	Residual strain, %	$\Delta E/E$ (6 K, 10 K for Nb)	$\Delta E/E$ (300 K)
	⟨111⟩	—	$1.5\cdot10^5$	0.25	$7.65\cdot10^{-5}$	$7.2\ \cdot10^{-4}$
				0.019	$7.41\cdot10^{-5}$	$7.23\cdot10^{-4}$
Mo	⟨110⟩	7	$1.2\cdot10^5$	0.24	$1.16\cdot10^{-3}$	$6.4\ \cdot10^{-3}$
				0.59	$2.79\cdot10^{-3}$	$2.13\cdot10^{-2}$
	⟨941⟩	—	$0.95\cdot10^5$	0.34	$9.25\cdot10^{-4}$	$7.0\ \cdot10^{-3}$
	⟨100⟩	~2	$1\cdot10^4$	0.65	$1.14\cdot10^{-2}$	$2.64\cdot10^{-2}$
Nb		10	$2\cdot10^3$	15	$1.33\cdot10^{-2}$	$8.8\ \cdot10^{-2}$
	Polycrystal	500	60	5	$7.32\cdot10^{-2}$	$7.69\cdot10^{-2}$
	⟨100⟩		—	0.82	$9.07\cdot10^{-4}$	$6.73\cdot10^{-3}$
Fe	⟨941⟩	~1	—	0.84	$9.95\cdot10^{-4}$	$4.31\cdot10^{-3}$
				2.76	$4.39\cdot10^{-3}$	$1.48\cdot10^{-2}$

induced deformation, and hence determining the quantities Δ_d and τ_d, can be distinguished. The most important processes in the low-temperature region are quasiviscous flow of dislocations,[2,6,7] the motion of dislocation segments in the force field of trapping centers,[2,8,9] the formation of kink pairs at dislocations,[3] and migration of geometrical kinks along a dislocation.[4,5,10,11] In most cases, an analysis of these processes by acoustic methods was carried out by using the temperature and amplitude dependences of sound absorption, while similar dependences of dislocation modulus defect were practically not used for this purpose. Moreover, while a large number of theoretical publications were devoted to detailed interpretation of dislocation anomalies of sound absorption, peculiarities in variation of the dislocation modulus defect were not studied sufficiently. The lack of information is especially noticeable in the temperature dependences of elastic modulus defect. In some cases, this led to erroneous assumptions and even unjustified generalizations concerning the dislocation contribution to the modulus defect measured in a wide temperature interval. An analysis of some of these assumptions will be given below in the discussion of the obtained experimental results.

In the present communication, we report on systematic experimental results on the temperature dependences of the Young modulus defect in some bcc transition metals (Mo, Fe, and Nb), which were obtained in the temperature range 6–300K. Typical features of these dependences are revealed and analyzed on the basis of available theoretical concepts concerning the dynamic behavior of dislocations in crystals.

EXPERIMENT

The samples were cut from Mo, Fe, and Nb single crystals of various purity and orientation. The integral measure of sample purity in the case of Mo and Nb single crystal was the residual resistance $RRR=R_{300}/R_0$ reduced and extrapolated to 0 K. The orientation of monocrystalline samples was determined by using Laue diffraction patterns. For the sake comparison, one of Nb samples was polycrystalline with an average grain size smaller than 0.1 mm. The initial density of growth dislocations was $\sim10^5-10^6$ cm^{-2}. The main parameters of the samples under investigation are given in Table I.

Acoustic measurements were made by the method of a double compound vibrator.[12] Longitudinal standing waves with an oscillatory frequency ~90 kHz were excited in the samples. The application of resonant methods in an analysis of small variations in elastic moduli is most expedient since these methods can ensure a relative error in the measurements of the elastic modulus as small as 10^{-8}. We measured the resonant frequency of forced vibrations of the samples from which the corresponding velocity of sound and elastic moduli were determined. The temperature dependences of the resonant frequency of the samples were measured in undeformed and deformed samples in the temperature range 6–300 K at a constant amplitude of ultrasonic strain $\varepsilon \sim10^{-7}$. Special measures was taken to carry out experiments in the amplitude-independent range; for this purpose, the amplitude dependences of the resonant frequency of the samples were measured preliminarily. As a rule, the amplitude ''margin'' of the beginning of amplitude dependence was not smaller than strain. The dislocation component of the modulus defect was determined from formula (2). Temperature dependences of decrement of vibrations (which were reported earlier and are not presented here) were measured simultaneously.

The relation between acoustic properties of the samples and dislocation processes was established by introducing fresh dislocations in the samples by deforming them at room temperatures to residual plastic strain varying from 0.019 to 15% for different samples.

DISCUSSION OF THE RESULTS OF MEASUREMENTS

The results obtained for different metals differ noticeably both qualitatively and quantitatively; for this reason, the results will be described and analyzed separately.

Molybdenum

Figure 1(a) shows the temperature dependences of $\Delta E/E$ obtained for samples with different orientations at approxi-

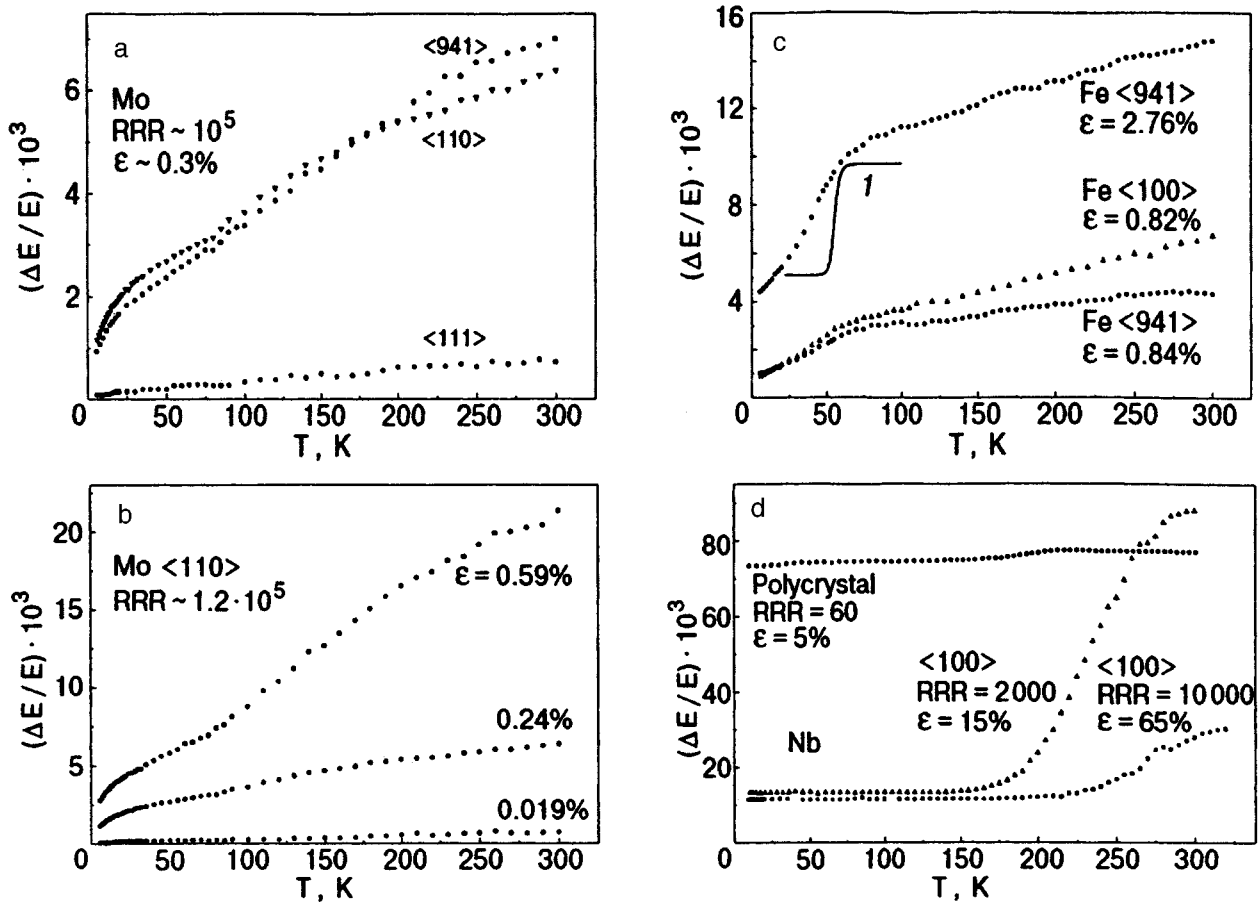

FIG. 1. Temperature dependences of modulus defect for various orientations of samples and various preliminary plastic strains in Mo (a,b), Fe (c) (curve *1* describes the dependence $(\Delta E/E)(T)$ defined by formulas (2) and (5) for the activation energy $U=0.071$ eV and frequency of attempts $\nu_0=5\cdot10^{12}$ s^{-1}),[24] and Nb (d).

mately the same level of a preliminary plastic deformation. The main feature of the $(\Delta E/E)/(T)$ curves is the monotonic and considerable increase in the dislocation component of modulus defect in the entire temperature range. The value of $\Delta E/E$ at room temperature is almost an order of magnitude larger than its value at 6 K (see Table I). This peculiarity was considered earlier by us[13] and by Wire and Granato[14] who obtained results for NaCl and copper. Figure 1b shows that the observed effect is preserved upon an increase in residual plastic strain and in the absolute value of $\Delta E/E$, although the relative change with temperature becomes slightly smaller. Wire and Granato[14] assumed that the behavior of $\Delta E/E$ in NaCl and Cu is the same and that it is due to the movement of dislocation segments in the Cottrell field of interaction with point defects, which increases statistically with temperature. However, the proposed model, first, gives an increase in modulus defect not more than by a factor of four, which does not correlate with most of our results, and second, such a behavior of $(\Delta E/E)(T)$ is not universal (see below).

It should be noted that in some publications (see, for example, Refs. 15, 16) the deformation modulus defect was used for obtaining the temperature dependence $B(T)$ of the dislocation drag coefficient. It was assumed implicitly that the entire deformation modulus defect is due to quasiviscous relaxation of dislocations, which, in accordance with the Granato-Lücke theory,[2] has the following expression for the modulus defect in the range of low vibrational frequencies $(\omega\tau_{dv}\ll1)$ and amplitudes:

$$\left(\frac{\Delta E}{E}\right)_v \approx \Delta_v = \frac{48Gb^2}{\pi^4 C}\,\Omega\Lambda L^2, \tag{3}$$

where G is the shear modulus, b the modulus of the Burgers vector, C linear tension of dislocations, Ω the orientational factor, Λ the dislocation density, and L the length of a dislocation segment. Since $C\approx Gb^2/2$, the quasiviscous contribution to modulus defect must be virtually independent of temperature, which contradicts most of experimental results. At high frequencies for which $\omega\tau_{dv}\sim1$, the modulus defect associated with quasiviscous flow of dislocations must decrease upon an increase in temperature due to an increase in the dislocation drag coefficient B since, according to Granato and Lücke,[2] the relaxation time τ_{dv} increases with temperature in this case:

$$\tau_{dv}=\frac{B(T)L^2}{\pi^2 C}. \tag{4}$$

To our knowledge, the decrease in the value of $\Delta E/E$ with increasing temperature was detected experimentally only

once,[17] and hence we can state that the quasiviscous component of dislocation relaxation does not dominate as a rule in deformed crystals. Consequently, the use of $\Delta E/E$ for determining $B(T)$ and other characteristics of a viscous flow of dislocations requires at least a preliminary analysis of the temperature dependence of the modulus defect as, for example, in Ref. 15. It should also be borne in mind that no clearly manifested acoustic anomalies (absorption peaks, etc.) were observed on the temperature dependences of decrement $\delta(T)$ in molybdenum in the range of temperatures and plastic strains under investigation,[18–20] in contrast to the case when the behavior of $B(T)$ was studied, and the $\delta(T)$ curve had a relaxation peak. Kobelev *et al.*[21] proposed an algorithm for separating the quasiviscous and relaxation components of sound absorption and modulus defect, which includes information on the position of the relaxation peak on the temperature axis as an essential element.

The behavior of the modulus defect in the helium temperature range, in which a sharp increase in the value of $\Delta E/E$ gives way to a more gently sloping region above ~ 25 K, is of considerable interest. The height of the ''step'' formed in this case increases with preliminary plastic strain. This peculiarity correlates with a considerable increase in the decrement in this temperature region.[12,18,19] It will be shown below that the presence of a ''step'' can indicate a strong acoustic relaxation at temperatures below 10 K. Another peculiarity of this type, which is clearly manifested at relatively high strains, is observed near 150 K.

Iron

Temperature dependences of the modulus defect in high-purity Fe single crystals proved to be similar to a certain extent to those obtained for molybdenum (see Fig. 1c). At temperatures 60–70 K, the $(\Delta E/E)(T)$ curves have a well-defined inflection (''step''). As in the case of Mo, the total modulus defect and the height of the ''step'' increase with preliminary plastic strain in the samples. The position of the ''step'' and the variation of its height with preliminary strain correlate with the presence of the so-called α-peak on the temperature dependences of the decrement near 55 K. The height of this peak increases with plastic strain, while the position on the temperature scale remains unchanged. It was proved in Refs. 21–23, that the α-peak in Fe is due to the thermally activated formation of pairs of double kinks at 'non-screw' dislocations. For thermally activated relaxation processes, the relaxation time τ_{th} can be written in the form

$$\tau_{\text{th}} = \nu_0^{-1} \exp(U/kT), \tag{5}$$

where ν_0 is the frequency of attempts, U the activation energy, and k the Boltzmann's constant. In Ref. 22, the following activation parameters were obtained for the γ-peak in Fe: $U \simeq 0.071$ eV and $\nu_0 \simeq 5 \cdot 10^{12}$ s^{-1}. The solid curve in Fig. 1c shows the dependence $(\Delta E/E)(T)$ obtained by formulas (2) and (5) taking into account the above activation parameters. It can be seen that formulas (2) and (5) predict a much narrower temperature region of transition from a nonrelaxed to relaxed state than that observed in experiments. Moreover, the increase in $\Delta E/E$ with temperature continues after the transition also, although this increase is slower than in the peak region. This is apparently associated with the fact that deformation defects responsible for relaxation have a wide distribution of activation parameters, and the end of one of thermally activated relaxation processes extended on the temperature scale in most cases overlaps with the extended beginning of the next process corresponding to a higher temperature. In this way, a continuous spectrum of mechanical relaxations is formed. The increment of intensities of these relaxations increases considerably for $\omega\tau_d \to 1$, but is not equal exactly to zero in any case. This explains the continuous increase in the deformation modulus defect in Mo and Fe.

Niobium

The experimental results obtained in Nb single crystals and polycrystals differ considerably from the results for Mo and Fe described above. The dependences $(\Delta E/E)(T)$ presented in Fig. 1d have extended segments in the low-temperature region (from 10 to ~ 200 K), in which the temperature dependence of the modulus defect is utterly absent in spite of considerable value of $\Delta E/E$ after plastic deformation. This means that thermally activated relaxation processes in Nb in the temperature range $\sim 10-200$ K,[1)] which are connected with deformation defects and have a typical relaxation time of the order of $1/\omega$, are either absent or suppressed to a considerable extent. A sharp increase in the value of $\Delta E/E$ in single crystals at higher temperatures, which correlates with the acoustic absorption peak in this temperature range as in the case of Mo and Fe, indicates the emergence of such a process in the high-temperature region of the temperature range under investigation.

CONCLUSIONS

1. Single crystals of Mo and Fe display a monotonic increase in the dislocation component of the modulus defect in the temperature range 6–300 K at ultrasonic frequencies ~ 90 kHz, indicating the presence of a large number of thermally activated microscopic relaxators (trapped dislocation segments and kink pairs) with a wide spectrum of activation parameters. This can be, for example, due to a distribution of dislocation segments over length and/or a change of this distribution with temperature.

2. Niobium single crystals and polycrystals are characterized by the extended ($\sim 10-200$ K) segment on which the modulus defect is independent of temperature. In all probability, thermally activated processes with a relaxation time close to the reciprocal cyclic frequency $1/\omega$ of vibrations are either absent, or suppressed significantly in this temperature range.

3. In temperature regions where the increment of the modulus defect increases abruptly (i.e., a ''step'' is formed on the $(\Delta E/E)(T)$ curves), temperature dependences of sound absorption have relaxation peaks. The ''step'' is blurred in temperature more strongly than predicted by the rheological model of a ''standard linear rigid body'', which also points to a wide distribution of activation parameters of corresponding relaxation processes.

The author is grateful to V. D. Natsik for his interest to this research and for fruitful discussions and to L. N. Pal-Val for assistance in experiments and in the preparation of the manuscript.

This research was carried out under partial financial support of the Swiss National Science Foundation (grant No. 7UKPJ048645).

*E-mail: palval@ilt.kharkov.ua

[1)]Here we report on the experimental data obtained for Nb in the temperature range above the superconducting transition temperature $T_c \simeq 9.3$ K. The results obtained in the temperature range 2–12 K were described and discussed earlier in Refs. 10 and 11.

[1] A. Novick and B. Berry, *Relaxation Phenomena in Crystals* [Russian transl.], Atomizdat, Moscow (1975).
[2] A. V. Granato and K. Lücke, J. Appl. Phys. **27**, 583 (1956).
[3] A. Seeger and P. Schiller, in *Physical Acoustics. Principles and Methods* (ed. by W. Mason), vol. 3, pt. A, Academic Press, New York (1966).
[4] G. Alefeld, J. Appl. Phys. **36**, 2642 (1965).
[5] A. Seeger and C. Wüthrich, Nuovo Cimento B **33**, 38 (1976).
[6] M. I. Kaganov, V. Ya. Kravchenko, and V. D. Natsik, Usp. Fiz. Nauk **111**, 655 (1973) [Sov. Phys. Usp. **16**, 878 (1973)].
[7] V. I. Alshits and V. L. Indenbom, Usp. Fiz. Nauk **115**, 3 (1975) [Sov. Phys. Usp. **18**, 1 (1975)].
[8] M. Koiwa and R. R. Hasiguti, Acta Metall. **13**, 1219 (1965).
[9] V. L. Indenbom and V. M. Chernov, Phys. Status Solidi A **14**, 347 (1972).
[10] P. P. Pal-Val, V. D. Natsik, and L. N. Pal-Val., Fiz. Nizk. Temp. **21**, 647 (1995) [Low Temp. Phys. **21**, 505 (1995)].
[11] V. D. Natsik and P. P. Pal-Val., Fiz. Nizk. Temp. **23**, 1229 (1997) [Low Temp. Phys. **23**, 922 (1997)].
[12] P. P. Pal-Val and H.-J. Kaufmann, Fiz. Nizk. Temp. **9**, 325 (1983) [Sov. J. Low Temp. Phys. **9**, 163 (1983)].
[13] P. P. Pal-Val and H.-J. Kaufmann, *Abstracts of Papers to 21th All-Union Conf. On Low Temp. Phys.*, pt. 4, Kharkov (1980).
[14] G. L. Wire and A. V. Granato, J. Phys. (Paris) **46**, C10–167 (1985).
[15] V. Ya. Platkov, V. P. Efimenko, and V. I. Startsev, Fiz. Tverd. Tela (Leningrad) **9**, 2799 (1967) [Sov. Phys. Solid State **9**, 2200 (1967)].
[16] N. P. Kobelev and Ya. M. Soifer, Fiz. Tverd. Tela (Leningrad) **17**, 1516 (1975) [Sov. Phys. Solid State **17**, 989 (1975)].
[17] G. A. Alers and D. O. Thompson, J. Appl. Phys. **32**, 283 (1961).
[18] H.-J. Kaufmann and P. P. Pal-Val, Phys. Status Solidi A **62**, 569 (1980).
[19] H.-J. Kaufmann, P. P. Pal-Val, D. Schulze, and V. I. Startsev, J. Phys. (Paris) **42**, C5–55 (1983).
[20] P. P. Pal-Val and H.-J. Kaufmann, Cryst. Res. Technol. **19**, 1049 (1984).
[21] N. P. Kobelev, Ya. M. Soifer, and V. I. Alshits, Fiz. Tverd. Tela (Leningrad) **21**, 1172 (1979) [Sov. Phys. Solid State **21**, 680 (1979)].
[22] P. P. Pal-Val and S. Kadeckova, Phys. Status Solidi A **94**, K29 (1986).
[23] P. P. Pal-Val, V. D. Natsik, and S. Kadeckova, Phys. Status Solidi A **105**, K37 (1986).
[24] P. P. Pal-Val, V. D. Natsik, and S. Kadeckova, Philos. Mag. A **56**, 407 (1987).

Translated by R. S. Wadhwa

Negative thermal expansion of fullerite C_{60} at liquid helium temperatures

A. N. Aleksandrovskii, V. B. Esel'son, V. G. Manzhelii, and B. G. Udovidchenko

B. Verkin Institute for Low Temperature Physics and Engineering, National Academy of Sciences of Ukraine, 47, Lenin Ave., 310164, Kharkov, Ukraine[1]

A. V. Soldatov and B. Sundqvist

Umea University, Department of Experimental Physics, 90187 Umea, Sweden[2]

(Received August 8 1997)
Fiz. Nizk. Temp. **23**, 1256–1260 (November 1997)

The thermal expansion of fullerite C_{60} has been measured in the temperature range 2–9 K. A compacted fullerite sample with a diameter of about 6 mm and height of 2.4 mm was used. It was found that at temperatures below ~ 3.4 K the linear thermal expansion coefficient becomes negative. At temperatures above 5 K our results are in good agreement with the available literature data. A qualitative explanation of the results is proposed. © *1997 American Institute of Physics.* [S1063-777X(97)01611-3]

A considerable body of data already exists on the physical properties of fullerites.[1] Regarding the thermal expansion, however, no data yet exist on the thermal expansion of C_{60} and other fullerites at temperatures below 5 K (Ref. 2), although one may expect that at liquid helium temperatures there are peculiarities typical of orientational glasses in the behavior of the thermal expansion of C_{60}. In this paper we report the results of measurements of the thermal expansion of C_{60} carried out in the temperature range 2–9 K. Since C_{60} has a cubic lattice, its thermal expansion is isotropic and fully described by a single thermal expansion coefficient. It is therefore not necessary to use single crystals in thermal expansion studies.

The sublimated C60 powder used in our experiment for sample preparation was supplied by Term USA, Berkely, CA, and had a nominal purity of better than 99.98%. No traces of solvents were found by Raman analysis within its accuracy (0.1% by mass). Room-temperature powder x-ray diffraction pattern of the material displayed sharp peaks from fcc structure ($a = 14.13$ Å). In an atmosphere of dry argon the C60 powder was loaded in a small piston-cylinder device used for the sample preparation. After subsequent compacting of the powder at about 1 GPa, the sample (pellet of 6 mm in diameter and about 2.4 mm in height) was immediately transferred into a glass tube and dried under dynamic vacuum 10^{-6} Torr for about 16 h. The compacting procedure was done in air and did not exceed 15 min. Finally, the sample was sealed in vacuum 10^{-6}, shielded from light, and kept in that state for 3 months until the beginning of dilatometric measurements. Before mounting the sample, the glass cell containing the sample was opened in argon atmosphere at excessive pressure of about 200 Torr. During insertion of the sample into the measuring cell of the dilatometer, the sample was exposed to air for no more than 20 min and then was evacuated. During the measurements the vacuum in the dilatometer cell was maintained at the level of 10^{-6} Torr.

The measurements of the linear thermal expansion were carried out in the ILTPE of the National Academy of Sciences of Ukraine by using a capacitive dilatometer,[3] which was specially modified for the measurements on C_{60}. The resolution of the dilatometer was $2 \cdot 10^{-9}$ cm. The sample was transported to Kharkov in a vacuum glass cell shielded from light and was held in a high vacuum during the measurements.

The dilatometer was constructed in such a way that all its elements capable of affecting the measured thermal expansion of the sample due to their own thermal expansion were held at constant temperature in a liquid helium bath. The temperature of the sample was measured by a reference germanium resistance thermometer and a differential thermocouple. Since the sample was in a vacuum chamber, it was well insulated thermally. Figure 1 shows a schematic drawing of the measuring cell of the dilatometer. A thermometric block containing the sample thermometer, a thermometer to control the temperature, and a sample heater were mounted on the objective table (*4*) of the dilatometer with which a good thermal contact was established. The fullerite sample studied (*7*) was also located on this table. The temperature difference between the upper and lower parts of the sample was measured by a differential thermocouple (gold-iron alloy versus copper), which measured the temperature difference between the objective table (*4*) of the dilatometer and a fine aluminum foil gasket (*3*) 0.02 mm thick and a 7 mm wide, which is located between the upper part of the sample and a sapphire hemisphere (*6*). Thermal connections between the objective table and the structural elements of the dilatometer and those with the displacement gauge were made by sapphire-sapphire point contacts. Because of the hardness and thermal conductivity of single-crystal sapphire, such contacts were found to perform very well in dilatometers.[4,5] According to the data of Carr and Swenson,[4] the thermal expansion of a sapphire single crystal along the direction making a 60° angle with respect to the hexagonal axis is $\alpha = 1.2T^{2.2} \cdot 10^{-11}$ K^{-1} in the temperature range under

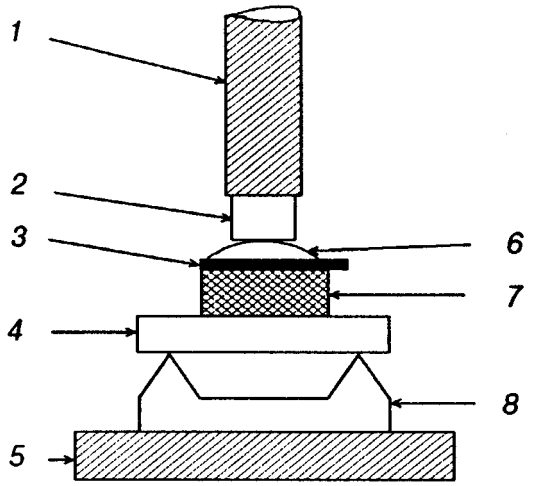

FIG. 1. Schematic drawing of the measuring cell of the dilatometer: rod to sensitive displacement transducer (*1*); sapphire tip (*2*); aluminum packing (*3*); sapphire objective table of the dilatometer (*4*); base for the objective table (*5*); sapphire hemisphere (*6*); C_{60} sample (*7*); sapphire support for the dilatometer objective table (*8*). Elements *1, 2, 5,* and *8* are in a liquid helium bath held at constant liquid helium temperature.

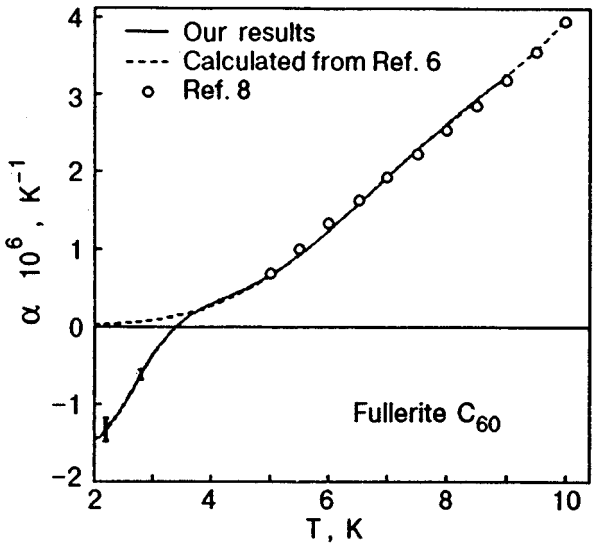

FIG. 2. Linear thermal expansion coefficient of fullerite C_{60}.

consideration. For the direction along the axis this magnitude is probably even smaller since at room temperature the linear thermal expansion of sapphire along the hexagonal axis is an order of magnitude smaller than that in the basal plane.[6] Therefore, in order to have a minimal thermal expansion the sapphire was cut from a single crystal of artificial sapphire in such a way that the direction along which thermal expansion measurements of the studied samples were made coincided with the direction of the hexagonal axis of the sapphire crystals. It should be noted that since we did not know the true contribution of the sapphire and the aluminum foil to the results of thermal expansion measurements of C_{60}, we made additional studies to determine this contribution. From the data obtained by us it was found that this contribution was smaller than the experimental resolution of our setup in the whole range of temperatures studied.

Temperatures below 4.2 K were obtained by pumping out liquid helium into a small container which was in thermal contact with the sample and by continuously refilling it by using the capillary method of DeLong *et al.*[7] The elongation of the sample was measured by a two-terminal capacitive gauge connected so as to determine the frequency of a tunnel diode oscillator circuit. The block containing the capacitive displacement gauge and the tunnel diode oscillator were also placed in a liquid helium bath at constant temperature.

The change in the length of the sample was determined by increasing the temperature and decreasing it. Data on the temperature and sample length were measured once a minute and processed in real time by a computer.

The measurements were made by a temperature step technique. At the beginning of each measurement the sample was held at constant temperature T_1 and the output of the displacement gauge was constant. The temperature of the objective table with the sample was then changed to a temperature T_2, which from that moment was held constant. When the temperature variation of the sample no longer exceeded 0.001 K per minute, we determined the change in its length because of the temperature change from T_1 to T_2. The temperature steps were 0.1–0.3 K, depending on the temperature region. In the temperature range below 4.2 K eight runs were made as the temperature was raised and then lowered, while in the temperature range above 4.2 K three runs were made.

This procedure determined the relative elongation of the sample ($\Delta L/L_0$) as a function of temperature, and the thermal expansion was determined by differentiating these results with respect to temperature.

Figure 2 shows the final results for the linear thermal expansion coefficient α of C_{60} as a function of temperature (the solid curve). The error bars show the estimated experimental errors. A marked increase in the error below 2.5 K is worth noting; however, we have failed to find the reason for this behavior. The most interesting and, at first glance, unexpected result is the negative thermal expansion observed below about 3.4 K. Such a phenomenon has been observed previously in other molecular crystals at liquid helium temperatures, namely, in methane below 8 K (Refs. 8–10) and in a dilute solution of nitrogen in argon at $T<3.5$ K (Ref. 11). For comparison, we show as open circles the existing experimental data from dilatometric studies of the linear thermal expansion coefficient of a single crystal of C_{60} (Ref. 2). In the overlapping temperature range 5–9 K an excellent agreement is observed between these data and our results. As another comparison, the dashed curve shows the results of a calculation of linear thermal expansion coefficient obtained from data for the specific heat capacity of C_{60} (Ref. 12), assuming that the Grüneisen law $\gamma=3\alpha V/C\chi$ is valid, i.e., the behavior expected for α in a quasi-harmonic model for the crystal lattice. Data for the compressibility χ and molar volume V were obtained from Refs. 12–14, and the Grüneisen coefficient γ is assumed to be equal to 3 (Ref. 13), which is close to the Grüneisen coefficients for rare gas solids and for simple molecular crystals with dominant central interactions.[15,16] If instead we use the present data for α to

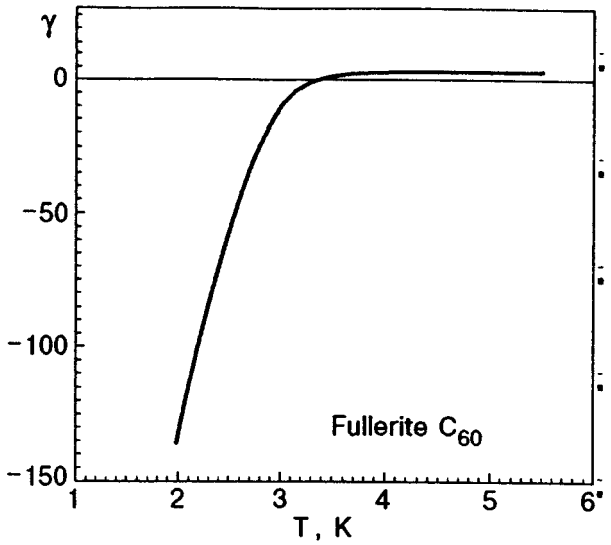

FIG. 3. The Grüneisen coefficient of fullerite C_{60}.

calculate an ''effective'' Grüneisen parameter as a function of temperature, we find that at temperatures below 3.4 K the Grüneisen coefficient is negative and reaches very large values Fig. 3. For a glassy (disordered) material such as an orientationally disordered sc C_{60} we would expect to find a comparatively small contribution to the thermal expansion, which would be proportional to absolute temperature, but against the observed background of very large negative values such a component is impossible to see.

As mentioned above, a negative thermal expansion coefficient has previously been observed in some other molecular crystals, and it is reasonable to assume that the effect observed here arises from the same mechanism. In the case of molecular crystals a negative thermal expansion can arise from the tunneling of molecules between different orientational states with identical energies. It is well known [17] that tunnel energy levels split up into several levels E_i equal to the number of energy equivalent states of the molecule. The Grüneisen coefficient for such levels, $\gamma_i = -(d \ln E_i)/(d \ln V)$, is negative since the magnitude of the separation between the new levels increases with decreasing height and width of the barrier, which prevents a molecule from rotating. In turn, the indicated parameters of the barrier decrease with increasing volume V of the solid in such a way that the derivative of E_i with respect to V is positive and γ_i is negative. In the Grüneisen law approximation $\alpha = \gamma C$, where C is the specific heat and γ is the effective Grüneisen coefficient. It thus follows that at sufficiently low temperatures, where the rotational motion of molecules occurs mainly through tunneling, the thermal expansion coefficient must be negative. The tunnel splitting of energy levels depends exponentially on the height U of the barrier,[17] while U, in turn, has a power dependence on the crystal volume V.[18] The result is that the Grüneisen coefficients are very large.[19,20] The unusually large negative values of γ obtained here are therefore strong evidence for the tunneling nature of the negative thermal expansion.

These considerations are, of course, common for all substances whose molecules have orientational degrees of freedom, but in most cases the thermal expansion becomes negative only at very low temperatures which are beyond the reach of experiment because of the presence of very high barriers that prevent the molecules from rotation. The barrier U, which prevents fullerene molecules from rotating in the solid phase, is also rather high[21] and it seems surprising that tunnel splitting of the levels can reveal itself at such a high temperature as a few degrees. The lowest librational energy levels of fullerite in a low-temperature phase are about 7.3 and 8.5 cm^{-1} (Refs. 22–24). A possible reason for the large tunnel splitting is that the low-temperature ($T < 90$ K) phase of C_{60} is an orientational glass, and for some molecules in the glass the barrier may appear to be significantly lower than that is observed in experiments on crystals with orientational order. Local deformations arising in C_{60} during the formation of the orientational glass[25] might also decrease the value of U. Note that the structure of the glass and, hence, the coefficients α and γ may depend on the history of fullerite samples, and on the type and number of impurities in them.

Finally, impurity atoms and small molecules can be located in interstitial voids and tunnel between them at low temperatures. In principle, this situation must lead to a splitting of their tunnel levels and account for the negative contribution to the thermal expansion. The presence of impurities in the molecular interstitials has also been shown to change the critical temperature for the orientational transition[26] and thus should also have an effect on the barrier U. We therefore note that a small concentration of argon may exist in our sample, which was prepared in an argon atmosphere. On the other hand, the probability of tunneling must be highest for light molecules such as H_2 and for He atoms, but significantly smaller for the comparatively heavy atoms of argon.

Although we can thus explain qualitatively the effect which we observed, no detailed explanation has yet been found. The influence of, for example, the sample history and impurities on the effect requires further investigation, and it would also be interesting to extend the studies to lower temperatures.

We wish to thank A. I. Prokhvatilov and M. A. Strzhemechny for participation in the discussion of the results.

This work was financed, in part, by the Royal Swedish Academy of Sciences and by the State Foundation for Fundamental Research of the Ministry of Science and Technology of Ukraine (Project N2.4/117). B.S. and A.V.S. also acknowledge financial support from the Swedish Research Councils for the Natural Sciences (NFR) and Engineering Sciences (TFR).

[1]E-mail: aalex@ilt.kharkov.ua
[2]E-mail: bertil.sundqvist@physics.umu.se

[1]M. S. Dresselhaus, G. Dresselhaus, and P. C. Eklund, Science of Fullerenes and Carbon Nanotubes, Academic Press, San Diego (1996).
[2]F. Gugenberger, R. Heid, C. Meingast, P. Adelmann, M. Braun, H. Wuhl, M. Haluska, and H. Kuzmany, Phys. Rev. Lett. **69**, 3774 (1992).
[3]A. M. Tolkachev, A. N. Aleksandrovskii, and V. I. Kuchnev, Cryogenics **15**, 547 (1975).
[4]R. H. Carr and C. A. Swenson, Cryogenics **4**, 76 (1964).

[5] K. O. McLean, C. A. Swenson, and C. R. Case, J. Low Temp. Phys. **7**, 77 (1972).
[6] Fizicheskii Enziklopedicheskii Slovar' [in Russian], Sovietskaja Enziklopedia, Moscow (1962), Vol. 2.
[7] L. E. De Long, O. G. Symko, and J. C. Wheatley, Rev. Sci. Instrum. **42**, 147 (1971).
[8] D. C. Heberlein and E. D. Adams, J. Low Temp. Phys. **3**, 115 (1970).
[9] A. N. Aleksandrovskii, V. B. Kokshenev, V. G. Manzhelii, and A. M. Tolkachev, Fiz. Nizk. Temp. **4**, 915 (1978) [Sov. J. Low Temp. Phys. **4**, 435 (1978)].
[10] Yu. A. Freiman, Fiz. Nizk. Temp. **9**, 657 (1983) [Sov. J. Low Temp. Phys. **9**, 335 (1983)].
[11] A. N. Aleksandrovskii, V. G. Manzhelli, V. B. Esel'son, and B. G. Udovidchenko, Low Temp. Phys. **108**, 279 (1997).
[12] W. B. Beyermann, M. F. Hundley, J. D. Thompson, F. N. Diederich, and G. Gruner, Phys. Rev. Lett. **68**, 2046 (1992).
[13] M. A. White, C. Meingast, W. I. F. David, and T. Matsuo, Solid State Commun. **94**, 481 (1995).
[14] A. Lundin and B. Sundqvist, Phys. Rev. B **53**, 8329 (1996).
[15] M. Klein and A. J. Venables (Eds.), Rare Gas Solids, Academic Press, London, New-York, San Francisco (1976).
[16] Physics of Cryocrystals, V. G. Manzhelii and Y. A. Freiman (Eds.), AIP Press, American Institute of Physics, Woodbury, New York (1997).
[17] L. D. Landau and E. M. Lifshitz, Quantum Mechanics [in Russian], Nauka, Moscow (1989).
[18] V. G. Manzhelii, E. A. Kosobutskaya, V. V. Sumarokov, A. N. Aleksandrovskii, Yu. A. Freman, V. A. Popov, and V. A. Konstantinov, Fiz. Nizk. Temp. **12**, 151 (1986) [Sov. J. Low Temp. Phys. **12**, 86 (1986)].
[19] C. R. Case, K. O. McLean, C. A. Swenson, and G. K. White, Thermal Expansion-1971, AIP Conference Proc., New York (1972), p. 312.
[20] G. R. Case and C. A. Swenson, Phys. Rev. B **9**, 4506 (1974).
[21] C. Meingast and F. Gugenberger, Mod. Phys. Lett. B **7**, 1703 (1993).
[22] G. Kato, C. Yokomizo, H. Omata, M. Sato, T. Ishii, and K. Nagasaka, Solid State Commun. **93**, 801 (1995).
[23] S. Huant, J. B. Robert, G. Chouteau, P. Bernier, C. Fabre, and A. Rassat, Phys. Rev. Lett. **69**, 2666 (1992).
[24] T. Yildirim and A. Harris, Phys. Rev. B **46**, 7878 (1992).
[25] S. V. Lubenets, V. D. Natsik, L. S. Fomenko, A. P. Isakina, A. I. Prokhvatilov, M. A. Strzemechny, N. A. Aksenova, and R. S. Ruoff, Low Temp. Phys. **23**, 251 (1997).
[26] G. A. Samara, L. V. Hansen, R. A. Assink, B. Morosin, J. E. Schirber, and D. Loy, Phys. Rev. B **47**, 4756 (1993).

This article was published in English in the original Russian journal. It was edited by S. J. Amoretty

In memorium of Andrei Stanislavovich Borovik-Romanov

Fiz. Nizk. Temp. **23**, 1261 (November 1997)
[S1063-777X(97)01711-8]

Andrei Stanislavovich Borovik-Romanov passed away on July 31, 1997 in Australia where he had gone to attend the International Congress on Magnetism (ICM-97). His demise came as a complete surprise to all of us, for right until the end he was displayed extraordinary activity both in science and in his interaction with friends and colleagues. He spoke about his latest results on nuclear magnetic resonance in antiferromagnets with a trigonal one-dimensional structure with the same type of enthusiasm and pride that accompanied his account about his discoveries of weak ferromagnetism, piezomagnetism of antiferromagnets, and spin current in superfluid ^{3}He. The role of Andrei Stanislavovich in the development of magnetism and low temperature physics is not confined just to his own discoveries. His participation in conferences, seminars, and meetings of the Council on magnetism which he headed for many years were very fruitful and raised a considerable interest in reports containing really important results. As the editor-in chief of the Journal of Experimental and Theoretical Physics, he promoted new ideas in many fields of physics. His impact on research in the fields of magnetism and low temperature physics extended far beyond Moscow. Presenting the results of his research activity in an extremely lucid and intelligible manner, Andrei Stanislavovich won acclaim in many countries (Switzerland, England, USA, Japan, etc.). His beneficent influence on the growth of physics in the Ukraine and especially in Kharkov can hardly be overestimated.

We shall cherish forever fond memories of Andrei Stanislavovich, who was not only a talented physicist, but also highly intelligent and a good-minded person.

Editorial Board

Translated by R. S. Wadhwa

Anatolii Illarionovich Zvyagin (1937–1991) On the 60th birth anniversary

Fiz. Nizk. Temp. **23**, 1262–1263 (November 1997)
[S1063-777X(97)01811-2]

The 60th birth anniversary of the leading Ukrainian scientist, Professor Anatolii Illarionovich Zvyagin, Corresponding Member of the National Academy of Sciences of the Ukraine, falls on November 14, 1997. All through his scientific activity, he was associated with the Physicotechnical Institute for Low Temperature Physics and Engineering headed by him since 1988. His style was distinguished by perception, precision, perfection and the appropriate choice of the subject of investigation. The mainstay of his scientific activity was the study of low-symmetry and low-dimensional magnetic insulators. His scientific intuition and a wide range of perception were responsible for the choice of this subject which is one of the most important topics in solid state physics today. It is in this field that Dr. Zvyagin attained the most impressive results. In his investigations of low-dimensional magnets, Dr. Zvyagin observed and studied subthreshold two-magnon absorption of antiferromagnets in the microwave range.

His discovery in 1983 of exchange branches in the spin wave spectra of a low-dimensional antiferromagnet, which are analogs of optical phonons, and the study of their interaction with ordinary ''acoustic'' magnons, are of special sig-

nificance in the physics of magnetism. His works aimed at finding the effect of low symmetry on various branches off energy excitations in highly anisotropic magnetic crystals, i.e., electron, magnon, and phonon excitations, have become classical. He obtained important results in essentially low-temperature structural and magnetic phase transitions in crystals with a strong spin–phonon interaction.

Anatolii Illarionovich earned fame not only as a leading scientist, but also as a talented scientific organizer. Owing to his zeal, benevolence, facility to infuse others with his ideas, and readiness to share his ideas and experience with his colleagues, he gathered talented and devoted scientists to carry out many investigations, including the study of ferroelastic materials, viz., molybdates and tungstates of rare-earth metals which undergo low-temperature magnetic and structural phase transitions. A specific manifestation of the cooperative Jahn–Teller effect, i.e., a spontaneous deformation of different signs and the splitting of a crystal into sublattices, a peculiar structural analog of an antiferromagnet, were observed in these materials. The results obtained in this field by Dr. Zvyagin were highly acclaimed and triggered intense studies of such ferroelastics both in Ukraine and abroad. A. I. Zvyagin was an active member of various Academic Councils. He was also a member of the Editorial Board of this journal. Dr. Zvyagin paid a lot of attention to the promising young scientists. The seminars in his department were an excellent school for them, and very interesting topics and speakers were selected for these seminars which were marked by a friendly atmosphere and lively discussions, and always attracted large audiences. As a Professor at the Kharkov Polytechnical Institute, he delivered lectures for many years on the physics of magnetism, semiconductor physics, radiospectroscopy, and quantum electronics.

The fruitful research and organizational activity of Dr. Zvyagin won wide acclaim and appreciation. For his cycle of works on ''Discovery and Study of New Types of Resonances, Structures and Magnetoelastic Anomalies in Low-Temperature Antiferromagnets'', he won the Ukrainian State Award in 1991. The pupils, friends and followers of Anatolii Illarionovich cherish the fondest memories about this outstanding scientist and person, and are continuing the investigations initiated by him.

Editorial Board

Translated by R. S. Wadhwa